

Plasma instabilities in Hall Thrusters : a theoretical and numerical study

Federico Petronio

▶ **To cite this version:**

Federico Petronio. Plasma instabilities in Hall Thrusters : a theoretical and numerical study. Plasma Physics [physics.plasm-ph]. Institut Polytechnique de Paris, 2023. English. ⟨NNT : 2023IPPAX030⟩. ⟨tel-04401336⟩

HAL Id: tel-04401336

https://theses.hal.science/tel-04401336v1

Submitted on 17 Jan 2024

HAL is a multi-disciplinary open access archive for the deposit and dissemination of scientific research documents, whether they are published or not. The documents may come from teaching and research institutions in France or abroad, or from public or private research centers.

L'archive ouverte pluridisciplinaire **HAL**, est destinée au dépôt et à la diffusion de documents scientifiques de niveau recherche, publiés ou non, émanant des établissements d'enseignement et de recherche français ou étrangers, des laboratoires publics ou privés.



HAL Authorization

INSTITUT POLYTECHNIQUE DE PARIS

NNT : 2023IPPAX030

Thèse de doctorat

Plasma instabilities in Hall thrusters: a theoretical and numerical study

Thèse de doctorat de l'Institut Polytechnique de Paris
préparée à l'École polytechnique

École doctorale n°626 École doctorale de l'Institut Polytechnique de Paris (EDIPP)
Spécialité de doctorat : Optique, Laser et Plasma

Thèse présentée et soutenue à Palaiseau, le 27 Avril 2023, par

FEDERICO PETRONIO

Composition du Jury :

Jerome Perez Professeur, Laboratoire de Mathématiques Appliquées, ENSTA Paris	Président
Gwenael Fubiani Directeur de recherche, LAPLACE, Université de Toulouse, CNRS	Rapporteur
Aaron Knoll Senior Lecturer, Department of Aeronautics, Emperial College London (UK)	Rapporteur
Francesco Taccogna Researcher, ISTP, CNR (IT)	Examinateur
Igor Kaganovich Professor, PPPL, Princeton University (USA)	Examinateur
Benjamin Laurent Ingénieur, Safran Spacecraft Propulsion	Examinateur
Anne Bourdon Directeur de recherce, LPP, Ecole Polytechnique, CNRS	Directrice de thèse
Pascal Chabert Directeur de recherce, LPP, Ecole Polytechnique, CNRS	Co-directeur de thèse

FEDERICO PETRONIO

PLASMA INSTABILITIES IN HALL THRUSTERS: A THEORETICAL AND NUMERICAL STUDY

PLASMA INSTABILITIES IN HALL THRUSTERS: A THEORETICAL AND NUMERICAL STUDY

FEDERICO PETRONIO





Instabilités dans les plasmas des propulseurs à effet Hall : une étude théorique et numérique

2019-2023

Federico Petronio: *Plasma instabilities in Hall Thrusters: a theoretical and numerical study*, Instabilités dans les plasmas des propulseurs à effet Hall : une étude théorique et numérique, © 2019-2023

Caelum non animum mutant qui trans mare currunt

The sky changes upon those who cross the sea, not their spirit

Book I, Epistle XI, line 27
Horace

ABSTRACT

Hall thrusters (HTs) are electric propulsion systems widely used in space applications since their invention in the '60s. Their $\mathbf{E} \times \mathbf{B}$ configuration allows for ionizing a propellant gas, usually xenon, and accelerating outwards the ions to create thrust. Hall thrusters are used for an increasing diversity of space missions, including telecommunications, Earth observation, scientific exploration, and deep space missions. However, the physics of low-temperature low-pressure magnetized plasmas, typical of these thrusters, is complex; several plasma processes that have direct relevance to the thruster performance and lifetime are still poorly understood. Therefore, currently, long and expensive life tests are required to design and develop new thrusters.

It is necessary to develop in the coming years a new experimental/numerical methodology to propose innovative designs, capable of meeting the issues and challenges of the space industry. Towards this objective, this thesis presents theoretical and simulation results on the physics of low-temperature low-pressure magnetized plasmas in the radial-azimuthal and axial-azimuthal planes of a HT. A 2D Particle-In-Cell (PIC) code, *LPPic*, has been enriched by adding the effects of the third dimension (i. e., the one not considered in the simulation) and an external electric circuit, to get closer to real thrusters. Moreover, a spectral reconstruction technique to locally calculate the power spectral density, the Two-Points Power Spectral Density (PSD2P), has been implemented to analyze the simulation results.

Plasma instabilities have a direct impact on discharge physics and thruster performance, as they strongly influence the anomalous electron transport in the axial direction. In this work, we present a theoretical study on the development of instabilities by deriving a 3D dispersion relation. The 3D dispersion was simplified to recover the best-known 1D and 2D dispersions for this type of plasma and theoretical results were compared with the results of PIC simulations. The radial-azimuthal simulations made it possible to formalize a criterion for the growth of the Modified Two-Stream Instability (MTSI) and to evaluate its contribution to the anomalous transport. For their part, the axial-azimuthal simulations allowed us to characterize the Ion Transit-Time Instability (ITTI), better understanding its growth and its effect on the population of low-energy ions in the plasma plume. In addition, these simulations have explained the propagation of the Ion Acoustic Wave (IAW) in the discharge: this instability starts in the central part of the thruster channel and propagates towards the cathode and anode.

Eventually, *LPPic* has been used to study the influence of different input parameters (cathode electron temperature, anode voltage, mass flow rate, magnetic field shape, propellant gas) on the discharge characteristics and on the thruster performance. The stability of the *LPPic* code with respect to large variations in input values suggests that a 2D PIC code could be used in an experimental/numerical methodology to design new devices selecting interesting configurations/operating conditions before running 3D PIC simulations.

RESUMÉ

Le propulseur à effet Hall (HT) est un système de propulsion électrique largement utilisé dans le domaine spatial depuis son invention dans les années 1960. Sa configuration $\mathbf{E} \times \mathbf{B}$, autrement dit *en champs croisés*, permet d'ioniser un gaz, généralement du xénon, et d'accélérer les ions pour générer de la poussée. Ces propulseurs jouent un rôle essentiel dans diverses missions spatiales, telles que les télécommunications, l'observation de la Terre et l'exploration spatiale lointaine. Cependant, leur fonctionnement repose sur des plasmas froids magnétisés à basse pression, dont la physique est extrêmement complexe. De nombreux phénomènes liés à ces propulseurs restent encore peu compris, mais leur compréhension est cruciale pour améliorer leurs performances et leur durée de vie.

Actuellement, la conception et le développement de nouveaux propulseurs à effet Hall nécessitent des essais de durée de vie longs et coûteux. Il est donc impératif de développer une méthodologie expérimentale/numérique plus efficace pour relever les défis de l'industrie spatiale. Dans ce contexte, la présente thèse propose une approche basée sur des résultats théoriques et des simulations pour étudier la physique des plasmas froids magnétisés à basse pression, en se concentrant sur les plans radial-azimutal et axial-azimutal d'un propulseur à effet Hall. Pour mener à bien ces recherches, le code de simulation Particle-in-Cell (PIC) 2D, appelé *LPPic*, a été amélioré en ajoutant une troisième dimension non simulée et un circuit externe afin de mieux représenter les propulseurs réels. De plus, une technique de reconstruction spectrale (PSD2P) a été mise en œuvre pour analyser localement la densité spectrale de puissance et évaluer les résultats des simulations.

Une attention particulière a été portée aux instabilités du plasma, qui ont un impact significatif sur la physique de la décharge et les performances du propulseur. Ces instabilités affectent le transport anormal des électrons dans la direction axiale, ce qui peut influencer considérablement le fonctionnement du propulseur. Dans le cadre de cette thèse, une étude théorique du développement des instabilités a été réalisée en dérivant une relation de dispersion tridimensionnelle. Cette relation de dispersion 3D a ensuite été simplifiée pour retrouver les relations de dispersion 11D et 2D déjà connues pour ce type de plasmas. Les résultats théoriques ont été comparés aux données issues des simulations PIC. Les simulations réalisées dans le plan radial-azimutal ont permis d'établir un critère pour le développement de l'instabilité modifiée à deux faisceaux (MTSI) et d'évaluer son impact sur le transport anormal des électrons. De plus, les simulations effectuées dans le plan axial-azimutal ont permis de mieux caractériser l'instabilité de transit des ions (ITTI), de comprendre sa croissance et d'étudier son effet sur la population d'ions à basse énergie présente dans le jet du propulseur. Les simulations dans le plan axial-azimutal ont également révélé la formation de l'instabilité acoustique ionique (IAW) dans la partie centrale du canal du propulseur, qui se propage ensuite vers la cathode et l'anode.

En outre, le code *LPPic* a été utilisé pour étudier l'influence de différents paramètres d'entrée tels que la température électronique de la cathode, la tension de l'anode, le débit massique, la forme du champ magnétique et le propergol sur les

caractéristiques de la décharge et les performances du propulseur. Les résultats obtenus ont montré que le code *LPPic* est stable même avec de grandes variations des valeurs d'entrée, ce qui suggère qu'un code PIC 2D pourrait être utilisé dans une approche expérimentale/numérique pour concevoir de nouveaux dispositifs. Cette approche permettrait de pré-sélectionner des configurations ou des conditions de fonctionnement intéressantes avant de réaliser des simulations PIC 3D plus coûteuses.

En conclusion, cette thèse présente une méthodologie numérique innovante pour l'étude des propulseurs à effet Hall. Les résultats théoriques et les simulations numériques ont permis de mieux comprendre la physique des plasmas froids magnétisés à basse pression et ont ouvert la voie à des conceptions plus avancées. Cette recherche contribue à l'affinement de la modélisation des propulseurs à effet Hall, afin d'en améliorer les performances, tout en réduisant les coûts associés à leur développement.

PUBLICATIONS

List of publications of the author in peer reviewed journals. A complete list of all the publications and contributions of the author is available here.

[1] Federico Petronio, Antoine Tavant, Thomas Charoy, Alejandro Alvarez Laguna, Anne Bourdon, and Pascal Chabert. "Conditions of appearance and dynamics of the modified two-stream instability in ExB discharges." en. In: *Physics of Plasmas* 28.4 (Apr. 2021), p. 043504. ISSN: 1070-664X, 1089-7674. DOI: 10.1063/5.0046843.

[2] Willca Villafana, Federico Petronio, Andrew C. Denig, Marylin J. Jimenez, Denis Eremin, Laurent Garrigues, Francesco Taccogna, Alejandro Alvarez Laguna, Jean-Pierre Boeuf, Anne Bourdon, Pascal Chabert, Thomas Charoy, Benedicte Cuenot, Kentaro Hara, François Pechereau, Andrei I. Smolyakov, Dymitro Sydorenko, Antoine Tavant, and Olivier Vermorel. "2D radial-azimuthal particle-in-cell benchmark for E × B discharges." In: *Plasma Sources Science and Technology* 30.7 (July 2021), p. 075002. ISSN: 0963-0252, 1361-6595. DOI: 10.1088/1361-6595/ac0a4a.

[3] Federico Petronio, Thomas Charoy, Alejandro Alvarez Laguna, Anne Bourdon, and Pascal Chabert. "Two-dimensional effects on electrostatic instabilities in Hall Thrusters. I. Insights from particle-in-cell simulations and two-point power spectral density reconstruction techniques." In: *Physics of Plasmas* (Jan. 2023). DOI: 10.1063/5.0119253.

[4] Federico Petronio, Thomas Charoy, Alejandro Alvarez Laguna, Anne Bourdon, and Pascal Chabert. "Two-dimensional effects on electrostatic instabilities in Hall Thrusters. II. Comparison of particle-in-cell simulation results with linear theory dispersion relations." In: *Physics of Plasmas* (Jan. 2023). DOI: 10.1063/5.0119255.

ACKNOWLEDGMENTS

Few times in adult life does one have the opportunity to reflect on the past and express gratitude to those who have contributed to one's journey. This thesis manuscript is for me one of those rare occasions, and I am grateful for that.

First and foremost, I would like to express my deepest gratitude to my advisors, Anne Bourdon, and Pascal Chabert. Your boundless energy and visionary leadership have created and guided the propulsion team at LPP with kindness and wisdom. You should take great pride in the growth and accomplishments of our team. Anne, as my first contact at LPP, I will always be grateful for the warm welcome I received at the lab and for your guidance and support throughout the challenging early months of my doctorate until its completion. Pascal, I am sincerely thankful for your constant scientific enthusiasm and your ability to understand, discuss, and solve problems. May your inspiration never cease. I am also immensely grateful to Alejandro Alvarez Laguna for his openness and availability. Our conversations have greatly enriched my Ph.D. journey.

A Ph.D. thesis is not directed by official supervisors alone. The contributions of colleagues are equally important for its development. For this reason, I would like to extend my heartfelt appreciation to Antoine Tavant and Thomas Charoy. Antoine, you introduced me to PIC and guided me during the initial months. I owe you a tremendous debt of gratitude for your patience with me as a newcomer. Thomas, thank you for your invaluable help and support when I began working "on the other plane." This thesis would not have been here without you.

If my Ph.D. has reached a successful conclusion, it is due to the wonderful people I have encountered along the way. First, I would like to acknowledge my colleagues in the PhDarium, Benjamin, Edmond, Tarek, and Nicolas, who have transformed this experience into a remarkable adventure. May our friendship endure beyond our doctorates. A special mention goes to Benjamin, who came to me in 2019 with the words, "There's a Ph.D. position open in LPP...". I would also like to recognize the contributions of other colleagues with whom I have had enlightening exchanges throughout these years: Louis, Lui, Alexandre, and Loic. I am grateful to the people of LPP for fostering a wonderful environment and for their dedication to science each day. In particular, Olivier, David, Cyril, and Garrett, among others, meeting all of you has been an incredible opportunity for me. I would also like to extend my best wishes to the new team members, Anatole and Pierre. I am confident that you will be satisfied with your Ph.D. as I am with mine.

I would like to express my gratitude to all the people I have collaborated with over the years. Firstly, I want to thank Benjamin, Willca, and Guillaume for our fruitful collaboration, and Umesh and the HLST team of CINES for their support. Latterly, I extend my appreciation to the members of the $E \times B$ community, as well as my Ph.D. committee. I am proud to be part of this community.

I firmly believe that one's character is shaped by the people they meet during life. If I am who I am today, it is thanks to those who have left me something and have shared this journey with me: Beso, Felpo, Leo, Mirio, Miso, Picci, Sara, Noe, Giorgio, Katia, Iaia, Guaro, Giacomo, Checca, Francesca, and Alessandra. You hold great significance in my life. When living abroad, it is essential to build a new life in the place you call home. Brigi, Giulia, Tommi, Lien, Michele, Sara, Matte, Ste, Carlo, Ivan, and Tchos, thank you for being there for me throughout these years. A special thanks also to Franco for his music, to Javier for his writings, and to Alessandro for his lectures.

Lastly, I want to express my gratitude to my family. To my parents Carlo and Elisa, who have always believed in and supported me; to my siblings, Rosa and Francesco, for their unwavering backing—I am here for you, just as you have been there for me; and to my grandparents, Rosalia, Luciano, and Vitta, I am fortunate to have spent a significant part of my life with you.

In conclusion, I would like to extend a special thank you to Elisa. Without you, I would have lost my way. While I am neither pessimistic nor optimistic enough to make any prediction, I am rational enough to genuinely hope that we will be there for each other for the longest time.

CONTENTS

1 INTRODUCTION 1
1.1 Space propulsion . . . 1
1.1.1 Chemical or electric propulsion . . . 2
1.1.2 EP history . . . 3
1.1.3 Electric propulsion systems . . . 4
1.1.4 EP parameters . . . 5
1.2 Hall thrusters . . . 6
1.2.1 Hall thruster basics . . . 6
1.2.2 Plasma boundaries . . . 9
1.2.3 Hall thruster anomalous transport . . . 10
1.2.4 Plasma instabilities in Hall thrusters . . . 12
1.2.5 Main challenges . . . 15
1.3 Hall thruster plasma modeling . . . 16
1.3.1 Plasma modeling basics . . . 16
1.3.2 Plasma parameters . . . 18
1.3.3 Plasma modeling techniques . . . 19
1.4 Scope and outline of the thesis . . . 22
2 PLASMA INSTABILITIES 23
2.1 Why instabilities? . . . 24
2.2 The electrostatic dispersion relation . . . 24
2.2.1 Derivation of the 3D dispersion relation . . . 25
2.2.2 Ion acoustic wave . . . 28
2.2.3 Modified Two-Stream Instability . . . 30
2.2.4 Ion transit-time instability . . . 33
2.2.5 Resistive modes . . . 35
2.2.6 Other electrostatic instabilities . . . 36
2.3 Plasma instability spectral analysis . . . 37
2.3.1 Discrete Fourier Transform . . . 37
2.3.2 Two-points power spectral density . . . 38
2.3.3 Dynamic Mode Decomposition . . . 41
2.4 Chapter summary . . . 42
3 NUMERICAL METHODS 43
3.1 PIC challenges . . . 44
3.2 *LPPic*: a 2.5D PIC code for Hall thrusters . . . 44
3.2.1 Numerical implementation of LPPic . . . 44
3.2.2 The radial-azimuthal simulations . . . 49
3.2.3 The axial-azimuthal simulations . . . 51
3.2.4 Development and optimization of *LPPic* . . . 54
3.3 Scaled permittivity effect . . . 55
3.3.1 Effect of the permittivity scaling on the computational cost . . . 56
3.3.2 Effect of the permittivity scaling on plasma parameters . . . 57
3.3.3 Effect of the permittivity scaling on the plasma instabilities . . . 63

3.3.4 Effect of the permittivity scaling on the mobility . . . 66
3.3.5 Other effects on instabilities . . . 67
3.4 The circuit implementation . . . 69
3.4.1 Circuit equations and coupling with the PIC code . . . 69
3.4.2 Transfer Function . . . 70
3.4.3 Analysis of the circuit effect on PIC simulations of different domain sizes 73
3.4.4 Effect of the cathode temperature on the circuit response . . . 77
3.4.5 Current in the circuit components . . . 77
3.5 Chapter summary . . . 78
4 RADIAL–AZIMUTHAL INSTABILITES 81
4.1 Radial-azimuthal PIC simulations . . . 82
4.2 Analysis of MTSI . . . 82
4.2.1 The PIC model . . . 83
4.2.2 Methods used for the analysis of PIC results . . . 84
4.2.3 Study of the onset of MTSI in PIC simulations . . . 85
4.2.4 Effect of the dimension of the computational domain on the MTSI . . . 87
4.2.5 Influence of the domain the azimuthal length . . . 88
4.2.6 Impact of plasma density and axial electric field on the MTSI . . . 90
4.2.7 Summary of results, comparison with previously published results and discussion . . . 92
4.2.8 Evolution of the plasma properties with the MTSI . . . 95
4.3 Radial-azimuthal benchmark . . . 100
4.3.1 Test case description . . . 101
4.3.2 Selected benchmark results: electron temperature, plasma density and frequency analysis . . . 102
4.4 Chapter summary . . . 105
5 AXIAL–AZIMUTHAL SIMULATIONS SPECTRAL ANALYSIS 107
5.1 Axial-azimuthal simulations . . . 107
5.2 Spectral analysis of the BM phases . . . 108
5.2.1 Analysis during the growing phase of the BM . . . 112
5.2.2 Analysis in the decreasing phase of the BM . . . 112
5.2.3 Analysis over the entire BM period . . . 115
5.2.4 Summary . . . 115
5.3 Instabilities in axial-azimuthal simulations . . . 118
5.3.1 The IAW in two dimensions . . . 118
5.3.2 The ion transit-time instability . . . 128
5.4 Chapter summary . . . 136
6 VIRTUAL RADIAL (THIRD) DIMENSION 137
6.1 Third radial dimension modeling . . . 138
6.1.1 Choice of the model for the virtual-*r* . . . 139
6.1.2 The Bohm flux at the walls . . . 139
6.1.3 Numerical implementation of the virtual-*r* . . . 140
6.2 Study of the effect of the virtual-r in 2D axial-azimuthal PIC simulations 144
6.2.1 Macroscopic effects of the virtual-*r* . . . 146
6.2.2 Influence of the virtual-*r* on the instabilities . . . 153
6.2.3 Effect of the virtual-*r* on the thruster performance . . . 160
6.2.4 Summary of important results . . . 163

6.3 Secondary Electron Emission effects . . . 163
6.3.1 SEE Model . . . 163
6.3.2 SEE in virtual-*r* PIC simulations . . . 165
6.4 Analysis of consistent virtual-*r* width . . . 166
6.4.1 PIC results . . . 166
6.4.2 Mass utilization efficiency . . . 169
6.5 Chapter summary . . . 170
7 LPPIC: AN ENGINEERING TOOL 171
7.1 Introduction . . . 172
7.2 Analysis of the BM dynamics using a PIC run . . . 172
7.2.1 Analysis of breathing mode . . . 172
7.2.2 Impact of electron temperature and densities on the ionization mechanism in the BM . . . 176
7.2.3 Study of the drift balance in the BM . . . 177
7.2.4 Electron transport in the axial direction of the thruster . . . 179
7.2.5 Discussion of the main results on the BM . . . 181
7.3 Variation of the HT configuration . . . 181
7.3.1 Anode voltage variation . . . 181
7.3.2 Neutral gas mass flow rate . . . 188
7.3.3 Magnetic field variation . . . 193
7.3.4 Alternative propellants . . . 197
7.3.5 Study of the cathode temperature . . . 201
7.4 Chapter summary . . . 205
8 CONCLUSION 207
8.1 Summary . . . 207
8.1.1 Results from the linear theory . . . 207
8.1.2 Results in the radial-azimuthal simulation plane . . . 208
8.1.3 Results in the axial-azimuthal simulation plane . . . 209
8.2 Perspectives . . . 210
8.2.1 *LPPic* code improvements . . . 210
8.2.2 Comparison with experiments . . . 210
8.2.3 Use the 2.5D *LPPic* code as a design tool for future HTs . . . 211
A APPENDIX 213
A.1 Other circuit implementation . . . 213
A.2 Axial-azimuthal simulation list . . . 215
A.3 Pseudo-virtual radial dimension . . . 216
A.3.1 Introduction . . . 216
A.3.2 Mono-domain . . . 216
A.3.3 Other approaches . . . 217
A.3.4 Conclusions on pseudo-3D . . . 219

BIBLIOGRAPHY 221

LIST OF FIGURES

Figure 1.1 A Hall thruster in operation. Image from CNES, february 2015. 4
Figure 1.2 An ion thruster in operation. Image from *qinetiq.com*. 4
Figure 1.3 HT schematic from Boeuf [110]. 7
Figure 1.4 Ionization (red), magnetic field (blue) and electric field (green) profiles along the thruster axis. The dashed line represents the thruster channel exit. The HT community often refers to the thruster axis as x-axis, to the azimuthal direction as y-axis and to the radial direction as z-axis. 8
Figure 1.5 Representation of instabilities on the frequency spectrum. . . 13
Figure 1.6 The various methods to simulate a plasma. 19
Figure 2.1 Schematic representation of a HT in 3D. The magnetic field is along the z direction, the stationary electric field is along the x direction and the $\mathbf{E} \times \mathbf{B}$ drift occurs in the negative y direction. The cathode is not represented. 25
Figure 2.2 (a) Phase space of the growth rate $\tilde{\gamma}(\tilde{k}_y, \tilde{k}_z)$; (b) frequency $\tilde{\omega}_r(\tilde{k}_y, \tilde{k}_z)$ as calculated numerically from the dispersion relation in Eq. (2.12). The green line shows the position of $\max(\tilde{\gamma})$ obtained with the analytical solution of Eq. (2.15). The black dashed lines in (a) and (b) show the cuts reported in (c) and (d) for, respectively, the growth rate and the frequency. In (c) and (d) the full lines are obtained by solving numerically Eq. (2.12), while the dashed lines are obtained from Eq. (2.14). From Ref. [177]. 32
Figure 2.3 Spectrum in the azimuthal direction calculated from the PIC electron density signal extracted from the plume of an axial-azimuthal simulation: The spectrum is obtained using a 2D FFT technique in (a) and with the PSD2P technique in (b). The PIC signal analyzed is the electron density fluctuations at a fixed axial position for a time interval of 8 µs. The low resolution of the FFT is related to the fact that we used a standard 2D FFT. . 40
Figure 2.4 Dynamic Mode Decomposition applied to the azimuthal electric field in the radial-azimuthal benchmark case. The field is divided in different frequency ranges. The range is indicated in the title of each subfigure. We notice that the signal in (a) is almost zero: this is coherent with the fact that the azimuthal electric field has a null average. 41
Figure 3.1 The PIC/MCC simulation cycle. 45
Figure 3.2 The null collision model used in *LPPic*. 49

Figure 3.3 Radial-azimuthal simulation domain representation. The magnetic field is homogeneous and directed radially (vertically in the image) and the static electric field is homogeneous and directed out of plane. 50
Figure 3.4 The simulation domain for the axial-azimuthal simulations. The simulation domain is a 2D slab of the azimuthal direction. The simulation domain is bounded by the cathode (grounded) and the anode (at high voltage). The cathode is modeled as a quasi-neutral surface. The anode voltage is controlled by an external circuit. 51
Figure 3.5 (a) Speedup dependency on the chosen node type. (b) Speedup dependency on the number of nodes. Adapted from [197]. . . 55
Figure 3.6 Discharge current evolution for different values of the permittivity scaling α_0. 56
Figure 3.7 (a) electric potential and (b) axial electric field averaged over the entire duration (300 µs) simulation for the four cases. . . . 58
Figure 3.8 The spatially averaged value of the axial electric field evolution over time for the four permittivity scaling values. The shaded area covers a 2% interval around the theoretical value (dashed line) calculated with Eq. (3.4). 59
Figure 3.9 Postion (a), value (b) of the maximum of the axial electric field and FWHM (c) of its profile as a function of time for the four cases. The discharge current (d). 60
Figure 3.10 The maximal standard deviation of the fluctuation in the azimuthal direction of the azimuthal electric field is shown in (a). The average maximal standard deviation of the fluctuation in the azimuthal direction of charge density (b), azimuthal electric field (c), and potential are plotted vs the reciprocal of the scaling factor, $1/\sqrt{\alpha_0}$. 62
Figure 3.11 Average energy density profiles. The results are normalized by the same quantity. 63
Figure 3.12 Each row corresponds to a different value of α_0: 4, 16, 32, and 64 from top to bottom. The first column (a, d, g, j) shows a PSD in the axial direction, while the second (b, e, h, k) in the azimuthal one. The last column shows four snapshots. The chosen times correspond to the growing phase of the BM. We highlight the fact that for each α we use different limits in the $k-$range and ω-range. 65
Figure 3.13 Variation of the (a) frequency and (b) wavenumber of the most unstable mode as a function of $\alpha_0^{-1/2}$. The error bars are calculated as the standard variation of the evolution of these value in time. The yellow lines show the linear fits. 66

Figure 3.14 Evolution of the mobility during the BM cycle for the four cases with different scaling factors. Discharge current of the four cases are shown in the first row, the scaling is indicated in the title. The subfigures (b-d) show the axial profiles of the mobility at four different times of the BM cycle. For each case the precise time is indicated by the dot in the first row that has the same color of the frame in (b-d). 68
Figure 3.15 Scheme of the circuit of a HT. The generator applies a DC voltage U_g. The voltage drop at the plasma boundaries and the discharge current are U and I, respectively. 69
Figure 3.16 Bode diagram representing Eq. (3.13) using the chosen circuit parameters: $R = 60\,\Omega$, $L = 4.4\,\text{mH}$ and $C = 15\,\text{nF}$. From Ref. [201] 71
Figure 3.17 The transfer function $H(\omega)$ calculated with Eq. (3.14) for different values of the circuit components. The base solution (red) is compared to a varied resistivity (a), inductance (b), and capacitance (c). 72
Figure 3.18 The simulation mesh is composed of squared cells. The neutral gas is injected at the anode (left) and the electrons at the cathode (right). The axis of the thruster is x and the azimuthal direction is y. We use periodic boundary conditions in the azimuthal direction. The magnetic field intensity is represented by the purple line. It is perpendicular to the simulation plane (along z) and does not change along the azimuthal direction. Please refer to Table 3.2 for a detailed list of the simulation parameters. From Ref. [201] 74
Figure 3.19 Time evolution of the discharge current (a) and the anode potential (b) in 2D PIC axial-azimuthal simulations with an azimuthal length, $L_y = 1\,\text{cm}$ without RLC circuit, and with two different RLC circuits: case 1 is for standard HT circuit components ($R = 50\,\Omega$, $L = 340\,\mu\text{H}$ and $C = 10\,\mu\text{F}$); case 2 is for the optimized set of parameters ($R = 60\,\Omega$, $L = 4.4\,\text{mH}$ and $C = 15\,\text{nF}$). From Ref. [201]. 74
Figure 3.20 Time evolution of the discharge current (a) and the potential (b) in 2D PIC axial-azimuthal simulations with an azimuthal length, $L_y = 4\,\text{cm}$ without RLC circuit, and for two RLC circuits: case A and case B as defined in Table 3.2. 77
Figure 3.21 Time evolution of the discharge current (a) and the potential (b) in 2D PIC axial-azimuthal simulations with an azimuthal length, $L_y = 4\,\text{cm}$ for two T_e^{cath} of injection: case B (5 eV) and case C (0.1 eV). 78
Figure 3.22 Time evolution of the current in the circuit components and voltage drop on each circuit component in 2D PIC axial-azimuthal simulations with an azimuthal length, $L_y = 1\,\text{cm}$, for the optimized RLC circuit in case 2. 79

Figure 3.23 Time evolution of the current in the circuit components and voltage drop on each circuit component in 2D PIC axial-azimuthal simulations with an azimuthal length, $L_y = 4\,\text{cm}$, for the RLC circuit in case C. 79

Figure 4.1 Schematic representation of the radial-azimuthal (zy) simulation domain, with periodic boundary conditions in $y-$direction and two perfectly reflecting walls at the edges of the z one. The snapshot represents the axial current density at 1.5 µs in a simulation domain $1.28\,\text{cm} \times 1.28\,\text{cm}$. Figure from Petronio *et al.* [177]. 84

Figure 4.2 Snapshots of the azimuthal electric field in case no. 3. In (a) we observe the ECDI. The MTSI appears in (b). Figures (c) and (d) show the transition to a chaotic behavior of the system. Adapted from [177]. 87

Figure 4.3 Evolution of the MTSI amplitude mode calculated from the E_y spectrum of four PIC simulations with different radial lengths. The linear regressions used to calculate $\tilde{\gamma}^{PIC}$ are shown by the dashed lines. The azimuthal length is 1.28 cm for all the cases shown here. Adapted from [177]. 88

Figure 4.4 2D snapshots of the azimuthal electric field E_y at $t = 1.5\,\mu\text{s}$ for (a) $L_z = 3.84\,\text{cm}$ (case no. 5) and (c) $L_z = 1.92\,\text{cm}$ (case no. 3). In (b): evolution of the MTSI mode amplitude in the E_y spectrum. The dashed lines in (b) represent the linear regression calculated during the instability growth. Adapted from [177]. 89

Figure 4.5 Snapshots ($t = 1.20\,\mu\text{s}$) of E_y for three different PIC simulations with $L_z = 2.56\,\text{cm}$. (a): $L_y = 0.32\,\text{cm}$, only ECDI (case no. 12). (b): $L_y = 0.64\,\text{cm}$, one MTSI period (case no. 13). (c): $L_y = 2.56\,\text{cm}$, four MTSI periods (case no. 14). Adapted from [177]. 90

Figure 4.6 2D snapshots of the azimuthal electric field E_y at $t = 1.20\,\mu\text{s}$ for (a) the nominal density $n = 5 \times 10^{16}\,\text{m}^{-3}$ (case no. 4) and (b) a larger density $n = 2 \times 10^{17}\,\text{m}^{-3}$ (case no. 15). In (c): evolution of the MTSI mode amplitude in the two cases. Adapted from [177]. 91

Figure 4.7 In (a) the full lines show the position $(\tilde{k}_y, \tilde{k}_z)$ of the maximum of $\tilde{\gamma}$ for different axial electric field calculated from the fluid DR Eq. (2.12). The triangles show the position of $\gamma_{\max}$ obtained with the simplified analytical DR Eq. (2.15). In (b) we show the growth rate $\tilde{\gamma}(\tilde{k}_y)$ for $\tilde{k}_z = 0.035$ for different values of the axial electric field. Adapted from [177]. 92

Figure 4.8 2D snapshots of the azimuthal electric field E_y at $t = 1.20\,\mu\text{s}$ if (a) $E_x = 10\,\text{kV/m}$ and $L_y = 0.64\,\text{cm}$ (case no. 13), (b) $E_x = 30\,\text{kV/m}$ and $L_y = 0.64\,\text{cm}$ (case no. 16) and (c) $E_x = 30\,\text{kV/m}$ and $L_y = 1.28\,\text{cm}$ (case no. 17). Notice that in (a) E_y is magnified by a factor 3. Adapted from [177]. 93

Figure 4.9 The blue line shows the instability limit in Eq. (2.15). The red points represent the couples $(\tilde{k}_y, \tilde{k}_z)$ for which the MTSI is observed. Next to each point, we report the related simulation labels. The purple points represent the allowed couples $(\tilde{k}_y, \tilde{k}_z)$, corresponding to a half-wavelength radially and a single wavelength azimuthally, in the cases where MTSI is not observed. Notice that cases no. 4, 13, 14 and no. 3, 5, 15 correspond to the same point. The details about each simulation are reported in Table 4.2. Adapted from [177]. 93

Figure 4.10 Positions of the maximum of γ (blue line), calculated with the simplified analytical DR Eq. (2.15), and allowed (k_y, k_z) (bullet points) using the parameters of (a) Tavant *et al.* [136] (couple with half-wavelength in the radial direction and one in the azimuthal direction) and (b) Janhunen *et al.* [129] (couples for half-wavelength in the radial direction and one, two, three and four wavelengths of MTSI in the azimuthal direction). The numerical fluid DR calculated from Eq. (2.12) for the value of k_z imposed by the boundary conditions is shown for (c) Tavant *et al.* [136] and (d) Janhunen *et al.* [129]. The dashed green lines correspond to the allowed k_y, imposed by the periodic boundary conditions. Since the density used in these cases is different, the results are not normalized. From [177]. . 94

Figure 4.11 Evolution of the radial temperature for different PIC simulation cases with: $L_y = 0.64\,\text{cm}$ and $L_z = 1.92\,\text{cm}$ cm (case no. 10), $L_y = 0.32\,\text{cm}$ and $L_z = 1.92\,\text{cm}$ (case no. 11), $L_y = 0.64\,\text{cm}$ and $L_z = 2.56\,\text{cm}$ (case no. 12), $L_y = 0.32\,\text{cm}$ and $L_z = 2.56\,\text{cm}$ (case no. 13). The red lines correspond to cases for which the MTSI propagates. Adapted from [177]. 96

Figure 4.12 Axial mean mobility from the PIC (crosses), the correlation term (orange), or the DMD-decomposition (μ_{LF} red, μ_{HF} pink) during the simulation calculated for (a) case no. 12 without MTSI and (b) case no. 13 with MTSI. Adapted from [177]. 97

Figure 4.13 PIC case no. 3, with $L_y \times L_z = 1.28\,\text{cm} \times 1.92\,\text{cm}$. (a) Time evolution of the k-spectrum of the azimuthal electric field. (b) Normalized plot of the 2D FFT of the azimuthal electric field $E_y(y, z = L_z/2, t)$ with $y \in [0, L_y]$ and $t \in [20\,\mu\text{s}, 30\,\mu\text{s}]$. The solid white line shows the ion acoustic dispersion relation in Eq. (4.2), the dashed line shows the growth rate of the IAW, Eq. (2.9), magnified 25 times, the green line shows the linear sound relation as in Eq. (4.5). Adapted from [177]. 99

Figure 4.14 Temporal evolution of the plasma parameters in the radial-azimuthal benchmark case. (a) the mean electron temperature evolution in axial (x), azimuthal (y) and radial (z) directions. (b) the overall mean ion (n_i) and electron (n_e) densities. 102

Figure 4.15 The FFT of E_y averaged radially over three different intervals. The vertical lines represent from left to right the peak of the MTSI, the peak of the ECDI first resonance, and the peak of the ECDI second resonance. 103
Figure 4.16 The radial (along z) average profiles of (a) the electron temperature and (b) the ion and electron density. The shaded areas represent a $\pm 2.5\%$ around the Benchmark value. 104
Figure 4.17 The statistical convergence of the simulation. (a) the mean final density as a function of the weight factor q_f. (b) the corresponding axial profiles. The markers in (a) have the same color as the corresponding line in (b). The nominal case of the Benchmark is the yellow one. 104
Figure 5.1 **Case A** with $T_e^{\text{cath}} = 5\,\text{eV}$. (a) The discharge current. The four points indicate the times at which the profiles in (b-e) and (f-i) are taken (the marker color corresponds to the frame color in the bottom line). In the central line panels, we show the axial profiles of electron temperature (red) and electron density (black) at the chosen times. The purple line represents the magnetic field profile on a linear scale. In the bottom panels, we show the axial profiles of the cyclotron frequency ω_{ce}, the anomalous collisional frequency ν_t, and of the classical collisional frequency ν_{class}. The dashed black line represents the thruster exit plane. From Ref. [201]. 110
Figure 5.2 **Case C** with $T_e^{\text{cath}} = 0.1\,\text{eV}$. (a) The discharge current. The four points indicate the times at which the profiles in (b-e) and (f-i) are taken (the marker color corresponds to the frame color in the bottom line). In the central line panels, we show the axial profiles of electron temperature (red) and electron density (black) at the chosen times. The purple line represents the magnetic field profile on a linear scale. In the bottom panels, we show the axial profiles of the cyclotron frequency ω_{ce}, the anomalous collisional frequency ν_t, and of the classical collisional frequency ν_{class}. The dashed black line represents the thruster exit plane. From Ref. [201]. 111
Figure 5.3 **Case A, growing phase of the BM**. In (a) and (b): PSD2P maps calculated in the axial direction in the channel and the plume. In (d) and (e): PSD2P maps calculated in the azimuthal direction at the same axial positions. The white rings represent the max of the PSD2P. In (c): a snapshot of the electron density map at $t = 294\,\mu\text{s}$. The arrows represent the instability direction, which is calculated by the k_x and k_y in the spectra. Each frame corresponds to the arrow with the same color. In (f): axial profile of the electron density at $t = 294\,\mu\text{s}$. From Ref. [201]. . 113

Figure 5.4 **Case C, growing phase of the BM.** In (a) and (b): PSD2P maps calculated in the axial direction in the channel and the plume. In (d) and (e): PSD2P maps calculated in the azimuthal direction at the same axial positions. The white rings represent the max of the PSD2P. In (c): a snapshot of the electron density map at $t = 263\,\mu s$. The arrows represent the instability direction, which is calculated by the k_x and k_y in the spectra. Each frame corresponds to the arrow with the same color. In (f) axial profile of the electron density at $t = 263\,\mu s$. From Ref. [201]. . 114

Figure 5.5 **Case A, decreasing phase of the BM.** In (a) and (b) we show the PSD2P calculated in the axial direction in the channel and the plume. In (d) and (e) we show the PSD2P calculated in the azimuthal direction at the same axial positions. The maximal density is very close to $x = 0.96\,cm$ (i. e., the axial position chosen for the other figures), so we performed the analysis at a position slightly closer to the anode. The white rings represent the max of the PSD2P. In (c) a snapshot of the electron density map at $t = 316\,\mu s$ is shown. The arrows represent the instability direction, which is calculated by the k_x and k_y in the spectra. Each frame corresponds to the arrow with the same color. In (f) we report the electron density axial profile at $t = 316\,\mu s$. From Ref. [201]. 116

Figure 5.6 **Case C, decreasing phase of the BM.** In (a) and (b) we show the PSD2P calculated in the axial direction in the channel and the plume. In (d) and (e) we show the PSD2P calculated in the azimuthal direction at the same axial positions. The white rings represent the max of the PSD2P. In (c) a snapshot of the electron density map at $t = 272\,\mu s$ is shown. The arrows represent the instability direction, which is calculated by the k_x and k_y in the spectra. Each frame corresponds to the arrow with the same color. In (f) we report the electron density axial profile at $t = 272\,\mu s$. From Ref. [201]. 117

Figure 5.7 (a) Numerical solution of Eq. (2.8) with plasma parameters extracted from PIC simulations ($4\,cm \times 4\,cm$ axial-azimuthal domain with an electron temperature of injection at the cathode of 0.1 eV) at the axial position of $x = 2.5\,cm$, corresponding to the channel exit (i. e., $k_x \approx 0$ and $k_y \approx 430\,m^{-1}$). Bottom: Azimuthal (b) and Axial (c) PSD2P map calculated at the channel exit. The green and blue lines in (b) and (c) represent the azimuthal and axial projections of the IAW as shown in (a). The dashed lines in (b) and (c) show the DR calculated inside the channel, while the solid lines represent the DR calculated at the channel exit. From Ref. [202]. 119

Figure 5.8 (a) The discharge current evolution during a given BM oscillation. The different color bands indicate the six time intervals where we performed the PSD2P. In (b) we show the amplitude of the IAW mode along the thruster axis, each color line corresponds to the time-interval with the same color in (a). The solid black line and the vertical dashed black line represent the magnetic field shape and its maximum axial position, respectively. In (c-h) we show 6 snapshots of the plasma density n_e at the beginning of each of the six time intervals. From Ref. [202]. 121

Figure 5.9 In (a) and (b) the 2D color plots show the PSD in azimuthal and axial directions, respectively. In green, we draw the best IAW DR as in Figure 5.7. The corresponding growth rate of Eq. (2.9) (magnified by a factor 8) is plotted in blue. From Ref. [202]. . 123

Figure 5.10 (a) Debye length (red) and electron azimuthal drift velocity (blue) mean profiles between 234 and 238 µs. (b) The maximum growth rate from Eq. (5.2). We remind the reader that the value of λ_D has been increased by a factor of 8 by scaling the permittivity. From Ref. [202]. 123

Figure 5.11 The axial profiles of sound speed and ion axial velocity calculated at $t = 262\,\mu s$. The arrows indicate the direction of propagation and convection of the wave. From Ref. [202]. 124

Figure 5.12 (a-d) PSD2P calculated in the axial direction at four different axial positions indicated above each figure. The green lines represent the axial IAW calculated as in Figure 5.7. (f-i) PSD2P calculated in the azimuthal direction at the same axial positions. The blue lines represent the azimuthal IAW calculated as in Figure 5.7. In (e) a snapshot of the electron density map at $t = 263\,\mu s$ is shown. The arrows represent the instability direction, which is calculated by the k_x and k_y in the spectra. Each frame corresponds to the arrow with the same color. In (j) we show the electron temperature axial profile at $t = 263\,\mu s$. From Ref. [202]. 126

Figure 5.13 Schematic of the Snell refraction of an instability propagating from region 1 of thickness δx with propagation velocity v_1 to region 2 where the propagation velocity is $v_2 < v_1$. From Ref. [202]. 127

Figure 5.14 (a) An electron density snapshot and (b) the angle measured by PIC simulations (blue dots) and the one calculated using the Snell law (red dots). From Ref. [202]. 128

Figure 5.15 (a) The axial profile of the two ITTI branches for $k_x = 40\,m^{-1}$. The *plus* branch is traced in green and the *minus* branch is in black. In (b) and (c) the lines represent the profile of γ_m (red) and γ_p (blue) for four different values of k_y. From Ref. [202]. . 129

Figure 5.16 Azimuthal (a) and axial (b) PSD2Ps. In (c) a snapshot of the electron density at $t = 282\,\mu s$ is shown. The green line in (b) represents the ITTI frequency, calculated as in Eq. (2.17). The dotted vertical red line in (c) reports the position of the ion sonic point and the vertical dash-dotted blue line represents the axial position at which the PSD2P is calculated. The dispersion in the azimuthal direction is not displayed, since the expression in Eq. (2.17) was calculated in the small k_y limit. From Ref. [202]. 131

Figure 5.17 (a) the discharge current during several periods of the BM. (b) a zoom of the discharge current between 275 and 295 µs. (c) Fast Fourier Fransforms (FFTs) calculated from the current with the same color in (a). (d) the average spectrum. From Ref. [202]. 132

Figure 5.18 (a) The discharge current in a decreasing phase of the BM. The two vertical black lines bound a single ITTI oscillation. For this ITTI oscillation, in (b) and (c), we show the time evolution of the ion density and the axial electric field, respectively. From Ref. [202]. 132

Figure 5.19 (a-d) Ion velocity distribution functions at four different axial positions at the end of a decreasing BM cycle, corresponding to the time indicated by the dashed line in (e). In (d) the shaded blue band represents the slow ions, while the shaded red band represents the fast ions. 134

Figure 5.20 (a) Velocity of the slow (red) and fast (orange) ions packets. Percentage of slow (b) and fast (c) ions. (d) Discharge current density. 135

Figure 6.1 Black lines: plasma density profile between two walls. (a) interpretation of the 2D simulation as a thin slab of plasma at the bulk center. (b) interpretation of the 2D simulation as a thick slab of plasma accounting for the entire bulk. 141

Figure 6.2 Radial (along z) profiles of (a) the electrons (brown) and ions (green) density and (b) charge density. The insets show the sheath-bulk transition. The red dashed lines delimit the sheath region. The test case corresponds to the radial-azimuthal benchmark [180] and the profiles are calculated at steady-state. 143

Figure 6.3 Blue dashed, dotted and solid lines represent the electron, ion, and total axial current densities at quasi-steady-state, respectively. The red markers represent the radial current density calculated from the radially absorbed particles and the black line represents the Bohm current density profile, calculated using plasma density and temperature. As one may notice, any particle is removed in the plume (i. e., for $x > 2.5\,cm$). 144

Figure 6.4 Plasma potential (a) and current (b) density profiles for the simulation with $L_y = 1$ cm for different values of the virtual-r length. 146
Figure 6.5 Plasma potential (a) and current (b) density profiles for the simulation with $L_y = 4$ cm for different values of the virtual-r length. 147
Figure 6.6 Mean (a) and relative standard deviation (b) of the current. Mean (c) and relative standard deviation (d) of the anode voltage. The circles represent the results obtained with $L_y = 1$ cm, while the diamonds represent the results obtained with $L_y = 4$ cm. The colors are indicated on top. 147
Figure 6.7 Absorbed current for $L_y = 1$ cm (a) and $L_y = 4$ cm (b), respectively. The absorbed current is divided by the total axial current for $L_y = 1$ cm (c) and $L_y = 4$ cm (d), respectively. 149
Figure 6.8 (a) mean absorbed current for $L_y = 1$ cm (circles) and $L_y = 4$ cm (diamonds). (b) Ratio of the absorbed current over the total axial current for $L_y = 1$ cm (circles) and $L_y = 4$ cm (diamonds). 149
Figure 6.9 Electron temperature (red) and density (green) for $L_y = 1$ cm with different L_z. The shaded area shows the standard deviation around the mean value. 150
Figure 6.10 Temporal evolution at quasi-steady-state of the electron temperature (a-d) and density (e-h) for $L_y = 1$ cm. The red, green, blue, and yellow lines show the evolution at $x = 0.5$ cm, 1.5 cm, 2.5 cm and 3.5 cm, respectively. Each column corresponds to L_z value reported in the title. 151
Figure 6.11 Electron temperature (red) and density (green) for $L_y = 4$ cm with different L_z. The shaded area shows the standard deviation around the mean value. 152
Figure 6.12 Temporal evolution during the BM cycle of the electron temperature (a-d) and density (e-h) for $L_y = 4$ cm. The red, green, blue and yellow lines show the evolution at $x = 0.5$ cm, 1.5 cm, 2.5 cm and 3.5 cm, respectively. Each column corresponds to L_z value reported in the title. 152
Figure 6.13 Each column shows the EVDF for different virtual-r thicknesses: no virtual-r (a,e and i), L_z =4 cm (b,f and j), $L_z = 2$ cm (c,g, and k), $L_z = 1$ cm (d,h, and l) and each row a different axial position: $x = 0.5$ cm (a,b,c and d), $x = 2$ cm (e,f,g, and h) and $x = 3.5$ cm (i,j,k and l). 154
Figure 6.14 (a) Temporal evolution of the discharge current. The thick lines show the analyzed BM cycles. From these intervals are extracted the frequency (b) and amplitude (c) of the BM oscillations. The colors are reported on the legend on top. 155
Figure 6.15 Evolution of the BM frequency for different values of the wall losses in a 1D fluid code developed at LPP (similar to the one described in Ref. [175]). The coefficient α is used to decrease or increase the wall losses. The standard wall losses correspond to $\alpha = 1$. 156

Figure 6.16 (a) FFT of the current for different values of virtual-r with $L_y = 1$ cm. (b) The dominant frequency. The colors are reported on the legend on top. 156
Figure 6.17 Wavenumeber (a) and frequency (b) corresponding to the most unstable mode calculated by Eq. (6.4) for different values of the electron temperature. 157
Figure 6.18 PSD2P time-axial spectra at $x = 3.5$ cm for no virtual-r (a), $L_z = 4$ cm (b), $L_z = 2$ cm (c) and $L_z = 1$ cm (d). The time at which is map is calculated is indicated in the subfigure title. . 159
Figure 6.19 PSD2P at $x = 2.0$ cm for no virtual-r (a), 4 cm (b), 2 cm (c) and 1 cm (d). The time at which is map is calculated is indicated in the subfigure title and a snapshot of the density at that time is shown in the bottom figures (e-h). 160
Figure 6.20 Specific impulse (a), thrust power (b) and mass efficiency (c), and thrust power-to-power ratio (d), as a function of the virtual-r thickness. The results are reported for both cases with $L_y = 1$ cm and 4 cm, as indicated in the legend at the bottom. 161
Figure 6.21 Power losses at the walls as a function of the virtual-r thickness. The time evolution is shown for cases with $L_y = 1$ cm (a) and 4 cm (b). In (c) we show the average power losses and (d) the total I-V power provided by the generator. 162
Figure 6.22 Axial currents profiles in a case with $\bar{\sigma} = 0.25$. The blue, green, and red markers correspond to the electron, ion, and SEE current density profiles, respectively. The black line shows the Bohm current density as calculated from Eq. (6.1). 164
Figure 6.23 Current (a) and anode potential evolution for a simulation with $L_y = 1$ cm and $\tilde{L}z = 2$ cm. Two different values of the SEE emission rate are considered: $\bar{\sigma} = 0.5$ (green) and $\bar{\sigma} = 0.8$ (blue), while the red line represents the base case. 165
Figure 6.24 Electron temperature (red) and density (green) for $L_y = 1$ cm with different values of $\bar{\sigma}$ with $L_z = 2$ cm. The shaded area shows the standard deviation around the mean value. 166
Figure 6.25 Current (a) and anode potential evolution for a simulation with $L_y = 4$ cm and $\tilde{L}_z = 4$ cm. Three different values of the SEE emission rate are considered: $\bar{\sigma} = 0.25$ (green), $\bar{\sigma} = 0.50$ (blue), and $\bar{\sigma} = 0.75$ (yellow), while the red line represents the base case. 167
Figure 6.26 Current (a) and anode potential evolution for a simulation with a virtual-r with $\tilde{L}_z = 1.55$ cm and two different azimuthal lengths ($L_y = 1$ cm and 4 cm). 168
Figure 6.27 Radial power losses (a) and I-V power (b) for the simulations with $L_y = 1$ cm and $L_y = 4$ cm. 168
Figure 6.28 Fluxes for $L_y = 1$ cm (a) and $L_y = 4$ cm (b). Mass and acceleration efficiencies for $L_y = 1$ (c) and $L_y = 4$ cm (d). 169

Figure 7.1 Spatiotemporal evolution of normalized gas density n_g (a), gas speed v_g (b), electron density production rate by ionization S_{iz} (c), electron density n_e (d), electron azimuthal speed $v_{e,y}$ (e), electron temperature T_e (f), ionization rate coefficient $K_{iz} = S_{iz}/n_g n_e$ (g) and axial electric field E_x(h). The maps are obtained by averaging azimuthally at every time. The color scale is the same for all the plots. In (i) we show the total current evolution. The vertical dashed lines allow to separate four phases of the BM cycle. 173

Figure 7.2 (a) Neutral density temporal evolution at three different positions. (b) Maximal normalized amplitude evolution of S_{iz}, n_e, T_e and E_x. The dashed vertical lines as in Figure 7.1 separate the different BM phases. These data are extracted directly from PIC outputs. 175

Figure 7.3 Each column represents a time instant (indicated in the first row). The first row shows the electron temperature profiles, the second the gas and electron density, the third the ionization rate coefficient K_{iz}, and the fourth the electron density production rate S_{iz}. These data are extracted directly from PIC outputs. 176

Figure 7.4 (a)-(d) Profiles of the electron velocity along the thruster axis. The red line represents the $\mathbf{E} \times \mathbf{B}$ drift, the green is the diamagnetic drift, the blue is the sum of the two, and the black is the drift as it is extracted by the electron speed in the PIC simulation. In (e) we show the discharge current, where the red markers indicate the instants analyzed in the above figures. 178

Figure 7.5 Diamagnetic drift profile along the thruster axis at different times (Top row). The velocity $v_{D,1}$ is calculated in the isothermal approximation, while $v_{D,2}$ considers the gradient of the entire pressure term. The density, temperature, and pressure profiles are shown in the bottom row. 179

Figure 7.6 (a) Spatiotemporal evolution (i. e., the temporal evolution of the axial profile) of R_{ei} over the span discussed before. In (b) we report the same data, but we zoom on the region indicated by the ruby rectangular box in (a), i. e., $1\,\text{cm} < x < 2\,\text{cm}$ and $170\,\mu\text{s} < t < 200\,\mu\text{s}$. In (c) we show the discharge current evolution. The dashed vertical lines help to define the different times of the discharge. 180

Figure 7.7 Discharge current (a) and anode potential (b) as a function of time, for different anode voltages. 182

Figure 7.8 Average discharge current (a) and anode potential (c). (b) and (d) show the standard deviation of the discharge current and of the anode potential, respectively, divided by the corresponding mean value. 183

Figure 7.9 Average I-V power absorbed by the thruster for different generator voltages. 183

Figure 7.10 (a) Normalized FFT of the current for different anode voltages. (b) Evolution of the BM frequency as a function of the anode voltage. The blue line shows a polynomial fit of type $\omega = aV_0^{1/4} + b$, with a and b two coefficients calculated with linear regression. . . . 184
Figure 7.11 Mean electron temperature and density for different imposed anode voltages. . . . 185
Figure 7.12 Mean electron azimuthal velocity ($v_{e,y}$, blue) and ion axial temperature ($v_{i,x}$, brick red) for different imposed anode voltages. The horizontal dashed line represents the ideal exhaust ion velocity. . . . 185
Figure 7.13 (a) Specific impulse, (b) thrust, (c) mass efficiency, and (d) thrust power-to-power ratio as a function of the anode voltage. 187
Figure 7.14 Current (a) and anode potential (b) temporal evolution for different values of the neutral gas flow rate. . . . 188
Figure 7.15 Current (a) and anode potential (b) temporal evolution for different values of the neutral gas flow rate. . . . 189
Figure 7.16 Average I-V power absorbed by the thruster for different mass flow rates. . . . 190
Figure 7.17 From the current (a), we calculated the BM frequency (b), mean current, and the BM amplitude (c), for different values of the neutral gas flow rate. In (a) we show explicitly the filtered BM peaks. . . . 191
Figure 7.18 Electron temperature (red) and density (blue) profiles for different values of the neutral gas flow rate. . . . 192
Figure 7.19 Specific impulse (a), thrust (b), mass efficiency (c), and thrust power-to-power ratio (d) for different mass flow rates. . . . 193
Figure 7.20 Current (a) and potential (b) for different values of $B_{\max}$, the peak value of the magnetic field, for azimuthal length $L_y = 1\,\text{cm}$. 194
Figure 7.21 Current (a) and potential (b) for different values of $B_{\max}$, the peak value of the magnetic field, for azimuthal length $L_y = 4\,\text{cm}$. 195
Figure 7.22 Average I-V power absorbed by the thruster for different values of $B_{\max}$. . . . 196
Figure 7.23 Electron temperature (red) and density (green) profiles for different values of the magnetic field. . . . 196
Figure 7.24 Specific impulse (a), thrust (b), mass efficiency (c), and thrust power-to-power ratio (d) for different values of the magnetic field maximum value. . . . 197
Figure 7.25 Current (a) and potential (b) for different propellants. . . . 199
Figure 7.26 Electron (solid lines) and ion (dashed lines) current profiles for different propellants at $5\,\text{mg/s}$, averaged over the last $25\,\mu\text{s}$ of simulation. . . . 199
Figure 7.27 Electron density and temperature profiles for different propellants averaged between 250 and $300\,\mu\text{s}$. . . . 200
Figure 7.28 Specific impulse (a), thrust (b), mass efficiency (c), and thrust power-to-power ratio (d) for different propellants. . . . 201
Figure 7.29 Current temporal evolution for different cathode temperatures. 202

Figure 7.30 Amplitude of the oscillation as a function of the cathode temperature. . . . 203
Figure 7.31 Average electron temperature (red) and density (green) profiles for different values of the cathode temperature. The shaded areas cover ± one standard deviation of the profiles. . 204
Figure 7.32 Profiles of the temperature (red) and temperature gradient (blue) in the plasma plume for different values of the cathode temperature. . . . 204
Figure 7.33 Profiles of the electron (solid lines) and ion (dashed line) average currents for different values of the cathode temperature. 205
Figure A.1 Discharge current (a) and voltage (b) with a 2nd order scheme. The results are shown for two simulations with $L_y = 1cm$ and $L_y = 4\,\text{cm}$. . . . 214
Figure A.2 Current (a) and potential (b) evolution in a 1 cm × 4 cm simulation. . . . 217
Figure A.3 Axial profile (a) and radial (b) profile of the plasma potential in a 1 cm × 4 cm simulation. In (c) we show the current density evolution and in (d) a snapshot of the ion density. . . . 218
Figure A.4 Axial profile (a) and radial (b) profile of the plasma potential in a 1 cm × 4 cm simulation at the current peak at $t = 178.4\,\mu\text{s}$. 218

LIST OF TABLES

Table 3.1 Simulation parameters and estimated total CPUh cost of a 300 µs of physical time (for *LPPic*). . . . 57
Table 3.2 Operating and numerical parameters used in PIC simulations. With a small axial-azimuthal domain (4 cm × 1 cm), 3 simulation cases are considered: one without circuit and cases 1 and 2 with circuits. With a larger axial-azimuthal simulation domain (4 cm × 4 cm), 3 simulation cases are considered: one without circuit and cases A and B with circuits. . . . 75
Table 4.1 Operating and numerical parameters used in PIC simulations. No scaling permittivity is used. . . . 85
Table 4.2 The simulation cases from 1 to 5 are analyzed in Section 4.2.4, from 6 to 14 in Section 4.2.6 and from 15 to 17 in 4.2.7. The simulation parameters are the ones specified in Table 4.1 if not otherwise stated. If present, $\tilde{\gamma}^{PIC}$ and $\tilde{\omega}_r^{PIC}$ represent the growth rate and the frequency of the MTSI, respectively. [1]Initial density, $n_0 = 2 \times 10^{17}\ \text{m}^{-3}$. [2]Axial electric field, $E_x = 3 \times 10^4\ \text{V/m}$. 86
Table 6.1 Operating and numerical parameters used in PIC simulations. 145
Table 6.2 Frequency of the ITTI mode calculated from the PSD2P maps. . 159

Table 6.3 Engineering parameters for the simulations with consistent virtual radius. 168
Table 7.1 Characteristics of the used gases. 198
Table 7.2 Current density and its standard variation calculated between 100 µs and 350 µs. 203
Table A.1 List of all axial-azimuthal simulations in this thesis. 215

ACRONYMS

BM Breathing Mode
CINES Centre Informatique National de l'Enseignement Superieur
CFL Courant–Friedrichs–Lewy
DFT Discrete Fourier Transform
CRM Collisional Radiative Model
DMD Dynamic Mode Decomposition
DK Direct Kinetic
DR Dispersion Relation
EVDF Electron Velocity Distribution Function
EP Electric Propulsion
FWHM Full Width at Half Maximum
ECDI Electron Cyclotron Drift Instability
FFT Fast Fourier Fransform
HT Hall Thruster
IAW Ion Acoustic Wave
ITTI Ion Transit-Time Instability
IITSI Ion Ion Two-Stream Instability
LPP Laboratoire de Physique des Plasmas
LH Lower Hybrid
MCC Monte Carlo Collisions
MPI Message Passage Interface
MSHI Modified Simon–Hoh Instability
MTSI Modified Two-Stream Instability
PIC Particle-In-Cell
PSD2P Two-Points Power Spectral Density
PSD Power Spectral Density

SEE Secondary Electron Emission
SHI Simon–Hoh Instability
SPT Stationary Plasma Thruster
TSI Two-Stream Instability
UH Upper Hybrid

1 INTRODUCTION

Chapter contents

1.1 Space propulsion 1
1.1.1 Chemical or electric propulsion 2
1.1.2 EP history 3
1.1.3 Electric propulsion systems 4
1.1.4 EP parameters 5
1.2 Hall thrusters 6
1.2.1 Hall thruster basics 6
1.2.2 Plasma boundaries 9
1.2.3 Hall thruster anomalous transport 10
1.2.4 Plasma instabilities in Hall thrusters 12
1.2.5 Main challenges 15
1.3 Hall thruster plasma modeling 16
1.3.1 Plasma modeling basics 16
1.3.2 Plasma parameters 18
1.3.3 Plasma modeling techniques 19
1.4 Scope and outline of the thesis 22

1.1 SPACE PROPULSION

Space propulsion is the field of engineering that is focused on designing and developing systems that generate thrust and move spacecraft through space. One category of propulsion systems is Electric Propulsion (EP), which by using electric energy accelerates a propellant that is expelled outside the spacecraft to generate thrust. Electric propulsion systems are lighter and more efficient than traditional chemical propulsion systems, making them an excellent choice for long-duration missions and deep space exploration. Furthermore, they can produce high levels of specific impulse, enabling them to achieve greater speed per unit of propellant. Despite these advantages, due to their lower thrust output, electric propulsion systems are not suitable for quick maneuvers, where the chemical thrust is more advantageous.

Most EP devices use plasma to create the ions that are accelerated to produce thrust. Therefore, the study of electric thrusters is linked to that of plasma physics. Plasma physics is the study of matter in its fourth state, known as plasma, and deals with the collective behavior of electrons and ions in quasi-neutral electrified gases. The birth of plasma physics can be traced back to the late 19^{th} century when physicists first observed a glow in gas tubes. In the early 20^{th} century, Irving Langmuir performed experiments on the properties of gas discharges and coined the term *plasma* to describe the ionized gas [5]. However, it was not until the '40s that plasma physics emerged as a distinct field of study. Scientists could prove that plasmas are the most common phase of matter in the universe: according to some estimates, more than 99% of the entire visible universe is plasma. In the last 50 years, plasma physics has become a crucial field of study with applications in areas such as fusion energy, astrophysics, materials processing, and space science, among others.

1.1.1 Chemical or electric propulsion

Chemical and electric propulsion are two different types of propulsion systems used in space. Chemical propulsion relies on the combustion of chemical fuels, such as liquid hydrogen and oxygen, to generate high-velocity exhaust gases which provide thrust. On the other hand, electric propulsion uses electric energy to ionize a propellant and create plasma that generates thrust.

One of the primary differences between the two forms of propulsion is the efficiency of the systems. Chemical propulsion is comparatively less efficient than electric propulsion, requiring a substantial amount of fuel to generate a limited amount of thrust. In contrast, electric propulsion systems are much more efficient, using a minimal amount of fuel to produce a substantial amount of thrust. However, the thrust absolute value is different: chemical propulsion systems can produce high thrust (e. g., up to MN), making them ideal for quick maneuvers and launches, while EP systems have a much lower thrust, usually up to 500 mN.

Another distinction between the two forms of propulsion is the size and weight of the systems. Chemical propulsion systems are typically larger and heavier (i. e. considering the weight of the fuel) than electric propulsion systems, as they require large fuel tanks and other components to store and deliver the fuel. Electric propulsion systems, on the other hand, are much smaller and lighter, as they only require a small amount of fuel to produce thrust. This has an impact on the cost of the mission, even if the initial cost of an EP system might be higher than that of a chemical system.

In conclusion, chemical and electric propulsion are two different types of propulsion systems with different strengths and weaknesses. Chemical propulsion is ideal for quick maneuvers and launches, while electric propulsion is better for long-duration missions and deep space exploration. Both types of propulsion have their place in the field of space exploration, and the choice between them will depend on the specific requirements of a given mission.

1.1.2 EP history

Electric propulsion has a relatively short but significant history in the field of space exploration. The concept of using electric energy to ionize a propellant and generate a plasma to provide thrust was first evoked by the early 20th century, but it wasn't until the latter half of the 20th century that this technology began to be developed for practical use in space. A history of the birth of electric propulsion can be found in Ref. [56].

One of the earliest examples of EP is the ion engine, which was first tested in the '60s by NASA. The ion engine was initially used for satellite station-keeping and orbit-raising, but it rapidly found applications in deep space exploration. In the same years, in the Soviet Union, Alexei Ivanovich Morozov led the experimental and theoretical development of Stationary Plasma Thrusters (SPTs) [39], also named Hall Thrusters (HTs). We will adopt the latter name for the rest of this work. The HTs use a cross-field configuration to confine the plasma and accelerate ions to produce thrust. The HTs were successfully used in space from 1971 and hundreds of satellites have been equipped with them since [27]. Their development started in the West only during the last decade of 20th century.

The HTs are low-temperature plasma devices that are operated under low pressure conditions. A low-temperature plasma is characterized by cold neutrals and ions (i. e., ion temperature $T_i \lesssim 1\,\text{eV}$[1]) and by hot electrons (i. e., electron temperature $T_e \gtrsim 1\,\text{eV}$). These engines are designed to operate under low pressure in space. For this reason, on Earth, the HT are operated under vacuum conditions in specifically designed test benches.

In recent years, EP has become increasingly important for spacecraft propulsion. This is due, in part, to the increasing demand for more efficient propulsion systems, as well as the advent of new materials and technologies that have made EP more practical and cost-effective. Electric propulsion has been used in a number of missions, including deep space missions to explore the solar system and interplanetary spacecraft that are designed to study asteroids and comets. This technology has also been used in commercial communication satellites, which require precise station-keeping and orbit-raising capabilities.

The large variety of missions in which EP is currently used raised the problem of changing the power of the thruster. For example, HTs were historically operated with a narrow power range, i. e., $0.4 - 1\,\text{kW}$ [39]. The recent developments of the space market (e. g., the emergence of the CubeSat and the of constellations) and of the satellites technologies (e. g., high specific power generated by solar arrays) have led to the need and possibility of a more flexible power range [143, 159, 191], which resulted in the launch of large variety of new thrusters, among them the 5 kW HT PPS5000 [194] from Safran Spacecraft Propulsion.

In conclusion, the history of EP is a relatively short but significant one, and this technology has become increasingly important in the field of space exploration as demand for more efficient propulsion systems has grown. With continued advances in technology, it is likely that EP will continue to play an important role in the future of space exploration.

1 We remember that $1\,\text{eV} \approx 11\,604.5\,\text{K}$.

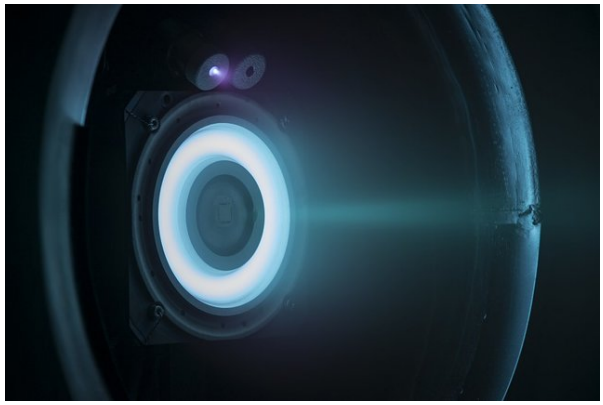


Figure 1.1: A Hall thruster in operation. Image from CNES, february 2015.

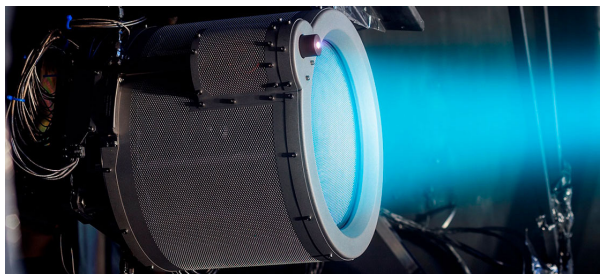


Figure 1.2: An ion thruster in operation. Image from *qinetiq.com*.

1.1.3 Electric propulsion systems

In the Section 1.1.2, we mentioned ion thrusters and Hall thrusters as two types of electric propulsion systems. In this section, we discuss the main characteristics of these two systems, and we introduce some other types of thrusters currently studied by the EP community.

The Hall thrusters, which are the main subject of this thesis, are composed by an annular channel, where the plasma is created. The neutral gas is injected at the channel bottom, which is at high voltage. A photo of a xenon-operated HT is shown in Figure 1.1. The electrons to sustain the discharge are provided by a cathode at channel exit, while the residence time of electrons in the discharge chamber is increased by the presence of a magnetic field. The voltage drop between the anode and the grounded cathode generates an electric field parallel to the thruster axis. The electric field profile depends on the plasma conductivity at different axial positions. The total efficiency of these thrusters is normally high, e. g., $\eta > 60\%$, while the specific impulse is limited by the power voltage (e. g., the I_{sp} is in the range $1000\,\mathrm{s} - 3000\,\mathrm{s}$).

The ion thrusters consist of a closed chamber in which different methods are employed to ionize as much gas as possible. One can see an ion thruster in operation in Figure 1.2. At one end of the chamber there is an electrostatic grid that is used to accelerate the ions to high velocities. These thrusters have a good efficiency $\eta > 60\%$ and a high specific impulse $I_{sp} > 2000\,\mathrm{s}$.

Resistojet and arcjet thrusters are two other types of electrothermal devices that are currently studied by the EP community. These systems use the expansion of the gas to produce thrust. Despite their apparent simplicity, they can have a good specific impulse $I_{sp} > 500\,s$. Other types of thrusters are currently used and developed, such as the magnetoplasmadynamic thrusters, pulsed plasma thrusters or electrospray thrusters. For a detailed discussion of these devices the reader should refer to Refs. [76, 108, 161].

1.1.4 EP parameters

In order to establish the crucial variables of EP devices, a set of parameters is utilized, some of which have been previously introduced. The objective of this section is to establish specific quantities for assessing the performance of EP devices, specifically Hall thrusters.

By considering Newton's second law, we can write the motion equation as

$$\mathbf{F}_{ext} + \dot{m}\mathbf{v}_{exh} = m\frac{d\mathbf{v}}{dt},$$

where $\mathbf{F}_{ext}$ is the sum of the external forces acting on the spacecraft, m is the spacecraft mass, $\mathbf{v}$ is the spacecraft velocity and $\mathbf{v}_{exh}$ is the exhaust velocity (i. e. the velocity of the expelled propellant). The force

$$\mathbf{T} = \dot{m}\mathbf{v}_{exh}$$

is named *thrust*. By considering a 1D problem with no external forces, one can integrate the previous expression from the initial time t_0 to the final time t_f, obtaining a velocity change

$$\Delta v = v_f - v_0 = v_{exh} \ln \frac{m_f}{m_0},$$

where m_0 is the initial mass and m_f is the final mass, both including dry and payload masses. The quantities v_0 and v_f are the initial and final velocities, respectively. This equation takes the name of Tsiolkovsky rocket equation [7] and represents the basic equation of rocket propulsion.

The total impulse is the integral of the thrust over the duration of the operation. However, it is more common to refer to the *specific impulse* I_{sp}, which represents the impulse delivered per unit of propellant consumed. The specific impulse is expressed as the ratio between the exhaust velocity and the gravitational acceleration g_0,

$$I_{sp} = \frac{v_{exh}}{g_0}.$$

The specific impulse is a very important quantity to evaluate the performance of a propulsion system.

In the case of devices such as ion thrusters or HTs, one can calculate the thrust produced by the ion beam as

$$T = \dot{m}v_{exh} = \Gamma_i m_i A_i v_{exh},$$

where Γ_i is the ion flux at the exit, m_i the ion mass and A_i the thruster open area. The previous expression is obtained by considering a 100% ionization: the neutral gas contribution to the thrust can be neglected. The thrust power can be calculated as

$$P_T = \frac{1}{2} m_i v_{\text{exh}}^2 \Gamma_i A_i.$$

The thrust power is not extremely significant by itself. However, it might give some important insights when compared to the power provided by the generator. In this thesis, we will often refer to the *I-V power* (i. e., P_{IV}), as the power absorbed by the discharge and P_{G} as the power provided by the generator. The ratio between the thrust power and the generator power is one of the crucial parameters to evaluate the performance of an EP device.

The overall efficiency of a device should take into account several components, from the efficiency of the voltage generator to the cathode efficiency, to the efficiency of some on-board systems (e. g., the coils that generate the magnetic field in a HT) or to the ionzation efficiency. Goebel and Katz [76] in Section 7.3.1 discuss in detail the efficiency in the specific case of HTs. In this thesis, we will focus mainly on the mass utilization efficiency,

$$\eta_m = \frac{\Gamma_i A_i}{Q_0},$$

where Q_0 is the imposed neutral flux of particles at the anode. This quantity can be also considered as the *ionization efficiency*, since it gives the fraction of the neutral flux that is ionized.

1.2 HALL THRUSTERS

In this section, we discuss the general concepts governing the operation of HTs, which are the subject of this thesis work. We will start by describing their main working principles, then we discuss in detail the main characteristics of their plasma discharge.

1.2.1 Hall thruster basics

A Hall thruster consists of a coaxial annular cavity, with one channel end that is left open and one is closed. A sketch of a HT section is reported in Figure 1.3. The neutral gas is injected at the closed end of the channel, while the accelerated ions leave the channel at the open end, creating the thrust. External coils provide a stationary external magnetic field directed mostly in the radial direction. The closed end of the channel is connected with a *RLC* circuit that keeps the anode at high voltage (some hundreds of volts). The walls are generally made of a dielectric material (ceramic). The plasma plume can be considered at low potential as well. The circuit at the other end of the plasma is closed by a hollow cathode. The cathode provides the electrons needed for ionization of the gas and those needed to neutralize the plasma plume. The potential difference between anode and cathode creates an electric field parallel to the thruster axis. Thus, the electric and magnetic fields form the so-called

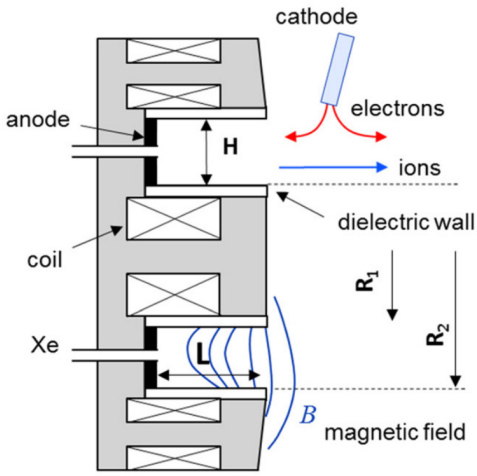


Figure 1.3: HT schematic from Boeuf [110].

$\mathbf{E} \times \mathbf{B}$ configuration. In the presence of this cross-field configuration, the electrons are trapped by the magnetic field lines and start drifting azimuthally in the annular channel, while being radially confined by the sheaths that form at the thruster inner walls. The azimuthal drift increases the residence time of electrons inside the thruster channel, thus increasing the ionization efficiency.

The collisional events that ionize the gas have an energy threshold (i. e., $\mathcal{E}_{\mathrm{Xe}} = 12.13\,\mathrm{eV}$ for xenon), that is achieved when the electrons reach a velocity of $\approx 2000\,\mathrm{km/s}$. Thus, the faster the electrons, the longer time each electron stays inside the thruster channel, the larger the ionization efficiency is. In modern HTs, the mass utilization efficiency is of the order of 90 %. The ions are created by electron impact ionization of the neutral gas injected at the anode. As one can see in Figure 1.4, the ions are produced inside the thruster channel and accelerated outwards by the axial electric field. Since the ion Larmor radius (i. e., $r_{L,i} = m_i v_{\perp,i}/qB$, with m_i ion mass, $v_{\perp,i}$ ion thermal velocity in the plane perpendicular to the magnetic field, q the elementary charge and B the magnetic field amplitude) is larger than the device dimensions (i. e., up to 1 m in HTs conditions), the ions are weakly magnetized (or even not magnetized) and they do not drift significantly in the azimuthal direction, contrary to electrons. Considering that the ions are generated in the inner part of the channel, most of them are accelerated by the entire anode/cathode voltage drop. Thus, in the plume, they should reach a velocity

$$v_{i,\mathrm{exh}} = \sqrt{e\frac{2V_\mathrm{a}}{m_i}},$$

where V_a is the anode voltage. The velocity $v_{i,\mathrm{exh}}$ is the exhaust velocity of ions and it is calculated above by considering monenergetic ions without collisions. With $V_\mathrm{a} = 300\,\mathrm{V}$, the exhaust velocity of ions is $20\,\mathrm{km/s}$ in the case of xenon. The presence of the $\mathbf{E} \times \mathbf{B}$ drift of electrons allows for having a large electric field directed axially, without a space-charge. This is one of the main advantages of the HTs compared to

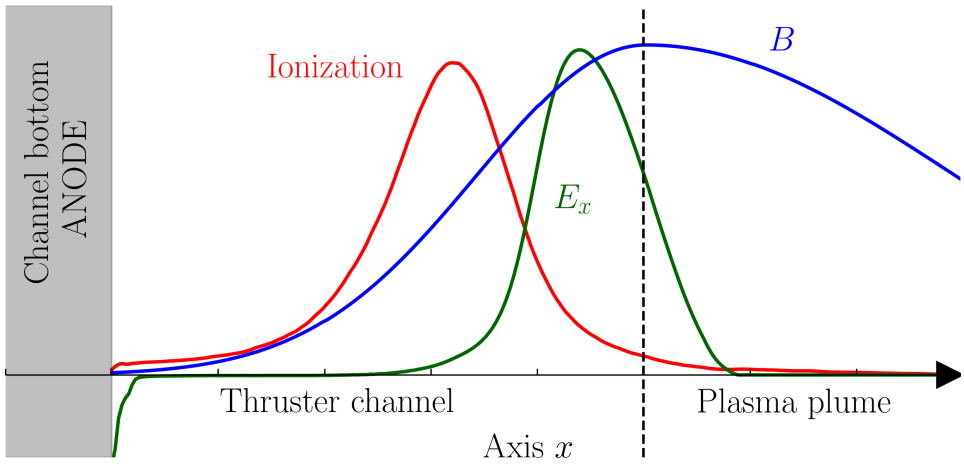


Figure 1.4: Ionization (red), magnetic field (blue) and electric field (green) profiles along the thruster axis. The dashed line represents the thruster channel exit. The HT community often refers to the thruster axis as x-axis, to the azimuthal direction as y-axis and to the radial direction as z-axis.

ion-gridded thrusters: ion current is not limited by space-charge effects, i. e., by the Child-Langmuir law.

If we only consider the transport caused by the fields, the electron motion is very restricted in the axial direction. However, the presence of electron-neutral collisions, electron-walls collisions and electrostatic fluctuations create a significant axial transport of electrons. The electrons that have entered the ionization region travel to the anode and are collected by the closed end of the channel. The acceleration of electrons to the anode must be controlled (hence the importance of the magnetic field configuration) to decrease the losses and increase the gas ionization efficiency.

Let us consider now the steady-state functioning of HT. For any configuration of magnetic and electric field, we can calculate the drift by dropping the term dv/dt in the Lorentz force equation for a single electron, as

$$\frac{dv}{dt} = \frac{q}{m_e}\mathbf{E} + \frac{q}{m_e}\mathbf{v} \times \mathbf{B} = 0.$$

Where q is the elementary charge, m_e the electron mass, $\mathbf{E}$ the electric field vector, $\mathbf{B}$ the magnetic field vector and $\mathbf{v}$ the particle speed. By taking the cross product with $\mathbf{B}$, we obtain

$$\mathbf{E} \times \mathbf{B} = \mathbf{B} \times (\mathbf{v} \times \mathbf{B}) = vB^2 - \mathbf{B}(\mathbf{v} \times \mathbf{B}),$$

with B the amplitude of the magnetic field. By considering the drift in the plane perpendicular to the magnetic field, we can write

$$v_{\mathrm{E}\times\mathrm{B}} = \frac{\mathbf{E} \times \mathbf{B}}{B^2},$$

which is the so-called $\mathbf{E} \times \mathbf{B}$ drift. In standard HT devices the electrons can reach the azimuthal velocity of 1×10^6 m/s. To understand on physical grounds what

happens, we need to think to an electron gyro-orbit. By assuming without loss of generality that the electron initial velocity has the same direction as the electric field, we have that an electron gains energy by the electric field for the first half orbit. It means that the velocity component in the plane increases, so does the Larmor radius. Conversely, in the second half orbit, it loses energy, so its Larmor radius decreases. Hence, the variation of the Larmor radius is the cause of the drift of the guiding center. This development is valid also for the ions, since no assumption was made on the particle mass or initial speed. However, the specific configuration of the HT prevents the ions with a mass m_i to drift in the azimuthal direction: their Larmor radius ($\rho_i = v_\perp/\omega_{ci} = v_\perp m_i/eB \propto m_i$) is larger than the device dimensions. In the previous expression $v_\perp$ is the thermal velocity component in the plane perpendicular to the magnetic field. In the same expression appears the cyclotron frequency, which is defined for electrons and ions, respectively, as

$$\omega_{c,e,i} = \frac{qB}{m_{e,i}}, \tag{1.1}$$

depending on the particle mass.

The Hall current in the azimuthal direction can be written as

$$\mathbf{J}_H = -en_e \frac{\mathbf{E} \times \mathbf{B}}{B^2},$$

where we introduced the electron density n_e. This current generates a Lorentz force density

$$\mathbf{f} = \mathbf{J}_H \times \mathbf{B},$$

that is exerted on the plasma in the axial direction. Thus, at steady-state, an equal force is exerted on the magnetic field structure. This is the actual mechanism that generates force translation from the axially accelerated ions to the thruster structure. Assuming the charge neutrality in the plasma, with a simple substitution, we can see that the force density on the ions is

$$\mathbf{f} = en_e\mathbf{E},$$

which is exactly the force accelerating outwards the ions.

1.2.2 Plasma boundaries

A laboratory plasma, such as a HT plasma, is confined inside a discharge chamber. Whenever plasma interacts with a wall, a sheath forms. A sheath is a region where quasi-neutrality is violated and a space charge forms. It is characterized by a higher density of ions and a lower density of electrons (at least when the wall is floating). At the interface between a plasma and a wall, the electron thermal flux is much larger than the ion thermal flux such that a large excess of electrons hit the wall. Once some electrons are absorbed, the plasma is no longer quasi-neutral. Thus, a directed ion flux towards the wall is generated to compensate the absorbed electron flux. At the HT channel walls, from the competition of the electron thermal motion and the ion drift towards the wall, the sheath forms. The sheath stabilizes when the ion flux

is balances to the electron flux (at least in 1D). With a rather simple mathematical development [83], one can demonstrate that the ion speed at the sheath edge is given by

$$u_{\mathrm{B}} = \sqrt{\frac{k_B T_e}{m_i}}.$$

The mechanism of formation of the sheath was first established by Bohm [1] and became a well-known book topic. For this reason, u_{B} takes the name of Bohm speed. Even if the ion flux $u_i n_i$ is constant in the sheath, the velocity and density at the wall are such that $u_{\mathrm{wall}} > u_{\mathrm{B}}$ and $n_{\mathrm{wall}} < n_{\mathrm{s}}$. Here, n_{s} is the density at the sheath edge. In the previous expression, we introduced the Boltzmann constant k_B, such that $k_B T_e$ represents the thermal energy.

The positive charge layer at the walls generates a voltage difference between the plasma and the walls, which is given in a floating sheath by

$$V_{\mathrm{sheath}} = \frac{k_B T_e}{2e} \ln\left(\frac{2\pi m_e}{m_i}\right),$$

in the case of a Maxwellian distribution of the electrons (the Maxwellian hypothesis is not always satisfied [37, 71]). As one may notice, the sheath voltage is a function of the electron temperature and electron-to-ion mass ratio. The acceleration of the ions through the sheath is at the origin of one of the main issues in HT design: wall erosion. The mechanism for accelerating the ions to impact a surface is a well-established technique in plasma processing, with a wide number of applications in surface treatment. What is fundamental for surface etching in nanoelectronics industry is detrimental for HTs.

In experiments, it has been observed [53] that the characteristics of the materials in contact with the plasma has a strong impact on the discharge behavior. In particular, the high energy electrons impacting the wall can emit a secondary electron that is accelerated back to the plasma. The frequency of this phenomenon, which is called Secondary Electron Emission (SEE), depends on the choice of the material, on the energy of the impinging electron and on the direction of the electron impact [51, 70, 71, 77, 85, 137].

1.2.3 Hall thruster anomalous transport

As we discussed in the previous sections, the electrons, that are trapped in the magnetic field lines, start to drift in the azimuthal $\mathbf{E} \times \mathbf{B}$ direction. The collisions allow the electron transport in an axial direction: the particles can jump from a magnetic field line to another and move towards the anode, creating the so-called cross-field transport.

We remember that in plasmas the conductivity and the electron mobility are related. The electron conductivity tensor $\bar{\bar{\sigma}}_0$ is such that

$$\mathbf{J} = \bar{\bar{\sigma}}_0 \cdot \mathbf{E} = nq\bar{\bar{\mu}}_0 \mathbf{E},$$

with $\mathbf{J} = nq\mathbf{u}$ the current density and $\bar{\bar{\mu}}_0$ the mobility tensor in a homogeneous plasma. These simplified expressions allow us to write elementary relation between

conductivity and mobility: $\bar{\bar{\sigma}}_0 = nq\bar{\bar{\mu}}_0$. In the following, we drop the tensor double line above the mobility symbol.

The classical collisional mobility in the direction perpendicular to the magnetic field can be calculated by the electron momentum conservation equation with a constant collision frequency [22], as

$$\mu^{\perp}_{\text{class}} = \frac{\frac{e\nu_c}{m_e}}{\nu_c^2 + \omega_{ce}^2}.$$

In the previous expression the classical mobility $\mu^{\perp}_{\text{class}}$ depends on the collision frequency ν_c of electrons with other species and on the electron cyclotron frequency $\omega_{ce} = eB/m_e$. We highlight that the relation

$$\mu^{\perp}_{\text{class}} = \frac{u_x}{E_x}$$

is true only for homogeneous plasma (i. e., where the pressure gradient is negligible).

Several experimental works [4, 45, 68] have observed that the mobility along the thruster axis is significantly larger than the one predicted by the classical theory presented here. This difference is estimated in 1 or 2 orders of magnitude, depending on the discharge conditions [74, 106]. For this reason, the idea of *anomalous mobility* was introduced. The first mechanism that was considered responsible for the increased mobility was the SEE [6, 39, 76]. The SEE is capable of breaking the closed Larmor orbits and induces a drift of the orbit center position upstream. However, several recent works [50, 67, 136] have suggested that this mechanism may not be sufficient to explain the overall anomalous transport.

The enhanced cross-field transport can be related to the fluctuations of electron density and electric field: when these fluctuations are correlated in time a force contributes to the electron transport in the axial direction. This mechanism was studied by Adam *et al.* [55] and Ducrocq [65]. A decade later, Coche and Garrigues [99] confirmed that finding using 2D Particle-In-Cell (PIC) simulations and Katz *et al.* [102] introduced the concept of drag force. This theory was later developed and validated by Lafleur and coworkers [106, 105, 118, 117, 133, 147], who found that the anomalous transport at the channel exit and in the plume is due to the plasma instabilities developing along the azimuthal periodic direction. Tsikata *et al.* [79, 81] have confirmed experimentally the presence of these high-frequency oscillations.

By writing the electron density fluctuation and azimuthal electric field fluctuations as δn_e and δE_y, we can introduce the electron-ion friction force, which is

$$R_{ei} = e\langle \delta n_e \delta E_y \rangle,$$

with the angular brackets accounting for a space (or time) average. The correlation term is zero when the electric field and the electron density are uncorrelated. However, when the fluctuations are correlated, the electron friction force is non-null. Lafleur *et al.* [105] proposed an expression for the anomalous mobility by considering the correlation of plasma fluctuations. According to this theory, the anomalous mobility is given by

$$\mu_{\text{anom}} = \mu_{\text{class}} \left(1 - \frac{\omega_{ce}}{\nu_c} \frac{R_{ei}/e}{n_e E_x}\right). \tag{1.2}$$

By considering a totally collisionless plasma, i. e., $\nu_c \to 0$, the classical mobility μ_{class} is null as well, while the anomalous mobility calculated in Eq. (1.2) becomes

$$\mu_{\text{anom}} = -\frac{R_{ei}/e}{n_e E_x B}.$$

We recall that R_{ei} is negative when the electron density and the electric field are correlated. It is fundamental to understand the physical mechanisms that contribute to the electron friction force R_{ei}, so to the plasma oscillations. Ducrocq [65] demonstrated the correlation of anomalous transport with the growth of the electron cyclotron drift instability. This finding is supported by several other works in the last decade [99, 113, 117, 133, 165, 198]. In the next section, we discuss in detail the plasma instabilities that are present in HTs and their role in anomalous transport.

1.2.4 Plasma instabilities in Hall thrusters

The HT $\mathbf{E} \times \mathbf{B}$ discharge is characterized by a number of plasma instabilities, that are studied in detail in Chapters 2, 4 and 5. First, what is a plasma instability? A plasma instability refers to a collective behavior of plasma in which the stationary state is locally or globally perturbed. Instabilities can be convective or absolute, depending on whether or not they are carried within plasma. To identify an instability, it is common to measure (experimentally or numerically) a spectrum and compare it to a Dispersion Relation (DR). A dispersion relation is obtained by solving an equation of type

$$\omega = \omega(\mathbf{k}),$$

with $\omega = \omega_R + \imath\gamma$ the complex frequency (with ω_R the real part and γ the growth rate) and $\mathbf{k}$ the wavenumber. Some authors refer to $\mathbf{k}$ as the wavevector. However, we decided to adopt the wavenumber definition, as it is more common in the literature, while wavevector normally designates the particle function in quantum mechanics.

In HTs, a great variety of instabilities is present, ranging from some kHz to GHz [11, 12, 16, 17, 39, 40]. A graphical representation of the frequency ranges of these instabilities is shown in Figure 1.5. In this chapter, we discuss just briefly the instabilities characteristics: a more detailed description is given in the rest of the thesis.

At low frequency (i. e., $10 \sim 100$ kHz) we observe the presence of rotating spokes [4, 87]. In the same frequency range, HTs exhibit the Breathing Mode (BM): a low frequency ionization instability that causes large variations in all the plasma parameters. These oscillations were observed in Ref. [20], and frequently reported after [33, 78]. At intermediate frequency, at the order of some hundreds of kHz, we have the ion transit time instabilities [59]. These instabilities owe their name to their characteristic time, since their period is similar to the time spent by ions in the acceleration region. In the same frequency range, we find the Ion Ion Two-Stream Instability (IITSI) [24]. Just beyond the threshold of the MHz, we have the Modified Two-Stream Instability (MTSI) [16], a radial-azimuthal instability that develops in the thruster channel. Finally, at ≈ 10 MHz we find the Electron Cyclotron Drift Instability (ECDI): as shown in the theory, this instability results from the coupling of Bernstein modes with an ion acoustic instability (i. e., the Ion Acoustic Wave (IAW)). In the following sections

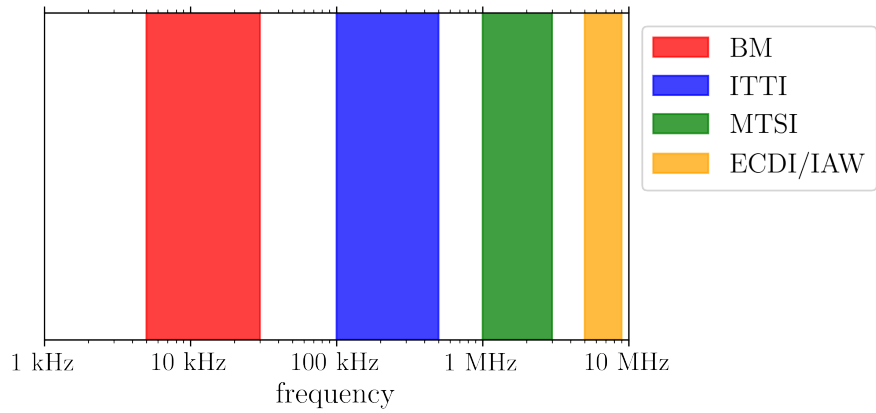


Figure 1.5: Representation of instabilities on the frequency spectrum.

we discuss the macroscopic characteristics of these instabilities, while the microscopic details are discussed in the next chapters.

1.2.4.1 *Breathing Mode*

The BM is a ≈ 10 kHz modulation of the discharge current, that is accompanied by the fluctuation of several plasma parameters, such as the species density and the electron temperature [20]. Due to its macroscopic effects on the discharge parameters, it was one of the first modes to be observed and studied in HTs. These large oscillations can be detrimental to the operation of the thruster. Firstly, because they can cause a large variation of the discharge current and plasma density, thus increasing the wall erosion. Secondly, because the oscillations may damage the electric circuit supplying the thruster.

The first studies about the development of the BM were made by Fife [35], who used a predator-prey Lotka-Volterra model to describe the consumption of neutrals (preys) by the charged species (predators). This model is extremely simple and explains the mechanism behind the BM, although it suffers from some inconsistencies. At the beginning of the discharge current growing phase, the ion populations starts to grow, increasing the ionization, thus the consumption of neutrals. This growth cannot be sustained forever, thus, at a given point, the neutral density is too low, slowing down the ionization and thus reducing the charged population. So, the discharge current decreases. When the neutral population is large enough, the trend changes sign and the current start increasing again, restarting the BM cycle. This model was later improved by Boeuf and Garrigues [33] and Barral and Ahedo [78], using 1D fluid simulations rather than 0D models.

In more recent years several works addressed this topic, in particular Lafleur *et al.* [175] and Chapurin *et al.* [169, 186]. In the first, Lafleur and coworkers have shown that the 0D model is not sufficient and that the system is always stable if one introduces a consistent neutral flow injection. By using a 1D model, Lafleur demonstrates that the BM mechanism is rather complex. During the growing phase, the increased electron temperature and ionization rate compensate for the decreasing

neutral density, so the overall discharge current increases. Then, it exists positive feedback between the growing plasma density and ionization rate, up to a certain threshold, at which this mechanism stops, and the plasma density drops, along with other plasma parameters. Alternatively, Chapurin and colleagues also studied the BM with a 1D fluid model. They found that the breathing mode is linked to the mechanism of ion backflow towards the anode.

To conclude about the BM, we can say that this instability, which does not have an electrostatic nature, is not a simple phenomenon, but rather a complex mechanism that is still not fully understood. Some macroscopic characteristics have been studied and explained by the HT community, however, the microscopic origin of this mode is still debated.

1.2.4.2 Ion transit-time instability

The ion transit-time instability is a $\approx$ 500 kHz instability that is characterized by a modulation of the discharge current and the ion density. This instability is linked to the ion transit time in the acceleration region and has been studied in different regimes experimentally [18, 104], numerically and theoretically [44, 54, 59, 75, 132, 145, 170, 202]. In several of these works the name Ion Transit-Time Instability (ITTI) is not used and the authors only refer generically to a *resistive* instability. The name ITTI might not be the most appropriate one, since the instability is not related to a boundary effect. However, we decided to keep this notation to be consistent with the literature.

This instability is macroscopically linked to the existence of a packet of low-energy ions in the thruster plumes. These ions are trapped in an electric field well and are not accelerated axially. So, these ions arrive in the plume with a velocity one order of magnitude lower than the one of the accelerated ions [115]. At the same time, some of the ions exhaust velocity is larger than the one imposed by the anode voltage. This effect appears to be related to the wave riding-mechanism: when the axial electric field oscillates, the ions experience an average acceleration that is larger than the one imposed by the anode voltage.

1.2.4.3 ECDI and MTSI

The Electron Cyclotron Drift Instability (ECDI), sometimes called EDI, electron drift instability, has been observed and studied for more than half a century now in different types of magnetized plasmas [11, 12, 14, 15]. In recent years, it gained a renewed celebrity because, as said previously, it is considered to be the main driver of the axial anomalous transport. The original DR, developed by Krall *et al.* [2, 3, 9], considers cold ions and a drifting Maxwellian for kinetic electrons. It demonstrates the coupling of magnetized electrons Bernstein modes with the ion acoustic wave.

When it became computationally possible, Ducrocq *et al.* [66] and Cavalier *et al.* [92] developed a method to solve numerically the DR and compared the results with solutions from simulations. Later, Lafleur and colleagues dedicated several works to the analysis of this instability [106, 105, 118, 117, 133, 170].

From an experimental point of view, Tsikata and coworkers used collective Thomson scattering to detect this instability in the HT plume [79, 81, 103]. Brown and Jorns also studied the presence of this instability [139]. The detection of this instability in

simulations is much more common, and several works discussed the growth of this instability and its development both in 1D [106, 128, 138, 165] and in 2D [94, 124, 99, 113, 129, 151, 177, 180, 198]. Villafana in his Ph.D. thesis [179] and in a recent work [203] discussed the presence of the ECDI also in 3D PIC simulations.

The resonances of the ECDI occur at fixed wavenumbers, which are multiples of

$$k_{\text{res}} = \frac{\omega_{\text{ce}}}{v_{d,e}},$$

where $v_{d,e}$ is the macroscopic mean drift velocity of the electrons. Below the wavenumber of the first resonance, the kinetic DR has another peak, which corresponds to the Modified Two-Stream Instability (MTSI).

The MTSI is a 2D instability that develops in the channel region [16, 129, 177, 180, 203], or in the near plume region [163], with a component parallel to the magnetic field and one to the $\mathbf{E} \times \mathbf{B}$ drift. This instability is characterized by a wavelength of some millimeters and a frequency of the order of 1 MHz and is responsible both for the anomalous transport in the axial direction and for an increased electron temperature in the direction parallel to the magnetic field.

The $\mathbf{E} \times \mathbf{B}$ community agrees on the fact that high frequency ECDI and MTSI instabilities are probably among the main drivers of anomalous transport in the HT plume [160].

1.2.5 Main challenges

If these devices have been used successfully for over half a century, why should we continue to study them? The answer is both simple and complex. It is simple because we know that NewSpace (e. g.,the emergence of private entities in the 21$^{\text{st}}$ century space market) is driving the development of a new generation of thrusters with a wide range of power and size. It is complex because the standard development technique used in the industry does not meet the requirements of the market: the trial-and-error method takes time and money.

For this reason, a large number of studies is nowadays conducted to improve the HT design and meet the growing requirements. The scaling methods used by some groups [84, 189], could derive some basic relations between the different components, but miss some important aspects of the HTs design. For this reason, other approaches are needed to better understand the physics of the HTs and its effects on the performance.

The key elements under study are the instabilities: the origin of most of them remains unclear. The BM oscillation cannot be simply explained, and we miss some model that can predict the frequency and amplitude of this oscillation, given the thruster parameters. Also, the high-frequency oscillations, which play a fundamental role in anomalous transport, are not fully understood and a little effort has been made to limit these oscillations. A reduced anomalous transport corresponds to an increased residence time of electrons in the thruster channel, which directly affects the ionization efficiency.

Moreover, the wall materials play a fundamental role. The erosion caused by the ion bombarding on the walls may significantly decrease the thruster efficiency and the

lifetime of the device. So, the study of the erosion mechanisms in different geometries is a key point in the development of new HTs.

1.3 HALL THRUSTER PLASMA MODELING

Plasma modeling, so the modeling of HTs, has represented a major challenge for the scientists of the last century. The complexity of these systems has favored the development of rather different techniques of describing the plasma discharges, depending on the plasma characteristics and the goal of the simulation itself.

1.3.1 Plasma modeling basics

A plasma can be described using different models. Let us consider a system of particles, each with 3D position $\mathbf{r}$ and velocity $\mathbf{v}$. In the six-dimensional phase space defined by the particles positions and velocities, we can introduce a distribution function $f(\mathbf{r}, \mathbf{v}, t)$ at the time t, such that

$$p = f(\mathbf{r}, \mathbf{v}, t) d^3\mathrm{r} d^3\mathrm{v}$$

represent the number of particles in the six-dimensional phase volume $d^3\mathrm{r}d^3\mathrm{v}$ at the position $(\mathbf{r}, \mathbf{v})$ and at time t. By studying the continuity of the distribution function [63], we can derive the equation of motion for the particles, which, coupled to Maxwell equations to or Poisson equation, becomes the Vlasov equation:

$$\frac{\partial f}{\partial t} + \mathbf{v} \cdot \frac{\partial f}{\partial \mathbf{r}} + \frac{q}{m} (\mathbf{E} + \mathbf{v} \times \mathbf{B}) \cdot \frac{\partial f}{\partial \mathbf{v}} = 0.$$

This equation neglects the effect of the correlation between pairs of particles at short distances and times, that can be included by adding a *collision term* at the right-hand side. Thus, we obtain the Boltzmann equation for the distribution function:

$$\frac{\partial f}{\partial t} + \mathbf{v} \cdot \frac{\partial f}{\partial \mathbf{r}} + \frac{q}{m} (\mathbf{E} + \mathbf{v} \times \mathbf{B}) \cdot \frac{\partial f}{\partial \mathbf{v}} = \left. \frac{\partial f}{\partial t} \right|_c . \tag{1.3}$$

Unfortunately, the Boltzmann equation is extremely complex to solve, since it is an integro-differential equation in six variables plus time. As we usually observe macroscopic quantities (i. e., averages over the velocity space), such as the density, the temperature, the velocity, *et cetera*, we can derive the momentum equations from the kinetic equation.

By averaging over the velocity phase-space, we can reduce the complexity of the dynamical equations and find the spatial distribution of some macroscopic quantities. To obtain these quantities we need to take some *velocity moments* of the distribution function calculated by the Boltzmann equation. The first moment is the density, which is defined as

$$n(\mathbf{r}, t) = \int f(\mathbf{r}, \mathbf{v}, t) d^3\mathbf{v}.$$

The flux of particles is defined as

$$\Gamma(\mathbf{r}, t) = n\mathbf{u} = n \langle \mathbf{v} \rangle_{\mathbf{v}} = \int \mathbf{v} f(\mathbf{r}, \mathbf{v}, t) d^3\mathbf{v},$$

where $\mathbf{u}(\mathbf{r}, t)$ is the mean, or *fluid*, velocity and $\langle\cdot\rangle_{\mathbf{v}} = 1/n \int f d^3\mathbf{v}$ the average over the velocity space. The isotropic temperature derives from the second moment, as

$$k_B T(\mathbf{r}, t) = \frac{m}{3n} \int (\mathbf{v} - \mathbf{u})^2 f(\mathbf{r}, \mathbf{v}, t) d^3\mathbf{v}.$$

If the temperature is not isotropic, we can define the *pressure tensor* as

$$\Pi(\mathbf{r}, t) = m \int (\mathbf{v} - \mathbf{u}) \otimes (\mathbf{v} - \mathbf{u}) f(\mathbf{r}, \mathbf{v}, t) d^3\mathbf{v}.$$

This tensor is a 3×3 matrix, with components

$$\Pi_{ij} = mn\langle (v_i - u_i) \left(v_j - u_j\right)\rangle_{\mathbf{v}},$$

with $i, j = 1, 2, 3$.

Once we have defined the moments of the distribution function, we can derive the equations of motion for the macroscopic quantities. By integrating all the terms of Eq. (1.3) over the velocity space, we can obtain the continuity equation for the density:

$$\frac{\partial n}{\partial t} + \nabla (n\mathbf{u}) = S.$$

In this equation S represents the particle loss or creation. Since the losses are usually negligible, we can write this term as a function of the ionization frequency ν_i, as $S = \nu_i n$.

The momentum conservation equation is obtained by integrating the Boltzmann equation multiplied by $m\mathbf{v}$ over the velocity space:

$$m \left[\frac{\partial}{\partial t} (n\mathbf{u}) + \nabla \cdot (n\mathbf{u} \otimes \mathbf{u}) \right] = qn (\mathbf{E} + \mathbf{u} \times \mathbf{B}) - \nabla \cdot \Pi + G_{\text{coll}}. \tag{1.4}$$

On the left-hand side the first term represents an explicit variation of the speed, while the second is the *inertial* term. On the right-hand side, the first term represents the Lorentz force, the second is the pressure tensor gradient and the third is the collision term. The collision term G_{coll} represents the time rate of variation of the momentum per unit volume due to the collision with other species. This term depends both on the momentum transfer collision and on the ionization events. This term should be calculated carefully, please refer to the literature for more details [90].

The solution of the Boltzmann equation at thermodynamic equilibrium has a Gaussian speed distribution, which is called the Maxwellian distribution. The Maxwellian distribution is defined as

$$f_{\text{M}}(v) = n \left(\frac{m}{2\pi k_B T} \right)^{3/2} \exp \left(-\frac{mv^2}{2k_B T} \right).$$

This distribution is a solution of the kinetic equation when the collision term is dominant. The thermal velocity of a species with mass m and temperature T is

$$v_{\text{th}} = \sqrt{\frac{2k_B T}{m}}.$$

The average speed can be obtained by integrating the distribution function over the velocity space is

$$\bar{v} = \left(\frac{8k_B T}{\pi m}\right)^{1/2}.$$

The flux directed through a surface, let us say w, is given by

$$\Gamma_w = \frac{1}{4} n \bar{v}.$$

The Maxwellian hypothesis about the distribution function is often used in the context of simulations since it allows us to simplify the calculations. However, it is not always a good approximation, since the distribution function can be very different when the plasma is not near thermal equilibrium. In a recent work on a plasma similar to the one studied in the current thesis, Alvarez Laguna *et al.* [182] have shown that the distribution function may be strongly non-Maxwellian.

1.3.2 Plasma parameters

To model a plasma, we need to define some characteristic physical quantities, besides the standard ones, that are the density, the temperature and the pressure. One can define the plasma frequency ω_p as the frequency of the plasma Langmuir oscillations. This gives a typical timescale for the plasma response. The plasma frequency for electrons and ions is defined as

$$\omega_{\mathrm{p},e,i} = \sqrt{\frac{n_0 e^2}{\epsilon_0 m_{e,i}}}.$$

This quantity gives information about the natural frequency at which the plasma would oscillate in the case of cold ions and electrons. The electron plasma frequency is much larger than the ion plasma frequency. In the conditions of a xenon operated HT, with a density of $n_0 \approx 1 \times 10^{18}\,\mathrm{m}^{-3}$. The first one has a value of $\omega_{\mathrm{p},e} \approx 50\,\mathrm{GHz}$, while the second one is $\omega_{\mathrm{p},i} \approx 1\,\mathrm{GHz}$.

To define the typical length scale, we introduce the Debye length λ_D, which reads

$$\lambda_D = \sqrt{\frac{\epsilon_0 k_B T_e}{n_0 e^2}},$$

where k_B is the Boltzmann constant and T_e is the electron temperature. The Debye length is the length of the shielding of a negative charge in the plasma. The value of the Debye length is related to the dimension of the plasma sheath at the boundaries: as one may notice $\lambda_D = v_{\mathrm{th},e}/\omega_{\mathrm{p},e}$. In the case of a HT with an electron temperature of 10 eV and the same density as before, the Debye length is $\lambda_D \approx 20\,\mu\mathrm{m}$. Both the plasma frequency and the Debye length depend on the density (λ_D depends on the temperature as well), thus, they may strongly vary along the Hall thruster axis (i. e., the plasma is much denser at the channel exit than in the plume. Similarly, the temperature peaks inside the channel and decreases significantly near the anode and the cathode).

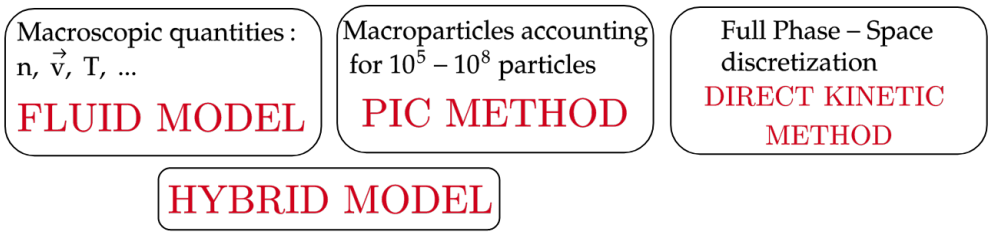


Figure 1.6: The various methods to simulate a plasma.

1.3.3 Plasma modeling techniques

The Boltzmann equation (1.3) is the most detailed description of the entire phase-space. However, solving the Boltzmann equation can be extremely costly, since one needs to discretize the full phase-space (i. e., space and speed). This Direct Kinetic (DK) approach is used by some solvers [62], also known as deterministic Boltzmann solvers, to provide a solution of the Boltzmann equations, however, its complexity prevents it from being used for long simulations. The PIC method is a numerical method that allows us to solve the Boltzmann equation in a much more efficient way. In this method, some *superparticles* (also called *macroparticles*) accounting for a large number of single physical particles are mapped on a discrete spatial grid and the evolution of the plasma is computed by solving the Lorentz-Poisson equation on the grid. The PIC method is used in many plasma simulations, including the ones in this work. Even if the cost of PIC simulations is lower than the one of DK simulations, it is still very high. This is why the PIC method is often used in combination with other methods, such as fluid method. Fluid simulations solve the conservation equations of the plasma, that are the so-called moments of the Boltzmann equation described in Section 1.3.1 (i. e., the first three moments are the continuity equation, the momentum equation and the energy equation). The fluid method is much less costly than the PIC method, but it is not able to capture the kinetic effects of the plasma, since it deals with macroscopic quantities such as density, temperature and pressure. Clearly, fluid modeling makes several assumptions that do not hold under every condition. For example, the assumption of a Maxwellian distribution function is often used in fluid simulations. The two techniques described above are sometimes used together in the so-called *hybrid* simulations. These simulations usually solve the faster electron dynamics using fluid equations, while the slower ion (and neutral) dynamic is solved with PIC. In the following sections we presents some details about the different modeling techniques reported above, briefly discussing their use by the $\mathbf{E} \times \mathbf{B}$ community in HTs simulations. A schematic representation of the different methods is shown in Figure 1.6.

1.3.3.1 Fluid simulations

Fluid simulations are among the most used plasma simulations, since they allow us to study macroscopic plasma quantities. However, as just said, the simple description of the plasma via fluid equations is obtained using some assumptions that are not

always valid. This approach deals with integrated quantities, so the effects linked to the discrete nature of the particles are inevitably lost.

If we take an infinite number of moments of the Boltzmann equation, we can retrieve a kinetic description of a plasma with fluid formalism (yet the Maxwellian assumption would still hold). Since we want to simplify the description of the plasma and not make it more complex, we need to limit the number of moments we use. The n^{th} moment depends on the $(n+1)^{\text{th}}$, hence, we need to introduce some closure terms to close the set of equations. As an example, the continuity equation depends on the fluid velocity $\mathbf{u}$, that can be derived in the momentum conservation equation. However, in this equation appears the pressure tensor Π. The expression of this term can be found by solving the energy conservation equation, and so on. The usual methods make some hypothesis on the pressure tensor or heat-flux, limiting the set of equation to the first two or three moments, respectively. Some works [182, 198] consider more moments, for an improved description of the plasma. The set of fluid equations is sometimes simplified by considering a drift/diffusion approximation for the electrons [75], which consists of neglecting the inertial terms and in writing a simpler expression for the momentum conservation equation.

Fluid codes have some other limitations. Indeed, several codes consider a quasi-neutral plasma (i. e., $n_i = n_e$). The quasi-neutrality hypothesis allows us to get rid of the Poisson equation but prevents any phenomenon that creates a space charge in the plasma [33, 52, 109]. As an example, the plasma fluctuations are often related to some deviation from the charge neutrality as well as the formation of the plasma sheath at the plasma boundaries.

The first works in the $\mathbf{E} \times \mathbf{B}$ community with full-fluid simulations were performed around 20 years ago [43, 48, 50, 51] in one dimension. More recently, the simulation domain was extended to two dimensions [57, 89, 123, 130].

The biggest drawback of fluid simulations for HTs is related to the anomalous transport. The anomalous transport is, as shown in Section 1.2.3, related to the electric field and density fluctuations. Fluid simulations do not always capture the correct growth rate for plasma instabilities, thus preventing the anomalous transport from being correctly modeled. For this reason, several works add an anomalous collisional term ν_{anom} to the standard collisional frequency in the momentum equation [35, 132, 175]. Clearly, this approach cannot reproduce perfectly the instabilities effect, for which kinetic simulations are needed.

1.3.3.2 Hybrid simulations

The hybrid simulations are a first attempt to include kinetic effects, still keeping a low computational cost. The first simulations were performed in the late '90s by several groups [33, 34, 38] and re-proposed many times since then. In these simulations normally the electron dynamics is treated as a fluid, while the heavy species are particles.

These simulations successfully reproduced the breathing mode and captured some of the transit-time instabilities [33, 35, 54, 69]. However, it fails in reproducing the high-frequency MHz instabilities, that are the major responsible for the anomalous transport [133].

1.3.3.3 *Kinetic simulations*

The weak electron collisionality in HTs (i.e., the mean free path of an electron is larger than the device dimensions) prevents efficient thermalization and therefore the distribution function is often not Maxwellian. Morozov in his book [39] proposed the idea of multiple electron populations with different temperatures. Moreover, the anisotropy related to the presence of the magnetic field further increases the deviation from Maxwellian (i.e., the electron temperature is not necessarily isotropic: the electron temperature perpendicular to the magnetic field may be larger than the parallel one).

As explained above, the non-Maxwellian character of the Electron Velocity Distribution Function (EVDF) cannot be captured in classical fluid or hybrid simulations. The kinetic simulations allow to capture the non-Maxwellian character of the plasma. Two families of kinetic models exist: the grid-based Boltzmann equation solvers [127] and the PIC/Monte Carlo Collisions (MCC) solvers [26]. The first one, also known as *Direct kinetic* method, solves the Boltzmann equation on a grid in discretized velocity phase-space [149]. This method is rather complex, since it solves a hyperbolic partial differential equation, coupled to a resolution of the electro-magnetic field. In the second one, the distribution function is recreated by using a large number of superparticles with different velocities. These particles move in a space-grid. The more particles are used, the better the description of the EVDF is. However, the computational cost increases significantly with the number of particles and in many cases the resolution gain is not worth the computational cost increase. A more sophisticated particle to grid interpolation [196] allows us to retrieve some kinetic effect that are otherwise not visible with the standard techniques. The implementation of the particle methods does not have any particular difficulty, since they require the solution of an ordinary differential equation for the particle motion and the Poisson elliptic partial differential equation.

In the last two decades the $\mathbf{E} \times \mathbf{B}$ community has been extremely active in the development of PIC/MCC codes. The first full-PIC 1D-radial codes were developed by Taccogna *et al.* [64, 73] and by Sydorenko *et al.* [70, 72, 77]. Later, when the importance of the azimuthal direction became clear, some authors developed the first 1D-azimuthal codes [66, 97, 105, 128]. More recently, different groups developed 2D radial-azimuthal codes [94, 113, 112, 129, 136, 153, 152, 151, 177, 180] to study the coupling of the azimuthal dynamics with the radial one. At the same time, the need for simulating the direction of the thrust lead to the development of axial-azimuthal codes [55, 99, 118, 131, 133, 124, 151, 141, 201, 202]. Axial-radial codes were developed as well [46, 101].

Recently, two international benchmarks [140, 180] have been organized to compare the different codes. The first organized by Thomas Charoy of Laboratoire de Physique des Plasmas (LPP) dealt with the simulation of the axial-azimuthal plane of a HT. The second, led by Villafana and organized by the LPP and the CERFACS groups, dealt with the simulation of the radial-azimuthal plane of a HT.

1.4 SCOPE AND OUTLINE OF THE THESIS

This thesis is part of the collaboration between LPP and Safran Spacecraft Propulsion, within the POSEIDON *ANR Chair*, started in 2017. Numerical simulations are a required step to ease the conception of the new generation of HTs and to reduce the development time. The principal objective of this study is to enhance the understanding of the physics underlying the operation of HTs and to develop more effective models for their accurate representation. Such models should guide the development of more efficient numerical tools, which can contribute to the design of next-generation thrusters. This thesis follows and completes those of Croes [112], Tavant [152] and Charoy [155], which have laid the foundation for the work presented here.

One of the most recognized characteristics of HTs is the presence of plasma instabilities, which strongly affect the electron transport along the thruster axis [118]. However, even if a large number of works have been published on the subject, a global view about electrostatic instabilities was still missing. For this reason, in Chapter 2 we derive a 3D electrostatic dispersion relation. By projecting this dispersion relation along the different thruster's planes, we show that the 3D dispersion contains the most known 1D and 2D DRs. With this top-down approach, we also show the need to consider the multi-dimensional nature of the instabilities in order to understand their development and propagation. However, the theory itself is not enough to understand the growth and the effects of the instabilities: simulations are required.

The simulations in this work are realized using a 2D PIC code, *LPPic*, that can simulate both the radial-azimuthal and axial-azimuthal planes of a HT. The code development and characteristics are discussed in Chapter 3. The radial-azimuthal simulations are analyzed in Chapter 4. In particular, in this chapter, we study the conditions allowing the growth of the MTSI and its effects on the anomalous transport. The instabilities in the axial-azimuthal plane, i. e., ITTI and the IAW, are discussed in Chapter 5, along with their most important effects on the plasma parameters. The comparison of the simulation results with the theory developed in Chapter 2 allows us to explain the origin and propagation of these instabilities.

The simulations discussed heretofore are purely 2D. However, we know that the third dimension plays a fundamental role in determining the plasma parameters. For this reason, in the subsequent chapter, Chapter 6, we discuss the introduction of the virtual third dimension, which takes into account the effects of the radial boundaries in an axial-azimuthal simulation. Later, in Chapter 7, we show how the abundant data resulting from PIC simulations can be used to study in detail the microscopic and macroscopic HT physics. In the latter part of that chapter, we use our PIC code to investigate the effect of changing the input parameters on the thruster physics and performance. Table A.1 summarizes the axial-azimuthal simulations presented in this thesis.

2 PLASMA INSTABILITIES

This chapter initially presents a comprehensive derivation of the 3D dispersion relation for electrostatic modes in $\boldsymbol{E} \times \boldsymbol{B}$ plasmas. Subsequently, it is shown that from this dispersion one can derive those of the ion acoustic wave (IAW), of the modified two-stream instability (MTSI) and of the ion transit-time instability (ITTI). The limits of validity of these dispersions relations and the conditions that favor the growth of the different modes are also discussed. The last part of the chapter delves into different techniques for computing space-time spectra. The primary focus is on the application of these methods to analyze and interpret particle-in-cell (PIC) data. The discussion provides a detailed analysis of various approaches (FFT, PSD2P, DMD) that can be employed to determine the spectra, outlining their respective advantages and limitations.

Chapter contents

2.1 Why instabilities? 24
2.2 The electrostatic dispersion relation 24
2.2.1 Derivation of the 3D dispersion relation 25
2.2.2 Ion acoustic wave 28
2.2.3 Modified Two-Stream Instability 30
2.2.4 Ion transit-time instability 33
2.2.5 Resistive modes 35
2.2.6 Other electrostatic instabilities 36
2.3 Plasma instability spectral analysis 37
2.3.1 Discrete Fourier Transform 37
2.3.2 Two-points power spectral density 38
2.3.3 Dynamic Mode Decomposition 41
2.4 Chapter summary 42

The results in this chapter have been partially published in Refs. [177, 202].

2.1 WHY INSTABILITIES?

The discussion in the previous chapter has shown that several instabilities in HTs play a fundamental role in discharge physics. By strongly influencing the anomalous electron transport in the axial direction, they have a direct impact on thruster performance. Gaining a deeper comprehension of these instabilities constitutes a crucial advance towards achieving a more effective modeling of HTs. In this chapter, we study theoretically the dispersion relations that govern the propagation of the electrostatic instabilities in HTs. We first derive a general 3D DR from the fluid equations. Subsequently, we derive the 2D DRs for the IAW, MTSI and the ITTI, and compare them to those of previous published works. We also discuss the limits of validity of these DRs and we propose some simplifications that provide a better understanding of the nature of these modes.

In the second part of the chapter, we propose and discuss some methods to calculate the spatiotemporal spectra, focusing on the application on PIC data. The comparison between theoretical dispersions and numerical simulations will be presented in Chapters 4 and 5.

2.2 THE ELECTROSTATIC DISPERSION RELATION

The HT plasma instabilities range from kHz to tens of MHz and propagate both in azimuthal and axial directions. These instabilities have been extensively studied theoretically [11, 12, 16, 17, 39, 66, 92, 106, 105], numerically [110, 144, 156] and experimentally [103, 74, 139]. However, due to their complexity and the interplay between these instabilities, the underlying physics is still not fully understood. ECDI is a short-wavelength ($\lambda \sim 1\,\mathrm{mm}$) high-frequency ($\omega \sim 7\,\mathrm{MHz}$) electrostatic instability that develops mainly along the $\mathbf{E} \times \mathbf{B}$ drift direction. This instability has been studied during the last 20 years [55, 94, 92, 99, 105, 133, 129, 150, 198] and has shown to have a significant impact on the electron transport in the axial direction. PIC simulations [118, 140, 177] have revealed that this instability evolves towards the IAW after some tens of microseconds. In addition to the ECDI, numerical studies have shown a radial-azimuthal electrostatic instability, that was named MTSI, with a longer wavelength (some millimeters) and a frequency in the MHz range [129, 163, 177, 180]. Hagelaar *et al.* [54], Barral *et al.* [59] and Fernandez *et al.* [75] found an axial electrostatic long-wavelength ($\sim 1\,\mathrm{cm}$) mid-frequency ($\sim 400\,\mathrm{kHz}$) instability that was called Ion Transit-Time Instability (ITTI). This instability develops in the thruster plume and its period is of the order of the duration of the transit of ions in the acceleration region. As anticipated, the ITTI is a resistive instability, similar to the one studied by Litvak and Fisch [44] in the azimuthal direction. Koshkarov *et al.* [132] have studied the axial growth and propagation of this mode. Recently, Charoy *et al.* [170] have shown the influence of the ITTI on the ion ejection velocity in PIC simulations. In the same frequency range, some experimental and numerical studies [158, 174] have observed the Ion-Ion Two Stream Instability (IITSI), which is related to the presence of doubly charged ions. Finally, in the low-frequency range ($\sim 10\,\mathrm{kHz}$), the Breathing Mode (BM) is found to be a low-frequency ionization instability. Despite the origin of this

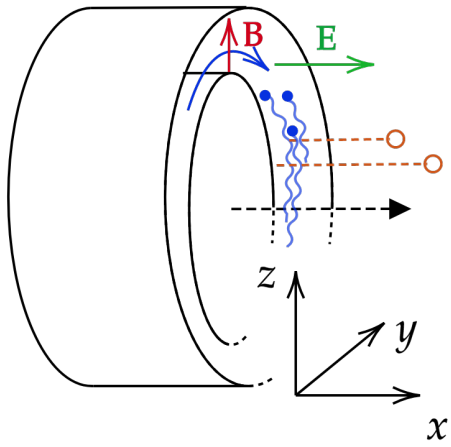


Figure 2.1: Schematic representation of a HT in 3D. The magnetic field is along the z direction, the stationary electric field is along the x direction and the $\mathbf{E} \times \mathbf{B}$ drift occurs in the negative y direction. The cathode is not represented.

instability not being fully understood [175, 169], it is commonly accepted that the BM should not be considered among electrostatic plasma instabilities, since it is mainly related to the oscillation of the densities and ionization rate.

2.2.1 Derivation of the 3D dispersion relation

In this section, we derive the DR from a fluid model that considers the continuity and momentum equations for electrons and ions, coupled by Poisson's equation. The derivation in this section does not introduce any new instability: we derive a general 3D DR and we show precisely the intervals of validity of the most studied DRs in HTs. Moreover, with a top-down approach, we show that it is possible to calculate a 2D version of the DRs of some instabilities that are usually considered mono-dimensional. As usual, we refer to the azimuthal direction as y, the axial direction as x and the radial direction as z. We consider the magnetic field $\mathbf{B} = B\hat{\mathbf{e}}_z$ is along the z direction, the stationary electric field $\mathbf{E} = E\hat{\mathbf{e}}_x$ is along the x direction and the $\mathbf{E} \times \mathbf{B}$ drift occurs in the negative y direction. A scheme of the used axes, concerning a HT, is provided in Figure 2.1.

Ions and electrons are assumed to be isothermal with an isotropic temperature. We recall that in HTs the electrons are magnetized, while ions are not. Consequently, we can neglect the effect of the magnetic field on ions. We perform a first-order perturbation of the densities (cf. Refs. [16, 122]), the velocities, and of the potential.

All the variables are written in the form $\xi = \xi_0 + \xi'$, where ξ_0 is the equilibrium and ξ' a small perturbation. The linearized fluid equations read

$$\begin{aligned}
&\frac{\partial n_e'}{\partial t} + \mathbf{v}_{e0} \cdot \nabla n_e' + n_0 \nabla \cdot \mathbf{v}_e' = 0, \\
&\frac{\partial n_i'}{\partial t} + \mathbf{v}_{i0} \cdot \nabla n_i' + n_0 \nabla \cdot \mathbf{v}_i' = 0, \\
&\frac{\partial \mathbf{v}_e'}{\partial t} + \mathbf{v}_{e0} \nabla \cdot \mathbf{v}_e' = -\frac{e}{m_e}(\mathbf{E}' + \mathbf{v}_e' \times \mathbf{B}) - \frac{k_B T_e}{m_e n_{e0}} \nabla n_e' - \nu_e \mathbf{v}_e', \\
&\frac{\partial \mathbf{v}_i'}{\partial t} + \mathbf{v}_{i0} \nabla \cdot \mathbf{v}_i' = \frac{e\mathbf{E}'}{m_i} - \frac{k_B T_i}{m_i n_{i0}} \nabla n_i' - \nu_i \mathbf{v}_i',
\end{aligned}$$

and Poisson's equation reads

$$\nabla^2 \Phi' = \frac{-e}{\epsilon_0}(n_i' - n_e'). \tag{2.1}$$

Here, $n_{i,e}$ are the ion and electron densities, $\mathbf{v}_{i,e}$ are the ion and electron fluid velocities, $\nu_{i,e}$ are the ion and electron collision frequencies, $m_{i,e}$ are the ion and electron masses, $T_{i,e}$ are the ion and electron temperatures, $\mathbf{E}$ is the electric field, $\mathbf{B}$ is the magnetic field, k_B is the Boltzmann constant and e is the elementary charge. The ionization has been neglected in the system. In HTs, this assumption is valid almost everywhere, but in the vicinity of the ionization peak. The steady-state solutions for electrons and ions are

$$\begin{aligned}
v_{e,0} \cdot \nabla v_{e,0} &= -\frac{e}{m_e}(\mathbf{E}_0 + V_{e,0} \times \mathbf{B}) - \frac{k_B T_e}{m_e n_{e,0}} \nabla n_{e,0} - \nu_e v_{e,0}, \\
v_{i,0} \cdot \nabla v_{i,0} &= \frac{e}{m_i}\mathbf{E}_0 - \frac{k_B T_i}{m_i n_{i,0}} \nabla n_{i,0} - \nu_i v_{i,0}.
\end{aligned}$$

Let us now consider a plane wave perturbation, i. e., $\xi' = \tilde{\xi} \exp[\imath(\mathbf{k} \cdot \mathbf{x} - \omega t)]$. By defining $\bar{\omega}_{e,i} \doteq \omega - \mathbf{k} \cdot \mathbf{v}_{e,i,0}$, the continuity equations can be written as

$$\frac{\tilde{n}_e}{n_0} = \frac{\mathbf{k} \cdot \tilde{\mathbf{v}}_e}{\bar{\omega}_e}, \tag{2.2}$$

$$\frac{\tilde{n}_i}{n_0} = \frac{\mathbf{k} \cdot \tilde{\mathbf{v}}_i}{\bar{\omega}_i}, \tag{2.3}$$

for electrons and ions, respectively. The discussion on the momentum equations has to be held separately for ions and electrons, since the former are not magnetized, while the latter are. With $\hat{\omega}_{e,i} \doteq \omega - \mathbf{k} \cdot \mathbf{v}_{e,i,0} + \imath\nu_{e,i}$, the linearized momentum equation for non-magnetized isothermal ions reads

$$\tilde{\mathbf{v}}_i = \frac{\left(v_{\mathrm{th},i}^2 \frac{\tilde{n}_i}{n_0} - \frac{e\tilde{\Phi}}{m_i}\right)\mathbf{k}}{\hat{\omega}_i}, \tag{2.4}$$

where $v_{\mathrm{th},i} = (k_B T_i / m_i)^{1/2}$ is the ion thermal velocity. The electron momentum equation is more complex, since the equations in x and y directions are coupled by the magnetic field. The linearized vector equation for isothermal magnetized electrons is

$$-\imath\omega m_e \tilde{\mathbf{v}}_e + m_e \tilde{\mathbf{v}}_e (\imath \mathbf{k} \cdot \mathbf{v}_{e0}) = e\tilde{\Phi}\imath\mathbf{k} - \tilde{\mathbf{v}}_e \times \mathbf{B} - m_e v_{\mathrm{th},e}^2 \imath\mathbf{k} - m_e \nu_e \tilde{\mathbf{v}}_e.$$

Each component reads

$$\tilde{v}_{ex}\left(\omega - \mathbf{k}\cdot\mathbf{v}_{e0} + \imath\nu_e\right) = \left(v_{\mathrm{th},e}^2\frac{\tilde{n}_e}{n_0} - \frac{e\tilde{\Phi}}{m_e}\right)k_x - \imath\tilde{v}_{ey}\omega_{ce},$$
$$\tilde{v}_{ey}\left(\omega - \mathbf{k}\cdot\mathbf{v}_{e0} + \imath\nu_e\right) = \left(v_{\mathrm{th},e}^2\frac{\tilde{n}_e}{n_0} - \frac{e\tilde{\Phi}}{m_e}\right)k_y + \imath\tilde{v}_{ex}\omega_{ce},$$
$$\tilde{v}_{ez}\left(\omega - \mathbf{k}\cdot\mathbf{v}_{e0} + \imath\nu_e\right) = \left(v_{\mathrm{th},e}^2\frac{\tilde{n}_e}{n_0} - \frac{e\tilde{\Phi}}{m_e}\right)k_z.$$

In the previous equations we introduced the electron thermal velocity $v_{\mathrm{th},e} = (k_B T_e/m_e)^{1/2}$ and the cyclotron frequency $\omega_{ce} = qB/m_e$. We solve the above system for the three velocity components, as follows

$$\begin{aligned}
\tilde{v}_{ex} &= \left(v_{\mathrm{th},e}^2\frac{\tilde{n}_e}{n_0} - \frac{e\tilde{\Phi}}{m_e}\right)\frac{\left(\hat{\omega}_e k_x - \imath\omega_{ce}k_y\right)}{\hat{\omega}_e^2 - \omega_{ce}^2},\\
\tilde{v}_{ey} &= \left(v_{\mathrm{th},e}^2\frac{\tilde{n}_e}{n_0} - \frac{e\tilde{\Phi}}{m_e}\right)\frac{\left(\hat{\omega}_e k_y + \imath\omega_{ce}k_x\right)}{\hat{\omega}_e^2 - \omega_{ce}^2},\\
\tilde{v}_{ez} &= \left(v_{\mathrm{th},e}^2\frac{\tilde{n}_e}{n_0} - \frac{e\tilde{\Phi}}{m_e}\right)\frac{k_z}{\hat{\omega}_e}.
\end{aligned} \tag{2.5}$$

Note that x and y are coupled, while the z direction (parallel to $\mathbf{B}$) is independent, as expected. By combining Eq. (2.4) and Eq. (2.5) with Eq. (2.3) and Eq. (2.2), respectively, we obtain

$$\frac{\tilde{n}_i}{n_0} = \frac{\frac{e\tilde{\Phi}}{m_i}k^2}{\hat{\omega}_i\bar{\omega}_i - k^2 v_{\mathrm{th},i}^2},$$
$$\frac{\tilde{n}_e}{n_0} = \frac{-\frac{e\tilde{\Phi}}{m_e}\left(\hat{\omega}_e^2 k^2 - \omega_{ce}^2 k_z^2\right)}{\hat{\omega}_e(\hat{\omega}_e^2 - \omega_{ce}^2)\bar{\omega}_e - \hat{\omega}_e^2 k^2 v_{\mathrm{th},e}^2 + \omega_{ce}^2 k_z^2 v_{\mathrm{th},e}^2}.$$

These expressions can be injected in the linearized Poisson equation, that reads

$$k^2\tilde{\Phi} = \frac{en_0}{\epsilon_0}\left(\frac{\tilde{n}_i}{n_0} - \frac{\tilde{n}_e}{n_0}\right),$$

to obtain the following isothermal fluid dispersion relation for a partially magnetized plasma:

$$0 = 1 + \chi_i + \chi_e = 1 - \frac{\omega_{\mathrm{p}i}^2}{\hat{\omega}_i\bar{\omega}_i - k^2 v_{\mathrm{th},i}^2} - \frac{\omega_{\mathrm{p}e}^2\left(\hat{\omega}_e^2 - \frac{k_z^2}{k^2}\omega_{ce}^2\right)}{\hat{\omega}_e\left(\hat{\omega}_e^2 - \omega_{ce}^2\right)\bar{\omega}_e - \hat{\omega}_e^2 k^2 v_{\mathrm{th},e}^2 + \omega_{ce}^2 k_z^2 v_{\mathrm{th},e}^2}, \tag{2.6}$$

where we remember the plasma frequencies defined as $\omega_{\mathrm{p}e,i} = \sqrt{n_{e,i}q^2/\epsilon_0 m_{e,i}}$, and where we have introduced the ion and electron susceptibilities, χ_i and χ_e.

The ion part of the fluid dispersion in Eq. (2.6) is similar to the ion dispersion in Ref. [66], that indeed was retrieved by a fluid ion model. The only differences are related to the assumption (cold ions, collisionless plasma, no ion drift) made by Ducrocq *et al.* in their model. The main discrepancies come out in the electron

part, where the kinetic DR shows k-resonances that are not captured by the fluid DR. The above 3D dispersion relation cannot be solved analytically to find $\omega = \omega(\mathbf{k})$. However, it can be simplified to retrieve the DRs of interesting waves/instabilities, such as the aforementioned ion acoustic wave [12, 117, 118], the modified two-stream instability [16, 129, 177] and the ion transit-time instability [59, 75].

2.2.2 Ion acoustic wave

2.2.2.1 The fluid IAW dispersion relation

The IAW, originally discussed by Gary and Sanderson in Ref. [11], has been observed in both axial-azimuthal and radial-azimuthal 2D PIC simulations [156, 110, 170, 117, 113, 177, 180]. In these works, in particular, in Refs. [117, 156, 170, 177], the IAW has been interpreted as the evolution of the ECDI in the saturated regime. In the next section, we propose a kinetic/fluid comparison that clarifies the relation between these two instabilities from a theoretical point of view. In Ref. [201], we have shown that although the IAW is mainly an azimuthal instability, it has a small axial component (along y). For this reason, to obtain the IAW dispersion relation from the general dispersion relation of Eq. (2.6), we project in the xy-plane by imposing $k_z = 0$. The electron susceptibility then reads

$$\chi_e = -\frac{\omega_{pe}^2}{(\hat{\omega}_e^2 - \omega_{ce}^2)\,\bar{\omega}_e/\hat{\omega}_e - k^2 v_{\mathrm{th},e}^2} = -\frac{1}{k^2\lambda_D^2}\frac{1}{\frac{(\hat{\omega}_e^2-\omega_{ce}^2)\bar{\omega}_e}{\hat{\omega}_e k^2 v_{\mathrm{th},e}^2} - 1}, \tag{2.7}$$

where the electron Debye length is defined as $\lambda_D^2 = v_{\mathrm{th},e}^2/\omega_{pe}^2$ and $k = \sqrt{k_x^2 + k_y^2}$. This expression can be simplified considering the typical characteristics of the IAW: a wavenumber in the range $\omega_{ce}/v_{\mathrm{th},e} \ll k \ll \omega_{ce}/v_{e,0}$ and a frequency ω in the MHz range (note that $v_{e,0}/\omega_{ce}$ is the distance traveled by the electron guiding center during one period of gyration and $v_{\mathrm{th},e}/\omega_{ce}$ is the gyroradius, hence the condition above implies that $v_{e,0} \ll v_{\mathrm{th},e}$). In this limit, we have $\omega_{ce} \gg \hat{\omega}_e$ and considering a weak collisionality implies that $\bar{\omega}_e \sim \hat{\omega}_e$. From these observations it follows that $(\hat{\omega}_e^2 - \omega_{ce}^2)\bar{\omega}_e / \left(\hat{\omega}_e k^2 v_{\mathrm{th},e}^2\right) \ll 1$, which allows writing a rather simple expression for the electron susceptibility, i.e., $\chi_e = 1/k^2\lambda_D^2$. By neglecting ion collisions and ion thermal velocity, we can write an explicit expression for the DR, as

$$\omega_{1,2} = \mathbf{k}\cdot\mathbf{v}_{i,0} \pm \frac{k\lambda_D\omega_{pi}}{(1+k^2\lambda_D^2)^{1/2}}, \tag{2.8}$$

which is the expression previously proposed by Gary [12]. The DR has no imaginary part and therefore does not predict the growth of the instability. Lafleur *et al.* [106] found from the kinetic theory the same expression for the real part of the DR, accompanied by the following growth rate, for a Maxwellian distribution,

$$\gamma_{1,2} \approx \pm\sqrt{\frac{\pi m_e}{8m_i}}\frac{\mathbf{k}\cdot\mathbf{v}_{e,0}}{\left(1+k^2\lambda_D^2\right)^{3/2}}. \tag{2.9}$$

2.2.2.2 Comparison with kinetic theory

The kinetic DR calculated by Krall *et al.* [2, 3, 9], considering cold ions and a drifting Maxwellian for electrons, in $k \sim k_y$ limit reads

$$0 = k_y^2\lambda_D^2\left(1-\frac{\omega_{pi}^2}{\omega^2}\right)+\left[1-I_0(\psi^2)e^{-\psi^2}+\sum_{n=1}^{\infty}\frac{2(\omega-k_y v_{e,0,y})^2 I_n(\psi^2)e^{-\psi^2}}{(n\omega_{ce})^2-(\omega-k_y v_{e,0,y})^2}\right], \quad (2.10)$$

where $\psi^2 = k_y^2 v_{th,e}^2/\omega_{ce}^2$ and I_n is the modified Bessel function of order n. A complete study of the kinetic DR can be found in the works of Ducrocq *et al.* [66] and Cavalier *et al.* [92]. It is interesting to note that this kinetic DR contains cyclotron resonances, that are not present in the fluid DR calculated in the previous section. These resonances ($k_y \approx n\omega_{ce}/v_{e,0}$) are the well-known ECDI modes [92, 106]. Following the work of Gary and Sanderson [11], this DR can be seen as the coupling of doppler-shifted electron Bernstein modes with the ion acoustic wave.

As noted by Krall [2], the electron cyclotron resonances are related to the angular non-uniformity of the distribution function perturbation. This fact is clearly in contradiction with the hypothesis of scalar isotropic pressure. The first resonance is simply related to the Lorentz force, i.e., an anisotropy related to the fluid velocity, so it can be predicted by a simplified fluid model.

The comparison of the kinetic DR in Eq. (2.10) and the fluid one of Eq. (2.6) in different intervals of k brings some useful insights. If we consider a long wavelength instability such that $k_y \ll \omega_{ce}/v_{th,e}$ (i. e., $k_y^2 v_{th,e}^2 \ll \omega_{ce}^2$, so $\psi^2 \to 0$), we can simplify the kinetic DR considering the terms up to ψ^2. The only Bessel functions contributing to the DR are the ones with $n = 0, 1$. Hence, the simplified kinetic DR reads

$$0 = 1-\frac{\omega_{pi}^2}{\omega^2}-\frac{1}{k_y^2\lambda_D^2}\frac{k_y^2 v_{th,e}^2}{(\omega-k_y v_{e,0,y})^2-\omega_{ce}^2}$$

and corresponds exactly to the fluid one projected along the $y-$axis (using the electron susceptibility in Eq. (2.7)) in the collisionless cold plasma limit (i. e., $\hat{\omega}_e = \bar{\omega}_e$ and $v_{th,e,i} \sim 0$). We note that this expression, derived from the fluid theory, predicts the presence of the first cyclotron resonance. However, if we consider the limit in which we have obtained this expression ($k_y \ll \omega_{ce}/v_{th,e}$) and that $v_{e,0,y} < v_{th,e}$, which is true in most of the cases, we observe that the resonance at $k_y = \omega_{ce}/v_{e,0,y}$ disappears since $k_y v_{e,0,y} < k_y v_{th,e} \ll \omega_{ce}$. In these conditions, the electron susceptibility becomes $\chi_e = \omega_{pe}^2/\omega_{ce}^2$, since $k^2 v_{th,e}^2 \ll |(\omega - k_y v_{e,0,y})^2 - \omega_{ce}^2| \approx \omega_{ce}^2$ and the DR simplifies to $\omega^2 \approx \omega_{ce}^2\omega_{pi}^2/\omega_{pe}^2$. If we consider a wavenumber as in the previous section (i. e., $\omega_{ce}/v_{th,e} \ll k_y \ll \omega_{ce}/v_{e,0,y}$) we have $e^{-\psi^2} \to 0$ and the kinetic DR in Eq. (2.10) simplifies to

$$0 = k_y^2\lambda_D^2\left(1-\frac{\omega_{pi}^2}{\omega^2}\right)+1,$$

that is exactly the fluid expression in Eq. (2.8) with no ion drift. The limit for $k_y \gg \omega_{ce}v_{e,0,y}$ is easily computed for both fluid and kinetic theories and reads $\omega^2 = \omega_{pi}^2$.

In conclusion, we have shown that in the fluid DR the cyclotron resonances with $n > 1$ are not captured. This can be explained by the fact that the fluid theory is not able to capture the angular asymmetries in the velocity space as the pressure is assumed to be isotropic. In addition, we have shown that in the limit of short and long wavelengths, the kinetic DR simplifies to the fluid DR.

2.2.3 Modified Two-Stream Instability

The modified two-stream instability is a radial-azimuthal instability, proposed by McBride *et al.* [16], that was recently studied in detail by Janhunen *et al.* [129] and Petronio *et al.* [177]. This instability owes its name to the Two-Stream Instability (TSI), which is a simple example of streaming instability (cf. Section 6.6 in Chen [22]). The TSI is characterized by the presence of fixed ions and drifting electrons, such that their drift is parallel to the instability propagation. When we consider an $\mathbf{E} \times \mathbf{B}$ discharge, the fields configuration is more complex: the instability propagation along the different directions is coupled by the presence of the magnetic field. For this reason, the $\mathbf{E} \times \mathbf{B}$ drifting electrons do not generate the standard two-stream instability, but a 2D version of it, which takes the name of *modified* two-stream instability, MTSI. The mechanism that provides the energy for this instability is the relative drift of magnetized electrons and unmagnetized ions.

As anticipated, it is possible to find the DR of the MTSI simplifying the general DR introduced previously. Limiting our interest to the yz-plane, the DR reads

$$0 = 1 - \frac{\omega_{\mathrm{p}i}^2}{\omega^2} - \frac{\omega_{\mathrm{p}e}^2}{\hat{\omega}_e^2 \dfrac{\hat{\omega}_e^2 - \omega_{\mathrm{c}e}^2}{\hat{\omega}_e^2 - k_z^2/k^2\omega_{\mathrm{c}e}^2} - v_{\mathrm{th},e}^2},$$

where we considered a collisionless approximation, (i. e., $\hat{\omega}_e = \bar{\omega}_e = \omega - \mathbf{k} \cdot v_{e,0}$) and no-drifting cold ions (i. e., $v_{i,0} = v_{th,i} = 0$). In the case of cold electrons ($v_{\mathrm{th},e} = 0$), the electron contribution to the DR, χ_e, simplifies to

$$\chi_e = -\frac{k_z^2}{k^2}\frac{\omega_{\mathrm{p}e}^2}{(\omega - k_y v_{e,0})^2} - \frac{k_y^2}{k^2}\frac{\omega_{\mathrm{p}e}^2\omega_{\mathrm{c}e}^2}{\left(\left(\omega - k_y v_{e,0}\right)^2 - \omega_{\mathrm{c}e}^2\right)}.$$

Injecting this expression in the full fluid DR, we obtain

$$0 = 1 - \frac{\omega_{\mathrm{p}i}^2}{\omega^2} - \frac{\omega_{\mathrm{p}e}^2 k_z^2}{(\omega - k_y v_0)^2 k^2} - \frac{\omega_{\mathrm{p}e}^2 k_y^2}{\left(\left(\omega - k_y v_{e,0}\right)^2 - \omega_{\mathrm{c}e}^2\right) k^2}. \tag{2.11}$$

This expression is exactly the one found by Janhunen *et al.* [129] in the case of cold electrons with kinetic theory. In the next section, we derive a stability criterion for the MTSI, similarly to what we have done in Ref. [177].

A simplification of the MTSI DR

To solve Eq. (2.11) numerically, we nondimensionalized the wavenumbers with the inverse of the electron Debye length λ_D, the frequency with the ion plasma frequency,

and the velocities by the Bohm speed $u_B = \lambda_D \omega_{pi} = \sqrt{k_B T_e / m_i}$. The dimensionless DR reads

$$1 - \frac{1}{\tilde{\omega}^2} - \frac{m_i}{m_e} \frac{\tilde{k}_z^2}{(\tilde{\omega} - \tilde{k}_y \tilde{v}_0)^2 \tilde{k}^2} - \frac{m_i}{m_e} \frac{\tilde{k}_y^2}{\left((\tilde{\omega} - \tilde{k}_y \tilde{v}_0)^2 - \frac{\omega_{ce}^2}{\omega_{pi}^2}\right) \tilde{k}^2} = 0, \tag{2.12}$$

with $\tilde{\omega} = \omega / \omega_{pi}$, $\tilde{k}_j = k_j \lambda_D$, and $\tilde{v}_0 = v_0 / u_B$. Note that, in the following, the dimensionless quantities are denoted with a tilde.

The solver uses scipy.optimize [166], which employs the Nelder–Mead method with the dimensionless convergence tolerance of $\xi = 10^{-12}$. For fixed $\tilde{k}_y$ and $\tilde{k}_z$, we solve for the complex frequency $\tilde{\omega} = \tilde{\omega}_r + i\tilde{\gamma}$, where $\tilde{\gamma} = \gamma / \omega_{pi}$ is the non-dimensional growth rate and $\tilde{\omega}_r = \omega_r / \omega_{pi}$ the non-dimensional frequency. Figure 2.2 shows an example of the solution $(\tilde{\gamma}, \tilde{\omega}_r)$ in the $\tilde{k}_y - \tilde{k}_z$ space for the classical values of the magnetic and electric field in HT (i. e., $B = 200\,\mathrm{G}$, $E = 1 \times 10^4\,\mathrm{V/m}$ and $v_0 = E/B$) with a $n = 5 \times 10^{16}\,\mathrm{m}^{-3}$ xenon plasma. In the bottom panels of the figure, the solid lines show the solution for the growth rate and frequency as a function of the azimuthal wavenumber for $\tilde{k}_z = 0.02$. The peak represents the MTSI resonance.

The dimensionless DR, i.e., Eq. (2.12), does not have a trivial analytical solution. However, it can be simplified using the following assumptions. First, in our range of interest, we have $\tilde{k}_z \ll \tilde{k}_y$, thus we can consider that $\tilde{k} \approx \tilde{k}_y$. Furthermore, as it is a low-frequency wave, the numerical solution of Eq. (2.12) verifies the following inequality $\tilde{\omega} \ll \tilde{k}_y \tilde{v}_0$. Lastly, in our range of interest, the radial wavenumber is such that $\tilde{k}_y \tilde{v}_0 \ll \omega_{ce} / \omega_{pi}$. Consequently, we further simplify the denominator of the fourth term. As a result, we obtain a simplified DR that reads

$$1 - \frac{1}{\tilde{\omega}^2} - \frac{m_i}{m_e} \frac{\tilde{k}_z^2}{\tilde{k}_y^4 \tilde{v}_0^2} + \frac{m_i}{m_e} \frac{\omega_{pi}^2}{\omega_{ce}^2} = 0. \tag{2.13}$$

The explicit solution for $\tilde{\omega}$ can be analytically calculated as

$$\tilde{\omega} = \left[1 + \frac{m_i}{m_e} \frac{\omega_{pi}^2}{\omega_{ce}^2} - \frac{m_i}{m_e} \frac{\tilde{k}_z^2}{\tilde{k}_y^4 \tilde{v}_0^2}\right]^{-\frac{1}{2}}, \tag{2.14}$$

with a singularity at

$$\tilde{k}_z = \left(\frac{m_e}{m_i} + \frac{\omega_{pi}^2}{\omega_{ce}^2}\right)^{\frac{1}{2}} \tilde{v}_0 \tilde{k}_y^2.$$

Considering that in HT conditions $m_e / m_i \ll \omega_{pi}^2 / \omega_{ce}^2$, the previous expression in dimensional form reads,

$$k_z = \frac{m_e E_x}{e B^2} k_y^2. \tag{2.15}$$

This equation gives the position of maximum growth rate, γ_{max}, in the $k_y - k_z$ space. Note that the spectral position of the MTSI resonance, γ_{max}, does not depend on the ion mass nor the plasma density, but only on the axial electric field and the radial magnetic field.

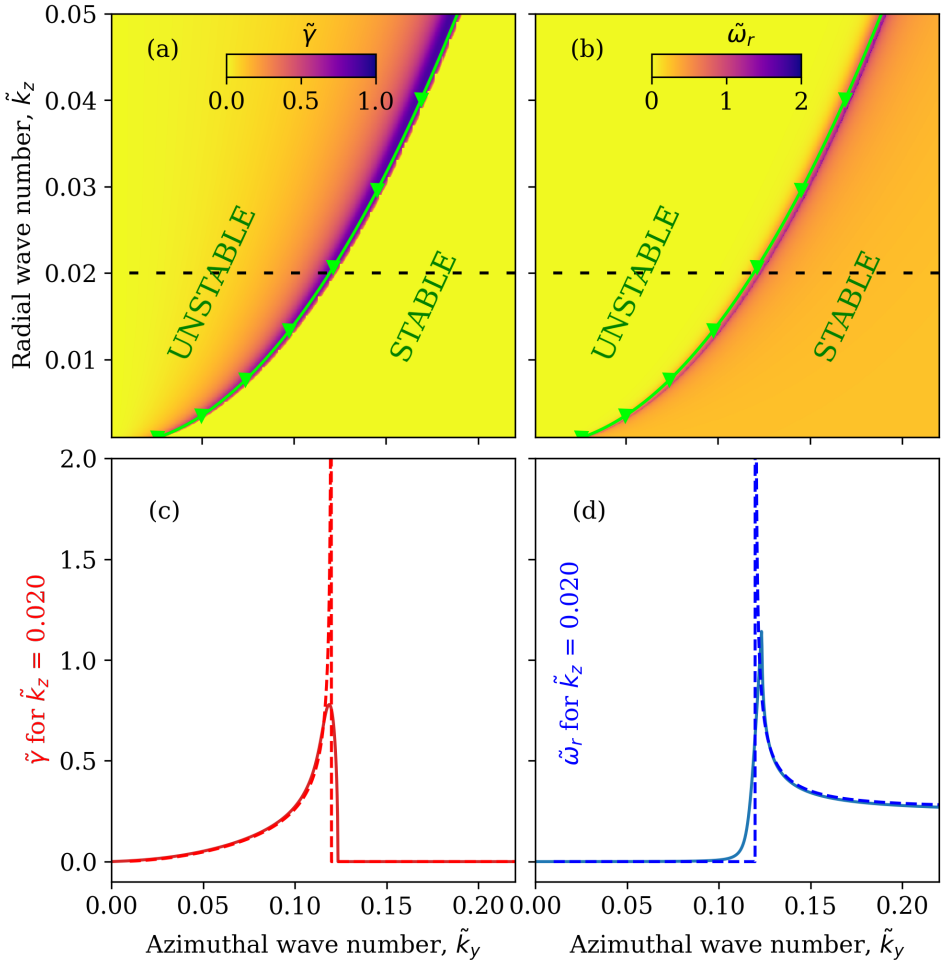


Figure 2.2: (a) Phase space of the growth rate $\tilde{\gamma}(\tilde{k}_y, \tilde{k}_z)$; (b) frequency $\tilde{\omega}_r(\tilde{k}_y, \tilde{k}_z)$ as calculated numerically from the dispersion relation in Eq. (2.12). The green line shows the position of $\max(\tilde{\gamma})$ obtained with the analytical solution of Eq. (2.15). The black dashed lines in (a) and (b) show the cuts reported in (c) and (d) for, respectively, the growth rate and the frequency. In (c) and (d) the full lines are obtained by solving numerically Eq. (2.12), while the dashed lines are obtained from Eq. (2.14). From Ref. [177].

In the upper panel of Figure 2.2, the position of the maximum growth rate as calculated with the simple relation of Eq. (2.15) is shown with a green line with triangular markers, delimiting the stable and unstable regions. One can note that this solution is in very good agreement with the position found with the numerical solution of Eq. (2.12). A comparison of the growth rate and frequency of both the simplified (dashed lines) and the full fluid solution (solid lines) for $\tilde{k}_z = 0.2$ is shown in the panels (c) and (d) of Figure 2.2. Note that in the vicinity of the MTSI resonance peak, the approximation $\tilde{\omega} \ll \tilde{k}_y \tilde{v}_0$ is not valid anymore and the simplified formula fails to capture the magnitude of the peak. Nevertheless, Eq. (2.15) remains a good approximation to identify the position of the MTSI peak in the $k_y - k_z$ space.

As a result of these observations, from Eq. (2.15), we can establish an analytical stability condition for the appearance of the MTSI in our PIC simulations. The unstable region in the $k_y - k_z$ space fulfills the following condition,

$$k_z \geq \frac{m_e E_x}{eB^2} k_y^2. \tag{2.16}$$

The boundary conditions of the PIC simulation define a discrete set of couples (k_y, k_z) in the unstable region, as explained below. In the case of a radial-azimuthal simulation, the azimuthal wavenumber is fixed by the periodic boundary conditions as $k_y = 2\pi m / L_y$ where m is a positive integer. Similarly, the Dirichlet boundary conditions for the electric potential allow the growth of instabilities with $k_z = p\pi / L_z$ where p is a positive integer. Consequently, the stability condition for our PIC setup can be expressed as

$$L_z / p \leq \frac{eB^2}{4\pi m_e E_x} (L_y / m)^2.$$

The $(m,\ p)$ couple corresponding to the mode with the largest growth rate will likely define the mode that develops in the PIC simulation. One should note that the growth rate shown in Figure 2.2 is obtained with a fluid DR which overestimates the growth rate at small radial wavelengths. In the kinetic dispersion relation [129], the growth rate decreases at large radial wavenumbers and, hence, the modes with small wavenumbers are more likely to appear. Under typical HT conditions, this implies that the p with a larger growth rate is $p = 1$, which corresponds to half wavelength in the radial direction. Eventually, under certain conditions, $p = 2$ can appear, which corresponds to one wavelength in the radial direction. Modes with larger p, although they are unstable, have a growth rate that is too small as compared to other instabilities.

In Chapter 5 we will compare the theoretical results above with the numerical solution of Eq. (2.12). Then, we will study the MTSI growth in PIC simulations, with particular attention to the conditions favoring its development.

2.2.4 Ion transit-time instability

Hagelaar *et al.* [54], Barral *et al.* [59] and Fernandez *et al.* [75] introduced an axial electrostatic long-wavelength ($\sim 1\,\text{cm}$) mid-frequency ($\sim 400\,\text{kHz}$) instability that was called ion transit-time instability (ITTI). This instability is a resistive instability, whose azimuthal propagation was studied by Litvak and Fisch [44]. It is interesting

to note that Chable and coworkers [61] studied a similar resistive instability in a low frequency (i. e., below 100 kHz) regime.

As previously, we consider a wave with both axial and azimuthal components (i. e., $\mathbf{k} = (k_x, k_y, 0)$ with $k_y \ll k_x$). By neglecting the ion thermal velocity $v_{\mathrm{th},i} = 0$ and the electron gyration around magnetic field lines, the DR reads

$$0 = 1 - \frac{\omega_{\mathrm{p}i}^2}{\hat{\omega}_i \bar{\omega}_i} - \frac{\omega_{\mathrm{p}e}^2}{\hat{\omega}_e \bar{\omega}_e - k^2 v_{\mathrm{th},e}^2}.$$

The ITTI is a rather low-frequency instability, so we have $\omega \ll \omega_{\mathrm{p}i}$, and the previous expression simplifies to

$$\frac{\omega_{\mathrm{p}i}^2}{\hat{\omega}_i \bar{\omega}_i} = -\frac{\omega_{\mathrm{p}e}^2}{\hat{\omega}_e \bar{\omega}_e - k^2 v_{\mathrm{th},e}^2}.$$

Moreover, since the ITTI is mainly axial and the ion drift in the azimuthal direction is very small (the ions are not magnetized in these conditions), we have $\mathbf{k} \cdot \mathbf{v}_{i,0} \sim k_x v_{i,0,x}$. As a result, these simplifications yield the following DR

$$\omega_{1,2} = k_x v_{i,0,x} - \frac{m_e}{m_i}\left(\mathbf{k}\cdot\mathbf{v}_{e,0} - \nu_e/2\right) \pm \left(\frac{m_e}{m_i}\left(2\left(\mathbf{k}\cdot\mathbf{v}_{e,0}\right)k_x v_{i,0,x} - \left(\mathbf{k}\cdot v_{e,0}\right)^2 + k^2 v_{\mathrm{th},e}^2\right) - \left(\frac{m_e}{m_i}\frac{\nu_e}{2}\right)^2 + \nu_e \frac{m_e}{m_i}(\mathbf{k}\cdot\mathbf{v}_{e,0} - k_x v_{i,0,x})\right)^{1/2}. \tag{2.17}$$

Fernandez *et al.* [75] used a model similar to the one proposed here for the ions, while they considered a drift/diffusion model for electrons, obtaining eventually a 1D-version of the DR in Eq. (2.17). By neglecting electron gyration, we are reducing our model to drift/diffusion as well. Note that this result corresponds to a situation of quasi-neutrality for the plasma. Recently, Koshkarov *et al.* [132] demonstrated that the effect of the finite Larmor radius and the electron inertia must be taken into account to have an instability growth rate vanishing at infinity. The effect of instability-driven turbulence in 2D is investigated in Koshkarov *et al.* [145].

Limit behavior of the ITTI

We define the two branches in Eq. (2.17) *plus* and *minus* waves (identified by the sign prior to the square root) and we designate them with the subscripts p and m, respectively. We observe that each branch can be stable or unstable (i. e., have a positive or negative imaginary part), depending on the plasma parameters, and an easy simplification of the radicand in the ITTI DR can explain why. We observe that the real part of this radicand is largely dominated by the *thermal* term (i. e., $k^2 v_{\mathrm{th},e}^2 \gg 2\left(\mathbf{k}\cdot\mathbf{v}_{e,0}\right)k_x v_{i,0,x} - \left(\mathbf{k}\cdot v_{e,0}\right)^2$) and, considering some reasonable values for the wavenumber, we also have that $m_e/m_i k^2 v_{\mathrm{th},e}^2 \gg \nu_e \frac{m_e}{m_i}(\mathbf{k}\cdot\mathbf{v}_{e,0} - k_x v_{i,0,x})$. Then, after some algebraic manipulation, real and imaginary parts of the simplified DR can be rewritten

$$\begin{aligned} \omega_{p,m} &= k_x(v_{i,0,x} \pm c_s), \\ \gamma_{p,m} &= \frac{\nu_e}{2}\frac{m_e}{m_i}\frac{kc_s \pm (k_y v_{e,0,y} - k_x v_{i,0,x})}{kc_s}, \end{aligned} \tag{2.18}$$

where $c_s = \sqrt{m_e/m_i} v_{\text{th},e}$. In these equations, we observe that the real part does not depend on the azimuthal direction, while the imaginary part does: the growth rate in Eq. (2.18) is proportional to the azimuthal electron drift (term $\nu_e \frac{m_e}{m_i} k_y v_{e,0,y}$). One may notice in Eq. (2.18), that the growth rate does not vanish for large k. As mentioned earlier, Koshkarov *et al.* [132] demonstrated that considering a finite Larmor radius and electron inertia results in a stabilization of the large wavenumbers. Eq. (2.18) can also be used to derive a stability condition for the *plus* and *minus* waves: *plus* wave is unstable if

$$v_{i,0,x} < c_s + v_{e,0,y} k_y / k_x,$$

and the *minus* wave is unstable if

$$v_{i,0,x} > -c_s + v_{e,0,y} k_y / k_x.$$

The ITTI is usually present downstream of the ion sonic point [170], where $v_{i,0,x} > c_s$, so if we consider a purely axial propagation ($k_y = 0$), the stability conditions presented above only allow the growth of the *minus* wave, as it was observed by Fernandez *et al.* [75]. The growth of the *plus* wave is only allowed downstream (i. e., where $v_{i,0,x} > c_s$), if we consider a non-null azimuthal component of the wavenumber. This underlines the importance of considering both directions: the driver of the ITTI instability is a combination of the electron azimuthal motion with the ion axial motion.

2.2.5 Resistive modes

The ITTI is a resistive-type instability, so we can compare it to similar instabilities, by dropping some of the approximations done in the previous sections. In particular, we study the differences between its DR and the one of some published works dealing with resistive modes [122, 132, 145]. Considering again the 3D dispersions in Eq. (2.6), we can write the DR in the axial-azimuthal plane (i. e., in the $xy-$plane) as

$$\frac{\omega_{\text{p}i}^2}{\hat{\omega}_i \bar{\omega}_i} = \frac{\omega_{\text{p}e}^2 \hat{\omega}_e}{\omega_{\text{c}e}^2 \bar{\omega}_e - \hat{\omega}_e k^2 v_{\text{th},e}^2}.$$

The main difference with the expression in Section 2.2.4 is that the electron inertia and the effect of magnetic gyration are now taken into account. Expressing explicitly the equation terms, we obtain

$$\frac{\omega_{\text{p}i}^2}{\left(\omega - \mathbf{k}\cdot\mathbf{v}_{i,0}\right)^2} = \frac{\omega_{\text{p}e}^2 (\omega - \mathbf{k}\cdot\mathbf{v}_{e,0} + \imath\nu_{e,i})}{\omega_{\text{c}e}^2 \left(\omega - \mathbf{k}\cdot\mathbf{v}_{e,0}\right) - \left(\omega - \mathbf{k}\cdot\mathbf{v}_{e,0} + \imath\nu_{e,i}\right) k^2 v_{\text{th},e}^2}. \tag{2.19}$$

This equation is the same studied by Koshkarov *et al.* [145] (i. e., based on a work by Smolyakov *et al.* [122]) in the context of the resistive mode instability connection with turbulence. The only difference with that work consists of the term depending on the diamagnetic drift speed which is not included in the current dissertation.

By defining the Lower Hybrid frequency as the geometric mean of the electron and ion gyrofrequencies, $\omega_{LH} = \sqrt{\omega_{\text{c}e}\omega_{\text{c}i}}$, the expression in the previous equation can be rewritten as

$$\frac{1}{\left(\omega - \mathbf{k}\cdot\mathbf{v}_{i,0}\right)^2} = \frac{\omega - \mathbf{k}\cdot\mathbf{v}_{e,0} + \imath\nu_e}{\omega_{LH}^2 \left(\omega - \mathbf{k}\cdot\mathbf{v}_{e,0} - \left(\omega - \mathbf{k}\cdot\mathbf{v}_{e,0} + \imath\nu_e\right) k^2 \rho_e^2\right)}, \tag{2.20}$$

with $\rho_e = v_{\mathrm{th},e}/\omega_{ce}$ the electron Larmor radius. The dispersion in Eq. (2.20) is exactly the 2D version of the one recently discussed by Koshkarov *et al.* [132]. In that work, the authors show that considering electron inertial and finite Larmor radius is fundamental to stabilize this mode for large values of k. The advantage of the development of this chapter is that it allows deriving directly an expression of the 2D resistive instability in the plane perpendicular to the magnetic field from a more general expression.

2.2.6 Other electrostatic instabilities

The 3D dispersion relation in Eq. (2.6) can be used to derive other well-known electrostatic instabilities, that we discuss hereafter. However, we recall that the dispersion above has been calculated in the electrostatic limit. Thus, some of the most well-known plasmas instabilities or waves (i. e., left and right principal waves, *et cetera*) cannot be derived from this expression.

Simply considering the electron part of the dispersion relation, by neglecting the collisions we obtain

$$\omega_e^2 = \omega_{\mathrm{p}e}^2 + k^2 v_{\mathrm{th},e}^2,$$

that is the standard DR of the electron plasma wave [22]. By neglecting the thermal velocity of both species and the electron collision frequency (i. e., which makes the DR non-resistive) we can retrieve from Eq. (2.19) the classical expression of the Lower Hybrid (LH) mode instability for a quasi-neutral plasma, which is given by

$$(\omega - \mathbf{k}\cdot\mathbf{v}_{i,0})^2 = \omega_{LH}^2.$$

This mode appears as a result of the competition between the magnetized electrons' inertia and the one of unmagnetized ions. So, it is interesting to notice that the resistive mode presented above is an evolution of the lower hybrid mode in the case of a collisional plasma where the electron temperature is not negligible. Now, by keeping the collisionless approximation, but considering a non-negligible electron temperature, we can write a correction the LH DR as

$$(\omega - \mathbf{k}\cdot\mathbf{v}_{i,0})^2 = \omega_{LH}^2 \left(1 + k^2\rho_e^2\right).$$

By including Poisson's equation, we easily obtain from Eq. (2.19)

$$\frac{1}{\hat{\omega}_i\bar{\omega}_i} = \frac{1}{\omega_{LH}^2\left(1 - k^2\rho_e^2\right)} + \frac{1}{\omega_{\mathrm{p}i}^2},$$

that is the expression correction proposed by Chen [22] (cf. Eq. (4.71) in Chen's book).

Furthermore, also the DR of the Upper Hybrid (UH) mode is contained in this expression. Considering, as usual, a collisionless cold plasma, in a frequency range in which $\omega \gg \omega_{\mathrm{p}i}$, we have that the DR simplifies to

$$(\omega - \mathbf{k}\cdot\mathbf{v}_{e,0})^2 = \omega_{ce}^2 + \omega_{\mathrm{p}e}^2.$$

This equation si the UH mode as reported by Chen [22]. The approach is of particular interest because it allows us to understand which approximations need to be considered and to directly observe their effects on the DR terms. Again, with no effort, we can include in the DR the effect of the electron temperature, obtaining

$$(\omega - \mathbf{k}\cdot\mathbf{v}_{e,0})^2 = \omega_{ce}^2 + \omega_{pe}^2 + k^2 v_{\mathrm{th},e}^2.$$

In fully magnetized plasmas, in the same frequency range treated here, one finds an electrostatic instability named Simon–Hoh Instability (SHI), which was introduced by Sakawa *et al.* [28]. More recently, Hara *et al.* [190] studied a version of this instability in the context of partially magnetized plasmas, the Modified Simon–Hoh Instability (MSHI). The dispersion relation of the MSHI cannot really be found in the limits discussed here. The calculation of the DR of this instability requires the consideration of a non-zero plasma density gradient, that has been neglected in our development (cf. Refs. [88, 122] for more details). To retrieve the result by Hara ad coworkers, one should include in the continuity and momentum equations the term $\nabla n/n_0$. Deriving a 3D DR within this framework is beyond the scope of the current work.

2.3 PLASMA INSTABILITY SPECTRAL ANALYSIS

The theory developed in this chapter clearly shows that a large number of instabilities may develop in $\mathbf{E}\times\mathbf{B}$ plasmas, even in a homogeneous background. However, the study of these instabilities and the analysis of their development might not be straightforward. In the following sections we analyze the main techniques that were used to process the $\omega - k$ spectra starting from PIC simulations data. In particular, we present the standard Discrete Fourier Transforms (DFTs), discussing its advantages and limits. The axial gradients in the plasma profile do not allow the use of the DFT along the axial direction. For this reason, we worked with a different technique, the Two-Points Power Spectral Density (PSD2P), presented subsequently. Finally, we introduce the Dynamic Mode Decomposition (DMD), which is a powerful tool to decompose the plasma oscillations in different frequency ranges.

2.3.1 Discrete Fourier Transform

The DFT is based on the decomposition of a signal into a sum of sinusoidal functions. The DFT of a periodic signal s of N samples is defined as

$$S_k = \sum_{n=0}^{N-1} s_n e^{-i\frac{2\pi}{N}kn},$$

for $k = -N/2, \ldots, N/2-1$. The sequence S_k is the DFT of the sequence s_n. Each of them is a sequence of complex numbers. The treatment described above can be extended to multiple dimensions. The FFT is a well-known and widely used technique in signal processing [25]. Since the '60s [8], the usage of FFT has been extended to a large number of different applications. The FFT is a particular algorithm that allows us to compute the DFT of a signal much more rapidly that other methods.

The DFT allows calculating the spectral components only at some given frequencies, which are defined as

$$\nu_k = \frac{k}{N\Delta x},$$

with Δx the sampling interval (the time or space between two consecutive samples). From this equation, we can calculate the frequency resolution as

$$\Delta\nu = \frac{1}{N\Delta x},$$

and the maximum frequency that can be resolved as

$$\nu_{\max} = \frac{N}{2}\Delta\nu.$$

From these expressions we can derive some important concepts about the DFT: (i) to ensure accurate signal capture, it is crucial to acquire input data with a sufficiently long sampling duration; (ii) the sampling interval must be small enough to resolve the signal; (iii) the signal must be periodic. These conditions are not always satisfied in the simulations. In particular, the instabilities, that are often periodic in the azimuthal direction, are not necessarily periodic in radial and axial ones. However, in the radial direction, the walls fix the plasma profiles at the boundaries, making the use of FFT still acceptable. Conversely, along the axial direction, the plasma profiles are not periodic at all. This is a problem for the DFT and in the following sections, we will discuss how to overcome it.

2.3.2 Two-points power spectral density

As discussed above, the DFT analysis does not allow us to distinguish how the local conditions impact the modes propagating in the axial direction. In order to overcome this issue, it is possible to use a Power Spectral Density (PSD) reconstruction technique named PSD2P. This technique is based on the works by Beall *et al.* [21] and by Dudok de Wit *et al.* [31] and allows us to calculate 2D wavenumber-frequency dispersion maps by studying the correlation of the signal (the electron density in our case) between two different points of the simulation. In more recent years, other methods have been developed to better resolve the 2D modes, among them MUSIC (MUltiple SIgnal Classification) [173] has been successfully used to obtain the time-space spectrum [181]. However, in this section, we chose to discuss and focus only on the PSD2P, in particular, because it allows deriving some information on the amplitude of the mode. By using this method, the reconstruction of the PSD is obtained in a very localized position of the simulation, as compared to standard FFTs. The impact of the local plasma parameters in axial modes can then be revealed even during a BM oscillation where strong axial gradients are present. In the next section, we describe concisely the technique developed by Beall *et al.* [21]. The reader can refer to this reference for more details.

PSD2P Technique description

To compute the spectrum along the axial direction, let us consider two probes at a fixed azimuthal position and at axial positions $x = x_1$ and $x = x_2$, and let χ_p be the

distance between them. Then take M pairs (x_1, x_2) along the azimuthal direction, one at every grid point. The PSD2P is applied on a time interval T, corresponding to N time steps, with $\Delta t = T/N$. The temporal signal is recorded and is noted $B^{(j)}(x_i, t)$, with $i = 1, 2$, and the superscript refers to the j^{th} pair. This signal is multiplied by the Hamming windowing function (e. g.,a raised cosine function), and its spectral components are calculated thanks to a DFT, as

$$B^{(j)}(x_i, \omega) = \frac{1}{N} \sum_{l=1}^{N} B_w^{(j)}(x_i, l\Delta t) \exp(-\imath\omega l \Delta t).$$

Here, the subscript w stands for *windowed* and the unit imaginary number $\imath = \sqrt{-1}$. The frequencies used to decompose the signal are computed as a function of the time step, as follows,

$$\omega = \left[-\frac{N}{2}, ..., -1,\ 0,\ 1, ..., \frac{N}{2} - 1 \right] \cdot \frac{2\pi}{T}.$$

For each pair of points and each frequency, we write the sample cross-spectrum as

$$H^{(j)}(\omega, \chi_p) = B^{(j)*}(x_1, \omega) B^{(j)}(x_2, \omega) = C^{(j)}(\omega) + \imath Q^{(j)}(\omega), \tag{2.21}$$

where the star indicates the complex conjugate. We construct a matrix of local wavenumbers, $k_p^{(j)}(\omega) = \Theta^{(j)}/\chi_p$, where the angle is given by

$$\Theta^{(j)} = \arctan[Q^{(j)}(\omega)/C^{(j)}(\omega)].$$

Similarly to Eq. (2.21), we can calculate the signal self-correlation for each point of each pair, as

$$S_i^{(j)}(\omega) = H^{(j)}(\omega, \chi_p = 0) = B^{(j)*}(x_i, \omega) B^{(j)}(x_i, \omega),$$

for $i = 1, 2$. Finally, the local power spectrum can be obtained by performing an ensemble average on the M pairs of points weighted by the self-correlation,

$$\hat{S}_l(k_x, \omega) = \frac{1}{M} \sum_{j=1}^{M} I_{[0,\Delta k)} \left(k_x - k_p^{(j)}(\omega) \right) \cdot \frac{1}{2} \left[S_1^{(j)}(\omega) + S_2^{(j)}(\omega) \right],$$

where $I_{[0,\Delta k)}(k_x)$ is an indicator function in the wavenumber space. In the present work, the wavenumber is discretized as a function of the time step and the distance between the two points, as follows,

$$k_x = \left[-\frac{N}{4}, ..., -1,\ 0,\ 1, ..., \frac{N}{4} - 1 \right] \cdot \frac{2\pi}{\chi_p}. \tag{2.22}$$

Other wavenumber discretizations are also allowed by this technique but are not discussed in this work. As it can be inferred from Eq. (2.22), with this method we can regularly detect the instability in a fixed range $[k_{\min}, k_{\max}]$, where $k_{\max}$ and $k_{\min}$ are the boundaries of the reconstruction axis. Whenever an instability has a wavenumber $\tilde{k}$ out of this range, the instability will appear on the map at a wavenumber $\tilde{k}^* \in [k_{\min}, k_{\max}]$, such that $\tilde{k}^* = \tilde{k} - n \cdot (k_{\max} - k_{\min})$ if $\tilde{k} > 0$ and

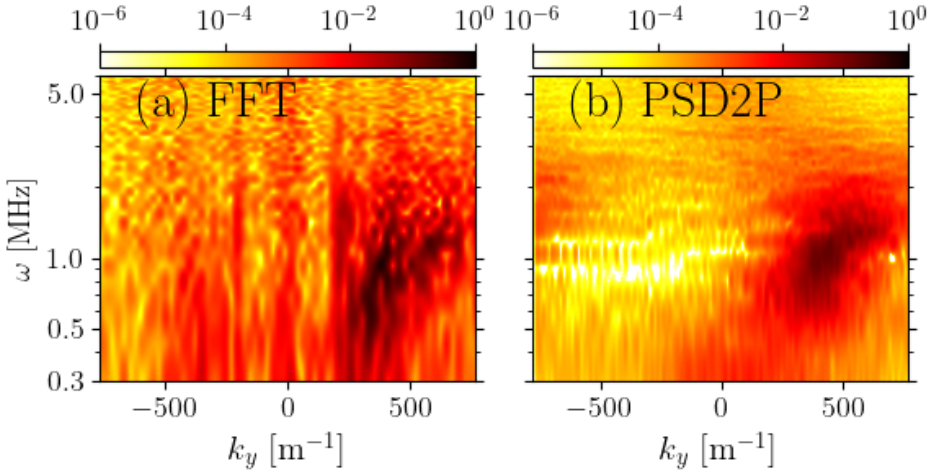


Figure 2.3: Spectrum in the azimuthal direction calculated from the PIC electron density signal extracted from the plume of an axial-azimuthal simulation: The spectrum is obtained using a 2D FFT technique in (a) and with the PSD2P technique in (b). The PIC signal analyzed is the electron density fluctuations at a fixed axial position for a time interval of 8 µs. The low resolution of the FFT is related to the fact that we used a standard 2D FFT.

$\tilde{k}^* = \tilde{k} + n \cdot (k_{\max} - k_{\min})$ if $\tilde{k} < 0$, with $n \in \mathbb{N}^+$. This technique can also be used to compute the spectrum in the azimuthal direction, with pairs (y_1, y_2) at fixed axial position.

Electron density fluctuations have been used rather than the commonly used electric field fluctuations. This is because the magnitude of a scalar quantity is preferable when one wants to study the DRs along two different directions. In particular, we noticed that using the azimuthal electric field gave noisier spectral maps when the electric field instability direction is not aligned with the PSD2P direction. Dudok de Wit *et al.* [31] developed an interesting variant of the method described above, using wavelet transforms and time averaging on a single pair of experimental points. This method is computationally more expensive, but it is more appropriate whenever one wants to calculate the spectrum using a small number of pairs (x_1, x_2), or even a single one.

To validate the results obtained by the PSD2P method, we have compared the spectrum in the azimuthal direction as computed by a standard FFT and by a PSD2P reconstruction. In Figure 2.3 we show an example of the spectrum calculated from the PIC electron density signal extracted from the plume of an axial-azimuthal simulation. A standard Fast Fourier Transform (FFT) map is shown in Figure 2.3 (a) while a PSD2P map is shown in Figure 2.3 (b). Both techniques can detect the modes with maximum amplitude, which corresponds to $\omega \approx 1\,\text{MHz}$ and $k_y \approx 500\ \text{m}^{-1}$. However, we can see that the PSD2P can capture the spectrum with higher resolution in both the wavenumber and the frequency.

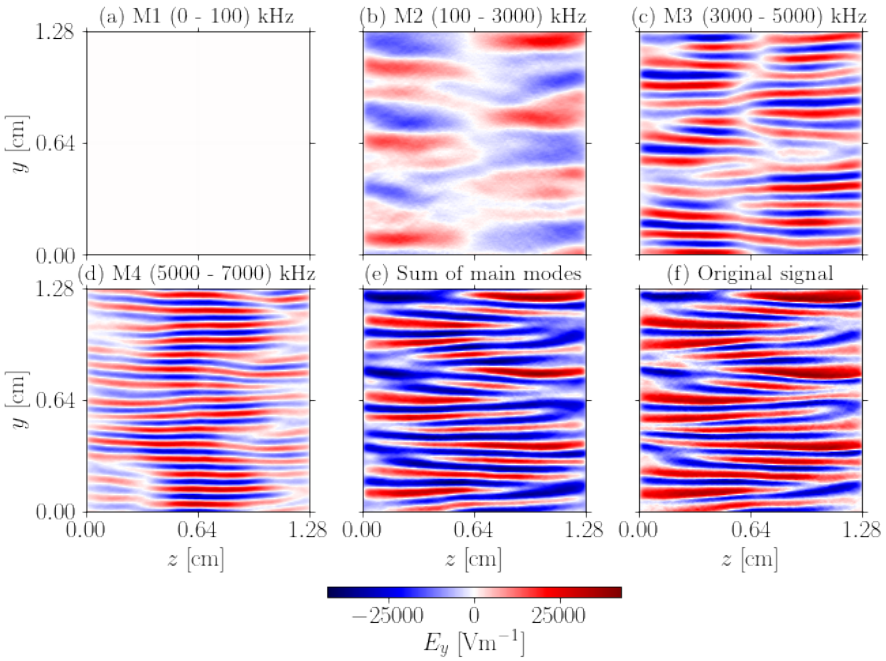


Figure 2.4: Dynamic Mode Decomposition applied to the azimuthal electric field in the radial-azimuthal benchmark case. The field is divided in different frequency ranges. The range is indicated in the title of each subfigure. We notice that the signal in (a) is almost zero: this is coherent with the fact that the azimuthal electric field has a null average.

2.3.3 Dynamic Mode Decomposition

The techniques presented above do not allow an active study of the signal temporal evolution. For this reason, to study the spatiotemporal evolution of the plasma dynamics we used a different technique, the DMD. The DMD is a data-driven technique developed by Schmid [80]. It is based on a *matrix-free* formulation, relying only on the input data, thus applicable also to the experimental flow data. As a result, this technique allows us to separate the signal coming from different modes. The interest of this technique in our case is that it allows disjoining the different instabilities, allowing a subsequent analysis of each one's effect separately.

In Figure 2.4 we observe the DMD applied to the radial-azimuthal benchmark case that we discuss in the next chapter. The decomposition is calculated using an algorithm based on the library Antares [86], developed by CERFACS. In the figure, the azimuthal electric field is divided with the DMD and each subfigure corresponds to a different frequency range. We see that this technique successfully allows us to separate the different instabilities and that recomposing the signal from the different modes allows us to recover the original signal, cf. (e) and (f).

However, the results from the DMD should be considered more qualitative than quantitative, since they not always capture correctly traveling waves. To identify precisely the unstable modes, we need to use the Fourier techniques described above

in this chapter. Nevertheless, the DMD is a very useful tool to study the temporal evolution of the signal and to visually identify the different instabilities.

2.4 CHAPTER SUMMARY

In this chapter, we have derived an expression for the 3D dispersion relation (DR) of electrostatic instabilities in $\mathbf{E} \times \mathbf{B}$ discharges, starting from an isothermal fluid model (continuity and momentum equation for electrons and ions) that considers Poisson equation. We have shown that it is possible to extract from it some simplified DRs that correspond to the most common instabilities observed in $\mathbf{E} \times \mathbf{B}$ discharges, in particular the Ion Acoustic Wave (IAW), Modified Two-Stream Instability (MTSI) the Ion Transit-Time Instability (ITTI) developing in the axial-azimuthal (xy) and radial-azimuthal (yz) planes of Hall thrusters. Moreover, we discussed the possibility to derive the DR of other electrostatic instabilities starting from the 3D DR in Eq. (2.6). We also highlighted the limits of this expression: its electrostatic nature and the fact that we consider a homogeneous plasma (no density gradient) do not allow to retrieve some well-known instability expressions, such as resistive drift, or MSHI. Other kinetic effects, such as the wave particle interaction, cannot be captured by this full fluid formulation.

In this Ph.D. work, the theoretical study of plasma instabilities is performed in the context of the numerical studies of this thesis. Thus, in the second part of the chapter we discussed some numerical techniques to detect and analyze the plasma fluctuations in the PIC simulations. In particular, we discussed briefly the working principles and limits of the DFT. Subsequently, we discussed in detail the PSD2P reconstruction technique, a FFT based technique that allows us to reconstruct the spectrum in any direction, using a limited amount of point pairs. We have shown that this technique is able to capture the spectrum with higher resolution in both the wavenumber and the frequency. Finally, we discussed the DMD technique, a data-driven technique that allows us to separate the signal coming from different modes. We illustrated how this technique successfully allows us to to separate the different instabilities and that recomposing the signal from the different modes allows us to recover the original signal.

3 NUMERICAL METHODS

This chapter explains the numerical methods utilized in this thesis to model Hall thrusters. It commences with an overview of the Particle-in-Cell (PIC) simulation methodology. Subsequently, it presents a description of the LPPic code, highlighting its salient features. Further, it expounds on several numerical aspects of the code, paying particular attention to the impact of scaling the vacuum permittivity. Finally, the last section of the chapter examines the coupling between the electric circuit and the PIC simulations of HTs, which is a critical aspect of the modeling process.

Chapter contents

3.1 PIC challenges . . . 44
3.2 *LPPic*: a 2.5D PIC code for Hall thrusters . . . 44
3.2.1 Numerical implementation of LPPic . . . 44
3.2.2 The radial-azimuthal simulations . . . 49
3.2.3 The axial-azimuthal simulations . . . 51
3.2.4 Development and optimization of *LPPic* . . . 54
3.3 Scaled permittivity effect . . . 55
3.3.1 Effect of the permittivity scaling on the computational cost 56
3.3.2 Effect of the permittivity scaling on plasma parameters . . 57
3.3.3 Effect of the permittivity scaling on the plasma instabilities 63
3.3.4 Effect of the permittivity scaling on the mobility . . . 66
3.3.5 Other effects on instabilities . . . 67
3.4 The circuit implementation . . . 69
3.4.1 Circuit equations and coupling with the PIC code . . . 69
3.4.2 Transfer Function . . . 70
3.4.3 Analysis of the circuit effect on PIC simulations of different domain sizes . . . 73
3.4.4 Effect of the cathode temperature on the circuit response . 77
3.4.5 Current in the circuit components . . . 77
3.5 Chapter summary . . . 78

The results in this chapter have been partially published in Ref. [201].

3.1 PIC CHALLENGES

Probing plasma devices, such as HTs, in a non-invasive manner presents an exceptionally challenging task. This difficulty has resulted in a shortage of experimental data, which, in turn, makes modeling plasma behavior an essential yet arduous task. Hence, the development and improvement of numerical tools to simulate plasma behavior is a crucial area of research in this field. It is imperative to treat the numerical models with utmost care. In this chapter, we provide an explanation of the model we have selected, including the rationale behind our choice, and discuss the numerical developments we have undertaken.

In Section 3.2 we introduced the plasma PIC simulations. These simulations are the main tool used in this work. In particular, we introduce the PIC code used in this thesis, *LPPic*, describing some of its features. Later, in Section 3.3, we discuss some numerical aspects of the code, with a particular attention to the effect of scaling of the vacuum permittivity. The final part of the chapter, corresponding to Section 3.4, is dedicated to the study of the coupling of the electric circuit with PIC simulation of HTs.

3.2 *LPPIC*: A 2.5D PIC CODE FOR HALL THRUSTERS

As aforementioned, the fluid modeling deals with the average (or integrated) behavior of the plasma, thus it treats the macroscopic properties as density, fluid velocity, temperature, *et cetera*, which is limited under non-equilibrium conditions. For this reason, a kinetic model is used in this thesis to study the plasma. The PIC code used at LPP, called *LPPic*, is a particle in cell code developed for approximately 8 years. This code was initiated by Vivien Croes [112] to simulate a radial-azimuthal simulation plane. The code was later developed by Antoine Tavant [152], who studied mainly the plasma-wall interactions. At the same time, Romain Lucken [146] worked on *LPPic* to study the PEGASES thruster [60] configuration. In more recent years, Thomas Charoy [155] adapted the code to simulate the axial-azimuthal plane of a Hall thruster. *LPPic* is a 2.5D code. This means that the Poisson equation is solved in a 2D simulation plane, while it is not solved in the out-of-plane direction; and that, at the same time, the particles have three space and velocity components. Thus, even if the electric field is not calculated self-consistently in the out-of-plane direction, the particle motion is followed also along this direction.

3.2.1 Numerical implementation of LPPic

Besides the general description of the working principles of a PIC code given in Chapter 1, in this section, we discuss in more detail the theory of a PIC simulation, with a particular interest in the characteristics of *LPPic*. In Figure 3.1 we show a classical PIC/MCC cycle as it is implemented in *LPPic*.

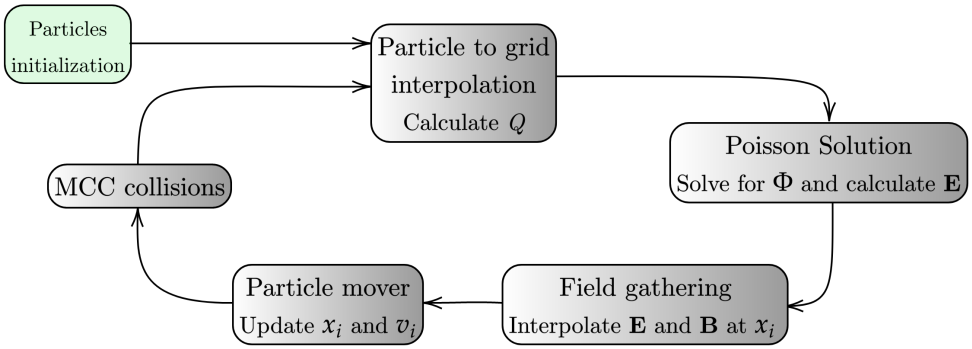


Figure 3.1: The PIC/MCC simulation cycle.

The PIC modeling is based on the assumption that the behavior of the plasma can be described by following the motion of a reduced number of superparticles, each one accounting for a large number of individual particles, and that their Coulomb interaction can be modeled by the electric and magnetic fields calculated at some fixed spatial points (the grid points). The statistical weight of each superparticle is indicated as q_f and should be seen as the number of real particles represented in the simulation by a single superparticle. When the spatial dimension of a simulation is not 3, as *LPPic* that is spatially 2D, more care needs to be dedicated to the parameter q_f. In a 3D simulation, a particle can be represented as a point in space, thus it is 0D. When the simulation dimension is lowered to two, two spatial components of each particle are well-defined, but the third is not. Similarly, in a 1D simulation, a particle has two undefined spatial components. This leads to an interesting interpretation of the weight factor unity of measure, which can be written as

$$\left[q_f\right] = \text{length}^{3-\text{N}}, \tag{3.1}$$

with N the simulation dimension. By considering a 2D simulation as a plane in a 3D space, the particles in the 2D simulation are a set of parallel lines, perpendicular to the 2D simulation domain. In the same way, in a 1D simulation, the particles are a set of 2D planes, perpendicular to the 1D simulation domain.

The mesh size Δx and the time step Δt are chosen, according to Birdsall and Langdon [23], to satisfy the following conditions,

$$\Delta t \leq \frac{0.2}{\omega_{pe}},$$
$$\Delta x \leq \frac{\lambda_D}{2}.$$

We recall that electron plasma frequency and Debye length are defined as

$$\omega_{pe} = \sqrt{\frac{n_e e^2}{\epsilon_0 m_e}},$$
$$\lambda_D = \sqrt{\frac{\epsilon_0 k_B T_e}{n_e e^2}}.$$

The first condition ensures that the plasma frequency is resolved, while the second ensures that the Debye length is resolved. Moreover, these conditions are proposed so that the vast majority of the particles in a single time step does not cross more than one mesh cell boundary. By considering the ratio between these two quantities we find the well-known Courant–Friedrichs–Lewy (CFL) condition, i. e., numerical stability criterion. One can notice that both these quantities depend on the plasma density n_e, on the elementary charge e, and on the vacuum permittivity ϵ_0. The computational cost of PIC simulations strongly limits the development of 3D simulations and of long and spatially wide 2D simulations. This cost depends on the choice of an extremely low time step and mesh size. Thus, if we want to relax the numerical constraint, we have several options:

- work with a reduced plasma density,
- work with an increased vacuum permittivity.

Increasing the elementary charge is not a usual approach.

In recent years, several scaling methods have been proposed to relax the plasma simulation constraints and so to lower the cost of these simulations. We identify four families of techniques: (a) the permittivity scaling [46], (b) the reduction of the heavy species mass or the increase of electron mass [46, 93, 134], (c) reduction of the plasma density [114] and (d) the self-similarity scaling of the system [58, 64]. In our work, we focused on vacuum permittivity scaling, as it was introduced by Szabo [46]. A more detailed discussion about the scaling techniques can be found in Ref. [167] by Yuan *et al.*, where the authors analyzed the consequences of scaling methods in PIC simulations in a miniaturized ion thruster.

Particles motion

From the charge distribution Q, the Poisson solver allows calculating the electric potential Φ in the electrostatic approximation, by solving the Poisson equation

$$\Delta\Phi = -\frac{Q}{\epsilon_0},$$

with ϵ_0 the electric vacuum permittivity. As discussed above, in some occasions we increased the permittivity to relax the numeric constraints of the PIC simulations, by scaling the vacuum permittivity a factor α_0. When it is the case, $\epsilon = \epsilon_0 \cdot \alpha_0$ is used instead of ϵ_0 in the Poisson equation. By deriving the electric potential Φ, one obtains the electric field $\mathbf{E}$ at each grid point. The particles move following the Lorentz equation

$$m\frac{d\mathbf{v}}{dt} = q\mathbf{E} + q\mathbf{v} \times \mathbf{B},$$

where m and q are the particles' mass and charge respectively. Then, the charge distribution Q is calculated by interpolating the charge of each particle on the grid points of the cell where it is located. More details about the interpolation method are given in Ref. [112].

The numerical method to move the particles on the grid depends on the magnetization of the particle. As we discussed above, in HTs, the Larmor radius of ions is

much larger than the device dimensions: thus, the ions are not magnetized, while electrons are. The non-magnetized particles are moved using a leap-frog scheme [23], as

$$\mathbf{v}^{t+1} = \mathbf{v}^t + \frac{q}{m}\mathbf{E}^t \Delta t,$$
$$\mathbf{x}^{t+1} = \mathbf{x}^t + \mathbf{v}^t \Delta t,$$

where Δt is the time step and t its index, i. e., $\mathbf{v}^t \doteq \mathbf{v}(t\Delta t)$. The magnetized particles (i. e. the electrons) are moved using a Boris scheme [10], which consists of a first half-step of the leap-frog scheme, followed by a rotation of the velocity vector around the magnetic field and by a subsequent second half-step of the leap-frog scheme. One should notice that this introduces a shift of $\Delta t/2$ between the position and the velocity of the particles. The shift might insert some error in the computation of the mean velocity. However, this method conserves the phase space volume, thus limiting the non-energy conservation error [95].

The Poisson solver

Solving the Poisson equation is a key step in the PIC simulation. The Poisson equation is solved in the simulation 2D-plane, while it is not solved in the out-of-plane direction. In 1D the solution of the Poisson equation is rather simple, thanks to the well-known Thomas algorithm for tridiagonal systems. In 2D the solution is more complex, and a direct solution of the system would require huge computational resources. Thus, 2D simulations usually demand the use of an iterative Poisson solver.

In *LPPic* we use HYPRE [47], which is a library for the solution of sparse linear systems on massively parallel computers using a multigrid approach. This library is used via PETSC [183]. Several tests have been conducted over the years and the HYPRE library is the most efficient and stable in our case. This stencil-based method is implemented in C, so needs a specific coupling with *LPPic*, which is coded in Fortran. Even if the code has been subjected to several optimizations, the Poisson solver remains one of the most time-consuming parts of the simulation.

The collision model

The collisions in plasmas are extremely important since they are the main source of ionization. A collision is a multi-body problem in which two (or more) particles interact. The collisions can be explained by using quantum mechanics and requires an extremely careful modeling. To do that, we introduce the concept of *cross-section*. The collisional cross-section is a means to quantify the probability of a scattering event and can be intended as an *effective area*. Considering two hard spheres of radius R and r respectively, the cross-section would be the conventional geometric momentum-transfer cross-section: $\sigma = \pi (R + r)^2$. However, when we pass to charged particles and real gases the calculation of the cross-section becomes a difficult task. The cross-sections used for the simulations in xenon and krypton of this thesis come from the Biagi database in LXCat [119], while iodine cross-sections are gathered by numerous sources [146].

In *LPPic* different electron-neutral and ion-neutral collisions have been implemented, while Coulomb collisions with short-range are neglected. For electrons, we considered elastic, inelastic (ionizing or not) collisions with a stationary neutral background. The mass ratio between neutrals and electrons makes the assumption of frozen neutral realistic. During an elastic collision, the electrons are deflected by the interaction with a neutral. In our model, we considered the energy transfer between electron and neutral, thus, the electron loses a (tiny) amount of its kinetic energy, changing direction. In an inelastic collision, an electron loses some of its energy to excite or ionize a neutral. If a neutral is excited, it relaxes by releasing its energy by photon irradiation or it remains in a metastable state. However, the fast relaxation processes in gases justify the assumption that the majority of the neutral atoms are in the ground state. Hence, in *LPPic* the collisions with an atom that is not in the ground state are neglected. After an excitation, an electron is scattered in a different direction with its energy reduced by the amount of energy of the excitation reaction. If the inelastic collision is ionizing the atom, the kinetic energy of the atom, reduced by the energy required to ionize, is divided equally to the two electrons, i. e., the original one and the one extracted from the atom. The produced atom is assumed at the same temperature as the neutral background gas. The ion-neutral collisions are modeled considering two types of scattering events: the isotropic scattering and the backscattering (charge-exchange). The neutrals do not remain fixed, since they have almost the same mass as the ions. The collisions are performed by creating a ghost neutral particle with a velocity extracted from a Maxwellian. The charge-exchange collisions are *momentum transfer* collisions, so, they require a particular modeling, as suggested by Phelps [29]. For a detailed discussion of these cross-sections and the way they are calculated, the reader should refer to 1.2.3 and 1.2.4 in Romain Lucken's Ph.D. thesis [146].

The collisions in *LPPic* are modeled using a MCC algorithm, following the development of Vahedi *et al.* [30]. This algorithm uses a *null collision* method, which reduces the number of collisions to be calculated. The method can be explained with the help of Figure 3.2. By adding an artificial collisional process, one can define the collision frequency $\tilde{\nu}$ as

$$\tilde{\nu} = n_g \max_{\mathcal{E}}(\sigma_{\mathrm{TOT}}(\mathcal{E})v).$$

In the previous expression, the neutral gas density n_g is assumed to be constant. The total cross-section $\sigma_{\mathrm{TOT}}(\mathcal{E})$ is obtained by summing over all the possible cross-section at the energy $\mathcal{E}$ and v represents the particle speed. The null collision method consists in adding another frequency ν_e to the total collision frequency, such that the sum of all collision frequencies does not depend on the energy, and it is equal to $\tilde{\nu}$. The fraction of particles P_{NC} that undergoes a collision event during a time step of duration Δt can be calculated as

$$P_{NC} = (1 - \exp(\tilde{\nu}\Delta t)) \cdot I_{\mathrm{tot}}.$$

In the previous expression I_{tot} is the total number of particles of a given species. Then, P_{NC} particles are selected randomly and for each of them, a collision is performed by picking a random number X. The j^{th} collision is performed when

$$\nu_j/\tilde{\nu} \leq X < (\nu_j + \nu_{j+1})/\tilde{\nu}.$$

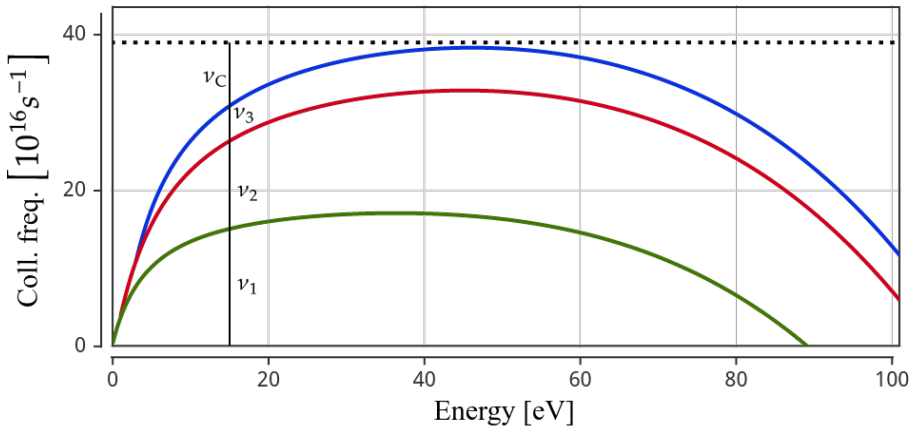


Figure 3.2: The null collision model used in *LPPic*.

If the selected collision is the null collision, there are no consequences or effects.

3.2.2 The radial-azimuthal simulations

The radial-azimuthal simulations are meant to simulate a section of the thruster channel. The simulation domain represents a limited portion of the azimuthal direction circumscribed between the outer and inner walls. The axial direction, along which the ions are accelerated, is not fully simulated. The choice of the axial position of the 2D radial-azimuthal plane is crucial: we selected the thruster exit, where the axial electric field is maximal and the anomalous mobility large. Since the axial particle motion is not self-consistently solved, the axial position of the simulation plane cannot be precisely identified.

The cartesian domain in the radial-azimuthal simulation is the one represented in Figure 3.3, where the horizontal axis represents the azimuthal direction and the vertical axis represents radial direction. The azimuthal direction is referred to as y and the radial as z. The radial boundaries are limited by some walls. Different walls can be used in *LPPic*: metallic walls (grounded) or dielectric walls. The walls may be absorbing, reflective or emissive. During his thesis, Antoine Tavant [152] studied in detail the different conditions related to use a different wall model and to the SEE. In the simulations presented in the current manuscript, only metallic walls absorbing and reflecting particles are used, to ease the study of the development of instabilities.

Some effects related to the device's azimuthal curvature [94, 126] (i. e., differential absorption, magnetic mirror, geometric expansion, centrifugal force, *et cetera*) are present in real devices. However, the simulation domain does not take into account the curvature. Moreover, the instabilities (i. e., ECDI, IAW, MTSI) have wavelength of the order of some millimeters at most, thus, all these phenomena can be studied also in a thin slab of the azimuthal direction. For these reasons we limited the azimuthal length to a few centimeters, employing periodic boundary conditions along this direction for both particles and fields.

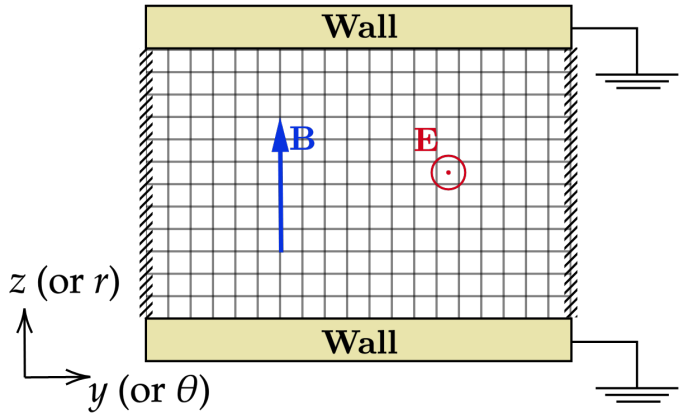


Figure 3.3: Radial-azimuthal simulation domain representation. The magnetic field is homogeneous and directed radially (vertically in the image) and the static electric field is homogeneous and directed out of plane.

A constant magnetic field is applied in the radial direction, perpendicularly to the radial walls. No amplitude gradient depending on the radial position is considered, nor is there any magnetic field component along a non-radial direction. We remember that the code used here is electrostatic, thus any other magnetic field is considered in the code but the static one.

The acceleration of the ions out of the thruster occurs thanks to an axial electric field generated by the anode-cathode voltage drop. Then, modeling the axial electric field is fundamental to reproduce the HT behavior. In our code, hence, we introduced an out-of-plane axial electric field constant in time and space and spatially homogeneous, as one can see in Figure 3.3. So, the field configuration described here generates an electron $\mathbf{E} \times \mathbf{B}$ drift in the azimuthal direction. One may notice that the electron drift velocity in this direction (i. e., $v_{\mathrm{E}\times\mathrm{B}} = E/B$) depends only on the magnetic and electric fields amplitudes, that are fixed by the chosen setup.

At the beginning of this section, we stated that in the *LPPic* 2.5D simulation the particles are moved in the 3D space, while the electric field is only solved in a plane. With an out-of-plane electric field E_x designed as the one described above, at each time step the energy of each particle increases by

$$\mathcal{E}_{e,i} = \left(\frac{qE_x \Delta t}{m_{e,i}} \right)^2 ,$$

where the subscript refers to the particle species. Héron and Adam [94] and Janhunen *et al.* [129] observed that no steady-state regime can be reached in this regime of continuous energy injection. If no collisions are considered, the heating along the x direction is not a problem and all the plasma dynamics along this direction can (and should!) be neglected. Conversely, when we consider collisional simulations, the artificial temperature enhancement due to the third velocity component redistributes in the other direction via collisions and collective motions (i. e., instabilities), diminishing greatly the realism of the simulation. For these reasons, a model of virtual axial direction has been introduced in the simulation. This model was first used by

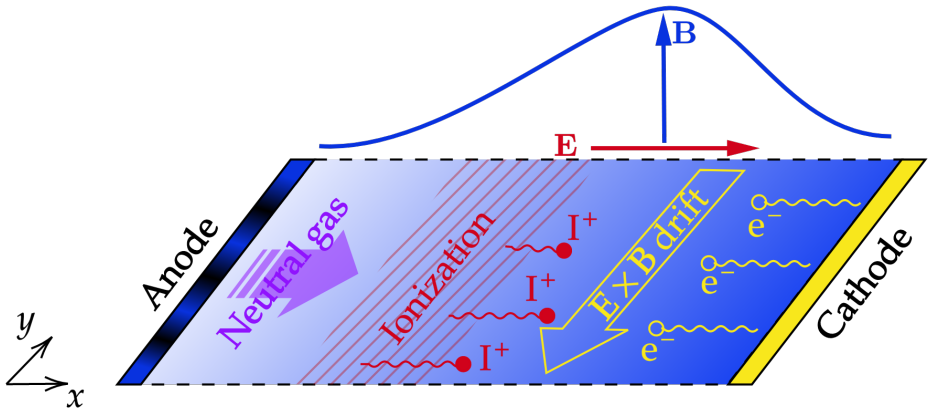


Figure 3.4: The simulation domain for the axial-azimuthal simulations. The simulation domain is a 2D slab of the azimuthal direction. The simulation domain is bounded by the cathode (grounded) and the anode (at high voltage). The cathode is modeled as a quasi-neutral surface. The anode voltage is controlled by an external circuit.

Lafleur *et al.* [105] in one dimension and subsequently adapted to 2D by Croes *et al.* [113]. In this model, we bound the axial out-of-plane direction between 0 and L_x. The particles reaching the boundaries are removed from the simulations. The charge neutrality and particle balance are maintained by reinjecting the axially absorbed particles into the simulation domain at the same (y, z) position. Since the electric field is directed as the positive x axis, the ions are injected at $x = 0$, while the electrons at $x = L_x$. A more detailed discussion about the axial convection model can be found in Antoine Tavant's thesis [152], in particular in Section 2.5 he compared different models of particle re-injection.

3.2.3 The axial-azimuthal simulations

The axial-azimuthal simulations are meant to simulate a plasma azimuthal section, from the bottom of the channel to some centimeters in the plume. The simulation represents a limited portion of the azimuthal circumference (normally some centimeters). In the axial direction, the simulation considers the thruster channel (i. e., $\approx 2.5\,\mathrm{cm}$) and some centimeters of the plume. The axial-azimuthal simulations were first developed by Antoine Tavant and Thomas Charoy to model the PPS1350 by Safran Spacecraft Propulsion [193]. Charoy's thesis contains a detailed description of the code and the simulation setup [155]. In this section, we only summarize the main features of the simulations. The new modules are discussed in the next chapters. Figure 3.4 shows a visual representation of the domain.

The 2D simulation domain (i. e., composed by the usual 2D cartesian grid with no curvature) has a constant in time magnetic field in the radial direction, so perpendicular to the simulation domain. The amplitude of the magnetic field varies axially and it is constant in the azimuthal direction. The anode (i. e., at the left in the figure) is at high voltage, while the cathode is grounded. This potential drop is responsible for

an intense axial electric field $E_x \approx 10 \times 10^3$ V/m. Periodic boundary conditions are applied in the azimuthal direction. The anode voltage is controlled by an external circuit. The circuit implementation is discussed hereafter. In this work, we use for the cathode a quasi-neutral (QN) model: at each time step the quasi-neutrality at the cathode is imposed by injecting the right number of electrons, in order to assure that globally the net charge in the last simulation cell is zero. When the last cell is charged negatively, any electron is injected at the cathode. The cathode model was studied in detail in Section 2.4 in Charoy's thesis [155].

The electrons injected from the cathode are accelerated towards the anode by the axial electric field. However, their path towards the anode is affected by the radial magnetic field. The electrons start to drift in the azimuthal direction, which is periodic in our simulation. The azimuthal drift is of the order of 10^6 m/s and increases the residence time (e. g., the residence time can be in the order of several tens of microseconds) of electrons in the thruster channel, hence, it is responsible for the high ionization efficiency of the HTs.

The ionization in *LPPic* is treated self-consistently. In the first version of the code [140], the electron/ion pairs were injected at a fixed rate. Conversely, in the current version of the code, the charged particles creation is performed within the MCC module described above, by considering electron impact ionization. The electrons are the only ones responsible for ionization, while the ions only make elastic and charge-exchange collisions. The ions, mostly created in the shaded region in Figure 3.4, are accelerated by the axial electric field towards the thruster plume, creating the thrust. The self-consistent ionization couples the plasma discharge with the neutral dynamics, allowing to reproduce the BM.

The neutrals are modeled with 1D fluid equations. The Euler equations are solved with a HLLC solver [36], which is fully described in Section 2.3 of the thesis of Thomas Charoy [155]. A fixed neutral flux rate is imposed at the anode, while open boundary conditions are imposed at the cathode boundary. The 1D Euler system solved in *LPPic* is

$$\begin{cases} \partial_t \rho_g + \partial_x(\rho_g u_g) & = S_1, \\ \partial_t(\rho_g u_g) + \partial_x(\rho_g u_g^2) & = -\partial_x P_g + S_2, \\ \partial_t E_g + \partial_x(E_g u_g) & = -\partial_x(P_g u_g) + S_3. \end{cases}$$

In the previous expression ρ_g is neutral density, u_g is the neutral fluid velocity, S_1 and S_2 the collisional source terms, S_3 the energy source term, P_g the neutral pressure, E_g the neutral energy, defined as

$$E_g = \frac{P_g}{\gamma - 1} + \frac{1}{2}\rho_g u_g^2.$$

The heat capacity γ is set equal to $5/3$, since we normally deal with monoatomic gases. The energy source term is defined as

$$S_3 = \frac{E_g - E^*}{\tau},$$

to make the energy converge to the an imposed term E^*, such that

$$E^* = \frac{\rho_g R T^*}{\gamma - 1} + \frac{1}{2}\rho_g u_g^2.$$

The parameter τ is chosen as low as 10^{-11} s. This imposed energy term makes the system isothermal, so, the energy equation becomes redundant. However, the presence of this term increases the stiffness of the system. In the current work, the neutral gas temperature is set to 640 K.

A constant mass flow of neutral gas is injected at the anode. In addition to that, the anode boundary condition also accounts for neutrals produced from ion recombination at the anode. The set of equations described above deals with a flux $\Gamma_g = \rho_g u_g$, hence, to obtain the real mass flow rate in the device we need to define the device area.

In real HTs devices, the presence of the radial dimension plays an important role in determining the characteristics of the plasma. As we discussed in Chapter 1, a Bohm flux of particles leaves the simulation domain at the grounded thruster walls. Moreover, the dynamics in the plasma plume is characterized by a high divergence angle [168]. However, since *LPPic* is a 2.5D code, the radial dynamics cannot be followed self-consistently. The Poisson equation is not solved along the out-of-plane direction; hence, the radial effects need to be introduced *indirectly* in axial-azimuthal simulations. In Chapter 7 of Tavant [152] Ph.D. thesis a first attempt of including some radial effects was performed. However, as will be discussed in Chapter 6, that model could not give a realistic description of the radial losses. We will therefore introduce a more consistent model of the radial losses in 2D simulations in Chapter 6.

Electron mobility in Hall thrusters

As discussed in Section 1.2.3 the electron anomalous transport plays a fundamental role in HTs. In the same section, we introduced the idea of friction force to model the instability contribution to the anomalous transport. We define here first what will be called classical mobility. By neglecting the acceleration and the inertia term in the electron momentum equation (1.4), we can write a 1D-drift/diffusion equation as

$$n_e u = \frac{q n_e E}{m \nu_e} - \frac{\nabla(n_e k_B T_e)}{m \nu_e}. \tag{3.2}$$

From this equation, one can define the collisional mobility, as

$$\mu = \frac{e}{m \nu_e}$$

and, if $k_B T_e$ does not vary spatially, the diffusion coefficient, as

$$D = \frac{k_B T_e}{m \nu_e}.$$

One should notice that the usual definition of the mobility along the electric field axis, i. e., $\mu = u/E$, is only valid if the diffusion part of Eq. (3.2) is neglected.

However, by writing the collisional frequency as $\nu_e = e/m\mu$ and injecting this in Eq. (3.2), one may define the mobility as

$$\mu_e = \frac{-u}{E - \nabla(n_e k_B T_e)/n_e q}. \tag{3.3}$$

Hence, to calculate the electron mobility from macroscopic plasma quantities, we need to use the diffusion term. This equation will be fundamental to estimate the mobility from PIC simulations and to derive the *anomalous* collisionality, cf. Chapters 5.

During the thesis of Thomas Charoy [155] a different approach was preferred. In order to evaluate the anomalous transport in the axial direction, only the correlation term R_{ei}, as defined in Section 1.2.3, was employed.

3.2.4 Development and optimization of *LPPic*

The *LPPic* code was started in early 2015 and later developed by several Ph.D. students [112, 146, 152, 155]. In 2019, *LPPic* was selected for optimization by the HLST team of Centre Informatique National de l'Enseignement Superieur (CINES). Thus, the LPP team and the CINES team worked together to rewrite the code in an optimized way. The development started in late 2019 and was performed by myself, Antoine Tavant and Thomas Charoy at LPP, while at CINES the work was led by Umesh Seth and Gabriel Hautreux within the HLST team of CINES. The collaboration ended after 1.5 years of work in June 2021. Below, we summarize the final results contained in the report produced at the end of the collaboration. These results have been published by the HLST team in Ref. [197].

Several steps were taken to optimize the code. The work started with optimizing memory access. The code was transformed from array of structures (AoS) (i. e., each particle is an individual Fortran derived type and they are allocated as a vector) to structure of arrays (SoA) (i. e., every element of the derived structure is an individual particle) to reduce memory and cache stalls. Other general optimizations included force reductions, efficient loop directions, efficient array indexing, preprocessor directives, compiler flag optimizations, and more. SIMD (Single Instruction and Multiple Data stream) vectorization pragmas were added to improve vectorization in some bottleneck parts of the code. The *LPPic* code uses the Hypre library for solving Poisson equations. The performance of the code was examined with several linear system solvers available with the Hypre library. The implementation of the Hypre solver in the code was optimized by removing some initialization steps from the main solver loop, which greatly improved the performance of the Poisson solver. The code was moved from an old compilation environment (Intel / Intelmpi), from versions of Hypre and the HDF5 library to a newer version of the overall environment. The code uses Message Passage Interface (MPI) communications to exchange data between processes. Blocking communications of MPI have been replaced by non-blocking communications of MPI to benefit from overlapping communications and computations. Input/output optimizations were made by providing the HDF5 code with independent and collective MPI-IO options. Efficient use of the lustre file system with appropriate stripping options to optimize overall input/output performance was also communicated to users.

Several cases of plasma dynamics were validated with the optimized code, obtaining a good scaling and speedup. Figure 3.5 (a) shows the speedup of the 1D helium benchmark case [96] at various stages of code optimization compared with the original version of the code. The leftmost point represents the baseline speedup value that corresponds to the original code on 2 nodes. The speedup was progressively increased up to 2.5 times compared to the original code for this small physical case. The code is massively parallelized, thus it is important to verify the proper scalability of the code on a large number of nodes. This feature has been tested on Landmark 2B benchmark case [140] with increased azimuthal dimension. As one can see in

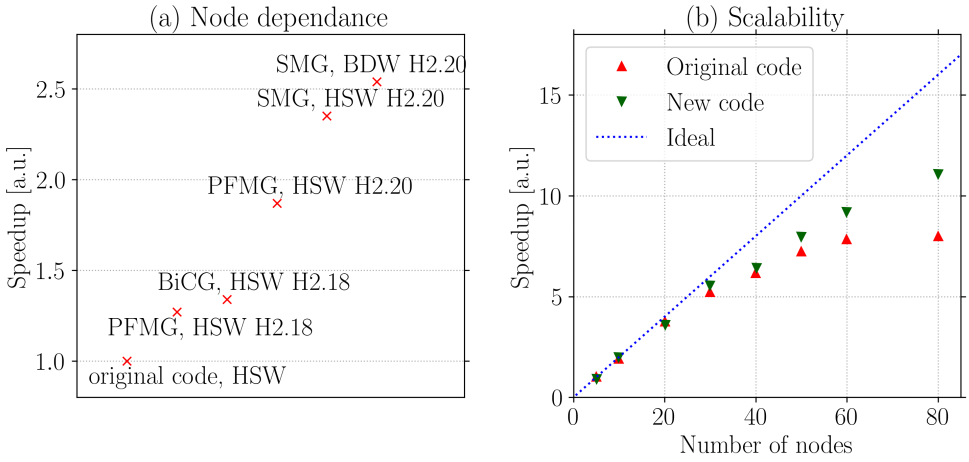


Figure 3.5: (a) Speedup dependency on the chosen node type. (b) Speedup dependency on the number of nodes. Adapted from [197].

Figure 3.5 (b), the code scales well up to 80 nodes. The more nodes we use, the more the performance is improved with respect to the original code. The code is now ready to be used for large-scale simulations.

The overall gain obtained rewriting *LPPic* is significant. The simulation time has been greatly reduced and the scalability of the application has been greatly improved. In addition, in 2022 the code was ported and turned on Joliot-Curie TGCC systems with AMD Rome 2.6 GHz (AVX2) nodes partition, with 128 cores per node, a much more energy efficient system than the cluster Occigen (Intel Xeon Haswell and Broadwell processors at 2.6 GHz with 24 and 28 cores per node, respectively), where the code has been used before.

3.3 SCALED PERMITTIVITY EFFECT

Particle-in-Cell (PIC) simulations require a lot of computational resources: this is a great limit to their development and use. As we discussed in Section 3.2.1, several options for reducing the cost of the simulations are currently being explored by the community. The approach used in the current work consists in increasing the value of the permittivity by a factor α_0, i. e., $\epsilon = \alpha_0 \epsilon_0$. The increment of the permittivity has a direct effect on the Debye length $\lambda_D = \sqrt{\epsilon k_B T_e / n_e e^2}$, which is increased by $\alpha_0^{1/2}$ and on the electron plasma frequency $\omega_{pe} = \sqrt{n_e e^2 / m_e \epsilon}$, which is reduced by a factor $\alpha_0^{1/2}$. Considering the constraints of an explicit PIC simulations as formulated by Birdsall and Langdon [23] (e. g., $\Delta t \leq 0.2/\omega_{pe}$ and $\Delta x \leq 0.5\lambda_D$), we have that both the time step and the cell size can be increased by a factor $\sqrt{\alpha_0}$. So, if the computational time scaled linearly, the use of a scaling factor α_0 to simulate given real spatial dimensions and duration reduces the overall cost of a simulation by a factor $\alpha_0^{3/2}$. In reality, the computational cost of a simulation is not linear with the number of grid points, e. g., the overall number of particles to be used varies as well. Thus, the gain that one can

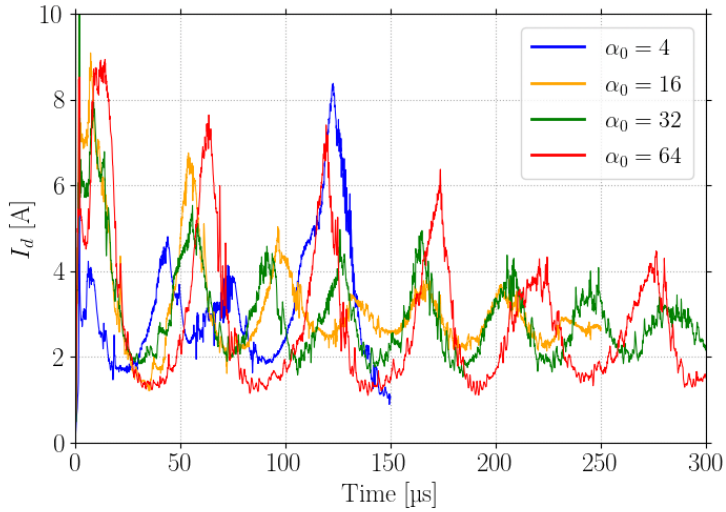


Figure 3.6: Discharge current evolution for different values of the permittivity scaling α_0.

obtain by reducing the number of grid points might be much larger than the one reported above, yet difficult to calculate exactly.

Nonetheless, scaling the permittivity has a cost: the simulations may considerably shift from reality. Charoy *et al.* [170] used this method in HTs PIC axial-azimuthal simulations, highlighting some of its effects on the plasma instabilities and therefore on the friction force. In this work, we study in more detail the effects of the scaling of permittivity on other important plasma parameters. In the following subsections, we analyze four simulations, some already used by Charoy in Ref. [170], with different scaling values $\alpha_0 = 4, 16, 32, 64$. The discharge current evolution in these simulations is plotted in Figure 3.6. The simulation with the smaller value of α_0 has been initialized in a configuration of a quasi-steady-state to ease convergence and shorten the physical time to reach steady-state, so to reduce the CPU time consumption.

3.3.1 Effect of the permittivity scaling on the computational cost

The domain used in simulation results presented in Figure 3.6 is the one described in Charoy *et al.* [170] and consists of the usual cartesian 2D mesh. The anode is at high voltage (i. e., 300 V in this case), while the cathode is grounded. Periodic boundary conditions are applied in the azimuthal direction. Neutral dynamics is simulated with Euler equations in 1D and the ionization is computed self-consistently within the MCC module. To satisfy the CFL condition the time step and grid size depend on the permittivity scaling: the larger the scaling, the larger will be the time and space steps.

Table 3.1: Simulation parameters and estimated total CPUh cost of a 300 µs of physical time (for *LPPic*).

α_0	dx	$y_{max} \times x_{max}$	dt	# of loops	total CPU cost
4	4×10^{-5} m	255×1000	4×10^{-12} s	7.5×10^7	3×10^6 CPUh
16	8×10^{-5} m	127×500	8×10^{-12} s	3.75×10^7	3.5×10^5 CPUh
32	11×10^{-5} m	88×353	11×10^{-12} s	2.65×10^7	1.0×10^5 CPUh
64	16×10^{-5} m	63×250	16×10^{-12} s	1.875×10^7	7.7×10^4 CPUh

In Table 3.1 we report the simulation parameters for the four simulations with different scalings, corresponding to a physical time of 300 µs. The CPUh cost of each simulation is estimated by the results obtained with *LPPic*. Since the code is highly parallelized, the total number of CPU hours is calculated by multiplying the actual duration of the simulation by the number of MPI processes used. In the table, we notice that the cost of the simulation decreases with the increase of the scaling factor, as expected. A more precise estimation of the cost of the simulations is difficult to obtain since for each simulation we used a different number of MPI processes and we know that the code does not scale perfectly. When we increase the number of MPI domains the performance decreases. In the case closer to reality (i. e., $\alpha_0 = 4$), the total cost of the simulation is extremely high: with our current capabilities, this simulation lasts for months and consumes millions of CPU hours. The number of cells in azimuthal and axial directions (i. e., x_{max} and y_{max}) are given for physical lengths of $L_y = 1$ cm and $L_x = 4$ cm, respectively. However, when the scaling is high a reduced azimuthal length does not allow the growth of all instabilities [170]. So, to allow the development of most of the instabilities, in the following, we analyze a simulation with $L_y = 1.5$ cm in the cases of $\alpha_0 = 32$ and $L_y = 2$ cm in the cases of $\alpha_0 = 64$.

3.3.2 Effect of the permittivity scaling on plasma parameters

3.3.2.1 Axial electric field

The PIC algorithm solves the Newton equation of motion for every superparticle: each superparticle is pushed in the grid depending on the electromagnetic forces acting on it. In an axial-azimuthal electrostatic simulation of a HT the potential at the axial boundaries is fixed: the cathode is grounded while the anode is at high potential (i. e., 300 V in our case). The axial electric field is responsible for the acceleration of the ions out of the thruster, in order to produce the thrust. Therefore, accurately representing it in the model is essential for effectively simulating the thruster's behavior. Theoretically, we have

$$\Phi_{anode} = \Phi(x = 0) = \int_0^{L_x} -\nabla\Phi(x)dx = \int_0^{L_x} E_x(x)dx = \langle E_x \rangle L_x, \tag{3.4}$$

with $\langle E_x \rangle$ the spatial average of the electric field value. By assuming Φ_x monotonic, the previous equation suggests that the electric field mean value does not directly depend

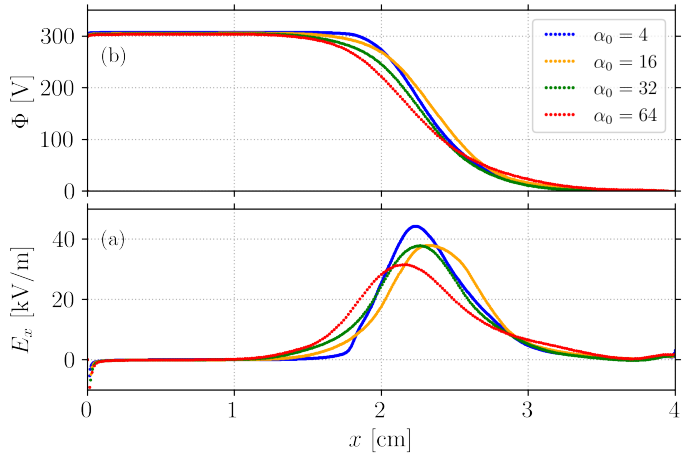


Figure 3.7: (a) electric potential and (b) axial electric field averaged over the entire duration (300 µs) simulation for the four cases.

on the scaling factor: $\langle E_x \rangle = \Phi_{\text{anode}}/L_x$. Conversely, if the monotonic assumption is not verified, the electric field might be affected by the scaling factor.

In Figure 3.7 we observe that the shape of the time-averaged electric field and of the potential: those profiles should not be interpreted as quasi-steady-state profiles since the oscillations remain strong all along the simulations. However, they are useful to have an idea of the shape of the potential and of the axial electric field. In particular, we observe in Figure 3.7 (a) that the average profile of the potential is monotonic in all cases. Nevertheless, we notice that some differences in the shape of the electric field are present: in the following, we study this effect.

The expression in Eq. (3.4) represents a steady-state solution, not taking into account the complex plasma dynamics (i. e., the presence of BM, ITTI and other instabilities). This equation shows that the average value of the electric field should depend only on the voltage drop at the boundaries and on the simulation axial dimension. In Figure 3.8 we report the spatially averaged value of the electric field as a function time for the four cases. The average value is calculated as the average of the electric field over the entire domain at a fixed time. The shaded area covers a 2% interval around the value (dashed line) calculated with Eq. (3.4). Hence, the results suggest that the average value of the axial electric field is always within a 2%% interval around the nominal value given by the expression above. The reason why the average electric field is lower than the theoretical one (dashed line) is related to the monotonic assumption for the potential shape: a positive gradient must be present. This is not visible in the averaged profiles shown in Figure 3.7 (a), but it will be discussed in detail in Section 5.3.2.2 in the study of the axial electric field profile related to the ITTI.

So far, we have suggested that the average value of the axial electric field should not depend on the permittivity scaling value. However, the shape of the axial electric field profile does depend on it. In Figure 3.7 (b) we observe that the electric field has a bell shape: it is zero at the boundaries and has a maximum approximately near the center of the domain. The amplitude and shape of the bell are different in the

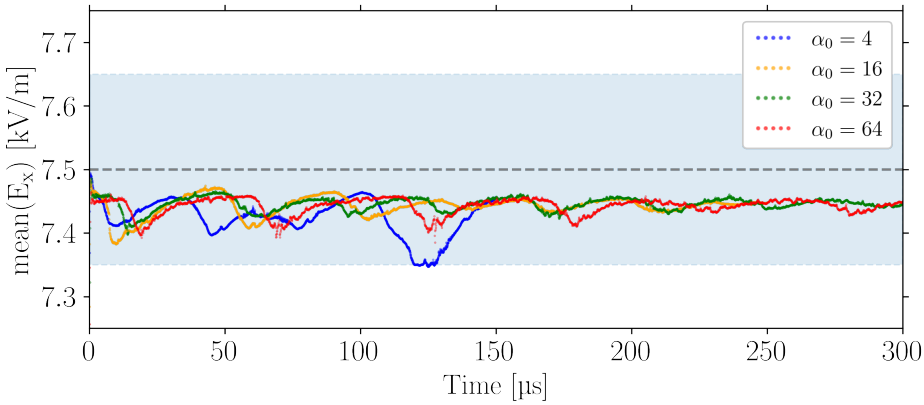


Figure 3.8: The spatially averaged value of the axial electric field evolution over time for the four permittivity scaling values. The shaded area covers a 2% interval around the theoretical value (dashed line) calculated with Eq. (3.4).

four cases. From these averaged profiles we can infer that the increased permittivity scaling causes a flattening of the profiles: the maximum electric field decreases, while the bell amplitude increases. However, since these profiles are averaged over a wide period in which plasma conditions are quite different, it is more accurate to study the temporal evolution of the electric field shape.

In Figure 3.9 we show the temporal evolution of the position of the maximum of E_x (a), the maximal value of E_x (b), and the Full Width at Half Maximum (FWHM) of the E_x bell (c). We observe that these quantities vary during the BM cycle: when the current grows, the maximal value of E_x grows as well, while the width of the bell decreases. At the same time, the position of the maximum of E_x moves towards the anode. Conversely, during the decreasing phase of the BM the value of max(E_x) decreases, i. e., the bell width increases, and the position of the maximum moves towards the cathode. The temporal evolution of the electric field shape is consistent with the temporal evolution of the plasma conditions: when the plasma is denser, the electric field is stronger, and the bell is narrower. When the plasma is less dense, the electric field is weaker, and the bell is wider. The larger bell-shape corresponding to lower electric field strength is consistent with what is observed by comparing Eq. (3.4) with Figure 3.8.

The position of the maximum, shown in Figure 3.9 (a), does not seem to depend much on the permittivity scaling factor. In all cases its value ranges between 2 and 3 cm, corresponding to the channel exit, ideally located at 2.5 cm. Conversely, the maximal electric field value drops when we increase the scaling factor (i. e., it goes from $\approx 65\,\mathrm{kV/m}$ when $\alpha_0 = 4$ to $\approx 36\,\mathrm{kV/m}$ when $\alpha_0 = 64$). The width of the axial electric field bell, represented by the FWHM in Figure 3.9 (c), appears to be much larger when the scaling is high and to be significantly lower when the scaling is low. When $\alpha_0 = 64$ the FWHM is about 2 cm, meaning that the electric field bell is occupying most of the simulation domain.

In conclusion, the discussion of the axial electric field carried out in this section shows that the average value of the electric field does not depend on the permittivity

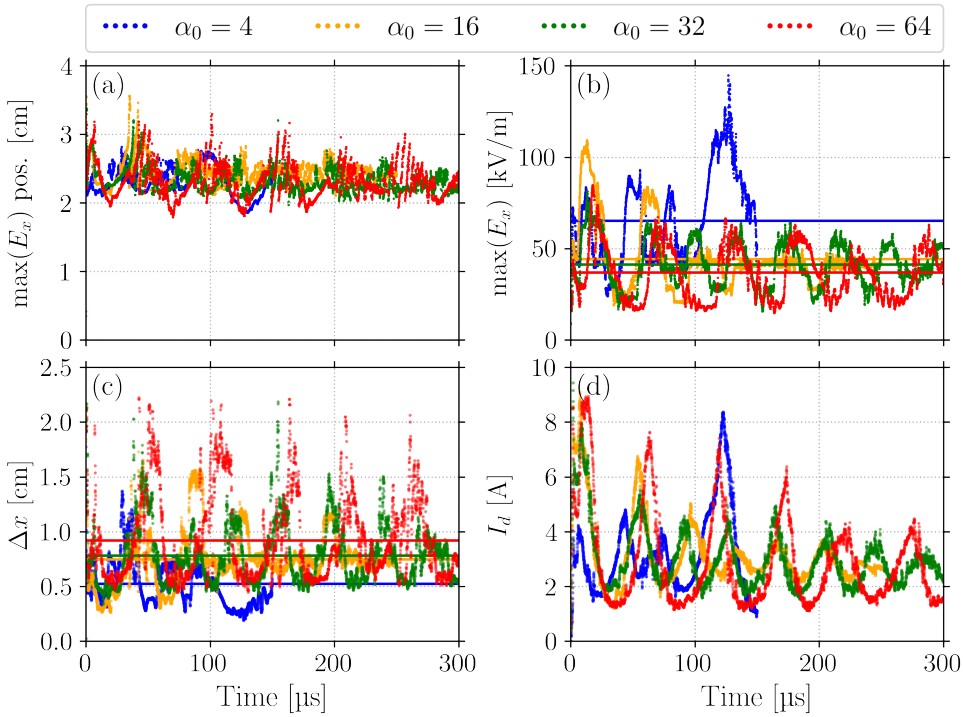


Figure 3.9: Postion (a), value (b) of the maximum of the axial electric field and FWHM (c) of its profile as a function of time for the four cases. The discharge current (d).

scaling factor. This is advantageous, because it means that the ion exhaust velocity is not affected by the scaling factor (i. e., as the conservation of energy suggests). Conversely, the shape of the electric field is affected. The larger scaling factor causes a flattening of the electric field profile, while the smaller scale factor causes a sharper profile.

3.3.2.2 Azimuthal electric field

We have seen that the axial electric field does not depend much on the permittivity scaling factor, but what about the azimuthal electric field? The mean value of the potential at each axial position is fixed by the axial boundary conditions. However, along the azimuthal direction, the potential is not fixed by the boundary conditions, but it only needs to be periodic. To understand the effect of permittivity scaling, let us assume that we have a small perturbation $\tilde{\Phi}$ in a mono-dimensional, homogeneous, and constant plasma potential. If we consider the classical theory of Debye shielding, we have that for a 1D case

$$\Phi(y) = \tilde{\Phi} \exp(-y/\lambda_D),$$

where we use the Debye length defined as usual as $\lambda_D^2 = \epsilon k_B T_e / n_0 e^2$. The electric field amplitude can be computed as the derivative of the potential; thus, we have that:

$$E = -\frac{d\Phi}{dy} = \frac{\tilde{\Phi}}{\lambda_D} \exp\left(-\frac{y}{\lambda_D}\right) \propto \frac{1}{\sqrt{\alpha_0}}. \tag{3.5}$$

So, the same plasma potential fluctuation induces a reduced azimuthal electric field response. When we include in our calculation a permittivity increment, it damps by a factor $\sqrt{\alpha_0}$ the electric field amplitude. Similarly, it is trivial to show that within the same hypotheses, the charge density fluctuations should not depend on α_0. First, we calculated at each time step and each axial position the standard deviation of the potential, the azimuthal electric field, and the charge density. Figure 3.10 (a) shows as an example the temporal evolution of the maximal standard deviation for the azimuthal electric field. In Figure 3.10 (b)-(d), we show at each time step the average maximal standard deviation of potential, the azimuthal electric field, and the charge density.

The fluctuations of the azimuthal electric field depend on the chosen α_0. The average fluctuation values, represented by the solid lines in Figure 3.10 (a) and reported in (c), depend on the scaling α_0 in the way predicted by Eq. (3.5): the larger the scaling, the smaller the fluctuation. The fluctuations of the charge density and of the potential seem to be affected by the scaling factor in a less net way. The charge fluctuations are damped by the increment of α_0, but we do not observe the linear behavior (proportional to α_0) that is predicted by the theory. The potential fluctuations seem not to follow a clear pattern. The difficulty of reading these data is probably related to the approximate way we adopted to calculate the amplitude of the fluctuations. In the next section, we analyze in more detail the effect of the permittivity scaling on the plasma instabilities, by using a more accurate method to study the fluctuations' characteristics.

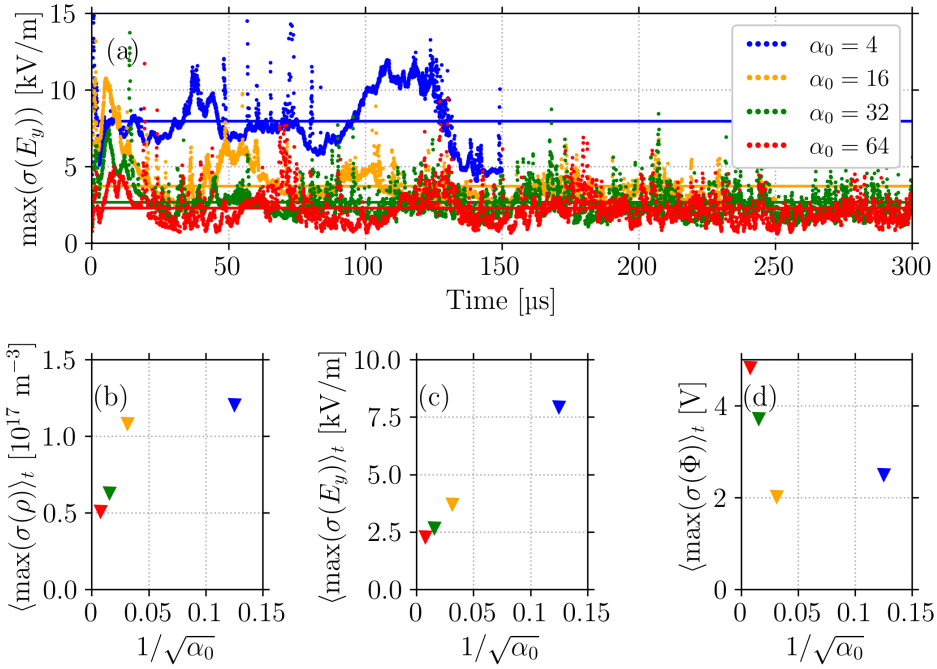


Figure 3.10: The maximal standard deviation of the fluctuation in the azimuthal direction of the azimuthal electric field is shown in (a). The average maximal standard deviation of the fluctuation in the azimuthal direction of charge density (b), azimuthal electric field (c), and potential are plotted vs the reciprocal of the scaling factor, $1/\sqrt{\alpha_0}$.

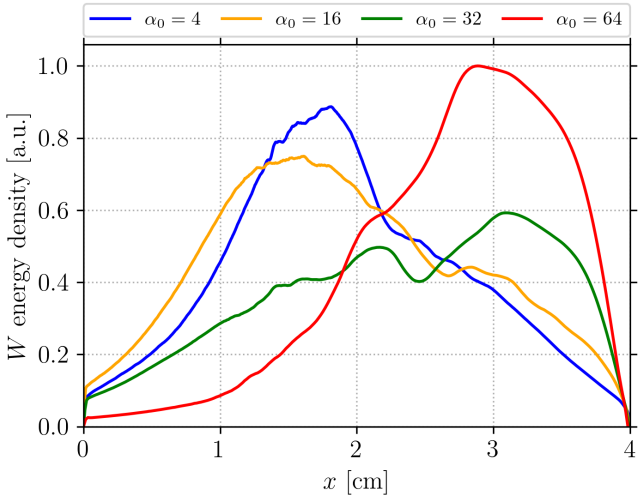


Figure 3.11: Average energy density profiles. The results are normalized by the same quantity.

To conclude this section, we analyze the axial profile of the time-average instability energy density. Considering the instability energy W calculated as in Lafleur *et al.* [106], we have

$$W = \frac{1}{2}\epsilon_0\alpha_0|\delta E|^2\omega\frac{\partial\epsilon}{\partial\omega} \approx 3\epsilon_0\alpha_0|\delta E|^2.$$

The fluctuation amplitude is estimated using the standard variation of the azimuthal electric field component in the azimuthal direction at each axial point. In Figure 3.11 we observe that the oscillation energy moves towards the anode: at high α_0 the peak is in the plume, while decreasing the scaling we observe an upstream shift of the energy density.

3.3.3 Effect of the permittivity scaling on the plasma instabilities

In previous works [156, 201], it has been observed that the permittivity scaling might have an effect on the numerous plasma instabilities that are present in the thruster. As already discussed in Chapters 1 and 2, one of the best-known plasma oscillation is the Ion Acoustic Wave (IAW). This instability develops in the external part of the thruster channel, and it is (mainly) an azimuthal instability. In a recently published work [202], we have shown that this instability also has an axial component. However, in this part we are interested in the macroscopic characteristics of the instabilities, so we consider only the azimuthal component of this mode. Considering the IAW DR

calculated by Lafleur *et al.* [105], the wavenumber and frequency corresponding to the maximum growth rate read

$$k_y^{\max} = \frac{1}{\sqrt{2}\lambda_D} \propto \frac{1}{\sqrt{\alpha_0}}, \tag{3.6}$$

$$\omega^{\max} \simeq \frac{\omega_{pi}}{\sqrt{3}} \propto \frac{1}{\sqrt{\alpha_0}}, \tag{3.7}$$

respectively, as discussed in Ref. [201]. In this section, we use the PSD2P described in Chapter 2 to estimate the frequency and wavenumber of the IAW in the four cases discussed above. Using this technique, we have calculated the $\omega - k$ spectrum along the axial and azimuthal directions in the plume, as one can see in Figure 3.12, for the four cases. Each case corresponds to a row, while the first column reports the spectrum calculated in the axial direction and the second in the azimuthal one. The last column shows four snapshots of the plasma potential. The times correspond to the growing phase of the BM, that is the discharge phase in which the IAW is stronger [170, 202]. We observe that the shape of the dispersion is rather similar in the four cases, but the absolute values of frequency and wavenumber change.

From the PSD2P we can obtain the frequency and wavenumber of the most unstable component of the IAW for each simulation. As one can see in Figure 3.13, the wavenumber and frequency of the most unstable mode are directly proportional to $\alpha_0^{-1/2}$, as predicted in Eq. (3.7). Interestingly, if we estimate using a linear fit the value of the most unstable mode corresponding to $\alpha_0 = 1$, we obtain $\omega_{\max} = 10.6\,\mathrm{MHz}$ and $k_{\max} = 5.46\,\mathrm{mm}^{-1}$. To verify this estimation, we need to compare it to an unscaled simulation. However, it is not trivial, since the plasma conditions strongly affect the frequency and wavenumber and we would need a case identical to the one analyzed here. The 2D axial-azimuthal benchmark case of Ref. [156] is a good candidate, even if the conditions are slightly different. This steady-state test case was analyzed by Ben Slimane *et al.* [185], using a virtual Thomson scattering, obtaining a frequency of 6.5 MHz for the same instability. The differences between our estimation of 10.6 MHz and the one measured of 6.5 MHz can be explained by analyzing the effect of the different plasma densities on the maximal frequency. The density in the plume in Ref. [156] is $\approx 1.5 \times 10^{17}\,\mathrm{m}^{-3}$, while in the current simulations it oscillates between $3 \times 10^{17}\,\mathrm{m}^{-3}$ and $5 \times 10^{17}\,\mathrm{m}^{-3}$. Equation (3.7) suggests that the maximal frequency is proportional to $\sqrt{n_i}$. Thus the frequency measured by [185] reported to our conditions should be in the range 9/12 MHz, which is in good agreement with our estimation. Proceeding in the same way for the wavenumber (i. e., the value measured by Ben Slimane is $1.27\,\mathrm{mm}^{-1}$), is less straightforward since the density is not the only parameter that affects the wavenumber: the electron temperature is also playing a role in defining the Debye length. By considering only the density variation we calculate an interval for the unscaled case from $1.8\,\mathrm{mm}^{-1}$ to $2.32\,\mathrm{mm}^{-1}$. So, the agreement, in this case, is not as good as for the frequency and makes clear the importance of considering the electron temperature for this analysis.

The linear fits in Figure 3.13 allow us to retrieve the maximum value of α_0 for which the instability will be fully observed. Those values are identified as $1/\sqrt{\alpha_0} = 0.091$ and $1/\sqrt{\alpha_0} = 0.065$, for wavenumbers and frequencies, respectively. Despite being rather close, these numbers correspond to values of α_0 of 120 and 238, respectively. The large difference in these values is related to the rather low number of points used

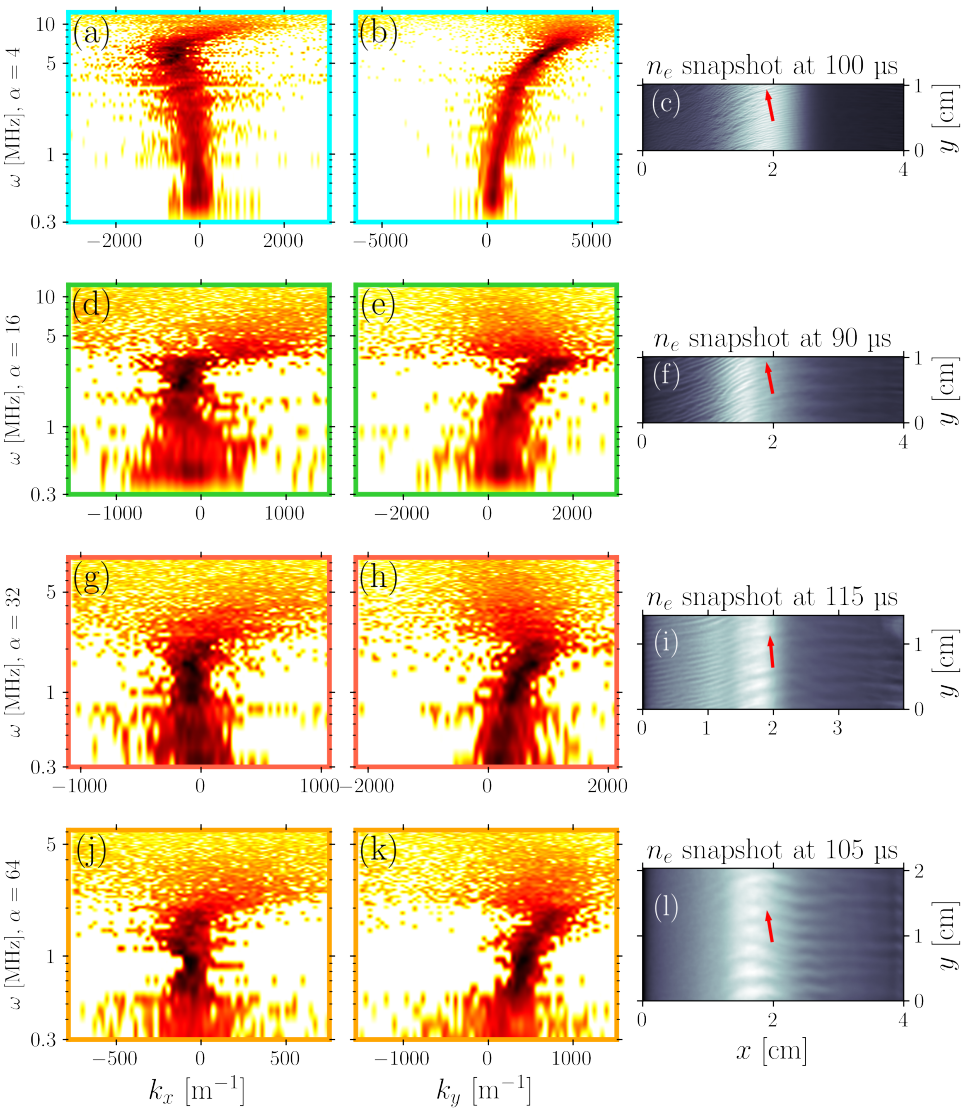


Figure 3.12: Each row corresponds to a different value of α_0: 4, 16, 32, and 64 from top to bottom. The first column (a, d, g, j) shows a PSD in the axial direction, while the second (b, e, h, k) in the azimuthal one. The last column shows four snapshots. The chosen times correspond to the growing phase of the BM. We highlight the fact that for each α we use different limits in the $k-$range and ω-range.

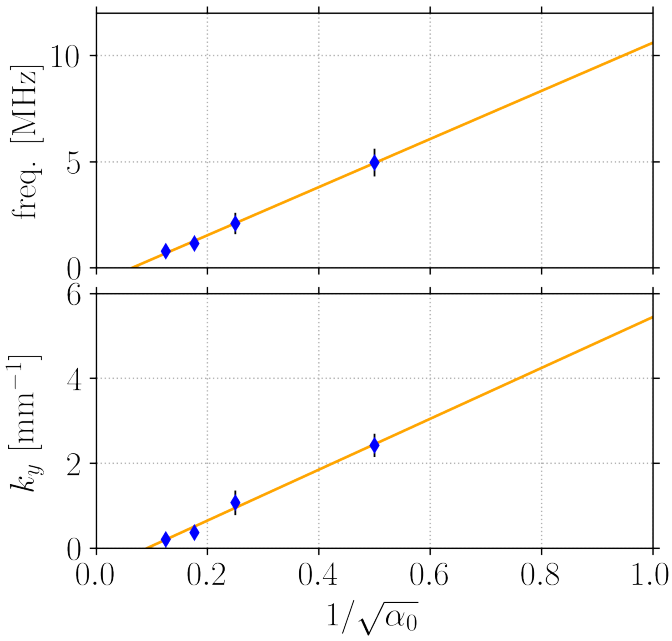


Figure 3.13: Variation of the (a) frequency and (b) wavenumber of the most unstable mode as a function of $\alpha_0^{-1/2}$. The error bars are calculated as the standard variation of the evolution of these value in time. The yellow lines show the linear fits.

to calculate the linear fit. They give a threshold of the maximum scaling that allows the appearance of instability. Below these values, we expect that no instability will be observed: this is particularly important for the HTs modeling, since the azimuthal instabilities are the main driver for the axial anomalous transport [133], as we discuss in the next Sections.

3.3.4 Effect of the permittivity scaling on the mobility

The discussion in the previous section showed that the increased permittivity scaling is reducing the amplitude of the plasma oscillations, thus reducing (with respect to reality) the transport in the axial direction. In this section, we analyze directly the mobility during the BM cycle for the four cases with different scaling factors. The mobility can be extracted from PIC simulations, as proposed in Eq. (3.3). The mobility is a measure of the electron transport in the plasma, and it is directly related to anomalous transport. In Figure 3.14 we show the evolution of the mobility during the BM cycle for the four cases. In the first row, we show the axial discharge current for the four cases and the times at which the mobility is calculated. The subfigures (b-d) show the axial profiles of the mobility at four different times of the BM cycle. We notice that the mobility profile varies significantly along the thruster, while the profile shape itself remains more or less the same during a BM oscillation. Figure 3.14 shows that the axial mobility is well calculated by the formula above. However, the mobility in the plume remains extremely noisy. The mobility appears to depend significantly

on the scaling during the growing phase of the BM (b,c), while this dependency seems to be reduced in the decreasing phase (d,e). By comparing the two extreme results, $\alpha_0 = 4$ and $\alpha_0 = 64$, we observe that in the channel the mobility is reduced by an order of magnitude for $\alpha_0 = 64$ in comparison to $\alpha_0 = 4$. This is in agreement with the previous discussion, where we showed that the amplitude of the plasma oscillations is reduced with the increased scaling. This is also consistent with what was observed by Charoy [156], by studying the friction force generated by the instabilities.

In summary, the discussion in this section has shown that it is arduous to study the effect of the scaling of permittivity on the mobility in PIC simulations, since (i) it is difficult to calculate the mobility directly from PIC data and (ii) the mobility changes during a BM cycle. However, comparing the axial profiles of the mobility calculated at different phases of the breathing mode shows that during the BM growing phase the scaled permittivity artificially damps the instabilities, which in turns reduces reduce the anomalous transport.

3.3.5 Other effects on instabilities

It is possible to further analyze the effect of the scaled permittivity on the plasma instabilities. The discussion about the IAW was carried out in the previous sections, hereafter we address the ECDI and ITTI. The scaled permittivity could also have some consequences on the frequency and amplitude of the BM. In this work, this aspect is not addressed.

Cavalier *et al.* [92] numerically solved the kinetic DR of the ECDI. Their results show that the ECDI DR depends on the ratio ω_{ce}/ω_{pi}. The ECDI resonances appear at fixed values of k_y, which do not depend on the vacuum permittivity. However, the frequency of the wave at the maximum growth rate and, even more important, the growth rate itself largely depends on the permittivity. Charoy *et al.* observed longer wavelengths [140, 170] when introducing a permittivity scaling.

Fernandez *et al.* [75] have shown that the ITTI DR does not depend on the permittivity scaling and this has been confirmed by Charoy *et al.* [170], who reported that the ITTI frequency was nearly independent of the scaling factor. The major impact of the scaling is on the oscillations amplitude. This is consistent with the observation of Fernandez, who suggested that the ITTI growth rate is proportional to the electron mobility (i. e., $\gamma_{ITTI} \propto \mu_e^{-1/2}$), that is reduced when the scaling factor increases, i. e., most likely because the anomalous mobility is governed by the ECDI/IAW, which as noted above, is damped by increasing the permittivity scaling.

One should however be aware that the coupling between the modes, in particular between the ITTI and the ECDI is non-linear, which makes it difficult to fully predict the exact impact of the permittivity scaling on the instabilities dynamics. Finally, the scaled permittivity could also have some consequences on the frequency and amplitude of the BM. In this work, this aspect is not addressed.

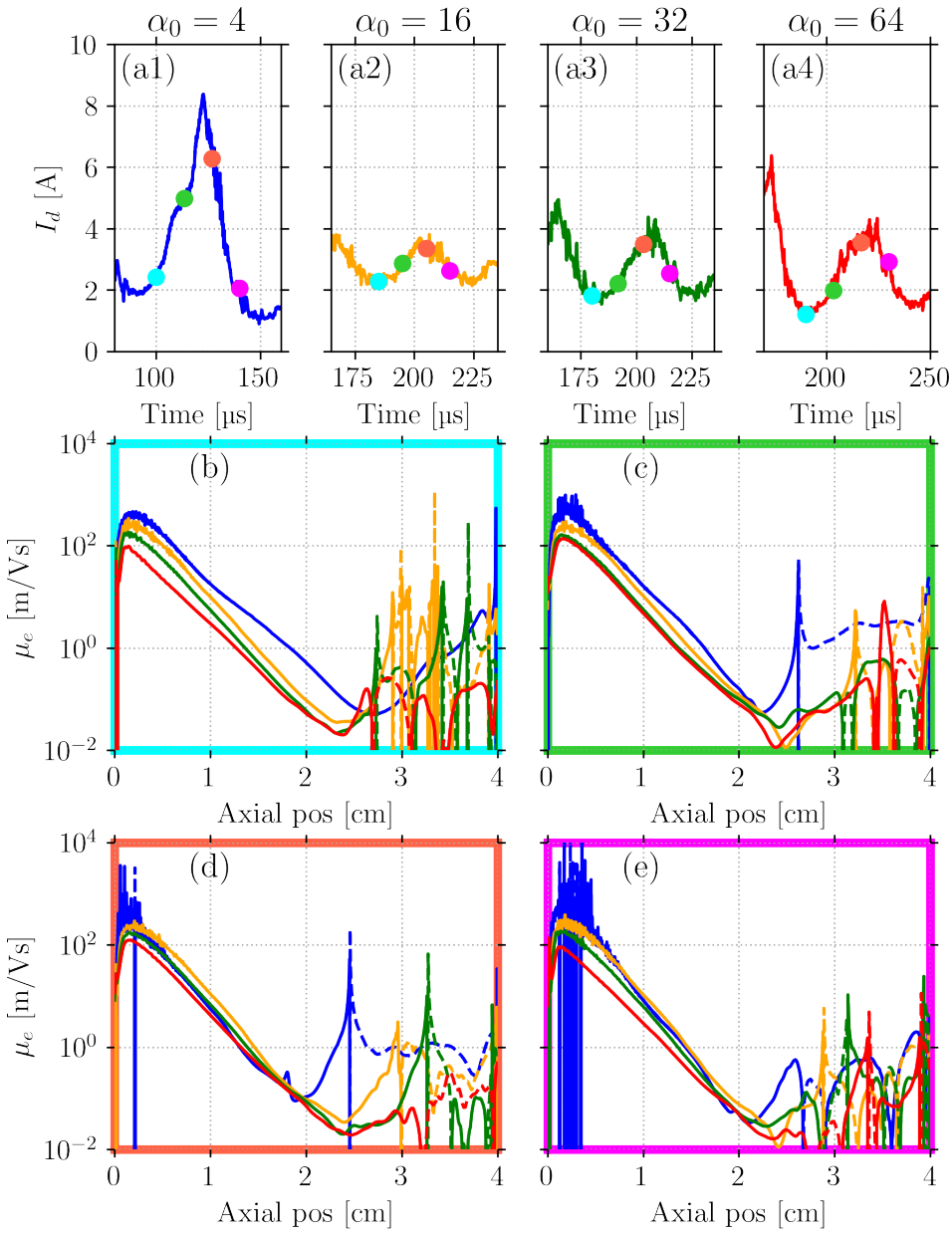


Figure 3.14: Evolution of the mobility during the BM cycle for the four cases with different scaling factors. Discharge current of the four cases are shown in the first row, the scaling is indicated in the title. The subfigures (b-d) show the axial profiles of the mobility at four different times of the BM cycle. For each case the precise time is indicated by the dot in the first row that has the same color of the frame in (b-d).

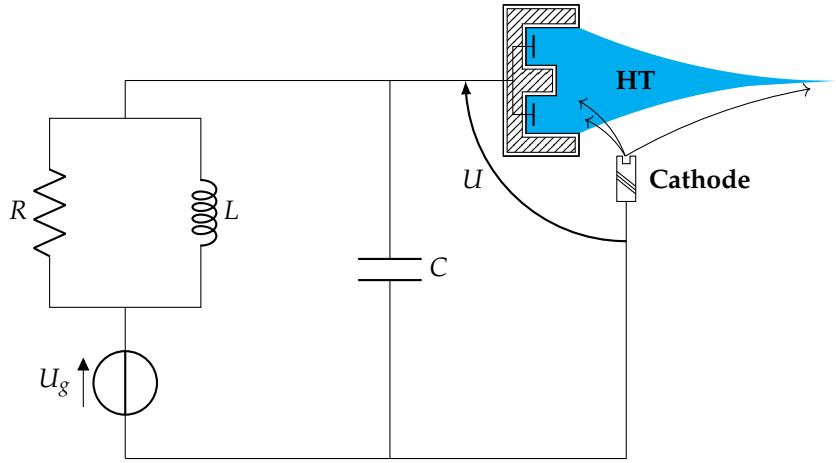


Figure 3.15: Scheme of the circuit of a HT. The generator applies a DC voltage U_g. The voltage drop at the plasma boundaries and the discharge current are U and I, respectively.

3.4 THE CIRCUIT IMPLEMENTATION

HT devices are powered by a DC voltage generator and are equipped with an RLC filter that controls the anode voltage [82]. The electric filter is a fundamental component of any HT device since it allows for both the control of the anode voltage and the reduction of the current fluctuations on the voltage generator. Despite its importance, it remains poorly studied and not much literature has been published on this topic. Several layers of complexity may be used to design the electric circuit; however, the main elements are fixed. The filter, sketched in Figure 3.15, is composed of a series of two parallels. The first is composed of a resistor R and an inductance L set in parallel, and the second by capacitance C in parallel with the discharge chamber. In this section, we analyze the modeling of the circuit and we compare the results of several PIC simulations in which we varied the circuit parameters.

3.4.1 Circuit equations and coupling with the PIC code

Using Kirchhoff's circuit laws, we have:

$$\begin{cases} I = I_r + I_l - I_c, \\ U = U_r - U_g, \\ I_c = C\dfrac{dU}{dt}, \\ U_l = U_r = RI_r = L\dfrac{dI_l}{dt}. \end{cases} \tag{3.8}$$

Where U_g is the DC applied voltage and the voltage drop at the plasma boundaries and the discharge current are U and I, respectively. The indices r, l, and c are used to define the voltage drop and current flowing in the different circuit components and

d/dt represents the time-derivative. With some algebraic manipulation, the above system simplifies to

$$\begin{cases} \dfrac{dI_r}{dt} + \dfrac{R}{L}\dfrac{dI_r}{dt} = C\dfrac{d^2U}{dt^2} + \dfrac{dI}{dt}, \\ I_r = \dfrac{U_g - U}{R}. \end{cases} \tag{3.9}$$

Let $\Delta U = U - U_g$, then the evolution of the circuit may be written as an ordinary differential equation for this variable, as follows,

$$C\frac{d^2\Delta U}{dt^2} + \frac{1}{R}\frac{d\Delta U}{dt} + \frac{1}{L}\Delta U = -\frac{dI}{dt}. \tag{3.10}$$

The equation above can be discretized and solved numerically, using the following temporal discretization,

$$\begin{cases} \dfrac{d^2\Delta U}{dt^2} = \dfrac{\Delta U_n - 2\Delta U_{n-1} + \Delta U_{n-2}}{\Delta t_{RLC}^2} + O\left(\Delta t_{RLC}^2\right), \\ \dfrac{d\Delta U}{dt} = \dfrac{\Delta U_n - \Delta U_{n-1}}{\Delta t_{RLC}} + \dfrac{\Delta t_{RLC}}{2}\dfrac{d^2\Delta U}{dt^2} + O\left(\Delta t_{RLC}^2\right) \\ \qquad = \dfrac{3\Delta U_n - 4\Delta U_{n-1} + \Delta U_{n-2}}{2\Delta t_{RLC}} + O\left(\Delta t_{RLC}^2\right), \\ \dfrac{dI}{dt} = \dfrac{I_{n-1} - I_{n-2}}{\Delta t_{RLC}} + O\left(\Delta t_{RLC}\right). \end{cases} \tag{3.11}$$

The circuit equation is solved every N_{RLC} PIC loops in order to average the current and avoid high-frequency noise. So, in the above equation, the RLC time step can be defined as a function of the PIC time step Δt, as $\Delta t_{RLC} = N_{RLC} \cdot \Delta t$. The discretization scheme is a second order scheme for the voltage, while it is first order for the current (calculated in PIC simulations), which means that, overall, the scheme is first order.

The voltage at the anode is set to $U_n = U(t = n \cdot \Delta t_{RLC})$, that is computed as $U_n = U_g + \Delta U_n$ from the following equation

$$\begin{aligned} \Delta U_n = \frac{L}{2RLC + 3L\Delta t_{RLC} + 2R\Delta t_{RLC}^2}\Big(&4(RC + \Delta t_{RLC})\Delta U_{n-1} \\ &- (2RC + \Delta t_{RLC})\,\Delta U_{n-2} \\ &- 2R\Delta t_{RLC}\,(I_{n-1} - I_{n-2})\Big). \end{aligned} \tag{3.12}$$

The current is averaged over N_{RLC} loops and Eq. (3.12) is solved using the current and voltage values at the previous time-steps to find the new anode voltage. This voltage is kept constant for the subsequent N_{RLC} time-steps. The results presented here are obtained using $N_{RLC} = 250$, which allows us to resolve the breathing mode with ~ 7500 time steps.

3.4.2 Transfer Function

In control systems engineering, the transfer function is a mathematical representation of the relationship between the input and output of a linear, time-invariant system. It provides a concise description of how the system behaves and can be used to design controllers that produce a desired response.

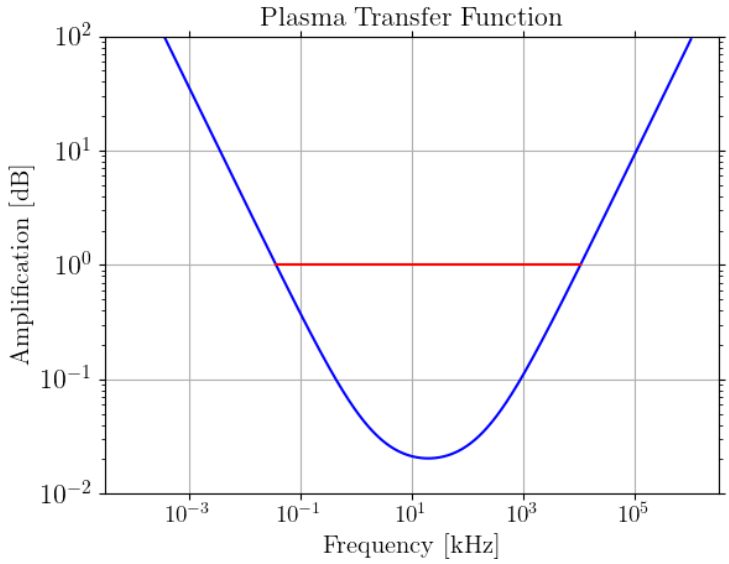


Figure 3.16: Bode diagram representing Eq. (3.13) using the chosen circuit parameters: $R = 60\,\Omega$, $L = 4.4\,\text{mH}$ and $C = 15\,\text{nF}$. From Ref. [201]

3.4.2.1 *Standard transfer function*

Two sets of circuit element values have been tested. The first set uses values implemented in some real HT devices and close to those used in Ref. [82]: $R = 60\,\Omega$, $L = 340\,\mu\text{H}$ and $C = 10\,\mu\text{F}$. This set is labeled "standard" in the following. The second set is found by analyzing the circuit transfer function. The linear frequency response of the circuit between the discharge electrodes (i. e., $G(\omega) = U(\omega)/I(\omega)$) reads

$$G(\omega) = \frac{-RLC\omega^2 + L\imath\omega + R}{RL\imath\omega}. \tag{3.13}$$

This equation is used to choose R, L, and C values to limit the discharge current oscillations in the conditions studied in this work. In Figure 3.16, we plot the Bode diagram of Eq. (3.13) for $R = 60\,\Omega$, $L = 4.4\,\text{mH}$ and $C = 15\,\text{nF}$. This set is labeled "optimized" in the following. As shown in Figure 3.16, with these values, the filter is adapted to damp the oscillations with a frequency around $\sim 20\text{kHz}$, i. e., near the BM frequency. However, as the discharge response is non-linear, we can expect that the circuit will not be able to completely filter out the current oscillations in the PIC simulations.

3.4.2.2 *Alternative transfer function*

The transfer function presented in the previous section is not unique. If we want to study the effect of an instability generated in the plasma on the voltage generator, we might use a different approach. By considering $H(\omega) = I_g(\omega)/I(\omega)$, we can write a transfer function that relates the fluctuations of the current in the plasma (I), with

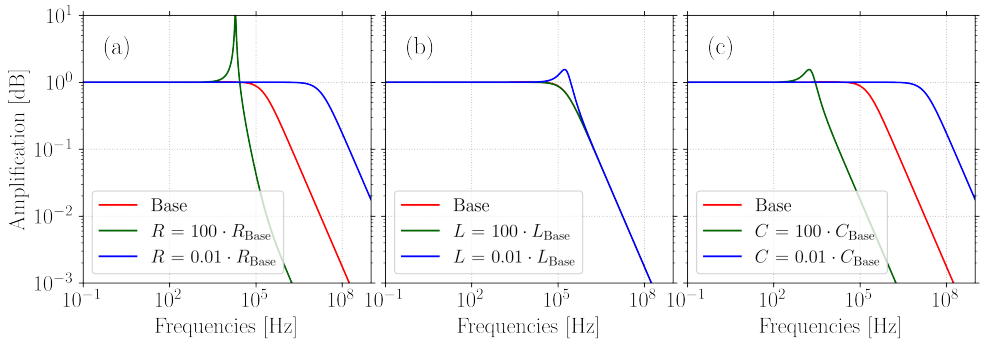


Figure 3.17: The transfer function $H(\omega)$ calculated with Eq. (3.14) for different values of the circuit components. The base solution (red) is compared to a varied resistivity (a), inductance (b), and capacitance (c).

the induced fluctuations on the current in the generator (I_g). This transfer function, calculated with linear approximation, is given by

$$H(\omega) = \frac{R + \imath\omega L}{-\omega^2 RLC + \imath\omega L + R}. \tag{3.14}$$

We notice that at low frequency we have $H(\omega \to 0) = 1$ and at high frequency $H(\omega \to \infty) \propto 1/\imath\omega RC$. With some analytical manipulations, we can write and compute the poles and zeros of this transfer function in the limit $LC \gg 4R^2C^2$. A pair pole/zero is found at a frequency $\omega_a = R/L$ and a single pole at $\omega_b = 1/RC - R/L$.

This transfer function can be useful to evaluate the current fluctuations in the generator caused by the plasma fluctuations. To investigate the robustness of the circuit one may vary the values of the components around the *base* values defined in the previous section, e. g., $R_{\text{Base}} = 60\,\Omega$, $L_{\text{Base}} = 4.4\,\text{mH}$ and $C_{\text{Base}} = 15\,\text{nF}$. In Figure 3.17 we show the result obtained by varying each impedance separately by a factor of 100 and 0.01. We observe that the base value has a gain of 1 up to $\approx 100\,\text{kHz}$, and subsequently a linear decrease (i. e., $H(\omega) = 1/\imath\omega RC$ for large frequencies). By increasing the resistance, we observe that a positive gain region produces at $\omega \approx 20\,\text{kHz}$: this is particularly destructive for the HTs since the BM is exactly at this frequency. The origin of this gain region is due to the values of ω_a and ω_b that are close to each other. The reduction of the resistance only pops up a variation of the pole position, that shifts at a higher frequency. The inductance variation generates less important variations on the gain. The only remarkable effect is a small positive gain region that appears at $\omega \approx 100\,\text{kHz}$ when we reduce the inductance L. By variating the capacitance, we are moving the pole at ω_b. By reducing the capacitance, we extend the unit gain region at high frequencies. Increasing the capacitance reduces the value of ω_b, and consequently, it shrinks the unit gain region. However, the ω_b approaches ω_a, a positive gain starts to appear.

The discussion in this section suggests that the transfer function and the consequent choice of the circuit parameter depend on the goal of the circuit: if the goal is to limit the oscillation within the plasma, one should consider the function G discussed in the previous section. Otherwise, if the circuit is used to protect the generator from

the plasma instabilities, the function H discussed here should be used. In the reality, a trade-off between the two approaches is needed.

3.4.3 Analysis of the circuit effect on PIC simulations of different domain sizes

The axial-azimuthal simulation setup used to study the effect of the circuit and subsequently to analyze the plasma instabilities is described extensively by Charoy *et al.* [140, 170] and Petronio *et al.* [201]. Its main characteristics are summarized in the following. In the rest of the section, we present several tests that are used to investigate the effect of the circuit on the discharge.

3.4.3.1 Description of the PIC setup

As sketched in Figure 3.18, the domain consists of the usual structured Cartesian mesh with axial and azimuthal lengths, L_x and L_y, respectively. The axial length $L_x = 4\,\text{cm}$ includes the discharge channel (between the anode at $x = 0$ and $x = 2.5\,\text{cm}$) and part of the plume for $2.5 \leq x \leq 4\,\text{cm}$. As always in our work, the curvature of the channel is not considered, and periodic boundaries are imposed in the azimuthal direction. The voltage at the cathode (right boundary) is fixed to zero, while the anode (left boundary) voltage is controlled by the electric circuit, as described in the previous section, with a DC voltage generator set to 300 V in most of the simulations. The magnetic field is in the out-of-plane z-direction, and it varies along the thruster axis as shown by the purple line in Figure 3.18, while it is constant along the azimuthal direction. Its maximal value is set to 170 G at the exit plane of the thruster channel. The plasma is initialized with a homogeneous density and at later times the discharge is sustained by ionization (within the MCC module). A constant mass flow $\dot{m} = 5\,\text{mg}\,\text{s}^{-1}$ of neutral gas is injected at the anode. A constant density of electrons and ions is set in every cell at the beginning of the simulation.

The simulation parameters, summarized in Table 3.2, are chosen to respect the CFL condition as set by Birdsall and Langdon [23], discussed in Section 3.2.1. A simulation with these numerical parameters is extremely costly in order to capture several BM periods. To relax the PIC constraints the permittivity scaling technique, described above, is used. In the simulations analyzed here, $\alpha_0 = 64$ has been used, leading to an increase of both Δt and Δx by a factor of 8.

3.4.3.2 Simulations with a small azimuthal length, $L_y = 1\,\text{cm}$

We first study 2D PIC axial-azimuthal simulations with a reduced azimuthal length, $L_y = 1\,\text{cm}$ with parameters given in Table 3.2. Figure 3.19 shows the time evolution of the discharge current and the anode potential for a base case without circuit, and for two different cases with RLC circuits discussed in Section 3.4: case 1 is for standard HT circuit components ($R = 50\,\Omega$, $L = 340\,\mu\text{H}$ and $C = 10\,\mu\text{F}$); case 2 is for the optimized set of parameters ($R = 60\,\Omega$, $L = 4.4\,\text{mH}$ and $C = 15\,\text{nF}$).

As seen in Figure 3.19 (a) a quasi-steady-state is reached after $\approx 100\,\mu\text{s}$ and the average current at steady-state is about the same for all three cases ($I_d^{mean} \simeq 3.3\,\text{A}$). The circuit effect is nonetheless significant. For the base case (without circuit) the standard deviation of the current after the transient phase is $\approx 0.58\,\text{A}$, and this

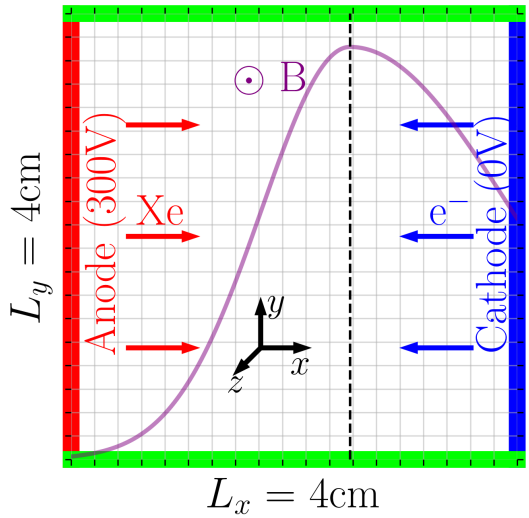


Figure 3.18: The simulation mesh is composed of squared cells. The neutral gas is injected at the anode (left) and the electrons at the cathode (right). The axis of the thruster is x and the azimuthal direction is y. We use periodic boundary conditions in the azimuthal direction. The magnetic field intensity is represented by the purple line. It is perpendicular to the simulation plane (along z) and does not change along the azimuthal direction. Please refer to Table 3.2 for a detailed list of the simulation parameters. From Ref. [201]

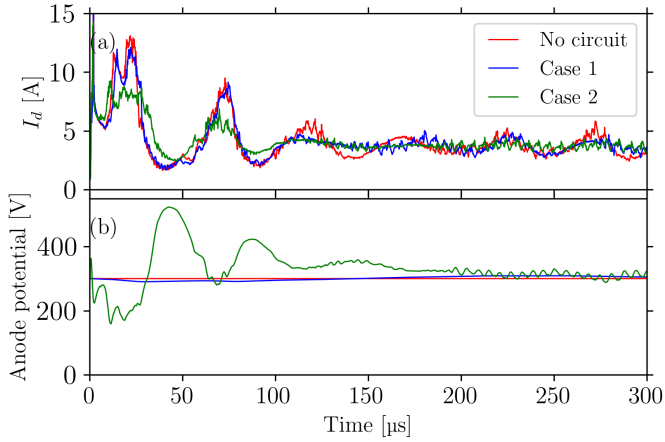


Figure 3.19: Time evolution of the discharge current (a) and the anode potential (b) in 2D PIC axial-azimuthal simulations with an azimuthal length, $L_y = 1\,\text{cm}$ without *RLC* circuit, and with two different *RLC* circuits: case 1 is for standard HT circuit components ($R = 50\,\Omega$, $L = 340\,\mu\text{H}$ and $C = 10\,\mu\text{F}$); case 2 is for the optimized set of parameters ($R = 60\,\Omega$, $L = 4.4\,\text{mH}$ and $C = 15\,\text{nF}$). From Ref. [201].

Table 3.2: Operating and numerical parameters used in PIC simulations. With a small axial-azimuthal domain (4 cm × 1 cm), 3 simulation cases are considered: one without circuit and cases 1 and 2 with circuits. With a larger axial-azimuthal simulation domain (4 cm × 4 cm), 3 simulation cases are considered: one without circuit and cases A and B with circuits.

Physical parameters	Symbol	Value	Unit
Gas		Xenon	(-)
Radial magnetic field (max)	B	170	G
Anode voltage	V_a	300	V
Cathode voltage	V_c	0	V
Axial length	L_x	4	cm
Azimuthal length	L_y	1.01 or 4.08	cm
Initial plasma density	n_0	5×10^{18}	m^{-3}
Initial electron temp.	T_e	1	eV
Initial ion temp.	T_i	0.05	eV
Neutral mass flow rate	$\dot{m}$	5	$mg\,s^{-1}$
Thruster section	$Area$	3.768×10^{-3}	m^2
Cathode inj. temp. (not case C)	T_e^{cath}	5	eV
Cathode inj. temp. (case C)	T_e^{cath}	0.1	eV
Circ. param. (Case 1 / 2, A, B / C)			
Resistance	R	50/60/20	Ω
Inductance	L	0.34/4.4/1.5	mH
Capacitance	C	10^4/15/1	nF
Simulation parameters			
Time step	Δt	1.6×10^{-11}	s
Cell size	$\Delta x = \Delta y$	1.6×10^{-4}	m
Num. of cells	$x_{max} \times y_{max}$	250 × 63 or 255	(-)
Initial num. of part. per cell	N/NG	400	part./cell
Num. of iter. between outputs	N_a	5000	(-)
Permittivity scaling	α_0	64	(-)

quantity decreases to $\approx 0.46\,\mathrm{A}$ for case 1. The BM oscillations are severely damped for case 2, i. e., with the optimized circuit (the current standard deviation drops to $\approx 0.23\,\mathrm{A}$). The filter has almost no impact on a higher frequency oscillation (at $\approx 200\,\mathrm{kHz}$) that is observed in all three cases. In Figure 3.19 (b) we observe that the anode voltage varies significantly during the first BM periods with the optimized circuit, while for case 1 the voltage variation is negligible (without circuit the anode voltage is constant). This study shows that the use of an optimized *RLC* circuit can completely damp the BM oscillations in cases where the standard deviation of the oscillations is small and, hence, close to a linear regime.

3.4.3.3 *Simulations with a larger azimuthal length,* $L_y = 4\,\mathrm{cm}$

We now consider some simulations with a larger azimuthal length, $L_y = 4\,\mathrm{cm}$, and investigate the effect of the temperature of electrons injected at the cathode boundary. Figure 3.20 shows the time evolution of the discharge current and the anode potential, without *RLC* circuit, and with two different sets of *RLC* circuit parameters: case A with $R = 60\,\Omega$, $L = 4.4\,\mathrm{mH}$ and $C = 15\,\mathrm{nF}$, case B with $R = 20\,\Omega$, $L = 1.5\,\mathrm{mH}$ and $C = 1\,\mathrm{nF}$. These two different sets of circuit parameters are designed to damp the BM oscillation with a very similar circuit response (calculated via Eq. (3.12)), but with different time constants (i. e., $\tau \propto 1/\sqrt{LC}$), such that $\tau_A < \tau_B$. First, we observe that without *RLC* circuit the frequency of the BM is similar to that of the small $L_y = 1\,\mathrm{cm}$ case (cf. Figure 3.19). However, as observed in Charoy *et al.* [170], the amplitude of the fluctuations increases dramatically (it is 5 to 10 times larger for $L_y = 4\,\mathrm{cm}$ than for $L_y = 1\,\mathrm{cm}$). As already mentioned, such large fluctuations have severe numerical consequences: (i) the PIC requirements may be violated near the peak (λ_D and ω_{pe} both depend on the plasma density), and/or (ii) the computational cost of each simulation becomes unrealistic, and (iii) the high current peaks are followed by low current phases during which the extinction of the discharge may occur. Therefore, the use of the *RLC* circuit is crucial to run simulations with an azimuthal domain length of several centimeters.

With an optimized *RLC* circuit and a temperature of emitted electrons of 5 eV (similar to that in Figure 3.19), we observe in Figure 3.20 case A that the circuit does not allow to completely damp the oscillations for $L_y = 4\,\mathrm{cm}$. Nevertheless, the circuit can successfully prevent the large unphysical fluctuations that were otherwise observed.

The different behaviors of case A and case B can be explained by the different choices of circuit parameters. In the first case, the BM frequency is lower than in the second case. The BM peaks appear to be more regular, while the amplitude of the fluctuations is of the same order of magnitude in both cases. It is also interesting to observe the anode modulation: the voltage oscillation is much larger in case A than in case B. The origin of this circuit behavior cannot be easily explained. The first hypothesis is that the different circuit parameters select one mode and not the other. However, the frequency of the two modes is very close and it is not trivial to link the non-linear behavior of the BM to the choice of the circuit impedances.

The fact that the BM is present for the $L_y = 4\,\mathrm{cm}$ cases, while it is almost perfectly damped for the $L_y = 1\,\mathrm{cm}$ cases (i. e., case 2), supports the idea that the simulations

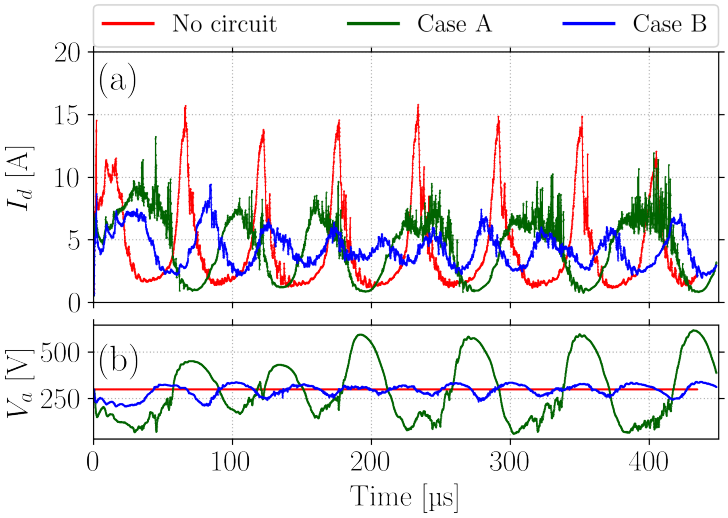


Figure 3.20: Time evolution of the discharge current (a) and the potential (b) in 2D PIC axial-azimuthal simulations with an azimuthal length, $L_y = 4\,\text{cm}$ without *RLC* circuit, and for two *RLC* circuits: case A and case B as defined in Table 3.2.

with small L_y do not capture all the complexity of the discharge physics, and more precisely the influence of the azimuthal modes on the axial modes.

3.4.4 Effect of the cathode temperature on the circuit response

The temperature of the electrons emitted from the cathode depends on the cathode device and may vary in time. In most axial-azimuthal PIC simulations, it has been traditionally fixed to a constant value ($T_e^{\text{cath}} = 5\,\text{eV}$ in the cases described heretofore). Without *RLC* circuit, Charoy [156] observed that the choice of the cathode temperature affects the discharge behavior. For this reason, we investigated the results obtained with a *RLC* circuit for two different cases: case B with $T_e^{\text{cath}} = 5\,\text{eV}$, the usual choice already presented above, and case C with lower $T_e^{\text{cath}} = 0.1\,\text{eV}$. The circuit parameters are kept the same. In Figure 3.21 we observe that the current oscillations and frequency are similar in both cases, however, the cathode temperature seems to have an impact on the BM frequency. Moreover, we observe a difference in the anode voltage evolution: in case C the oscillations around the mean value are smaller, while in B they are more pronounced. These oscillations remain, in any case, smaller than those observed in case A.

3.4.5 Current in the circuit components

Considering the optimized circuit, in this section, we analyze the evolution of the current and voltage drop on each circuit component. In Figures 3.22 and 3.23 we report the voltage drop over the parallel resistance/inductance (a) and the current (b) in the four circuit components: resistance, inductance, capacitance and plasma for

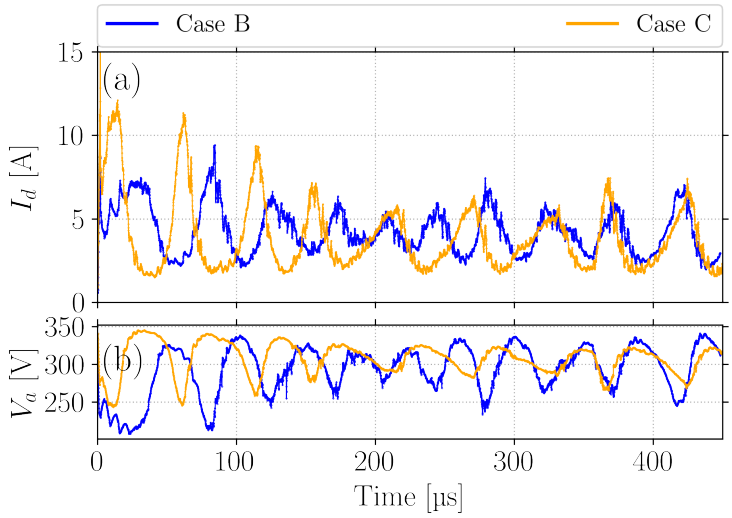


Figure 3.21: Time evolution of the discharge current (a) and the potential (b) in 2D PIC axial-azimuthal simulations with an azimuthal length, $L_y = 4\,\text{cm}$ for two T_e^{cath} of injection: case B (5 eV) and case C (0.1 eV).

$L_y = 1\,\text{cm}$ and $L_y = 4\,\text{cm}$, respectively. The voltage drop over the capacitance is the same voltage drop over the plasma and is reported in Figures 3.19 and 3.21.

In Figure 3.22 (a) the voltage drop over the parallel resistance/inductance converges to zero at steady-state. This is expected, as in Figure 3.19 we observed that voltage at the anode converge to the generator value. The low voltage drop over the resistance causes a very low current in that component, e. g., the green current in (b). The current in the capacitance depends on the voltage drop over the plasma, thus it is very low at steady-state. So, the only circuit component in which a significant amount of current flows is the inductance.

As we discussed in the previous section, the simulation with a larger azimuthal length has a much more complicated plasma dynamics. Thus, it allows a more interesting discussion about currents in the circuit components. Despite the large potential fluctuations at the anode, the current in the capacitance is close to zero during all simulations. Some high-frequency fluctuations are present during the decreasing BM phase, which disappear in the increasing phase. In the case with the small azimuthal length, we noticed that the current in the resistance was negligible: it is not the case when we increase the azimuthal length. The larger fluctuations of the anode voltage, which never stabilize at the nominal generator value, drive a non-zero current in the resistance. However, as before, the largest current remains the one in the inductance.

3.5 CHAPTER SUMMARY

In this chapter, we present the electrostatic PIC code used in LPP to simulate HTs. In particular, we gave a general description of the code features and modifications that

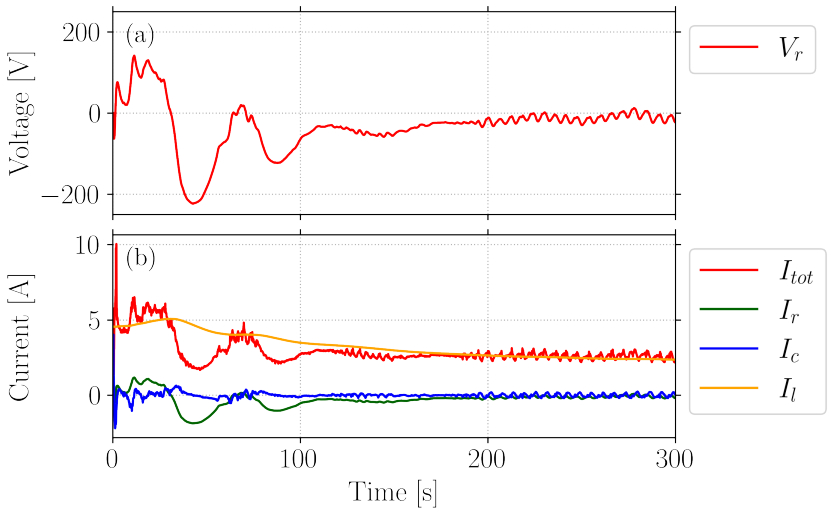


Figure 3.22: Time evolution of the current in the circuit components and voltage drop on each circuit component in 2D PIC axial-azimuthal simulations with an azimuthal length, $L_y = 1\,\text{cm}$, for the optimized *RLC* circuit in case 2.

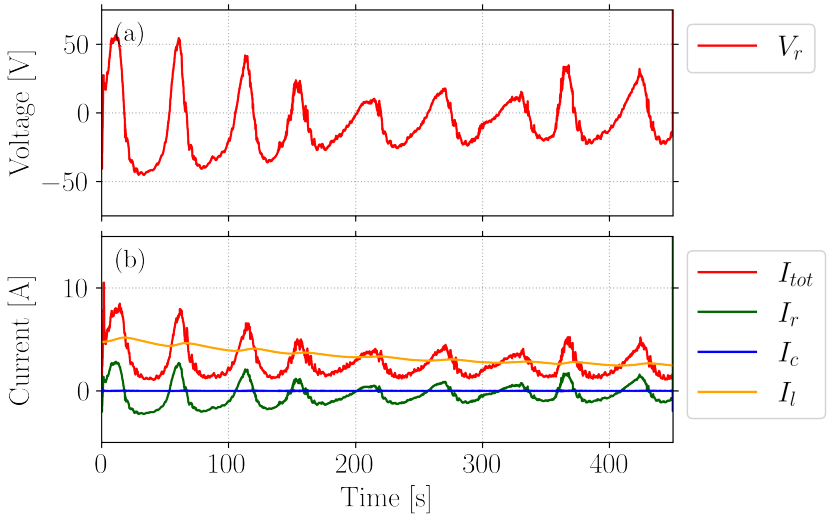


Figure 3.23: Time evolution of the current in the circuit components and voltage drop on each circuit component in 2D PIC axial-azimuthal simulations with an azimuthal length, $L_y = 4\,\text{cm}$, for the *RLC* circuit in case C.

have been made. The second part of the chapter is related to the analysis of the scaling permittivity in PIC simulations. We have shown that the scaled permittivity allows us to reduce the cost of the simulations while retrieving the majority of the physical parameters of the discharge. However, the variation of the permittivity strongly affects the wavenumber, frequency, and growth rate of the electrostatic instabilities. Eventually, we presented the circuit implementation in the PIC code. We have shown that the circuit can damp the BM, but that the damping is less effective when a large azimuthal domain is used. The investigation of different circuit parameters and implementations has allowed concluding that the 1^{st} order scheme for the current represents a good choice for the circuit implementation in PIC simulations. Moreover, we have shown that the circuit time constant needs to be small enough to allow the circuit to react properly during the reduced simulation time interval. A different circuit implementation is discussed in Appendix A.1.

It is worth noting an important aspect related to the current-potential phase shift. In our attempt to minimize the plasma oscillations by adjusting circuit parameters, we have caused these two quantities to be out of phase with each other. Specifically, when the current is at a low value, the potential is high and vice versa, as illustrated in Figure 3.20. This effect has an adverse impact on the overall performance of the thruster. When the voltage is high and the exhaust velocity can be maximized, the current is low, resulting in a reduction in thrust. Conversely, when the current is high, the ion exhaust velocity is reduced, causing further performance degradation. In conclusion, the present study shows that the choice of the circuit parameters is not trivial and requires a careful analysis of the plasma dynamics.

4 RADIAL-AZIMUTHAL INSTABILITES

The present chapter details the findings of our radial-azimuthal simulations. The first section reports several simulations aimed at studying the development of the modified two-stream instability (MTSI) and its impact on plasma dynamics, namely on the electron temperature and anomalous transport. The subsequent section focuses on presenting the key outcomes of the PIC radial-azimuthal benchmark, carried out as part of the LANDMARK project.

Chapter contents

4.1 Radial-azimuthal PIC simulations 82
4.2 Analysis of MTSI 82
4.2.1 The PIC model 83
4.2.2 Methods used for the analysis of PIC results 84
4.2.3 Study of the onset of MTSI in PIC simulations 85
4.2.4 Effect of the dimension of the computational domain on the MTSI 87
4.2.5 Influence of the domain the azimuthal length 88
4.2.6 Impact of plasma density and axial electric field on the MTSI 90
4.2.7 Summary of results, comparison with previously published results and discussion 92
4.2.8 Evolution of the plasma properties with the MTSI 95
4.3 Radial-azimuthal benchmark 100
4.3.1 Test case description 101
4.3.2 Selected benchmark results: electron temperature, plasma density and frequency analysis 102
4.4 Chapter summary 105

The results in this chapter have been partially published in Refs. [177, 180].

4.1 RADIAL–AZIMUTHAL PIC SIMULATIONS

In 2004, Adam *et al.* [55] proposed a model that accounted for azimuthal plasma dynamics as being responsible for the anomalous transport. In recent years, Lafleur and colleagues have published several papers [106, 105, 118, 117, 133] exploring the role of instabilities in enhancing electron transport. These papers have underscored the significance of the azimuthal direction in determining the plasma dynamics within HTs.

In our group at LPP, numerous efforts have been conducted to study the plasma dynamics with radial-azimuthal simulations. This work was initiated by Vivien Croes [112], who first designed the radial-azimuthal version of *LPPic*. These radial-azimuthal simulations allowed us to demonstrate [113] that the azimuthal instabilities developing at a fixed axial position contribute significantly to the increased axial transport. They demonstrated that the wall-plasma interactions only have an auxiliary role in the anomalous transport in the configuration investigated. The radial-azimuthal PIC simulations used by Tavant [152] analyzed the effect of the dielectric walls and the SEE on the plasma characteristics and sheath development [136, 153].

The importance of the radial-azimuthal simulations is largely recognized by the cold plasma $\mathbf{E} \times \mathbf{B}$ community [150, 160] and several works were published in the last decade [94, 116, 113, 129, 151, 164]. In 2021 a benchmark [180] proposed by LPP and CERFACS (viz., lead by Willca Villafana) brought together seven different groups to compare their PIC radial-azimuthal results. This test case allowed to demonstrate the presence of instabilities and to address some specific numerical aspects (e. g., particle convergence) of the radial-azimuthal simulations. The results of this benchmark are briefly presented at the end of this chapter.

The benchmark test case raised some questions about the instabilities that develop in radial-azimuthal simulations. Besides the well-known ECDI, a longer wavelength instability was observed. This instability was identified as the MTSI. Once the instability nature was confirmed, we wondered why such instability was present in some simulations and not in others and which were the consequences of the MTSI on the plasma dynamics. This question is addressed in the present chapter and was the subject of a publication in 2021 [177].

4.2 ANALYSIS OF MTSI

As we have seen in Chapter 2, in addition to the ECDI, another type of electrostatic instability having a component along the magnetic field is present in the radial-azimuthal plane of a HT: the MTSI [16, 19]. The MTSI is an electrostatic instability that appears under homogeneous plasma conditions (i. e., without density gradients) and is caused by the $\mathbf{E} \times \mathbf{B}$ differential drift between magnetized electrons and unmagnetized ions. As compared to the ECDI, it has a lower frequency and its component along the drift direction appears at longer wavelengths (in HT conditions, approximately 1 MHz and 5 mm). In addition, the MTSI has a component along the magnetic field, unlike the ECDI that is completely perpendicular to $\mathbf{B}$. The MTSI has

been found in simulations of collisionless shocks [16, 91] and, more recently, in simulations of $\mathbf{E} \times \mathbf{B}$ discharges [129, 163].

Janhunen *et al.* [129] studied the MTSI under typical HT conditions by calculating the dispersion relation with unmagnetized ions and magnetized electrons. The MTSI resonance peak was identified at low azimuthal wavenumbers with a radial component. Using a radial-azimuthal PIC simulation, they studied the MTSI characteristics and its coupling with ECDI modes. Nevertheless, in their work, the simulations do not reach a steady-state since absorbing walls were used without an ionization source and, hence, the plasma density was decreasing over time.

The presence of the MTSI in HTs is still not well understood as it has only been observed recently [129, 151] and not in previous radial-azimuthal PIC simulations [94, 113, 112, 136, 144]. The numerical noise due to a poor particle resolution was invoked as a possible explanation for this disagreement [128]. However, a recent study has shown that the convergence of PIC simulations with the number of particles in 2D is not as demanding as in 1D [140]. As a consequence, heretofore, there is not full agreement on the conditions for the appearance of the MTSI in 2D $\mathbf{E} \times \mathbf{B}$ PIC simulations and its impact on the discharge at steady-state.

In this chapter, we aim at clarifying the conditions for the development of the MTSI, by comparing the theoretical MTSI dispersion relation with PIC simulations under different setups that are relevant for HTs. Through these simulations, we identify the configurations that favor the growth of the MTSI by changing the azimuthal and radial lengths of the simulation domain, the plasma density, and the electric field intensity. As opposed to previous works, we achieve steady-state solutions by using reflecting walls in the radial direction, as previously done by Sengupta *et al.* [164]. This allows us to study in detail how the MTSI affects the discharge behavior at steady-state and its impact on the electron temperature, axial electron mobility, and k-spectrum.

4.2.1 The PIC model

In the current chapter, we consider a radial-azimuthal simulation of a plane of a HT with a 2D Cartesian mesh, as described in Section 3.2.2. A magnetic field $\mathbf{B}$ is imposed in the radial z direction while an electric field $\mathbf{E}$ is imposed in the axial x direction, which is perpendicular to the simulation plane. The plasma is assumed to be composed only of singly-charged xenon ions and magnetized electrons. Figure 4.1 shows a schematic representation of the simulation domain, in which the snapshot represents the axial current density with the MTSI modulation.

In the radial direction, the domain is bounded by two reflecting walls at a fixed potential $\Phi = 0$. At the reflecting walls, the particles impinging the boundary are reflected specularly, as done previously in Refs. [149, 164]. The use of these boundaries has two major advantages. (i) A steady-state is reached without the need for an artificial re-injection of particles, which may impact the development of the instabilities. The mean plasma density remains constant throughout the simulation, whereas the steady-state for energy is reached after around $5 - 10$ µs. (ii) The absence of the sheaths simplifies the physics at the system boundaries.

Despite the simulations being in 2D (radial-azimuthal), the evolution of the plasma in the axial direction is also treated to reach a steady-state. This kind of axial virtual model has been widely used before, both in 1D and 2D [113, 112, 105]. Even though

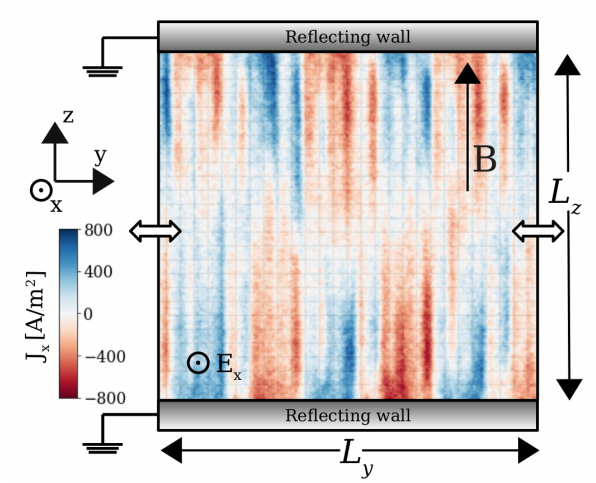


Figure 4.1: Schematic representation of the radial-azimuthal (zy) simulation domain, with periodic boundary conditions in $y-$direction and two perfectly reflecting walls at the edges of the z one. The snapshot represents the axial current density at 1.5 µs in a simulation domain 1.28 cm × 1.28 cm. Figure from Petronio *et al.* [177].

there is only one cell in the axial direction, two boundaries in this direction are considered at $x = 0$ and $x = L_x$. When one particle crosses one of these boundaries, another is re-injected at the other side at the same radial and azimuthal position with a velocity sampled from a Maxwellian flux distribution at the initial temperature. By doing this, the total energy of the plasma saturates after some time, which allows the simulation to reach a steady-state.

The physical and numerical parameters, if not otherwise stated, are presented in Table 4.1. The dimensions L_y and L_z will be varied in our study whereas the axial length L_x is fixed to 2 cm. As compared to previous works [136], in the present work, we aim at studying the evolution of the plasma oscillations with a larger azimuthal domain. Collisional processes and wall secondary-electron emission are not taken into account. As a result, the mean density of electrons and ions remains constant and equal to the initial one during the simulation. The electron-neutral collisions do not interfere with the instability mechanism [129]. Their collision frequency [110] ($\nu_{e,n} \sim 5$ MHz) is below the observed [129] growth rate of MTSI ($\gamma \sim 10$ MHz). The effect of the collisions at a steady-state is not investigated in this work. Statistical convergence has been tested by increasing the average number of particles per cell (N/NG) up to 400, without any major effect on the discharge characteristics. Numerical parameters have been chosen to satisfy the electrostatic PIC stability conditions as reported by Birdsall and Langdon [23], discussed in Section 3.2.1.

4.2.2 Methods used for the analysis of PIC results

The ECDI and MTSI can appear simultaneously in our PIC simulations. To study separately their characteristics, we use here 2D FFT of the azimuthal electric field E_y. The FFT is calculated both in the $k_y - k_z$ and in the $k_y - \omega$ phase spaces. As

Table 4.1: Operating and numerical parameters used in PIC simulations. No scaling permittivity is used.

Physical parameter	Symbol	Value	Unit
Radial magnetic field	B	200	G
Axial electric field	E_x	1×10^4	V/m
Axial length	L_x	2	cm
Gas		Xenon	(-)
Initial plasma density	n_0	5×10^{16}	m^{-3}
Initial electron temperature	T_e	10	eV
Initial ion temperature	T_i	0.5	eV
Neutral pressure	P_n	0	(-)
Simulation parameters			
Time step	Δt	1.5×10^{-12}	s
Cell size	$\Delta y = \Delta z$	5×10^{-5}	m
Initial number of particles per cell	N/NG	100	particles/cell
Number of iterations between outputs	N_a	1000	(-)

we discussed in Section 2.3.1, the FFT here is adapted, because periodic boundary conditions are employed in the azimuthal direction and specular grounded walls are used in the radial direction.

In order to get the MTSI growth rate γ^{PIC}, we calculate the FFT of E_y at every $N_a = 1000$ time steps, obtaining a 2D $k_y - k_z$ map. Once the ECDI and MTSI modes are identified in the map, we determine the MTSI amplitude in the spectrum and we plot it as a function of time. We determine its growth rate γ^{PIC} with a linear regression of the MTSI mode amplitude. Similarly, for the MTSI frequency ω_r^{PIC}, we use a FFT in the $k_y - \omega$ plane, at the radial position $z = L_z/4$. To stay away from the nonlinear saturation part of the simulation, we perform the FFT on an interval of 2 µs starting when the MTSI starts to grow. However, this time corresponds to only two or three periods of the MTSI, which results in a rough estimation of ω_r^{PIC}.

The MTSI has been observed to cause significant heating in the radial direction [129, 16]. In this chapter, we study the evolution of the mean radial electron temperature, $T_{e,z}$, that is computed at each grid point from the second moment of the distribution function and averaged over the whole simulation domain.

4.2.3 Study of the onset of MTSI in PIC simulations

In Section 2.2.3, we have proposed an analytical expression to locate the MTSI resonance peak in the wavenumber phase space. Here, these results are compared to 2D radial-azimuthal PIC simulations to identify in which configurations the MTSI grows. Table 4.2 contains a list of all the simulations that are analyzed in this section. We recall that the DR has been calculated in the limit $T_e \to 0$, while the results presented here are obtained at $T_e > 0$. The finite electron temperature may cause a broadening

Table 4.2: The simulation cases from 1 to 5 are analyzed in Section 4.2.4, from 6 to 14 in Section 4.2.6 and from 15 to 17 in 4.2.7. The simulation parameters are the ones specified in Table 4.1 if not otherwise stated. If present, $\tilde{\gamma}^{PIC}$ and $\tilde{\omega}_r^{PIC}$ represent the growth rate and the frequency of the MTSI, respectively.
[1]Initial density, $n_0 = 2 \times 10^{17}$ m^{-3}.
[2]Axial electric field, $E_x = 3 \times 10^4$ V/m.

Case number	L_y [cm]	L_z [cm]	$\tilde{\gamma}^{PIC}$	$\tilde{\omega}_r^{PIC}$
1	1.28	0.96	0.078	0.366
2	1.28	1.28	0.101	0.366
3	1.28	1.92	0.181	0.244
4	1.28	2.56	0.368	0.366
5	1.28	3.84	0.157	0.366
6	0.24	0.96	No MTSI	
7	0.48	0.96	0.067	0.244
8	0.24	1.28	No MTSI	
9	0.48	1.28	0.162	0.366
10	0.32	1.92	No MTSI	
11	0.64	1.92	0.202	0.244
12	0.32	2.56	No MTSI	
13	0.64	2.56	0.403	0.366
14	2.56	2.56	0.338	0.366
15[1]	0.64	2.56	0.369	0.366
16[2]	0.64	2.56	No MTSI	
17[2]	1.28	2.56	0.444	0.244

of the MTSI resonance peak, making the condition Eq. (2.16) less stringent. So, it is possible to observe the MTSI characterized by wavenumbers not strictly verifying this inequality, but such that

$$k_z \sim \frac{m_e E_x}{eB^2} k_y^2.$$

As an example, in Figure 4.2, we show the evolution of the azimuthal electric field during the onset of the ECDI and MTSI for a representative case (case no. 3). As it can be seen, the two modes mainly propagate in the azimuthal direction: one at a small wavelength and high frequency which corresponds to the ECDI, and another one at a larger wavelength that corresponds to the MTSI. As the growth rate of the ECDI is larger, it appears first, whereas the MTSI is visible after $\sim$1 µs. As it can be noted, the MTSI mode has a radial component, while ECDI does not. Specular reflection at the walls prevents the formation of the sheaths, which helps to estimate the wavenumber k_z of the MTSI mode along the magnetic field direction (z). In most of our simulations, we observe a half-wavelength between the upper and lower boundaries, with a node at $z = L_z/2$ and two anti-nodes at $z = 0$ and $z = L_z$, corresponding to a radial

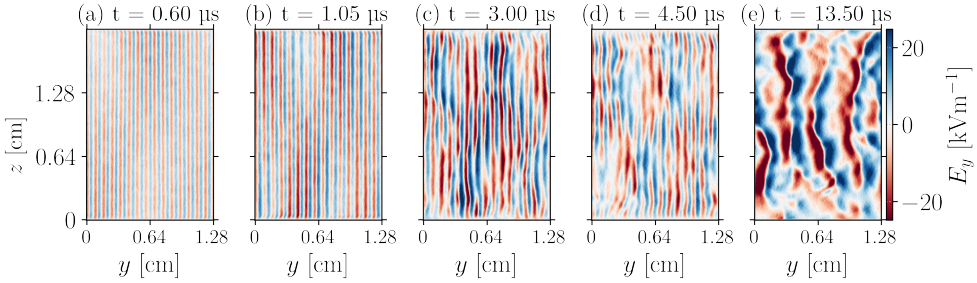


Figure 4.2: Snapshots of the azimuthal electric field in case no. 3. In (a) we observe the ECDI. The MTSI appears in (b). Figures (c) and (d) show the transition to a chaotic behavior of the system. Adapted from [177].

wavenumber $k_z = \pi/L_z$. After some microseconds, both oscillations are no longer in a linear regime, which results in a more chaotic regime with mainly large wavelength structures. In this section, we primarily focus on the linear regime of the instabilities.

4.2.4 Effect of the dimension of the computational domain on the MTSI

4.2.4.1 Influence of the domain radial length

As explained in Section 2.2.3, by changing the radial dimension of the simulation domain, the radial wavenumber $k_z = \pi/L_z$ of the MTSI DR varies. To quantify this effect on the instability, we vary the domain radial length L_z from 0.96 cm to 2.56 cm at constant domain the azimuthal length $L_y = 1.28$ cm. The temporal evolution of the MTSI amplitude of the azimuthal electric field for four different L_z is shown in Figure 4.3. Note that the growth rate of the MTSI is larger for increasing L_z. In addition, the value at which the electric field saturates is also larger for increasing L_z.

In these PIC simulations, the growing modes correspond to the unstable mode, compatible with the PIC boundary conditions, which is the closest to the MTSI peak, as predicted by the analytical formula of Eq. (2.15). Therefore, Eq. (2.15) can be regarded as a useful prediction of the wavelength of the fastest growing MTSI. The values of growth rate and frequency resulting from the PIC are different from those calculated with the fluid DR. Even if it is difficult to find a precise trend, the PIC growth rate appears to be 50% to 80% lower than the fluid one. The reason for this discrepancy can be attributed mainly to the $T_e = 0$ of the fluid DR and other kinetic effects that are present in the PIC simulation. Additionally, the MTSI frequency is inferred at 2 µs after the instability grows, which corresponds only to a few oscillation periods. As the instability grows to a nonlinear regime after a few periods, it is difficult to calculate the frequency accurately.

For large enough values of L_z, the largest growing MTSI mode can have an entire wavelength in the radial direction. In Figure 4.4, we show two cases with the same azimuthal length and different radial lengths: one with $L_z = 3.84$ cm (case no. 5, shown in panel (a)) and another with half this length ($L_z = 1.92$ cm, case no. 3, shown in panel (c)). As it can be seen, the case with a larger radial length shows an MTSI mode that has an entire wavelength in the radial direction whereas the other case has

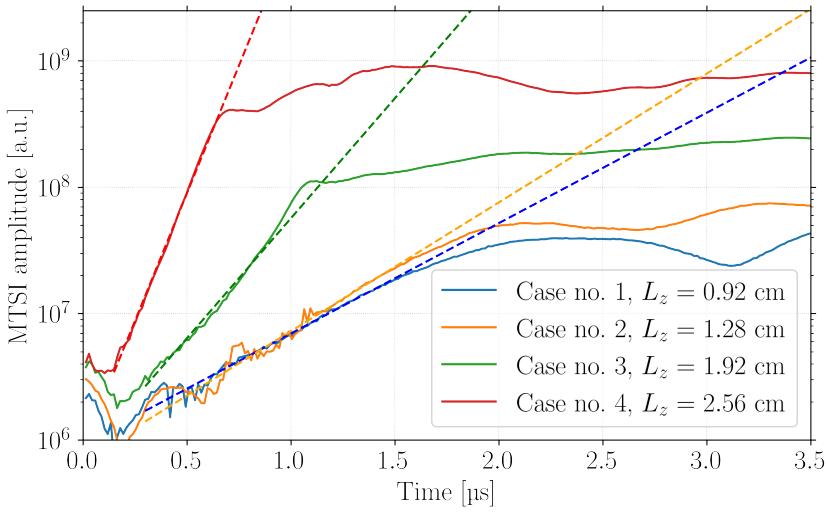


Figure 4.3: Evolution of the MTSI amplitude mode calculated from the E_y spectrum of four PIC simulations with different radial lengths. The linear regressions used to calculate $\tilde{\gamma}^{PIC}$ are shown by the dashed lines. The azimuthal length is 1.28 cm for all the cases shown here. Adapted from [177].

an MTSI with half wavelength in the radial direction. Interestingly enough, in both cases, the instability has the same k_y and k_z and, as shown in panel (b) of Figure 4.4, a similar growth rate. The delay in the growth could be due to the random initial distribution of particles.

4.2.5 Influence of the domain the azimuthal length

As explained in Section 2.2.3, the periodic boundary conditions in the azimuthal direction play an important role in the selection of the azimuthal wavelength of the MTSI. As a matter of fact, the azimuthal length may be too small to fit any k_y in the unstable region. This results in a simulation that spuriously does not develop the MTSI, as it is explained in the following.

The azimuthal boundary conditions select the modes such that $k_y = 2\pi m/L_y$ where m is a positive integer. To illustrate the effect of the azimuthal length on the MTSI, for the set of L_z studied in the previous section, we perform two different simulations: one with the azimuthal length smaller than the wavelength at the MTSI resonance and another one with the azimuthal length larger than the wavelength at the MTSI resonance. With reference to Table 4.2, we can see that the selection of the azimuthal domain length can have a dramatic influence on the simulation, precluding the formation of the MTSI when it is too small. Conversely, the MTSI in the PIC simulations behave as expected from the DR if the azimuthal domain length is large enough.

The effect of the azimuthal domain length on the instabilities is illustrated in Figure 4.5. In this figure, we show 2D snapshots of the azimuthal electric field E_y for three PIC simulations with the same radial length ($L_z = 2.56$ cm) but different azimuthal lengths L_y (from 0.32 cm to 2.56 cm). For too small L_y, only the ECDI

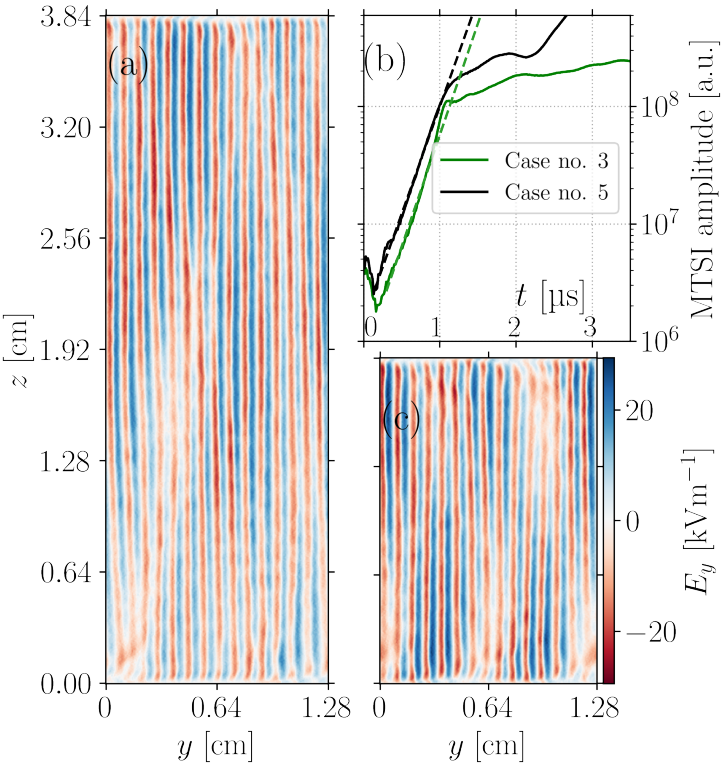


Figure 4.4: 2D snapshots of the azimuthal electric field E_y at $t = 1.5\,\mu s$ for (a) $L_z = 3.84\,cm$ (case no. 5) and (c) $L_z = 1.92\,cm$ (case no. 3). In (b): evolution of the MTSI mode amplitude in the E_y spectrum. The dashed lines in (b) represent the linear regression calculated during the instability growth. Adapted from [177].

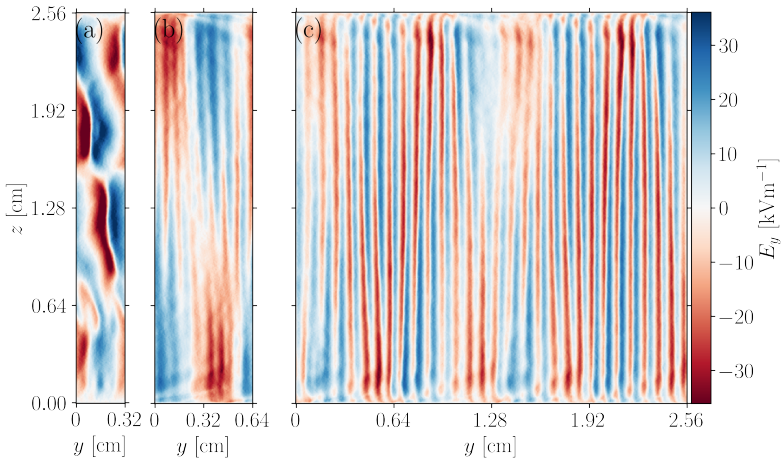


Figure 4.5: Snapshots ($t = 1.20\,\mu s$) of E_y for three different PIC simulations with $L_z = 2.56\,cm$. (a): $L_y = 0.32\,cm$, only ECDI (case no. 12). (b): $L_y = 0.64\,cm$, one MTSI period (case no. 13). (c): $L_y = 2.56\,cm$, four MTSI periods (case no. 14). Adapted from [177].

develops, while in the other two cases, the MTSI is also present. One can note that the same mode of MTSI develops in the cases (b) and (c) of Figure 4.5, although more periods of the same wave are captured in the case with a larger azimuthal domain.

In Section 4.2.4.1, we observed that the growth rate strongly depends on the value of the radial wavenumber. Here, we show that the MTSI can disappear if the azimuthal length is reduced below a certain threshold. Moreover, we observed that once this threshold is reached, the MTSI characteristics (wavelength and growth rate) are not affected if the domain is large enough in the periodic azimuthal direction.

4.2.6 Impact of plasma density and axial electric field on the MTSI

As explained in Section 4.2.1, the mean plasma density and axial electric field are imposed. As these two parameters vary along the axis of the thruster, in this section, we investigate their impact on the MTSI.

4.2.6.1 Influence of the plasma density

In the simplified dispersion relation, Eq. (2.14), the dependency of the MTSI dispersion relation on the plasma density is lost. It has been checked with the numerical solution of Eq. (2.12) that the plasma density has no impact on the MTSI on-set in our $k_y - k_z$ range of interest, under the typical conditions for HTs. This observation has been verified with two PIC simulations with the same geometry: one with the baseline density ($n_0 = 5 \times 10^{16}$ m^{-3}, case no. 4) and one with an increased plasma density ($n_0 = 2 \times 10^{17}$ m^{-3}, case no. 15).

Figure 4.6 shows 2D snapshots of the azimuthal electric field for the two PIC simulations: the one with our baseline density in 4.6 (a) and the one with larger density in 4.6 (b). We can see that the same long-wavelength MTSI is present for both cases. Moreover, in 4.6 (c), we observe that the MTSI amplitude evolves with a similar

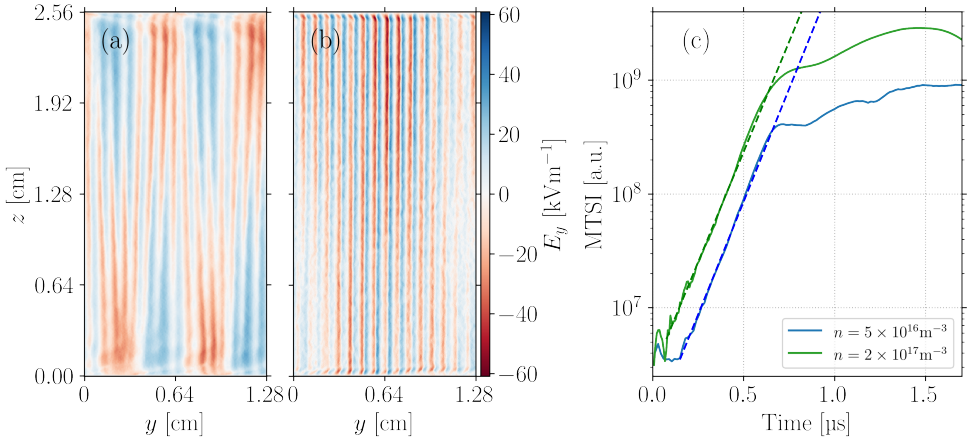


Figure 4.6: 2D snapshots of the azimuthal electric field E_y at $t = 1.20\,\mu s$ for (a) the nominal density $n = 5 \times 10^{16}\,m^{-3}$ (case no. 4) and (b) a larger density $n = 2 \times 10^{17}\,m^{-3}$ (case no. 15). In (c): evolution of the MTSI mode amplitude in the two cases. Adapted from [177].

growth rate of $\tilde{\gamma}^{PIC} = 0.369$. These PIC results agree with the conclusion drawn from the analytical dispersion relation: the MTSI does not depend on the plasma density. However, it is important to mention that the ECDI growth rate increases with the plasma density, as expected from Cavalier *et al.* [92], making it more difficult to observe the MTSI in denser plasmas.

4.2.6.2 *Influence of the axial electric field*

In Eq. (2.15), we showed that γ_{max} has a parabolic shape in $k_y - k_z$ space and that the leading coefficient is proportional to E_x/B^2. Therefore, the resonance peak depends on the electric and magnetic fields. In this section, we study the impact of varying the axial electric field E_x, with a constant magnetic field.

First, we calculate the DR with different axial electric fields. Figure 4.7 (a) shows the position of the maximum of $\tilde{\gamma}$ for different values of the electric field. Figure 4.7 (b) shows the corresponding growth rate for a fixed radial wavenumber. As the electric field increases, the MTSI peak shifts towards low azimuthal wavenumbers, and the growth rate increases. Additionally, we compare the position of γ_{max} with the simplified analytical expression of Eq. (2.15), showing good agreement.

To confirm these results with PIC simulations, we compare a case with the baseline electric field $E = 10\,kV/m$ (case no. 13) with the MTSI to a case with a higher electric field $E = 30\,kV/m$ (case no. 16). From our previous analytical studies, we expect that no MTSI grows in the latter case since the MTSI peak is shifted towards smaller k_y and the azimuthal wavelength of the MTSI is too large to fit in the domain. Figure 4.8 (a) and (b) show 2D snapshots of the azimuthal electric field corresponding to these two cases. We observe that while the MTSI modulation is visible for the baseline case, we observe only the ECDI for the case with a higher axial electric field, as expected. Nevertheless, as explained previously, if L_y is large enough to fit the wavelength of the MTSI, it appears in our PIC simulation. In Figure 4.8 (c), we reproduce the simulation

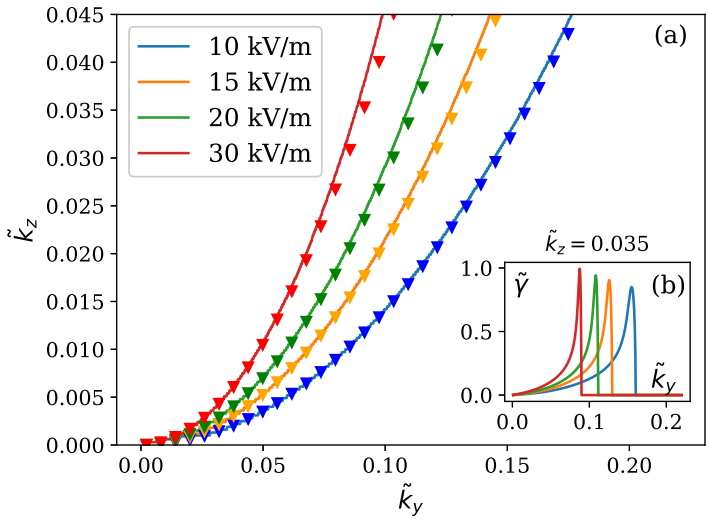


Figure 4.7: In (a) the full lines show the position $(\tilde{k}_y, \tilde{k}_z)$ of the maximum of $\tilde{\gamma}$ for different axial electric field calculated from the fluid DR Eq. (2.12). The triangles show the position of $\gamma_{\max}$ obtained with the simplified analytical DR Eq. (2.15). In (b) we show the growth rate $\tilde{\gamma}(\tilde{k}_y)$ for $\tilde{k}_z = 0.035$ for different values of the axial electric field. Adapted from [177].

at higher electric field with $L_y = 1.28\,\text{cm}$ instead of $0.64\,\text{cm}$. As the domain is large enough to fit the MTSI azimuthal wavelength, the MTSI appears. Additionally, its azimuthal wavelength is approximately twice larger than that in the case with the same domain dimensions and baseline electric field (case no. 4, in Figure 4.6 (a)), which is also in agreement with the prediction of Eq. (2.15).

4.2.7 Summary of results, comparison with previously published results and discussion

So far, we have extensively studied the linear regime and compared the results to the analytical expression that was derived in Section 2.2.3. In Figure 4.9, we show a summary of the simulation cases in the (k_y, k_z) phase space together with the position of maximum growth rate as expected with the conditions of Table 4.1. We see that the cases where the MTSI was observed are close to the parabola described in Eq. (2.15) that delimits the maximum growth rate of the MTSI. Alternatively, the purple bullets represent the allowed couples $(\tilde{k}_y, \tilde{k}_z)$, corresponding to one half-wavelength radially and a single wavelength azimuthally, for the cases where MTSI is not observed. These points are all in the stable region and far from the singularity. Despite there are some of the cases with MTSI that are in a stable region (but close to the frontier), the temperature may induce a broadening of the resonance peak, allowing the growth of the MTSI under conditions where the fluid DR with $T_e = 0$ is stable.

In the following, we extend these conclusions to previously published works presenting radial-azimuthal PIC simulations. For this purpose, we consider the condi-

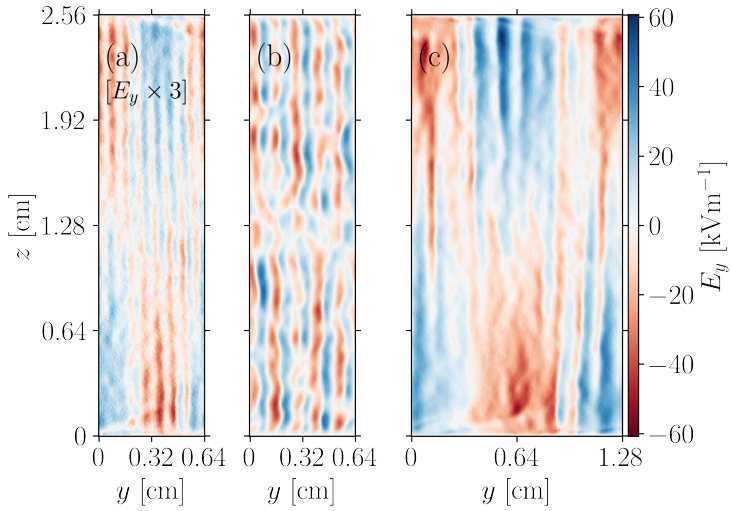


Figure 4.8: 2D snapshots of the azimuthal electric field E_y at $t = 1.20\,\mu s$ if (a) $E_x = 10\,kV/m$ and $L_y = 0.64\,cm$ (case no. 13), (b) $E_x = 30\,kV/m$ and $L_y = 0.64\,cm$ (case no. 16) and (c) $E_x = 30\,kV/m$ and $L_y = 1.28\,cm$ (case no. 17). Notice that in (a) E_y is magnified by a factor 3. Adapted from [177].

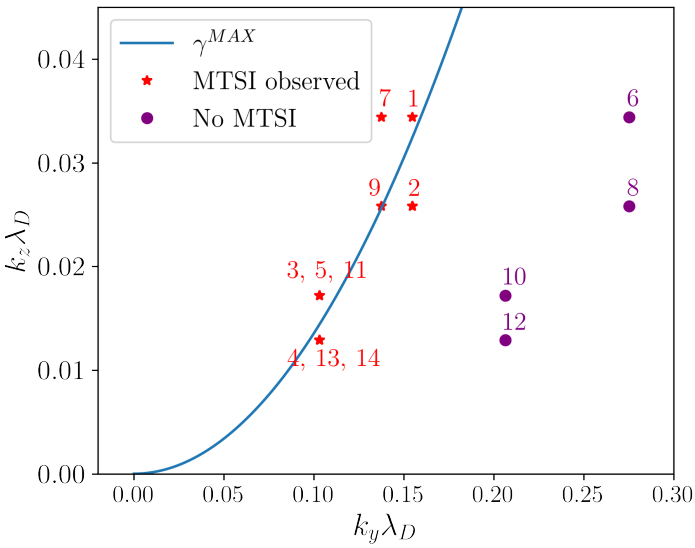


Figure 4.9: The blue line shows the instability limit in Eq. (2.15). The red points represent the couples $(\tilde{k}_y, \tilde{k}_z)$ for which the MTSI is observed. Next to each point, we report the related simulation labels. The purple points represent the allowed couples $(\tilde{k}_y, \tilde{k}_z)$, corresponding to a half-wavelength radially and a single wavelength azimuthally, in the cases where MTSI is not observed. Notice that cases no. 4, 13, 14 and no. 3, 5, 15 correspond to the same point. The details about each simulation are reported in Table 4.2. Adapted from [177].

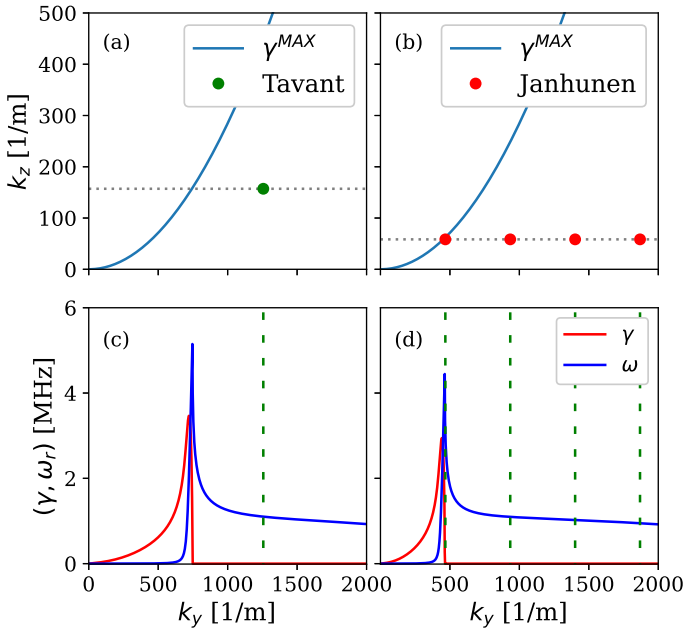


Figure 4.10: Positions of the maximum of γ (blue line), calculated with the simplified analytical DR Eq. (2.15), and allowed (k_y, k_z) (bullet points) using the parameters of (a) Tavant *et al.* [136] (couple with half-wavelength in the radial direction and one in the azimuthal direction) and (b) Janhunen *et al.* [129] (couples for half-wavelength in the radial direction and one, two, three and four wavelengths of MTSI in the azimuthal direction). The numerical fluid DR calculated from Eq. (2.12) for the value of k_z imposed by the boundary conditions is shown for (c) Tavant *et al.* [136] and (d) Janhunen *et al.* [129]. The dashed green lines correspond to the allowed k_y, imposed by the periodic boundary conditions. Since the density used in these cases is different, the results are not normalized. From [177].

tions used by Tavant *et al.* [136], where the MTSI was not observed, and these used by Janhunen *et al.* [129], where the MTSI was reported. In Figure 4.10 we show the position of the maximum growth rate, as calculated by the simplified DR, and the explicit resonances allowed by the periodic boundary conditions used in the azimuthal direction. In Figure 4.10 (a) and (c), we see that the k_y allowed by the boundary conditions in Tavant *et al.* is larger than the MTSI resonance peak, which explains why they did not observe any MTSI long-wavelength structures. Alternatively, Janhunen *et al.* observed one MTSI period in the azimuthal direction, which is in perfect agreement with the results of Figure 4.10 (b) and (d) as one of the resonances has a wavelength equal to the value at maximum growth rate.

In conclusion, Eq. (2.15) is a very useful analytical expression to determine if the PIC domain allows the MTSI to grow. Moreover, it also captures the dependence of the MTSI upon the physical conditions, i.e., density and imposed electric field.

4.2.8 Evolution of the plasma properties with the MTSI

We now study the impact of the MTSI on some macroscopic parameters of the discharge. First, we study the impact on the electron heating in the radial direction. Secondly, the effect of the MTSI on the anomalous electron mobility in the axial direction. For these studies, we compare cases with the same radial domain length L_z and two different azimuthal lengths L_y: one that is large enough to capture the MTSI and the other that is too small to develop the MTSI but large enough to capture the ECDI. Finally, we analyze the nonlinear regime in a case with a wider azimuthal dimension.

4.2.8.1 Evolution of the electron radial temperature

As noted by McBride [16], as the MTSI has a radial component, it produces a strong heating in the radial direction. In Figure 4.11, we show the evolution of the mean radial temperature $T_{e,z}$ for four cases, two with MTSI (red lines) and two without (blue lines). Note that the reflecting walls prevent any dissipation of energy in the radial direction and, hence, this results in radial heating in all cases. The saturation of the average energy is obtained only thanks to the axial convection model, as proposed by Lafleur *et al.* [105]

During the transient phase ($0 < t < 4.5\,\mu s$), when the instabilities are easy to distinguish, we can see in Figure 4.11 that heating in the radial direction starts much earlier in the cases with MTSI (red lines, cases no. 11 and 13) than without. Additionally, the case with the largest MTSI growth rate (solid red line) presents the largest heating. Alternatively, in the cases without MTSI, (blue lines, cases no. 10 and 12) the temperature does not depend on the radial length during the transient state. After the linear growth of the MTSI, the system becomes more chaotic and Figure 4.11 shows that the electron temperature in the radial direction at saturation is similar in cases with and without MTSI.

4.2.8.2 Mobility

The axial electron mobility $\mu = -u_{e,x}/E_x$, i.e., perpendicular to the yz simulation plane, is a crucial parameter in HT. Several studies have been conducted to relate the anomalous mobility and the instabilities propagating in the thruster [133, 106, 118, 105]. Recent studies [118, 138, 156] have observed that the ECDI enhances the transport in the axial direction. Here, we show that the long wavelength MTSI oscillations also contribute to this transport. Following the work of Lafleur *et al.* [105], it is possible to write the anomalous mobility as a function of the correlation between the oscillations of the azimuthal electric field E_y and the electron density,

$$\mu_{\text{eff}} = \frac{\frac{|q|}{m\nu_m}}{1+\frac{\Omega_{ce}^2}{\nu_m^2}}\left[1-\frac{\Omega_{ce}\left\langle \delta n_e \delta E_y\right\rangle}{\nu_m n_e E_x}\right],$$

where ν_m is the electron-neutral collision frequency. In this work, no collisions are considered. The above equation hence simplifies to

$$\mu_{\text{eff}} = -\frac{\left\langle \delta n_e \delta E_y\right\rangle}{n_0 E_x B}. \tag{4.1}$$

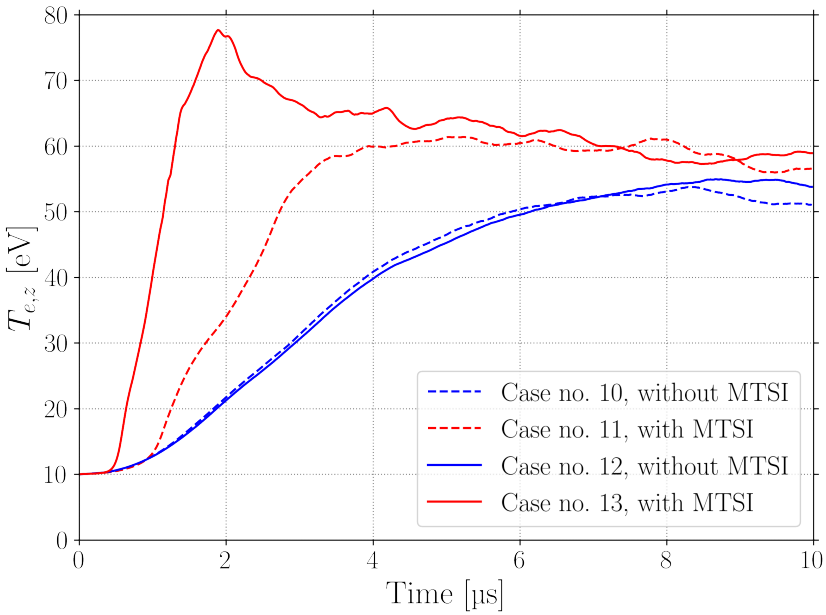


Figure 4.11: Evolution of the radial temperature for different PIC simulation cases with: $L_y = 0.64\,\text{cm}$ and $L_z = 1.92\,\text{cm}$ cm (case no. 10), $L_y = 0.32\,\text{cm}$ and $L_z = 1.92\,\text{cm}$ (case no. 11), $L_y = 0.64\,\text{cm}$ and $L_z = 2.56\,\text{cm}$ (case no. 12), $L_y = 0.32\,\text{cm}$ and $L_z = 2.56\,\text{cm}$ (case no. 13). The red lines correspond to cases for which the MTSI propagates. Adapted from [177].

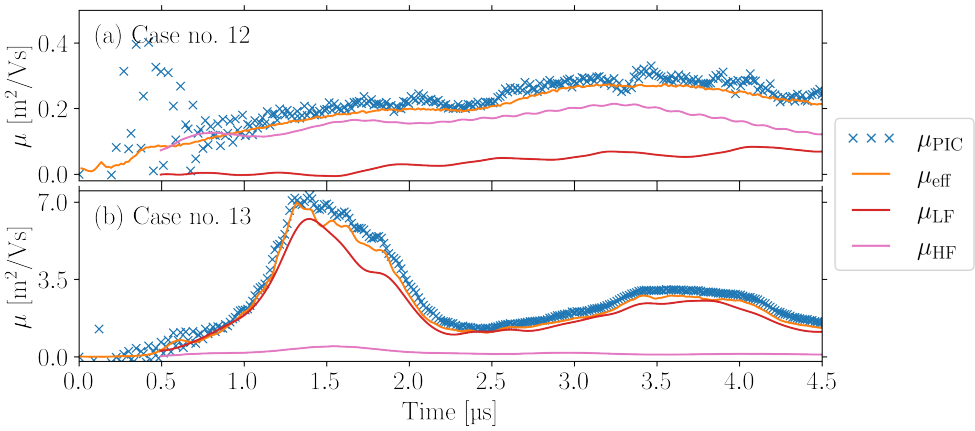


Figure 4.12: Axial mean mobility from the PIC (crosses), the correlation term (orange), or the DMD-decomposition (μ_{LF} red, μ_{HF} pink) during the simulation calculated for (a) case no. 12 without MTSI and (b) case no. 13 with MTSI. Adapted from [177].

To compare the influence of the MTSI on the mobility, we consider two cases, cases no. 12 and 13, without and with MTSI, respectively, during the transient phase ($0 \leq t \leq 4.5\,\mu s$) when the instabilities are easy to distinguish. Figure 4.12 (a) and (b) show that for the two cases, the measured PIC mobility is in good agreement with the effective mobility given in Eq. (4.1). We would like to highlight that this definition hence holds even in the presence of MTSI.

In order to understand how the different instabilities affect the mobility, we use a Dynamic Mode Decomposition (DMD) [80], i.e., a data-driven method that identifies the dominant spatial-temporal modes of a signal, as explained in the Chapter 2. Using this method, the total signal was divided into four frequency packets: the first one contains the low-frequency continuous components, the second one gathers the components near the MTSI frequency (between 0.1 and 3 MHz), the third one gathers these near the ECDI frequency (between 3 and 5 MHz) and the fourth one gathers these near to the second resonance of the ECDI frequency (between 5 and 7 MHz). By using this decomposition, we calculated the mobility corresponding to each packet using Eq. (4.1), where μ_{LF} is the mobility related to the range of frequencies around the MTSI and μ_{HF} is this related to ECDI. Figure 4.12 shows the mobility associated with the different modes for one case without MTSI (case no. 12 shown in panel (a)) and one case with the MTSI (case no. 13 shown in panel (b)). The mobility related to the second resonance of the ECDI is not shown since it is negligible. We verified in both cases that the sum of μ_{LF} and μ_{HF} corresponds almost perfectly to the measured PIC mobility.

In Figure 4.12 (a), for the case without MTSI we observe that up to $t = 3\,\mu s$, the main contribution to the mobility μ_{PIC} is due to μ_{HF}, corresponding to the ECDI. For $t > 3\,\mu s$, μ_{LF}, corresponding to the low-frequency components traveling at a frequency similar to MTSI start to play a significant role, making more difficult to distinguish the contribution of each mode as the discharge transits to a more chaotic mode. When the MTSI is present, in Figure 4.12 (b), we note that up to 4.5 µs, the mobility is completely dominated by the MTSI ($\mu \sim \mu_{LF}$). It is interesting to point out

that during this transient phase ($0 < t < 4.5\,\mu s$), in the case where the MTSI is present the mobility is one order of magnitude larger than the case without MTSI.

4.2.8.3 Nonlinear regime

Previous works [15] have found that nonlinear effects were playing a major role after some characteristic growth times. In our case, after the linear growth of the instabilities and their saturation, the system becomes more chaotic and the structures cannot anymore be identified as the superposition of only two modes, i.e., ECDI and MTSI.

The energy transition from short to long wavelength modes has been predicted theoretically [107] and also observed numerically in 1D and 2D PIC simulations [129, 128]. We recall that in our PIC simulations the total energy is not conserved because the energy is constantly injected by the imposed axial electric field. Therefore, the steady-state is reached only thanks to the convection in the virtual axial direction. In Figure 4.13 (a), we show the k-spectrum of the azimuthal electric field at $z = L_z/2$ for case no. 3. In the spectrum, for $t < 10\,\mu s$, we can distinguish the MTSI, the ECDI, and the second resonance of the ECDI. At the beginning of the simulation, as the ECDI grows faster, most of the energy is carried by the ECDI, while the intensity of the MTSI is lower. Later, at $t = 10\,\mu s$, we observe a mode transition towards low-k modes with now a negligible quantity of energy carried by the ECDI modes. At this point, we observe a broad spread of energy over k_y. This time corresponds to a more chaotic state of the system with the presence of structures that mostly exhibit large azimuthal wavelengths.

The spectral analysis in the $\omega - k_y$ phase-space provides important insights into the nonlinear state of the system. Lafleur *et al.* [118] suggested that the discrete ECDI transitions to the IAW, due to a resonance broadening mechanism. This has never been studied in the presence of MTSI. The dispersion relation in the IAW limit presented in Chapter 2 is given as [106]

$$\omega_r \approx \mathbf{k} \cdot \mathbf{v_i} \pm \frac{k c_s}{\sqrt{1 + k^2 \lambda_{D*}^2}}, \tag{4.2}$$

$$\gamma = \pm \sqrt{\frac{\pi m_e}{8 m_i}} \frac{k_y v_0}{(1 + k^2 \lambda_{D*}^2)^{3/2}}, \tag{4.3}$$

where $\mathbf{v_i}$ is the ion drift velocity, $c_s = \sqrt{q T_e / m_i}$ is the sound speed and λ_{D*} is the electron Debye length calculated in the nonlinear regime. In the case analyzed here, the ion speed is negligible, thus Eq. (4.2) simplifies to

$$\omega_r \approx \pm \frac{k c_s}{\sqrt{1 + k^2 \lambda_{D*}^2}}. \tag{4.4}$$

In the limit $k\lambda_{D*} \ll 1$, the previous equation can be simplified to the linear sound relation between the frequency and the wavenumber,

$$\omega_r \approx \pm k c_s. \tag{4.5}$$

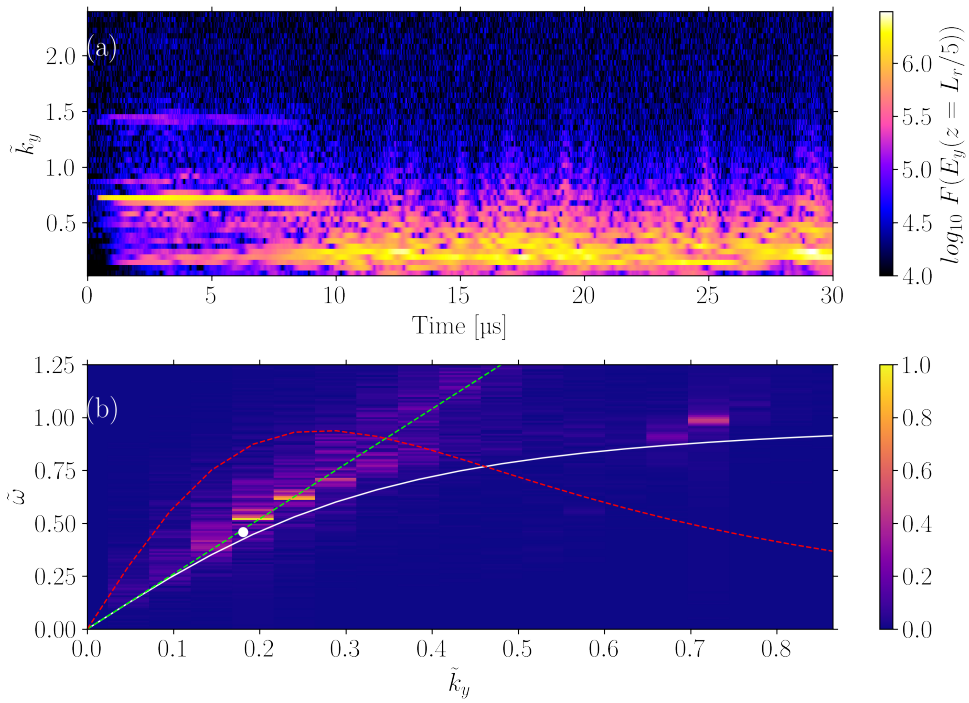


Figure 4.13: PIC case no. 3, with $L_y \times L_z = 1.28\,\text{cm} \times 1.92\,\text{cm}$. (a) Time evolution of the k-spectrum of the azimuthal electric field. (b) Normalized plot of the 2D FFT of the azimuthal electric field $E_y(y, z = L_z/2, t)$ with $y \in [0, L_y]$ and $t \in [20\,\mu\text{s}, 30\,\mu\text{s}]$. The solid white line shows the ion acoustic dispersion relation in Eq. (4.2), the dashed line shows the growth rate of the IAW, Eq. (2.9), magnified 25 times, the green line shows the linear sound relation as in Eq. (4.5). Adapted from [177].

In Figure 4.13 (b), we show the 2D FFT of the azimuthal electric field at $z = L_z/2$ between 20 and 30 µs for case no. 3. The linear dispersion relation for acoustic waves in Eq. (4.5) overlaps the observed instability spectrum. Moreover, the dominant wavenumbers observed correspond to the ones with the largest growth rate of Eq. (2.9). These results show that in the nonlinear regime the perturbations in the electric field travel at the sound speed, therefore a saturated IAW might be the dominant mode.

In the nonlinear stage, we do not observe significant variations in the electron temperature and axial mobility. In the case no. 3, the mean radial electron temperature grows during the linear regime and remains stable between 20 and 30 µs at $\sim 55\,\mathrm{eV}$ with a standard deviation $\sigma = 1.4\,\mathrm{eV}$. Similarly, in the same time interval, the mobility stabilizes to $\sim 1.4\,\mathrm{m^2/Vs}$ with fluctuation of the order of $0.2\,\mathrm{m^2/Vs}$. It is worth remarking that the absolute value of the mobility is considerably lower as compared to the values of $\sim 6\,\mathrm{m^2/Vs}$ obtained before by Tavant *et al.* [136] with a similar configuration. As they were imposing a higher axial electric field ($E_x = 20\,\mathrm{kV/m}$), their electron drift velocity was higher. The higher v_0 and the larger plasma density ($n_0 = 2 \times 10^{17}\mathrm{m^{-3}}$) used in their setup enhance the ECDI oscillations, which could explain their higher axial mobility.

4.3 RADIAL–AZIMUTHAL BENCHMARK

The validation of the codes against the experiments is a crucial, yet very difficult, task. Before we achieve validation, it is however necessary to perform a verification step, by performing a code-to-code comparison. In the low temperature plasma community, the 1D discharge benchmark by Turner *et al.* [96] is a reference for the verification of the PIC MCC modules and Poisson solvers. However, this benchmark is not representative of the HT conditions in a $\mathbf{E} \times \mathbf{B}$ thruster, which is more complex due to the presence of the magnetic field. Moreover, the very different motions of electrons and ions trigger numerous instabilities in HTs, that are not preset when using Turner's simulation setup. More recently, Charoy *et al.* [140] proposed a 2D axial-azimuthal benchmark, within the framework of the LANDMARK project [111], that successfully captured the main characteristics of the HT physics along the axial-azimuthal directions. However, the radial direction was not included in this benchmark. Thus, the purpose of the second benchmark proposed by LPP and CERFACS [180] was to model the plasma discharge in a radial-azimuthal section. The benchmark was conducted in 2020 and 2021 and brought together seven different groups to compare their PIC radial-azimuthal results, namely CERFACS from Toulouse (FR), LPP from Paris (FR), USASK from Saskatoon (CA), Stanford (US), ISTP from Bari (IT), RUB from Bochum (DE) and LAPLACE from Toulouse (FR). The test case was designed to be representative of the HT conditions in a $\mathbf{E} \times \mathbf{B}$ thruster at the channel exit. The test case is described in the following sections.

4.3.1 Test case description

The test case considered for the benchmark is composed of a cartesian grid, with squared cells, similar to the one described in Section 3.2.2, Figure 3.3. The azimuthal direction y is periodic, while the radial one z is bounded between two grounded walls, such that this time sheaths form. No dielectric layer is present in the simulation. The time step and the grid resolution are chosen according to Birdsall and Langdon [26] and the CFL condition is satisfied. The test case is composed of a quasi-neutral Xenon plasma with an initial density of $n_0 = 5 \times 10^{16}\,\mathrm{m}^{-3}$, an electron initial temperature of $T_e = 10\,\mathrm{eV}$, an ion temperature $T_i = 0.5\,\mathrm{eV}$, an axial electric field $E_0 = 1 \times 10^4\,\mathrm{V/m}$ and a homogeneous radial magnetic field of $B_0 = 200\,\mathrm{G}$. Only electrons and charged ions Xe^+ are considered in the simulation. The collisionless assumption was done, thus there was no need to consider a background plasma density. The numerical parameters are the ones reported in Table 4.1.

The particle losses at the walls (i. e., there is a Bohm flux of particles leaving the domain) are compensated by the injection of particles in a steady ionization profile. The ionization profile is chosen to be as similar as possible to one of the real devices: it has its maximum at the plasma bulk center and decreases towards the walls. The ionization profile $S(z)$ is given by

$$S(z) = S_0 \cos\left(\pi \frac{z - L_z}{z_2 - z_1}\right) \qquad \text{for } z_1 \leq z \leq z_2,$$
$$S(z) = 0 \qquad \text{for } z \leq z_1 \text{ or } z \geq z_2$$

with S_0 the maximum value of the source term, $z_2 - z_1$ the width of the ionization zone, and L_z is the channel width. The width of the ionization zone is set to be $\approx 1.1\,\mathrm{cm}$. The value of S_0 is chosen to compensate an average current density exiting at the wall of $100\,\mathrm{Am}^{-2}$, thus $S_0 = 8.9 \times 10^{22}\,\mathrm{m}^{-3}\mathrm{s}^{-1}$. More details about the way the number of particles' pairs is chosen and injected are given in the paper [180].

The virtual axis model

In Section 4.2.1 we addressed the importance of considering a third virtual dimension to limit the axial energy enhancement and reach a steady-state. For the benchmark test case, we used a model similar to the one discussed in Section 4.2.1 and in Refs. [106, 144, 138, 150, 113, 136]. However, some differences require to be pointed out. All particles are initialized at $x = 0$ (i. e., in the x direction the Poisson equation is not solved) with random radial and azimuthal coordinates. The particles are free to move, thus they are accelerated in the axial direction by the imposed electric field. The two virtual walls are located at $x = \pm L_x$: once a particle reaches the boundary it is removed from the simulation and a new particle with the same (y, z) coordinates is injected at $x = 0$ and its temperature is sampled by a Maxwellian distribution with fixed temperature. Here comes the main difference with the model discussed in Chapter 3. On one side, the ions are accelerated in the direction of the axial electric field and all of them are collected by the virtual wall at $x = +L_x$. On the other, most of the electrons, that are accelerated in the opposite direction, are collected by the wall at $x = -L_x$. However, some energetic electrons can gyrate along the magnetic field lines and reach the wall at $x = +L_x$, which was not possible using the model

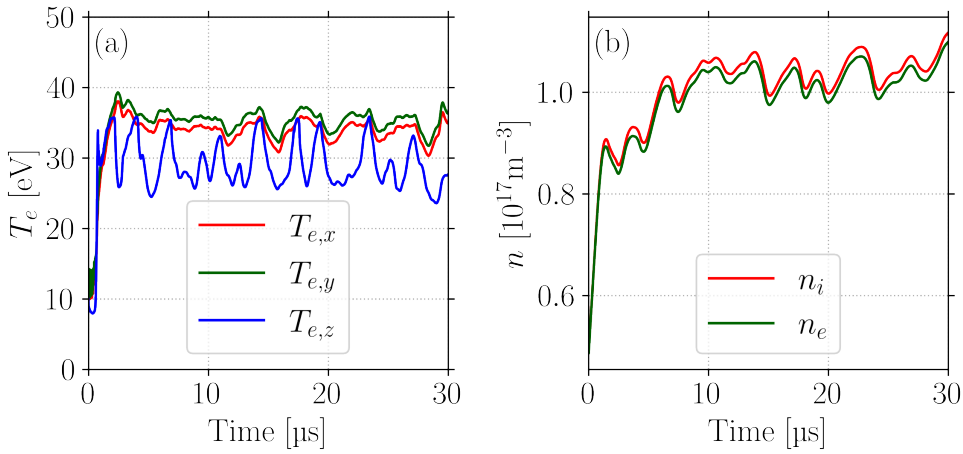


Figure 4.14: Temporal evolution of the plasma parameters in the radial-azimuthal benchmark case. (a) the mean electron temperature evolution in axial (x), azimuthal (y) and radial (z) directions. (b) the overall mean ion (n_i) and electron (n_e) densities.

discussed before. Doing several tests allowed us to notice that the choice of the virtual axis thickness and its model may strongly affect the plasma characteristics, in particular the electron temperature.

4.3.2 Selected benchmark results: electron temperature, plasma density and frequency analysis

For a complete discussion of the benchmark results, in particular for the discussion about the appearance of the ECDI and MTSI instabilities, the reader should refer to the paper [180]. Here, we study only the plasma parameters (temperature and density) and the frequency analysis. In Figure 4.14 we show the evolution of the electron temperature (a) and the electron and ion density (b). We observe that the temperature reaches its final value after a couple of microseconds: this is compatible with the travel time of the electrons between the center plane and the wall at which most of them are absorbed. After that, the temperature oscillates around a fixed value. We also observe that the fluctuations of temperature are rather high in the radial direction, while the temperature is stable in azimuthal and axial directions. These fluctuations are compatible with the variation of the MTSI intensity [180], which has been shown previously to provide heating of the electrons in the radial direction. The quasi-steady-state is reached after $\approx 10\,\mu s$: the mean density stabilizes, cf. Figure 4.14 (b), at a value of $\approx 1 \times 10^{17}\,m^{-3}$, but some oscillations are still present.

As mentioned before, an important characteristic of this simulation is the simultaneous presence of both the MTSI and of the ECDI. As discussed in Chapter 1 and 2, the ECDI is driven by the differential drift between electrons and ions, via the coupling of the IAW with the doppler-shifted Bernstein wave [11, 17]. The ECDI resonances occur at some specific values of the azimuthal wavenumber: $k_y = p\omega_{ce}/v_d$ with $p \in \mathbb{N}^+$ and $v_d = E_0/B_0$. As we have shown above, the typical MTSI wavenumber

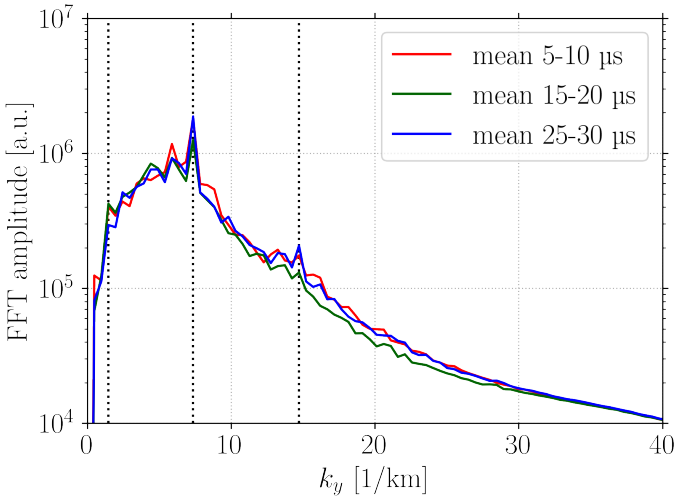


Figure 4.15: The FFT of E_y averaged radially over three different intervals. The vertical lines represent from left to right the peak of the MTSI, the peak of the ECDI first resonance, and the peak of the ECDI second resonance.

cannot be easily identified, but its value usually is well below the first ECDI resonance. In Figure 4.15 we report the FFT of E_y calculated in the azimuthal direction and averaged over every radial position and in time. What we observe is that it is possible to identify the low-k_y MTSI frequency and the first two harmonics of the ECDI at a slightly larger frequency. These mode characteristics have been retrieved by all the groups participating in the Benchmark [180].

To compare precisely the results, the ion density and electron temperature radial profiles (i. e., averaged azimuthally and in time) are reported in Figure 4.16. The time averaging interval is $25 - 30\,\mu s$. Both quantities show an excellent agreement between the codes, all the differences are within the $\pm 2.5\%$ of the mean value (i. e., reported by the red line in Figure 4.16).

Among the other studies, we performed a study about statistical convergence. Indeed, Okuda and Birdsall [13] have shown that a reduced number of superparticles can increase the number of numerical collisions (i. e., the numerical noise) in the PIC simulations. In Figure 4.17 (a) we report the mean final density as a function of the weight factor q_f and in (b) we report the corresponding axial profiles. One may remark that the markers in (a) have the same color as the corresponding line in (b). Figure 4.17 (a) shows that the weight factor should be no larger than $3 \times 10^6\,m^{-1}$. If it is the case, there is a significant deviation of the mean density from the converged value. This is also evident in (b), where the profiles of the cases with a low number of particles per cell are not converged to the good value obtained when the simulation has, on average, more than 100 particles per cell.

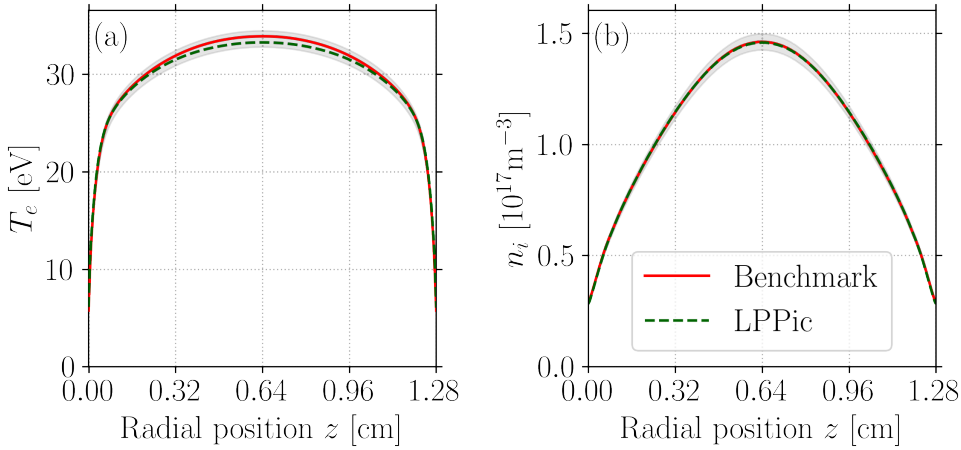


Figure 4.16: The radial (along z) average profiles of (a) the electron temperature and (b) the ion and electron density. The shaded areas represent a ±2.5% around the Benchmark value.

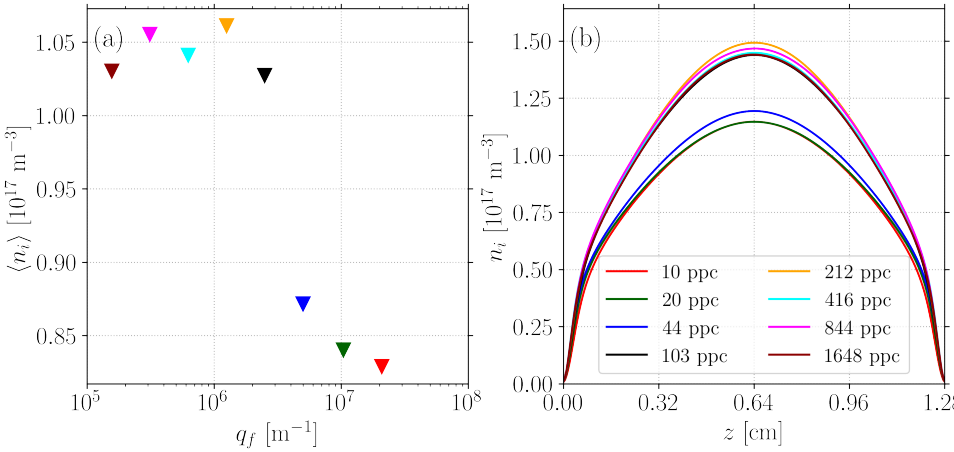


Figure 4.17: The statistical convergence of the simulation. (a) the mean final density as a function of the weight factor q_f. (b) the corresponding axial profiles. The markers in (a) have the same color as the corresponding line in (b). The nominal case of the Benchmark is the yellow one.

4.4 CHAPTER SUMMARY

In this chapter, we studied the evolution of the MTSI in $\mathbf{E} \times \mathbf{B}$ discharge conditions encountered in the radial-azimuthal (z, y) plane of Hall thrusters, by comparing the theory developed in Chapter 2 with numerical simulations. In the Chapter 2, we calculated an approximated version of the fluid dispersion relation of MTSI by Janhunen *et al.* [129], given by Eq. (2.13). By solving analytically this simplified dispersion relation, we have identified a stability criterion for the MTSI: the instability grows if one of the couples (k_y, k_z) allowed by the boundary conditions and domain lengths is such that k_z fulfills the condition given by Eq. (2.16). This analytical criterion has been compared to several 2D PIC simulations of $\mathbf{E} \times \mathbf{B}$ discharges in the radial-azimuthal (z, y) plane of Hall thrusters. We found that the dimensions of the simulation domain play a fundamental role in selecting the values of k_y and k_z. We verified that by choosing properly the domain dimensions L_y and L_z, it was possible to capture correctly the MTSI growth and its corresponding number of azimuthal periods. In particular, we showed that an azimuthal length that is smaller than a certain threshold prevents the MTSI from growing. Moreover, we showed that the MTSI growth does not depend on the plasma density, but is affected by the axial electric field (the required azimuthal domain L_y for the MTSI to grow is larger for increasing axial electric field). The previous results of Janhunen *et al.* [129] and Tavant *et al.* [136] have been analyzed by using the stability criterion derived in this paper, and we managed to explain the reason why only one MTSI period was observed by the former, and why the MTSI was not present in the latter.

We have also studied the impact of the MTSI on the macroscopic variables of the discharge. First, we have observed that during the early times of the simulation when the contributions of different instabilities are easy to distinguish, the MTSI is responsible for strong heating in the radial direction and enhances the axial electron mobility. For longer times, after the linear growth of the ECDI and MTSI and their saturation, the electric field oscillations are present in a wider spectrum of frequencies and wavelengths. In general, the initial oscillations evolve towards longer azimuthal wavelengths. In this nonlinear regime, we observed some instabilities that are compatible with an ion acoustic mode.

It is important to note that, due to the demanding computational requirements of PIC, the present study is performed in a simplified 2D setup where the collisions with the gas particles and the ionization events were neglected. For this reason, in future work, the use of simulations that account for the gas dynamics could help to study more consistently the MTSI characteristics for longer time spans. Additionally, all the results in this work are obtained with specular walls. These boundary conditions helped us to compare the simulations with our theoretical developments as the formation of the sheath was prevented. In most of our simulations, we observed a MTSI mode with half wavelength in the radial direction. However, the sheaths allow the growth of modes with a slightly larger value of k_z [12]. Unfortunately, the presence of sheaths prevents us from calculating the precise value of k_z, making more difficult the comparison between the PIC results and the fluid DR. The sheaths are expected to change the MTSI radial wavenumber, but the instability criterion is not strongly affected. This fact was verified as we have successfully applied our theory

to previous works [129, 136] where sheaths were present. Further work is needed to investigate the effect of sheaths in the evolution of the MTSI.

In the last part of this chapter, we reported the results obtained in an international benchmark, in which our group had a leading part, along with Willca Villafana at CERFACS, Toulouse. In the benchmark, we compared the results by seven groups of $\mathbf{E} \times \mathbf{B}$ discharges, representative for the radial-azimuthal plane of a HT. The benchmark has shown that all the codes can retrieve the most important electrostatic instabilities that appear in these conditions, the MTSI and the ECDI. Moreover, a statistical convergence study performed on the superparticles' weight showed that for the studied conditions the value of q_f should be less than $3 \times 10^6\,\mathrm{m}^{-1}$.

5 AXIAL-AZIMUTHAL SIMULATIONS SPECTRAL ANALYSIS

This chapter provides a summary of our research on instability development in the axial-azimuthal plane of HTs. The first section shows an analysis of the instabilities features of the BM growing and decreasing phases. In the subsequent section, the growth and development of the ion acoustic wave (IAW) are explored, and it is noted that this instability starts at the channel exit before propagating towards the anode and cathode. In the final part of the chapter, the ion transit-time instability (ITTI) and its impact on low-energy ions in the plasma plume are investigated.

Chapter contents

5.1 Axial-azimuthal simulations . . . 107
5.2 Spectral analysis of the BM phases . . . 108
5.2.1 Analysis during the growing phase of the BM . . . 112
5.2.2 Analysis in the decreasing phase of the BM . . . 112
5.2.3 Analysis over the entire BM period . . . 115
5.2.4 Summary . . . 115
5.3 Instabilities in axial-azimuthal simulations . . . 118
5.3.1 The IAW in two dimensions . . . 118
5.3.2 The ion transit-time instability . . . 128
5.4 Chapter summary . . . 136

The results in this chapter have been partially published in Refs. [201, 202].

5.1 AXIAL-AZIMUTHAL SIMULATIONS

The radial-azimuthal simulations discussed in Chapter 4 are extremely useful to study the physics of plasma-wall interaction. However, they are not sufficient to capture the basic physics of HT's, since they do not simulate the axial direction (i. e., the thrust direction). A 3D simulation would be the best option to include the dynamics along the three directions. Hirakawa and Arakawa in the '90s proposed the first model of 3D simulations [32]. Furthermore, there have been more recent

attempts to conduct 3D simulations [135, 179, 203]. However, the costs of 3D PIC simulations remain extremely high and most of the research is still conducted with 2D codes.

Despite the extensive literature about the azimuthal instabilities [66, 92, 129, 144, 133, 180], there are only a few studies [75, 185] of the axial modes, which may be due to the difficulty of calculating a spectrum in the axial direction, in which strong gradients are present. Here, we use the PSD2P method, developed by Beall *et al.* [21] and described in Chapter 2, to reconstruct the PSD spectrum at a given axial position.

The significance of the azimuthal direction on the performance of the thruster is now well established. Charoy and coworkers [170] initiated the study of the influence of the coupling of azimuthal and axial instabilities on plasma dynamics, specifically analyzing the BM phases. Despite their efforts, some aspects remained not fully explained. In this chapter, we introduce some improvements to Charoy's work and we use theoretical and simulation results to gain deeper insights into the growth and propagation of instabilities. This study allows us to better identify the effects of the instability on the thruster performance.

In Chapter 3 we described the main features of an axial-azimuthal simulation and the effect of the *RLC* circuit on some simulation cases. Some of these simulations are reconsidered here, where we first study the development of plasma instabilities during the different BM phases. Then, we compare the analytical DRs calculated in Chapter 2 to the spectra obtained from PIC simulations, using the PSD2P reconstruction technique (cf. Section 5.2). Subsequently, in Section 5.3, we investigate the origin and development of the IAW and ITTI, giving particular attention to the dispersions' 2D effects. In this chapter, the PSD2P method is used to analyze the instability spectra in cases A and C (i. e., 2D axial-azimuthal simulations with a 4 cm $\times$ 4 cm domain with an optimized *RLC* circuit) described in Chapter 3.

5.2 SPECTRAL ANALYSIS OF THE BM PHASES

To capture several periods of the BM and reach a quasi-stationary state with a PIC simulation, very long simulations are needed ($\approx$ 500 µs of physical time) with a computational cost of the order of weeks on thousands of CPUs. For this reason, as described in Chapter 3, we have used a scaling technique that consists in artificially increasing the vacuum permittivity [99]. It was shown that the artificial permittivity has an impact on the growth rate of the electrostatic instabilities and that it also increases artificially the wavelength of certain modes. For this reason, the azimuthal length used in this chapter (L_y = 4 cm) is larger than the typical length used in previous axial-azimuthal PIC simulations [124, 140].

It was previously observed that without ballast or filter, the BM oscillations may become extremely large and may even drive the discharge into unphysical conditions [155, 170]. Here, this problem is overcome by using an external *RLC* circuit [82] that strongly damps the discharge current oscillations. Such circuits are also used in experiments. Note that the circuit parameters values used in cases A and C, detailed in Table 3.2, are different. These parameters are chosen to test two different circuit responses: faster in A and slower in C.

As reported in Charoy *et al.* [170], the time evolution of the plasma discharge during a BM oscillation can be separated into two stages: the growing phase of the BM, where the dominant instabilities are the high-frequency mainly-azimuthal ECDI/IAW, and the decreasing phase of the BM where the intermediate frequency axial ITTI dominates. The spectra are generated both in azimuthal and in axial directions, which allows us to accurately determine the direction of the propagation of the various modes. This analysis of the direction of the propagation will be detailed further in Section 5.3, where we will analyze thoroughly the amplitude evolution of the spectra along the thruster axis.

In Figures 5.1 and 5.2 we plot the time evolution of the discharge current in cases A and C, respectively, with the axial profiles of electron temperature and density at different times during the BM period. First, we note that the BM frequency decreases when we use a lower injection temperature at the cathode. More importantly, in case A there is a strong high-frequency oscillation that is absent in case C. The axial profiles of electron temperature and density at different times in Figures 5.1 and 5.2 show that the plasma parameters oscillate more in the case of a higher injection temperature. The electron temperature profiles are, however, fairly similar in both cases. We observe that the temperature is higher in the decreasing BM phase, with a maximum at the channel exit (i. e., between 2 and 2.5 cm). The profiles show strong inhomogeneities in the axial direction, justifying the need of PSD2P to compute the fluctuations spectra along this direction. In the bottom row of Figures 5.1 and 5.2 we observe the axial profiles of the cyclotron frequency ω_{ce}, cf. Eq.(1.1), of the anomalous collision frequency ν_t and of the classical collision frequency ν_{class}. The anomalous collision frequency is calculated from the electron mobility in the axial direction as

$$\mu_{e,x} = \frac{v_{e,x}}{E_x + \nabla(n_e k_B T_e)/n_e e}, \tag{5.1}$$

by the usual mobility formula for magnetized plasmas: $\nu_t = m_e \omega_{ce}^2 \mu_{e,x}/e$, cf. Eq. (3.3). One should be aware of the discussion about the anomalous transport in Section 1.2.3: a more correct model of electron transport requires the inclusion of the friction force.

In both cases A and C, the profile of ν_t is rather smooth in the thruster channel, while it is noisier in the plume. This fact is related to the method of calculation of the mobility. Interestingly, we find the same trends and a similar order of magnitude for all the quantities. First, as expected, in both works, the anomalous collision frequency is higher than the classical one. In Dale *et al.* [142], the authors propose a similar graph in an experimental work in slightly different discharge conditions. They observe that the classical collision frequency decreases from the mid-channel to the first centimeters of the plume, while the anomalous collisional frequency increases: this is what we observe in our simulation results too.

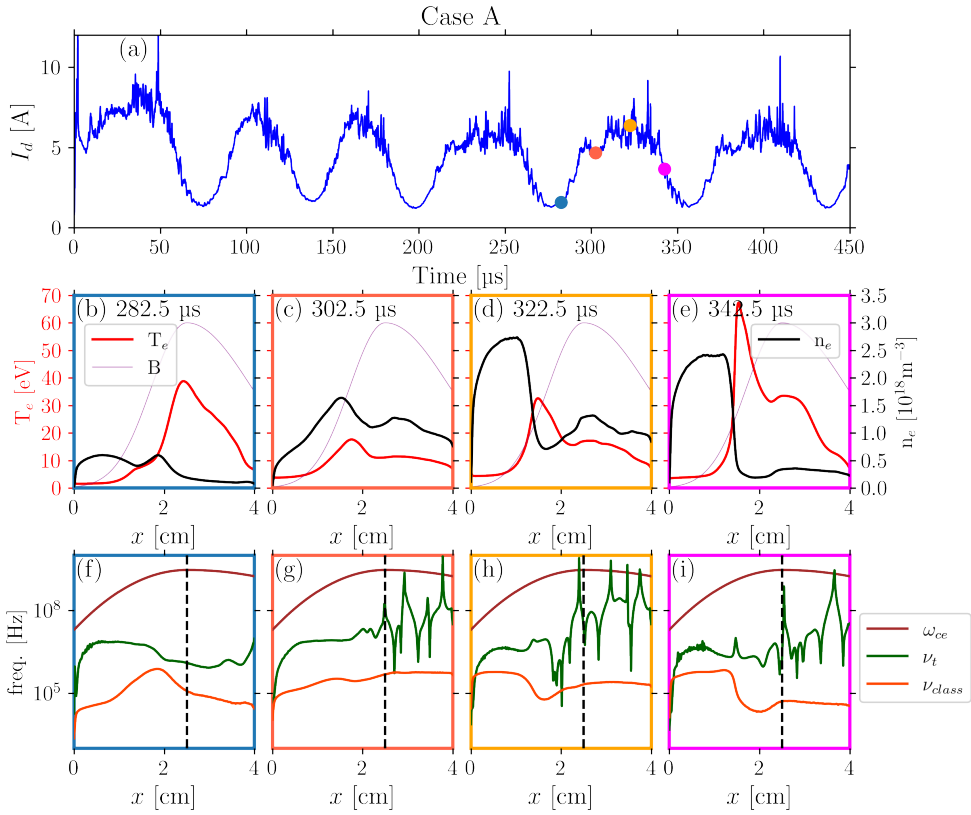


Figure 5.1: Case A with $T_e^{\text{cath}} = 5\,\text{eV}$. (a) The discharge current. The four points indicate the times at which the profiles in (b-e) and (f-i) are taken (the marker color corresponds to the frame color in the bottom line). In the central line panels, we show the axial profiles of electron temperature (red) and electron density (black) at the chosen times. The purple line represents the magnetic field profile on a linear scale. In the bottom panels, we show the axial profiles of the cyclotron frequency ω_{ce}, the anomalous collisional frequency ν_t, and of the classical collisional frequency ν_{class}. The dashed black line represents the thruster exit plane. From Ref. [201].

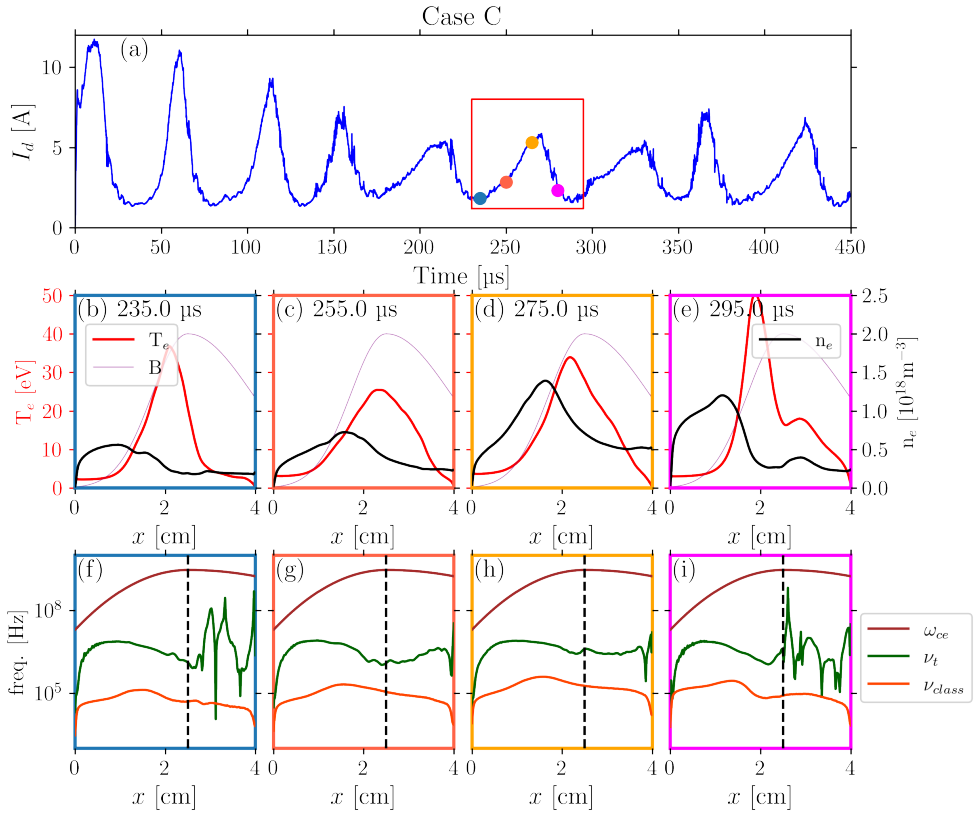


Figure 5.2: Case C with $T_e^{\text{cath}} = 0.1$ eV. (a) The discharge current. The four points indicate the times at which the profiles in (b-e) and (f-i) are taken (the marker color corresponds to the frame color in the bottom line). In the central line panels, we show the axial profiles of electron temperature (red) and electron density (black) at the chosen times. The purple line represents the magnetic field profile on a linear scale. In the bottom panels, we show the axial profiles of the cyclotron frequency ω_{ce}, the anomalous collisional frequency ν_t, and of the classical collisional frequency ν_{class}. The dashed black line represents the thruster exit plane. From Ref. [201].

5.2.1 Analysis during the growing phase of the BM

We present PSD2P maps during the growing phase of a BM oscillation in Figures 5.3 (case A) and 5.4 (case C). In both cases, we analyze both the axial and the azimuthal spectrum at two different points of the thruster, one inside the channel and one in the plume. In addition, we select the mode at high frequency with large amplitudes and we plot the direction of propagation.

As observed by Charoy *et al.* [170], the spectrum is dominated by the ECDI/IAW during the growing phase. We can distinguish two regions: one close to the anode, where the instability propagates at a finite angle with respect to the azimuthal direction, and one in the plume, where the propagation is essentially in the azimuthal direction. Inside the channel, plotted in subfigures 5.3 and 5.4 (a) and (d), we observe that there are only small differences between cases A and C. In both cases, we observe that the instability propagates with a significant angle, with an inclination of the wave vector towards the anode, as shown by the cyan arrows in Figures 5.3 and 5.4 (c). The most significant differences between case A and case C appear in the plasma plume, in the PSD2P maps of subfigures 5.3 and 5.4 (b) and (e). In case C Figure 5.4 (e), we identify the frequency and wavenumber corresponding to the ECDI at $\omega \approx 1\,\mathrm{MHz}$ and $k_y \approx 400\,\mathrm{m}^{-1}$, while the spectrum in Figure 5.3 (e) calculated for case A is more complex. The signature of the ECDI at high frequency and wavenumber is still seen, but the main mode is at lower frequency and wavenumber, within the range reported in Section 3.3 for the ITTI. It, therefore, appears that the PSD2P technique can capture the simultaneous presence of both modes.

As it can be seen in Figure 5.4 (b), the ECDI/IAW also has a signature in the axial direction. The mode with the largest amplitude is seen at $k_x = 0$. As a result, we observe a wave that propagates almost azimuthally. However, the axial dispersion map, which was not analyzed in previous works, suggests that the ECDI/IAW may have a 2D nature. The spectrum is broad and can be compared to the theoretical IAW dispersion relation, as already done in several works [170, 118, 177, 139, 138, 185]. This discussion about the 2D nature of the IAW and the comparison with the analytical DR will be carried out in Section 5.3.1.

In Figures 5.3 and 5.4 we see that the PSD2P technique successfully captures the bending of the wavefronts, observed in the density snapshots. In addition, we observe a change in the frequency of the dominant ECDI/IAW mode between the region near the anode and that near the thruster exit. These results are consistent with the change of direction in the propagation of the wave and change of frequency along the thruster axis as observed by Ben Slimane *et al.* [185] using virtual Thomson scattering. This will be further discussed in Section 5.3.1.3.

5.2.2 Analysis in the decreasing phase of the BM

The PSD2P maps of the decreasing phase of the discharge current are shown in Figures 5.5 and 5.6 for cases A and C, respectively. As already observed by Charoy *et al.* [170], the spectrum and dynamics of the instabilities are very different from those of the growing phase. In the thruster channel, we still observe an ECDI-like instability that propagates at a finite angle with respect to the thruster axis, but the spectrum in the plume changes drastically. In this region, we observe a longer-wavelength

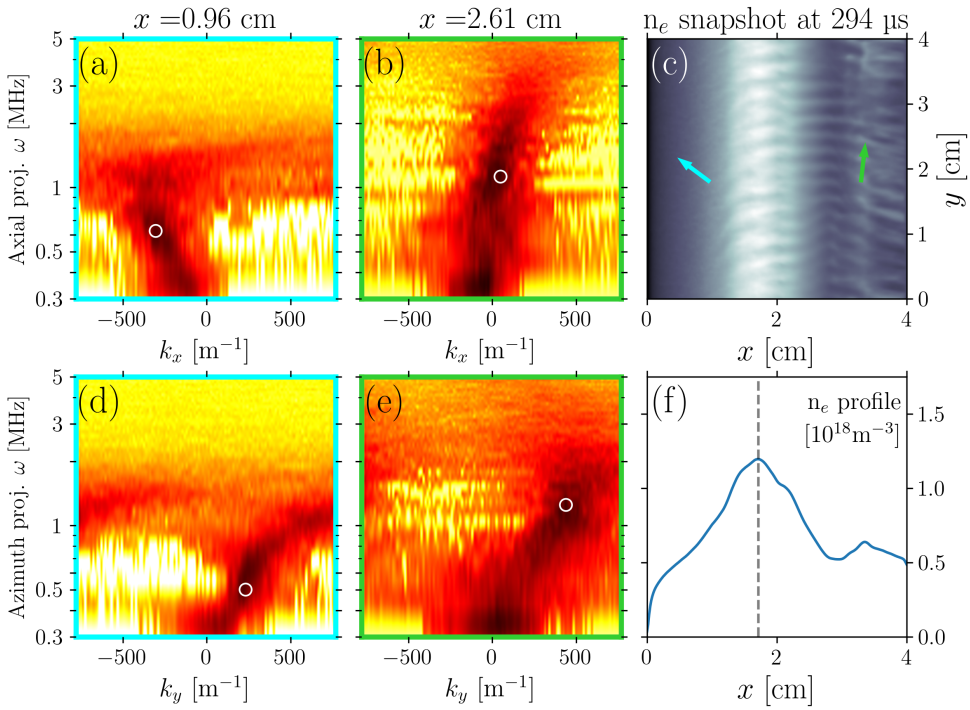


Figure 5.3: Case A, growing phase of the BM. In (a) and (b): PSD2P maps calculated in the axial direction in the channel and the plume. In (d) and (e): PSD2P maps calculated in the azimuthal direction at the same axial positions. The white rings represent the max of the PSD2P. In (c): a snapshot of the electron density map at t = 294 µs. The arrows represent the instability direction, which is calculated by the k_x and k_y in the spectra. Each frame corresponds to the arrow with the same color. In (f): axial profile of the electron density at t = 294 µs. From Ref. [201].

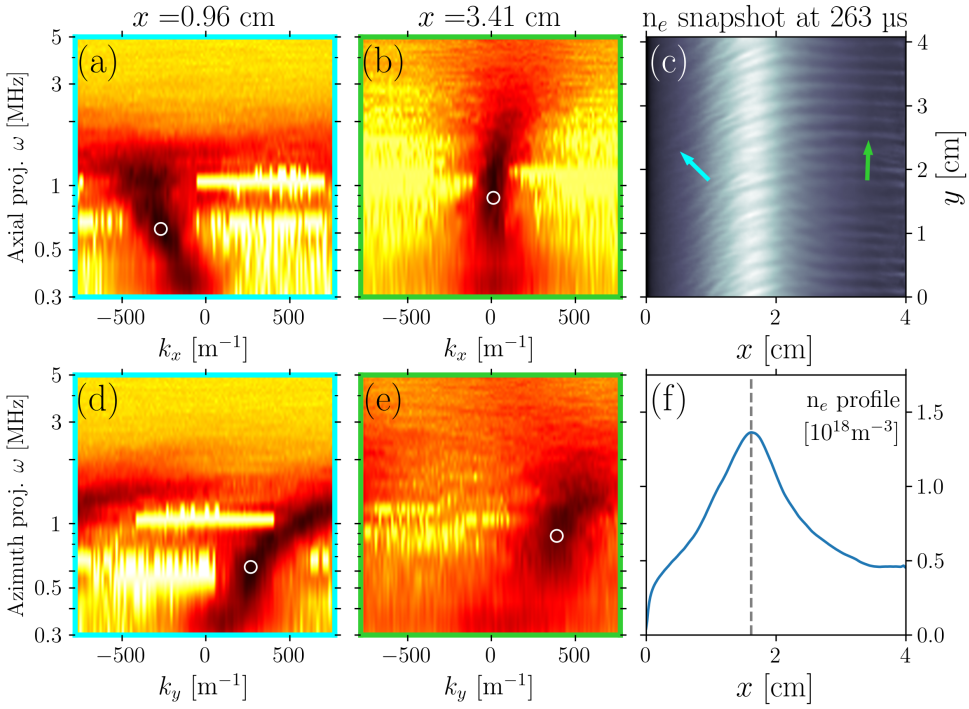


Figure 5.4: Case C, growing phase of the BM. In (a) and (b): PSD2P maps calculated in the axial direction in the channel and the plume. In (d) and (e): PSD2P maps calculated in the azimuthal direction at the same axial positions. The white rings represent the max of the PSD2P. In (c): a snapshot of the electron density map at t = 263 µs. The arrows represent the instability direction, which is calculated by the k_x and k_y in the spectra. Each frame corresponds to the arrow with the same color. In (f) axial profile of the electron density at t = 263 µs. From Ref. [201].

instability, directed mainly axially, identifiable as the ITTI. This instability, which has a frequency of the order of 500 kHz and a wavelength of the order of 1 cm, is also captured in the dispersion maps by the PSD2P technique. Its frequency in case A is of ≈ 600 kHz and in case C of ≈ 300 kHz, while the axial wavenumbers are $\approx 80\,\mathrm{m}^{-1}$ and $\approx 40\,\mathrm{m}^{-1}$, respectively. In the axial PSD2P map, we observe that the instability dispersion has approximately the same shape as the resistive mode identified by Fernandez *et al.* [75] in radial-axial simulations. A complete comparison between the linear theory and the PSD2P spectra is presented in Section 5.3.2.

Even if the azimuthal PSD peak remains at $k_y \approx 0$, we observe that the PSD2P map is not perfectly symmetric. In particular, we note in Figure 5.5 (e) that the azimuthal wavenumber is not perfectly centered at zero, as one would expect for a perfectly axial instability. This is a hint that the ITTI may have a small azimuthal component. It will be shown in Section 5.3.2 that this observation is crucial to understand the linear phase growth of this instability.

5.2.3 Analysis over the entire BM period

The comparison of the spectra of cases A and C during an entire BM period suggests the following. In case A, the ITTI is present in both phases and is dominant in the plume during the phase of discharge current collapse. In case C, two different dispersion maps are identified: one dominated by ECDI/IAW with almost no ITTI during the growing phase of the discharge current (i. e., in Figure 5.4, the instability in the plume is purely azimuthal), and another one dominated by the ITTI with almost no presence of ECDI/IAW in the plume during the decreasing phase of the discharge current. As further discussed in the following, the origin of this difference may be explained by the ITTI growth rate derived from fluid theory, which depends on the collision frequency [75], so on the electron temperature (the plume electron temperature is different in cases A and C).

5.2.4 Summary

All in all, both ECDI/IAW and ITTI instabilities have a dominant propagation direction (azimuthal for the ECDI/IAW and axial for the ITTI). However, thanks to the PSD2P technique, the two-dimensional character of these instabilities, that heretofore have been seen as mono-dimensional instabilities, has been demonstrated. In the next sections, we analyze in detail the 2D effects on the instabilities' growth and propagation, and it appears that 2D effects are very important.

In the previous section, we presented 2D PIC simulations of the axial-azimuthal plane of a Hall thruster coupled to a fluid model for the gas. We studied two 4 cm $\times$ 4 cm PIC simulations with different cathode injection temperatures (i. e., T_e^{cath} fixed to 0.1 or 5 eV) and circuit. For both cases, we observed that the ECDI/IAW instability dominates during the growing phase of the BM, while the ITTI is predominant in the decreasing phase of the BM. However, the injection temperature and the choice of the circuit elements have demonstrated to play a role in the development of the instabilities. In the case with low temperature, i.e., $T_e^{\mathrm{cath}} = 0.1$ eV (named "case C" above), the ITTI is not present during the growing phase of the current whereas the

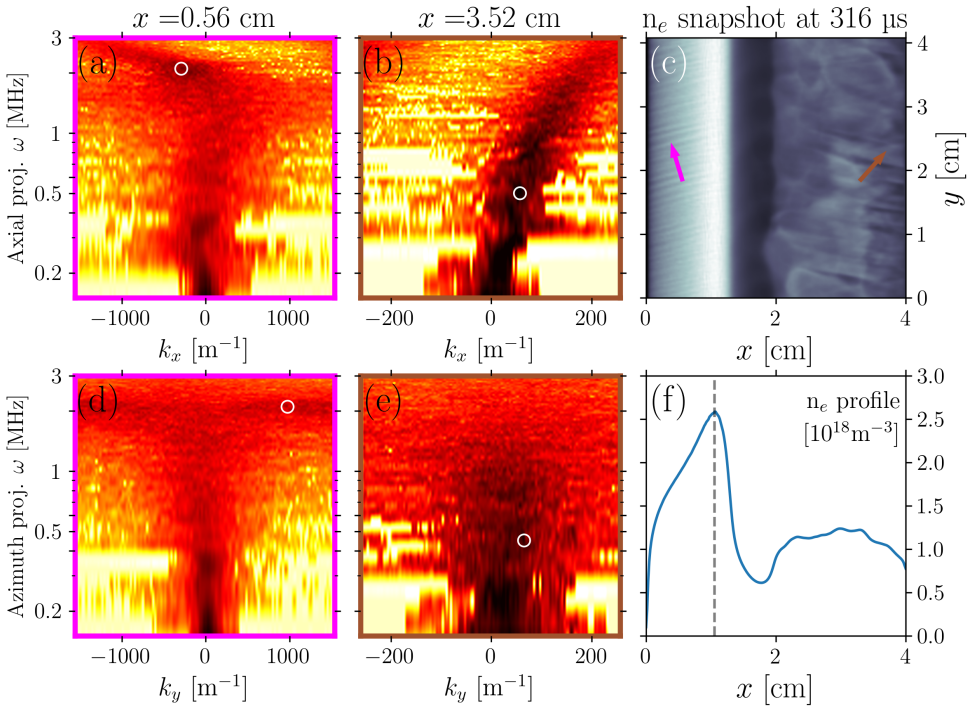


Figure 5.5: Case A, decreasing phase of the BM. In (a) and (b) we show the PSD2P calculated in the axial direction in the channel and the plume. In (d) and (e) we show the PSD2P calculated in the azimuthal direction at the same axial positions. The maximal density is very close to $x = 0.96$ cm (i. e., the axial position chosen for the other figures), so we performed the analysis at a position slightly closer to the anode. The white rings represent the max of the PSD2P. In (c) a snapshot of the electron density map at $t = 316$ µs is shown. The arrows represent the instability direction, which is calculated by the k_x and k_y in the spectra. Each frame corresponds to the arrow with the same color. In (f) we report the electron density axial profile at $t = 316$ µs. From Ref. [201].

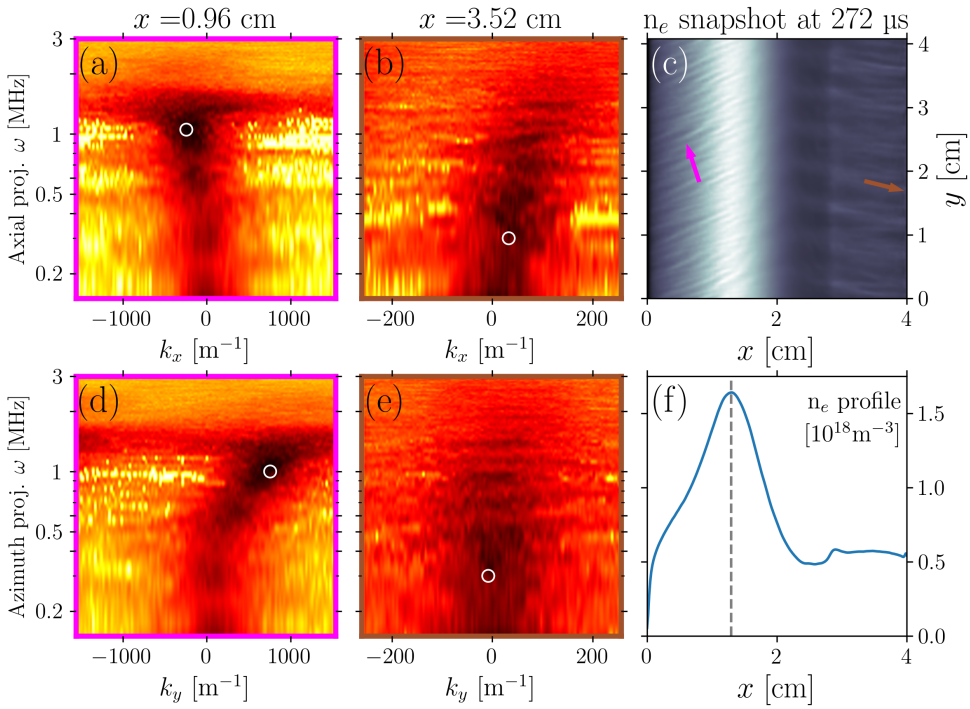


Figure 5.6: Case C, decreasing phase of the BM. In (a) and (b) we show the PSD2P calculated in the axial direction in the channel and the plume. In (d) and (e) we show the PSD2P calculated in the azimuthal direction at the same axial positions. The white rings represent the max of the PSD2P. In (c) a snapshot of the electron density map at $t = 272\,\mu s$ is shown. The arrows represent the instability direction, which is calculated by the k_x and k_y in the spectra. Each frame corresponds to the arrow with the same color. In (f) we report the electron density axial profile at $t = 272\,\mu s$. From Ref. [201].

IAW/ECDI disappears during the decreasing phase. In the case with $T_e^{\text{cath}} = 5\,\text{eV}$ and faster circuit (named "case A" above) we observed a persistent ITTI during both phases of the BM.

5.3 INSTABILITIES IN AXIAL–AZIMUTHAL SIMULATIONS

In this section, we focus on case C of Chapter 3 with the low injection temperature (i. e., $T_e^{\text{cath}} = 0.1\,\text{eV}$), with a slower circuit response (i. e., higher τ) as it gives the possibility to study the two instabilities separately. The different phases of this simulation are analyzed in detail in Section 5.3.1, where we compare the PSD2P maps to the analytical DRs obtained in Section 2.2. The analysis reveals key observations about the nature and the development of these $\mathbf{E} \times \mathbf{B}$ instabilities.

5.3.1 The IAW in two dimensions

The ion acoustic wave has been studied as a purely azimuthal instability in several works [170, 118, 177, 139, 138], while we observed that this instability has an axial signature as well. In Section 2.2.2 we derived a bi-dimensional dispersion relation (cf. Eq. (2.7)) for the IAW. By extracting λ_D, $\omega_{\text{p}i}$ and $\mathbf{v}_{i,0}$ from PIC data and substituting these values in Eq. (2.8), we can obtain the IAW frequency for different values of k_x and k_y. Figure 5.7 (a) shows a map of the IAW frequency for values of k_x and k_y in a typical range for IAW.

Since we are assuming that $k_x \neq 0$ and $k_y \neq 0$, the comparison of this DR map with a simulation spectrum requires a 3D transform of a signal in the $x - y - t$ space, which is not achievable in a convenient way. This issue can be overcome by considering that the main component of the IAW is an ECDI-like almost-purely azimuthal oscillation (i. e., such that $k_y \gg k_x$), represented as the black arrow in Figure 5.7 (a), with an azimuthal wavenumber $k_y^{\max}$. Thus, we can assume that the IAW is an instability developing around the $(k_x \approx 0, k_y \approx k_y^{\max})$ point in the $k-$space. When we perform a spectral analysis in the azimuthal direction, we then have to compare it with the 1D analytical DR calculated along the blue line in Figure 5.7 (a), which corresponds to a dispersion $\omega_{1,2}^{\text{azimuth}}(k_y) = \omega_{1,2}(k_y, k_x \sim 0)$ that is equivalent to the one commonly calculated for the 1D IAW. Oppositely, the 1D axial DR must be calculated considering that the azimuthal wavenumber component is not negligible and has a constant value $k_y^{\max}$. Thus, the dispersion that we observe in the axial direction corresponds to the one calculated along the green line in Figure 5.7 (a), i. e., $\omega_{1,2}^{\text{axial}}(k_x) = \omega_{1,2}(k_y \approx k_y^{\max}, k_x)$. The coefficients of these equations are calculated by averaging over y and over time the plasma parameters extracted from the PIC simulation. The value of $k_y^{\max}$ is calculated from the PSD2P numerical spectrum in the azimuthal direction.

A representation of these DRs is given in Figures 5.7 (b) and (c), where the blue and green lines represent the 1D DRs calculated along the corresponding lines in Figure 5.7 (a). The two color plots in these figures, displaying the azimuthal and axial PSD2Ps, are discussed and compared to the analytical DRs in Section 5.3.1.2. Here, we only emphasize the significant effect of the choice of the axial position at which we

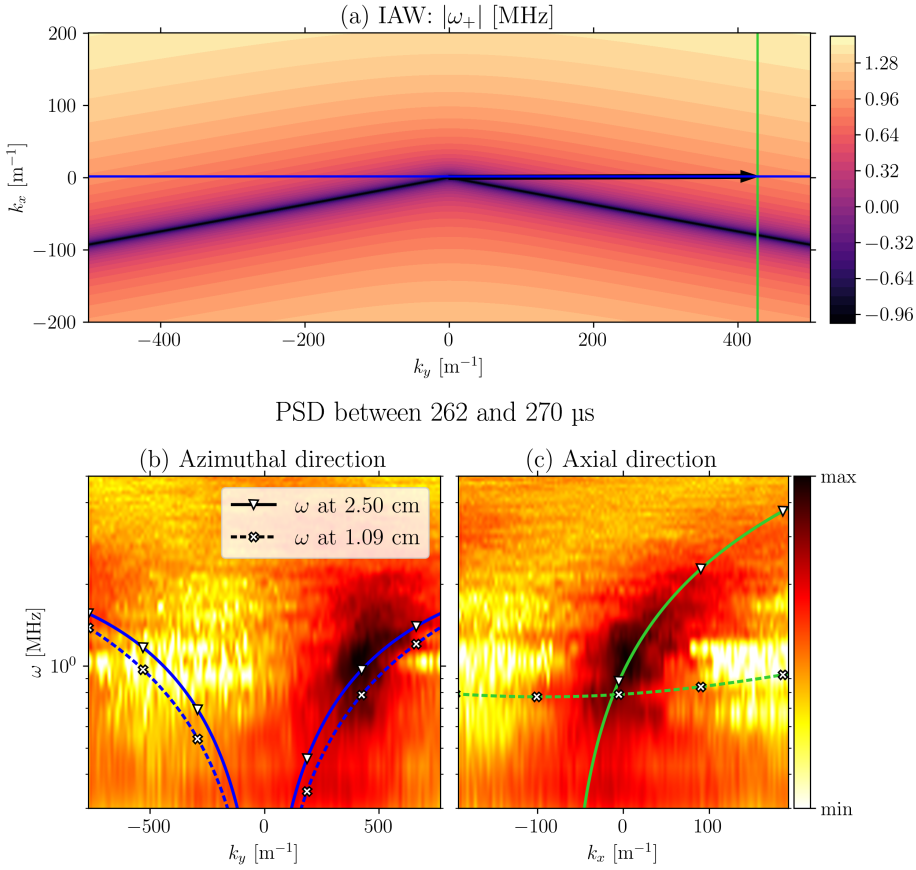


Figure 5.7: (a) Numerical solution of Eq. (2.8) with plasma parameters extracted from PIC simulations (4 cm × 4 cm axial-azimuthal domain with an electron temperature of injection at the cathode of 0.1 eV) at the axial position of $x = 2.5$ cm, corresponding to the channel exit (i. e., $k_x \approx 0$ and $k_y \approx 430\,\mathrm{m}^{-1}$). Bottom: Azimuthal (b) and Axial (c) PSD2P map calculated at the channel exit. The green and blue lines in (b) and (c) represent the azimuthal and axial projections of the IAW as shown in (a). The dashed lines in (b) and (c) show the DR calculated inside the channel, while the solid lines represent the DR calculated at the channel exit. From Ref. [202].

extract the plasma parameters: the axial DR varies drastically from the thruster inner channel to the channel exit.

5.3.1.1 Temporal evolution of the IAW amplitude

To study the evolution of the IAW during a BM cycle, we take six time-intervals of 8 µs, spanning from the start to the end of a BM cycle, as shown in Figure 5.8 (a). For each time-interval, we perform an axial and an azimuthal PSD2P at several positions along the thruster axis and we calculate from these PSD2P maps the intensity of the IAW peak (by summing axial and azimuthal contributions). Figure 5.8 (b) confirms that the IAW intensity profiles change significantly during the breathing mode, as was observed above. The study of the evolution of these profiles gives important insights into the growth and development of ion acoustic instability.

At the beginning of the growing phase of the BM, cf. Figure 5.8 (c), we observe that the IAW develops mainly in the external part of the channel and the plume (blue line in Figure 5.8 (b)), with a maximum at $x \sim 1.75$ cm, while almost no IAW is detected in the thruster inner channel. This observation remains true in the BM growing phase: green, orange, and yellow lines, i. e., Figs. 5.8 (d, e, f). Here, we observe that the maximal IAW intensity stays between $x = 1.5$ and 2 cm, and progresses slightly towards the anode at each subsequent time-interval. The IAW amplitude in the plume is smaller than the maximum and approximately constant in space, increasing at each time step of the growing BM phase. In the channel region near the anode, almost no IAW is detected in the first two intervals (blue and green). At t =254 µs we observe a consistent growth of the IAW also in this region, even if the IAW intensity near the anode remains significantly lower than the one at the thruster exit.

In the decreasing phase of the BM (magenta and brown lines, i.e., Figs. 5.8 (g, h)) we observe a major change in the IAW characteristics. The instability starts to move towards the anode, while in the central part of the thruster, almost no IAW is detected and a weaker residual IAW is detected in the plume region. The absolute value of the maximum, which is now near the anode, decreases. This means that a part of the instability energy has been dissipated or convected out of the simulation domain at the anode boundary. Similarly, the wave amplitude in the plume decreases: this is consistent with the observations of the previous section where the IAW almost disappears in the plume during the BM decreasing phase, which is dominated by the ITTI.

The analysis of the evolution of the IAW amplitude performed in this section using the PSD2P technique suggests that: (i) the instability forms at the beginning of the BM growing phase at a position near the channel exit, (ii) during the whole BM growing phase the instability strengthens at the channel exit and in the plume and starts to propagate also in the region next to the anode, (iii) eventually, in the BM decreasing phase, the IAW loses most of its energy at the cathode exit and in the plume, where the ITTI becomes dominant (cf. [201]), while it remains prevailing near the anode, even if it loses some of its energy.

5.3.1.2 The origin of the IAW

Although the discussion in the previous section has already given some important insights about the origin of the IAW instability, the comparison of the PSD2P maps

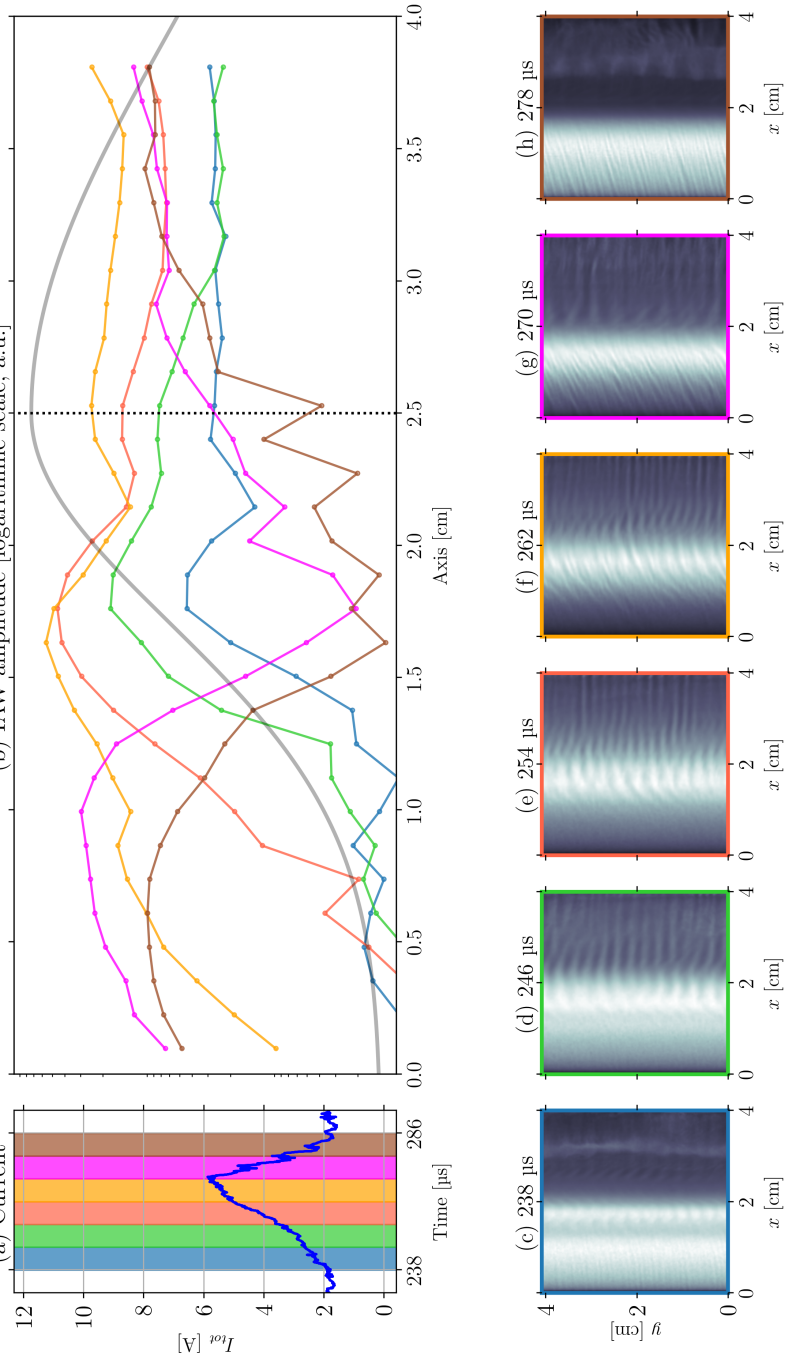


Figure 5.8: (a) The discharge current evolution during a given BM oscillation. The different color bands indicate the six time intervals where we performed the PSD2P. In (b) we show the amplitude of the IAW mode along the thruster axis, each color line corresponds to the time-interval with the same color in (a). The solid black line and the vertical dashed black line represent the magnetic field shape and its maximum axial position, respectively. In (c-h) we show 6 snapshots of the plasma density n_e at the beginning of each of the six time intervals. From Ref. [202].

with the analytical DR improves significantly our understanding of the growth of this instability. Since the shape of the spectrum along the thruster axis for $x > 2\,\text{cm}$ is rather constant and, as we see in Figure 5.8 (b), the amplitude does not vary either, we chose to calculate the PSD2Ps at the channel exit ($x = 2.5\,\text{cm}$, cf. Figure 5.7 (b) and (c)), and then to compare them to the analytical results obtained by Eq. (2.8). Since we want to study how the analytical DR varies when we change the time and the axial position, we work in a bi-dimensional parametric-space, that is difficult to compare to the dispersion relations maps obtained with the PSD2P. To identify the right time and axial position at which the instability forms, we dynamically adjusted the time and position of the calculation, verifying that the best fit of the PSD2P maps is obtained by calculating the dispersion at the beginning of the growing phase of the Breathing Mode, which is consistent with what we observed in the previous section. Similarly, we calculated the IAW analytical axial and azimuthal DRs at several axial positions, comparing them to the PSD2P maps. An example is shown in Figure 5.7 (b) and (c), where we plotted two DRs: one calculated in the channel near the anode (dashed line) and the other at the thruster exit (solid line). In Figure 5.7 (b) we can see that both the dispersion calculated in the channel and the dispersion calculated in the plume fit the azimuthal spectrum calculated with the PSD2P. Hence, it is difficult to conclude anything about the instability origin using only the spectrum in the azimuthal direction. As we have seen, the spectrum in the axial direction, reported in Figure 5.7 (c), has a well-defined shape, that helps us to identify the position where likely the IAW forms. We observe that the axial dispersion $\omega_{1,2}^{\text{axial}}(k_x)$ calculated at the channel exit is consistent with the spectrum, while the one calculated using the parameters extracted in the channel near the anode is not. Thus, these observations suggest that the instability is not originated from the channel and then convected outwards, as proposed in Ref. [170], but rather that the IAW arises in the central part of the simulation (between the density peak and the max of the magnetic field). This view is consistent with what has been observed in Section 5.3.1.1 concerning the evolution of the instability intensity.

The previous observation about the position at which the IAW originates can be consolidated by studying the characteristics of the IAW growth rate, calculated using kinetic theory by Lafleur *et al.* [105], the result of which is given in Eq. (2.9). In Figure 5.9 (a) we observe that in the azimuthal direction, the maximal growing wavenumbers are rather well predicted by the analytical γ, as already noticed in several other works [170, 118, 177]. The novelty is given by the result in (b), where we observe that the expression in Eq. (2.9) predicts the growth of a low-k_x mode, as it is indeed observed. From Eq. (2.9) one can easily compute the maximal value of the growth rate in the case of a purely azimuthal instability, as

$$\gamma_{\max} \approx \gamma\left(k_y = \frac{1}{\sqrt{2}\lambda_D}, k_x \approx 0\right) = \sqrt{\frac{\pi m_e}{54 m_i}}\frac{v_{e,0,y}}{\lambda_D}, \tag{5.2}$$

which is proportional to the ratio between the azimuthal drift of electrons and the Debye length. The axial profiles of these quantities at the beginning of the BM cycle are shown in Figure 5.10 (a) and the corresponding maximal growth rate profile is shown in Figure 5.10 (b). Observation of this profile shows a weak growth rate in the channel near the anode and in the plume. Definite evidence of a significant growth rate is observed in the central part of the simulation, with a plateau between ~ 1.4

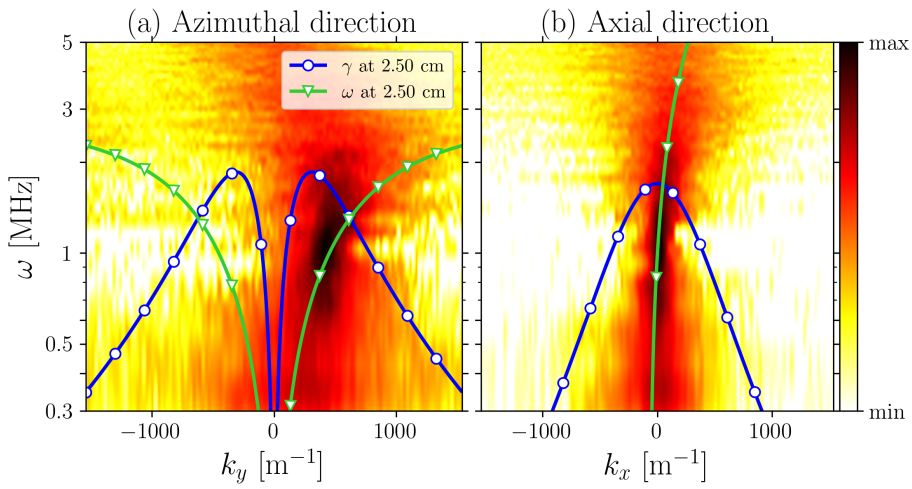


Figure 5.9: In (a) and (b) the 2D color plots show the PSD in azimuthal and axial directions, respectively. In green, we draw the best IAW DR as in Figure 5.7. The corresponding growth rate of Eq. (2.9) (magnified by a factor 8) is plotted in blue. From Ref. [202].

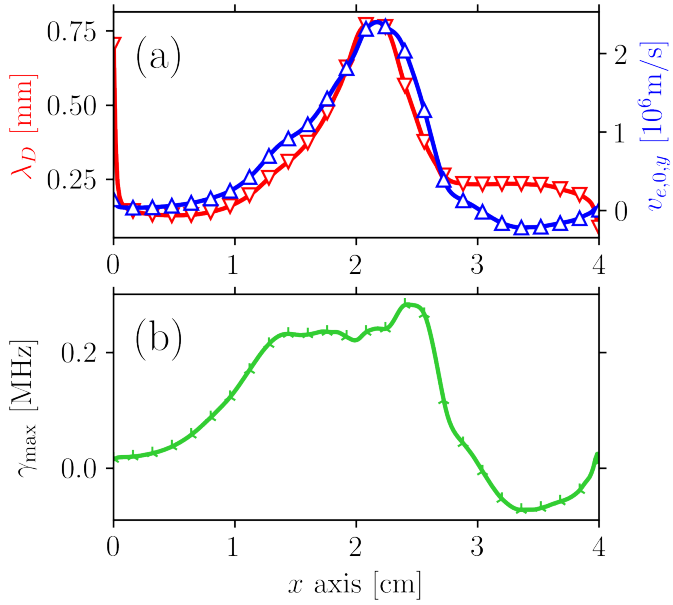


Figure 5.10: (a) Debye length (red) and electron azimuthal drift velocity (blue) mean profiles between 234 and 238 µs. (b) The maximum growth rate from Eq. (5.2). We remind the reader that the value of λ_D has been increased by a factor of 8 by scaling the permittivity. From Ref. [202].

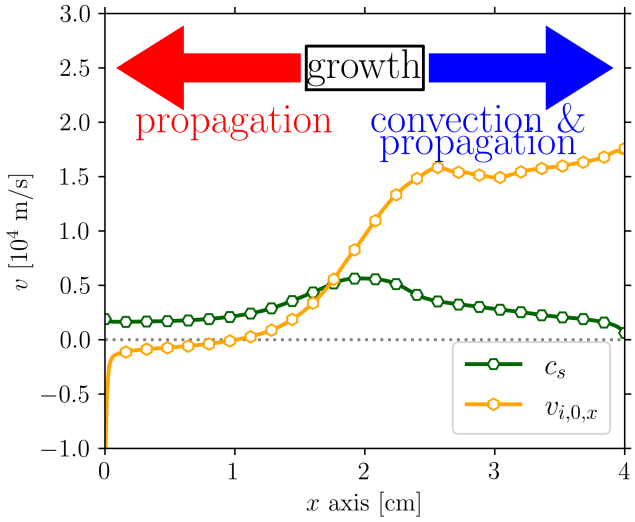


Figure 5.11: The axial profiles of sound speed and ion axial velocity calculated at $t = 262\,\mu s$. The arrows indicate the direction of propagation and convection of the wave. From Ref. [202].

and 2.7 cm. This corroborates the idea that the instability primarily grows in the external part of the discharge channel and subsequently propagates towards the anode and the cathode. In Figure 5.11 we observe that the ion flow is subsonic in the anode region (i. e., $x \lesssim 1.7\,cm$), which allows the propagation of the plasma wave. Conversely, when the flow becomes strongly supersonic in the plume region, we expect that a phenomenon of instability convection will couple with the propagation of the wave [118]. In Figure 5.11 we present a schematic summarizing the propagation and wave convection.

5.3.1.3 *The cause of the bending of the IAW instability*

Several works [140, 185, 158, 99] have reported the fact that the IAW/ECDI instability is purely azimuthal in the plume, while it propagates with a non-zero k_x component in the region next to the anode. To understand the reason why we observe a change in the instability direction we propose an analogy with the classical Snell theory of sound waves propagation in media with different sound velocities [148]. This theory (that can be extended from perfect gases to plasmas without further approximations) suggests that the propagation velocity of sound waves depends on the gas temperature.

As already discussed above, the PSD2P technique successfully captures the bending of the wavefronts, thus it can be used to study the evolution of the instability along the thruster axis. We have calculated the PSD reconstructed spectrum in axial and azimuthal directions at four different axial positions and the corresponding 8 PSD2P maps are shown in Figure 5.12. In this figure, the subfigures (a-d) display the axial PSD at different axial positions and the subfigures (f-i) show the corresponding azimuthal ones. In (e) we show a snapshot taken at $t = 263\,\mu s$ of the electron density and, superimposed to it, we draw the four arrows indicating the instability propagation

direction determined by the main components calculated in the PSD2P spectra. The instability propagates with $k_x \neq 0$ in the channel near the anode, as one can notice in Figs 5.12 (a) and (f), then the wavefronts fold in a position near the electron temperature peak and the instability direction becomes parallel to the azimuthal direction. Observing the subfigure pairs (c,h) and (d,i) we notice that the spectral maps do not vary much in the plume and that the axial and azimuthal dispersion relations of IAW (calculated as in the previous sections) successfully fit the dispersion maps at both positions.

The propagation without energy losses of a plane wave at an interface of two media implies the conservation of the wave frequency, otherwise the wave energy is not conserved. So, just considering that the parallel (to the interface of two media) wavenumber is conserved and that the wave velocity varies at the interface, we can easily obtain the Snell law for plane waves as

$$\text{cotan}\theta \mathrm{d}\theta = \frac{\mathrm{d}v}{v},$$

where θ is the propagation angle with respect to the normal to the interface and $v = \omega/k$ is the wave speed. Considering two regions of thickness δx, as shown in Figure 5.13, we can write the Snell law as

$$\frac{\sin\theta_1}{v_1} = \frac{\sin\theta_2}{v_2}, \tag{5.3}$$

where $v_{1,2}$ are the phase velocities in the two zones and $\theta_{1,2}$ are the corresponding angles. Extending classical gas theory to plasma, as a first approximation we assume that the hotter the plasma, the higher the propagation velocity of IAW. This is consistent with the result in Eq. (2.8), which suggests that this oscillation propagates at the Bohm speed, which is proportional to $T_e^{1/2}$. So, considering an instability forming in the region between the temperature peak and the thruster exit in the first phase of the BM growing phase, its propagation towards the anode is blocked by the temperature peak, which behaves as a barrier. By considering two propagation velocities v_1 and v_2, such that $v_1 < v_2$, corresponding to a lower temperature and a higher temperature, respectively, we use the Snell law to clearly explain the nature of this phenomenon. Using such velocities in Eq. (5.3), we have that the refraction angle θ_2 of a wave propagating almost parallel to the azimuthal direction ($\sin\theta_1 \sim 1$) is such that

$$\sin\theta_2 = \frac{v_2}{v_1} > 1.$$

Hence, this relation suggests that the propagation is forbidden from a zone with lower temperature to a zone with higher temperature and successfully explains the *barrier* behavior of the temperature peak. Moreover, this theory is confirmed by the slow instability convection towards the temperature peak that we observe in Figure 5.8 (b). Instability transport is not totally prohibited, as the temporal variation of plasma parameters allows some propagation beyond the temperature peak. The situation is different when we consider the region between the maximal temperature position and the anode. In this zone the electron temperature decreases (from right to left), so does the propagation velocity, and the wave propagation towards the anode is not anymore forbidden. The Snell-behavior hypothesis proposed in this section can

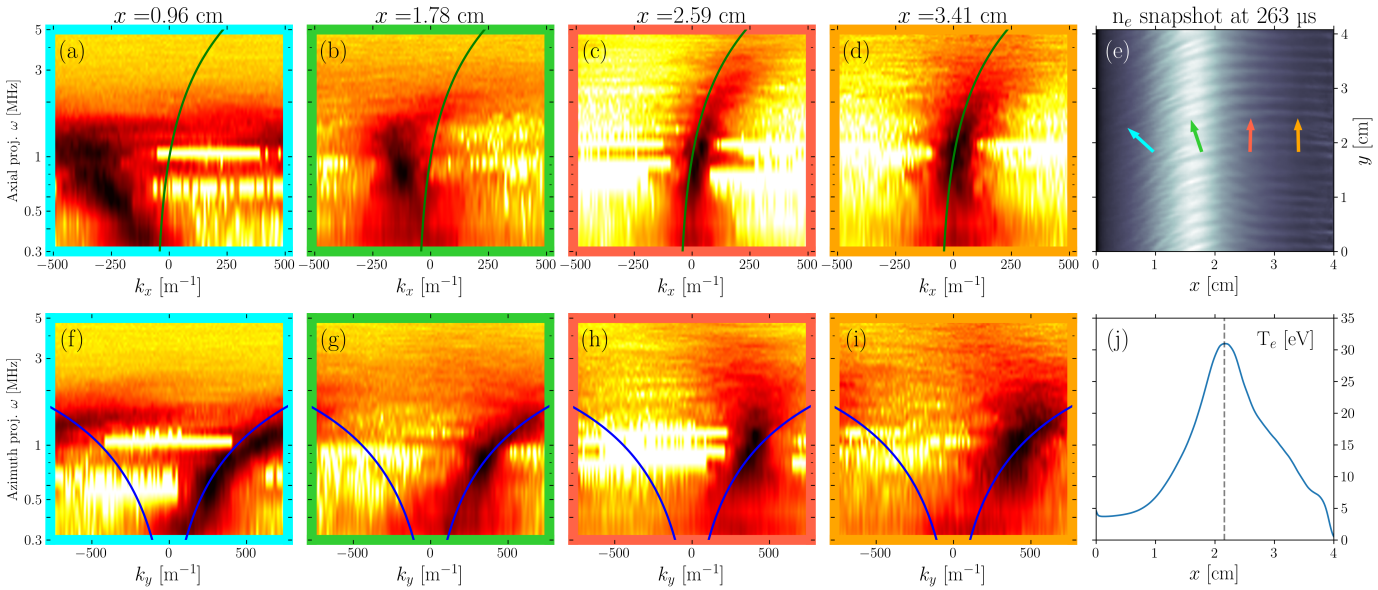


Figure 5.12: (a-d) PSD2P calculated in the axial direction at four different axial positions indicated above each figure. The green lines represent the axial IAW calculated as in Figure 5.7. (f-i) PSD2P calculated in the azimuthal direction at the same axial positions. The blue lines represent the azimuthal IAW calculated as in Figure 5.7. In (e) a snapshot of the electron density map at $t = 263\,\mu s$ is shown. The arrows represent the instability direction, which is calculated by the k_x and k_y in the spectra. Each frame corresponds to the arrow with the same color. In (j) we show the electron temperature axial profile at $t = 263\,\mu s$. From Ref. [202].

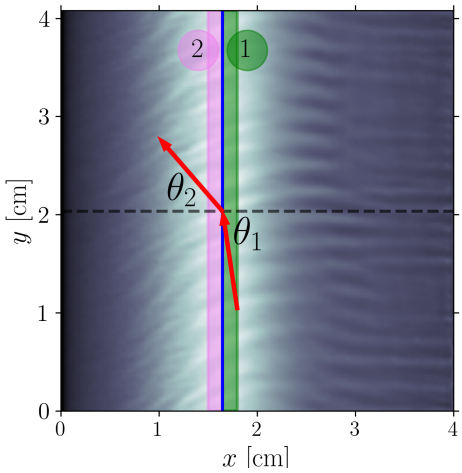


Figure 5.13: Schematic of the Snell refraction of an instability propagating from region 1 of thickness δx with propagation velocity v_1 to region 2 where the propagation velocity is $v_2 < v_1$. From Ref. [202].

be quantitatively validated by comparing along the $x-$axis the propagation angle of the main IAW mode (corresponding to the PSD2P intensity peak) calculated directly in the PSD2P maps with one estimated by Snell wave propagation formula.

Using axial and azimuthal PSD2P maps and selecting the values corresponding to the PSD peak we identified the values of ω_{max}, $k_{x,max}$ and $k_{y,max}$, corresponding to the intensity peak. In Figure 5.14 (a) we observe that the direction of the vector identified by the pair ($k_{x,max}$, $k_{y,max}$) successfully represents the wavefront propagation direction. The propagation angle measured with respect to the x axis, as θ_2 in Figure 5.13, is estimated by calculating the arctangent of $k_{y,max}/k_{x,max}$ and is plotted in Figure 5.14 (b) using blue markers. To apply the Snell method just described, we need to know the main mode phase velocity. It can be estimated by the ratio between the frequency ω_{max} and wavenumber k_{max}, this last obtained as

$$k_{max} = \sqrt{k_{x,max}^2 + k_{y,max}^2}.$$

The considerations made in the previous sections suggest that the propagation starts at the axial position x_1 at the right of the temperature peak (i. e., $x_1 = 2.25\,cm$). Thus, taking the velocity v_1 and angle θ_1 at this position, from the velocity v_2 at a generic position x_2 we can calculate using Eq. (5.3) the corresponding propagation angle θ_2. Using this method, we estimate the propagation angle at every axial position, obtaining the angles represented by the red marks in Figure 5.14 (b). The comparison of the angles directly measured in the simulation with the ones estimated by the Snell law shows good agreement all along the thruster axis, confirming the validity of our model. However, Figure 5.14 requires some additional discussion: firstly, we hypothesize that the origin of the underestimation of the angle in the channel is because we analyze a single time-interval and we do not consider the complex evolution of the propagation reported in previous sections. Secondly, we think that

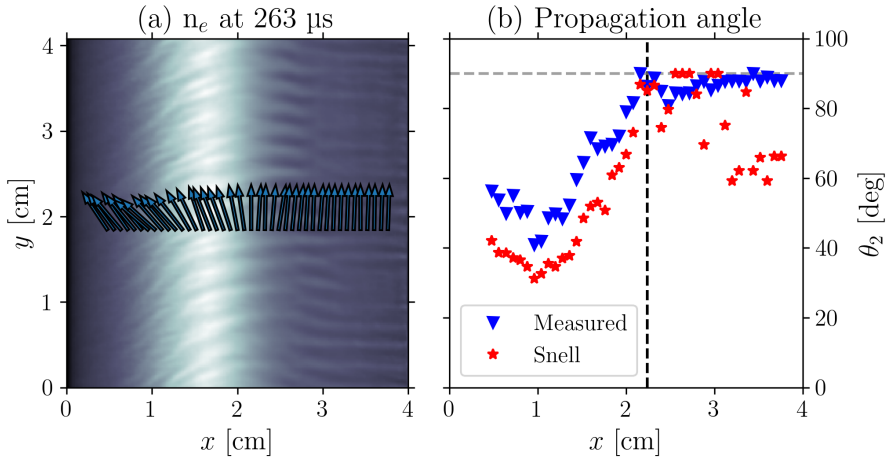


Figure 5.14: (a) An electron density snapshot and (b) the angle measured by PIC simulations (blue dots) and the one calculated using the Snell law (red dots). From Ref. [202].

the badly estimated angles in the plume are related to the rather spread out PSD2P spectra measured in this region, as visible by Figure 5.12 (i). Moreover, a phenomenon of instability convection may be present in this region of the simulation[118].

The model presented here helps us to interpret the IAW amplitude variation in Figure 5.8 (b). The IAW cannot propagate from a colder to a hotter region, since a hotter plasma corresponds to a larger propagation velocity. Thus, the IAW instability that develops in the central part of the simulation domain, is slowly convected towards the temperature peak and only a tiny fraction of its intensity can pass the barrier. When most of the instability power reaches the temperature peak and the temperature starts to decrease (at the beginning of the BM decreasing phase), the propagation is no anymore forbidden, so the instability propagates in the colder plasma at a different angle. In the previous discussion we assumed a rather simple relation of proportionality of the IAW propagation speed with the plasma temperature, that is probably true at first approximation, but that should be analyzed in more detail, since other factors may also play a role in this relation.

5.3.2 The ion transit-time instability

As shown in Section 5.2, the ITTI develops in the external part of the channel and in the plume, mainly in the decreasing BM phase. In this section, we study the analytical DR derived in Chapter 2 and we compare it to PSD2P maps that were obtained from PIC data, demonstrating the importance of considering the 2D nature of the ITTI.

5.3.2.1 The ITTI 2D spectrum

As mentioned above, the ITTI is difficult to capture since it mainly develops along the thruster axis and the standard techniques (i.e., based on the FFT) do not allow for studying the spectrum along this direction. Fernandez *et al.* [75] have calculated

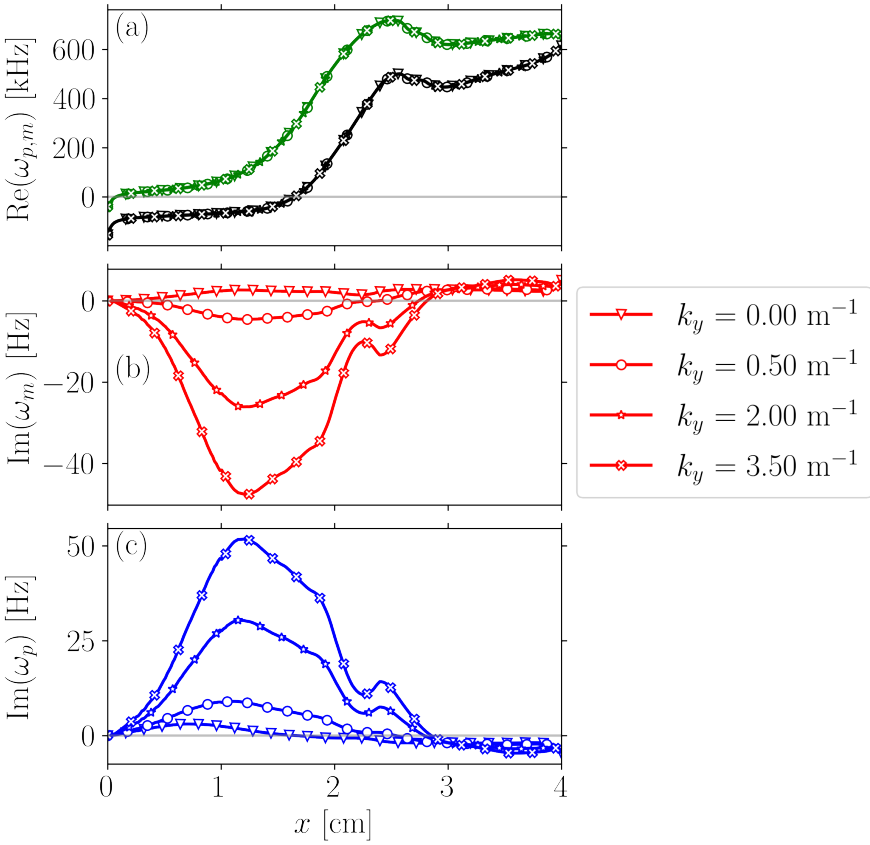


Figure 5.15: (a) The axial profile of the two ITTI branches for $k_x = 40\,\mathrm{m}^{-1}$. The *plus* branch is traced in green and the *minus* branch is in black. In (b) and (c) the lines represent the profile of γ_m (red) and γ_p (blue) for four different values of k_y. From Ref. [202].

an ITTI 1D dispersion relation by using fluid equations (continuity and momentum for ions, while the electrons are described by the continuity equation and by a drift/diffusion equation in which they introduced a collision frequency depending on the anomalous electron mobility). In Section 2.2.4, we have shown that an equivalent DR with two branches, cf. Eq. (2.17) can be obtained just by considering continuity and momentum equation for both electrons and ions. In addition, Fernandez *et al.* observed that the dispersion map calculated from their numerical experiment at the thruster exit was better described by the *plus* instability branch, with reference to the branches nomenclature given in Section 2.2.4. However, they found the paradox that in the 1D approximation this branch is stable. Here, we have shown that for $k_y \neq 0$ the *plus* branch has a positive growth rate and can be unstable.

Most of the parameters that appear in the ITTI DR can be estimated directly from the PIC simulation, while for the collision frequency appearing in Eq. (2.18) it is more subtle, because the fluid model does not consider the well-known anomalous mobility. If we consider the classical collision frequency measured in the simulation we obtain

growth rates in the kHz range, very far from what we observe in the PIC simulations. However, as suggested by Fernandez *et al.*, we can consider an *anomalous* collisionality depending on the anomalous mobility. The anomalous electron mobility in the axial direction (i. e., $\mu_{e,x}$) can be expressed, including the electron pressure gradient, as in Eq. (5.1) and the total collision frequency can then be estimated by the usual mobility formula for magnetized plasmas: $\nu_e = m_e\omega_{ce}^2\mu_{e,x}/e$. Once we have calculated the anomalous frequency, we only need to properly choose the values of axial and azimuthal wavenumbers to plot the ITTI growth rate profile along the x-axis. In the previous section we observe that the ITTI axial wavenumber can be estimated from the PSD2P maps and takes a value of $k_x \approx 40\,\mathrm{m}^{-1}$, while the azimuthal wavenumber is more difficult to estimate because of the rather broad azimuthal PSD. For this reason, in Figure 5.15 we calculate using the full ITTI dispersion (i. e., Eq. (2.17)) the axial profile of $\omega_{p,m}$ and $\gamma_{p,m}$ for four different values of k_y, always considering $k_x = 40\,\mathrm{m}^{-1}$. To have a better estimation of the growth rate it is necessary to consider the finite electron Larmor radius and electron inertia terms[132]. Figure 5.15 (a) confirms the weak dependence of the real part of the dispersion on the value of k_y, as predicted by the simplified DR in Eq. (2.18). Conversely, the imaginary part of the dispersion strongly depends on the value of k_y. If k_y is strictly equal to zero, we observe that the *minus* wave is unstable all along the axis, while the *plus* wave is unstable in the channel and damped in the plume. We observe that the *minus* wave is more damped for increasing values of k_y while the *plus* wave becomes increasingly unstable. In particular, we observe that the most unstable point of the profile is close to the ion sonic point, which was identified as the point where the ITTI grew[170].

In Figure 5.16, we show the numerical PSD2P calculated during a BM decreasing phase in the thruster plume. We observe that the ITTI *plus* wave calculated by Eq. (2.17) at the ion sonic point describes perfectly the dispersion from PIC simulations, while the *minus* wave corresponds to lower frequencies. This result, compared with the analysis in Figure 5.15, strengthens the idea that we need to consider an azimuthal component of the ITTI to predict the growth of the branch that is observed. As reported above, the main instability frequency calculated by the PSD2P is $\omega_{ITTI} \sim 350\,\mathrm{kHz}$ and propagates with a wavenumber $k_{ITTI} \sim 40\,\mathrm{m}^{-1}$ in the axial direction. In Figure 5.16 (a) we do not plot the azimuthal DR since the ITTI dispersion relation has been calculated in the small-k_y limit and it would be appropriate to plot it only for $k_y \ll k_x^{\max}$.

We can conclude that the ITTI, as the IAW, has a preferential direction (i. e., axial in this case), but that we need to consider a 2D dispersion relation to properly describe the instability growth. In particular, we have shown that the electron azimuthal drift is a paramount component of the ITTI growth rate.

5.3.2.2 The effect of the ITTI on the discharge current

In this section, we study the effect of the ITTI on a macroscopic parameter, the discharge current, that is usually analyzed in experiments through DFT techniques [171]. The discharge current that is measured in the PIC simulations at *quasi-steady-state* (for $t > 100\,\mu\mathrm{s}$) is shown in Figure 5.17 (a). In this figure, we can distinguish six BM periods. As reported in previous sections, the ITTI is stronger during the BM decreasing phase. For this reason, we expect that the effect of the ITTI on the discharge current will be visible mainly during this phase. In Figure 5.17 (b) we zoom on a

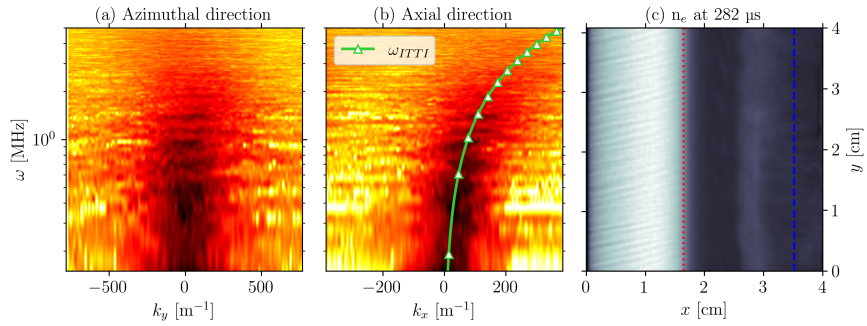


Figure 5.16: Azimuthal (a) and axial (b) PSD2Ps. In (c) a snapshot of the electron density at $t = 282\,\mu s$ is shown. The green line in (b) represents the ITTI frequency, calculated as in Eq. (2.17). The dotted vertical red line in (c) reports the position of the ion sonic point and the vertical dash-dotted blue line represents the axial position at which the PSD2P is calculated. The dispersion in the azimuthal direction is not displayed, since the expression in Eq. (2.17) was calculated in the small k_y limit. From Ref. [202].

single BM period and we clearly observe a modulation of the discharge current in the BM decreasing phase, that is not present in the BM growing phase. The large BM fluctuations in this simulation make it extremely difficult to observe precisely the ITTI in performing a FFT on the entire discharge current (even after high-pass filtering of the current signal). To overcome this issue, we have calculated the five spectra in the six BM decreasing phases, where the ITTI oscillation is stronger, obtaining the results in Figure 5.17 (c). The average spectrum in Figure 5.17 (d) evokes the presence of a modulation of the current at ≈300 kHz, that is exactly corresponding to the ITTI main frequency found in the previous section.

The ITTI is an ion instability, but until now the origin of this name could be unclear. In the previous paragraph, we have shown that it is possible to link the discharge current to the ITTI oscillations, but the mechanism has not been discussed yet. To illustrate it, in Figure 5.18 we study a single ITTI period (the one between the two vertical black lines in Figure 5.18 (a)). Looking at the evolution of the axial ion density profile in Figure 5.18 (b), we notice that the ITTI has a weak impact on the density in the channel region, while the transit of ions is visible in the acceleration region. between $t = 276.9\,\mu s$ and $279.3\,\mu s$ we observe a packet of ions moving along the acceleration region towards the cathode, creating the current modulation that we have observed. Interestingly, as soon as the packet has reached the cathode another packet starts to form at the beginning of the acceleration region. This behavior can be understood by looking at the axial electric field shape in (c). We notice an electric field well moving as the ions packet. This is particularly visible at $t = 279.66\,\mu s$, when the formation of the new packet of ions is sustained by the creation of a well in the electric field profile.

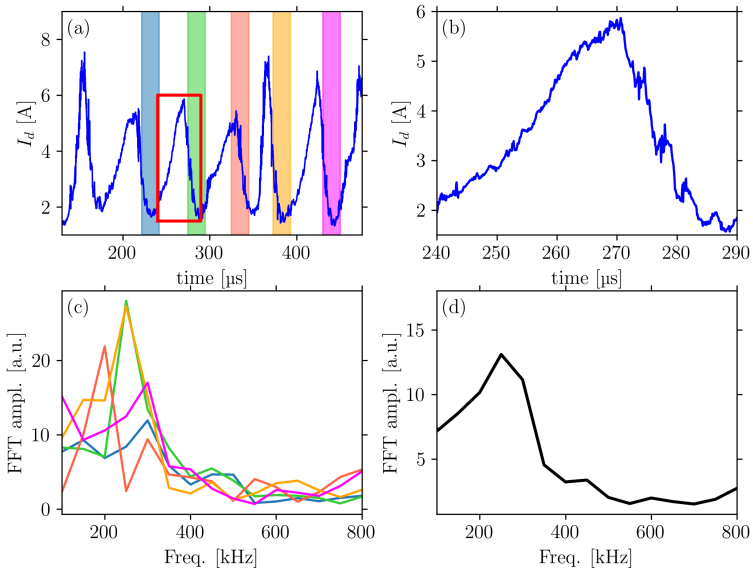


Figure 5.17: (a) the discharge current during several periods of the BM. (b) a zoom of the discharge current between 275 and 295 µs. (c) FFTs calculated from the current with the same color in (a). (d) the average spectrum. From Ref. [202].

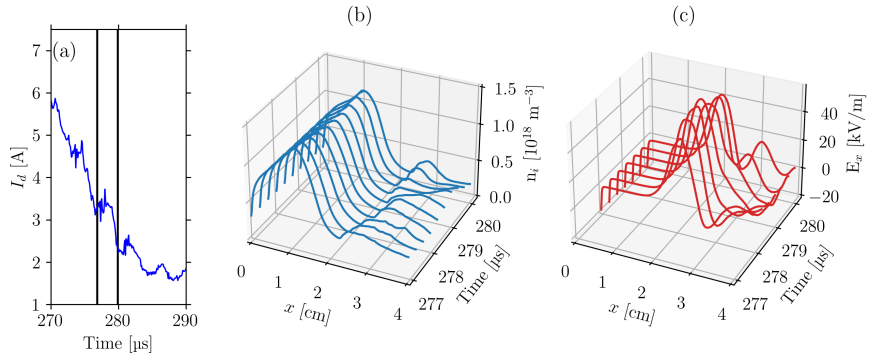


Figure 5.18: (a) The discharge current in a decreasing phase of the BM. The two vertical black lines bound a single ITTI oscillation. For this ITTI oscillation, in (b) and (c), we show the time evolution of the ion density and the axial electric field, respectively. From Ref. [202].

5.3.2.3 Number of low-speed ions in the acceleration region

The interaction of the HT plume with the spacecraft is a key parameter in the choice of the appropriate thrusting system since the backflow of charged particles can damage the spacecraft equipment or charge the spacecraft itself. In particular, the HT plume, composed of a large number of ions, has a large divergence, resulting in a high risk of ion contamination of the spacecraft surfaces [168]. The slow ions and the ions created by Charge Exchange events are more likely to return to the spacecraft, while fast ions escape more easily.

The discussion in the current Section 5.3.2 has demonstrated that the ITTI engenders the presence of slow ions in the plume, however, we have not treated an important point: which is the percentage of slow ions on the overall number of ions? To estimate the number of slow ions leaving the spacecraft, we considered the ion velocity distribution function and we studied the percentage of slow ions over the total number of ions. In Figure 5.19 we show the ion velocity distribution functions (i. e., for v_x, v_y and v_z) at four different axial positions at the end of a decreasing BM cycle. In (a) we observe that near the anode there is a backflow of ions (i. e., $\langle v_x \rangle < 0$), while the distribution along y and z is rather Maxwellian. At the channel center (b) we observe that ion drift is low: this is expected since the ions have not yet crossed the acceleration region. At the channel exit (c) most of the ions have been accelerated: we observe a strong asymmetry in the distribution along x. Finally, at the cathode (d) we observe again a strong asymmetry in the distribution along x and we distinguish two families of ions: the slow ions (shaded blue band) and the fast ions (shaded red band). The number of slow ions appears to be non-negligible with respect to the number of fast ones.

In Figure 5.20 we show the time evolution at a quasi-steady-state of the percentage of slow (b) and fast (c) ions. The slow ions are counted by integrating the peak of the distribution corresponding to the blue shaded band in Figure 5.19, while the fast ions are calculated by integrating the distribution in the proximity of the peak with the highest velocity (red shaded band). Moreover, Figure 5.20 (a) shows the velocity corresponding to the max of the fast (orange) and slow (red) ions peak and (d) the discharge current. In (a) we observe that the velocity of the fast ions is fluctuating around the nominal value given by

$$v_{x,\max} = \sqrt{2V_0/m_i}.$$

The percentage of slow ions needs to be compared with the different phases of the BM cycle. During the growing phase, where the ITTI is weak, the number of slow ions is rather low, almost null. Conversely, during the BM decreasing phase we observe in the evolution of the slow ions' percentage the usual modulations: some ions' packets push the fraction of slow ions up to the 40% of the total. A peak is usually followed by a valley, where the number of slow ions is similar to the value in the growing phase of the BM cycle. The number of fast ions in (c) represents approximately 80% of the total number of ejected particles, meaning that the number of slower ions is never negligible, but that the number of fast ions is almost always the dominant one. The modulation frequency of the number of slow ions during the BM decreasing phase is of the order of 300 kHz, so very close to the ITTI frequency discussed above.

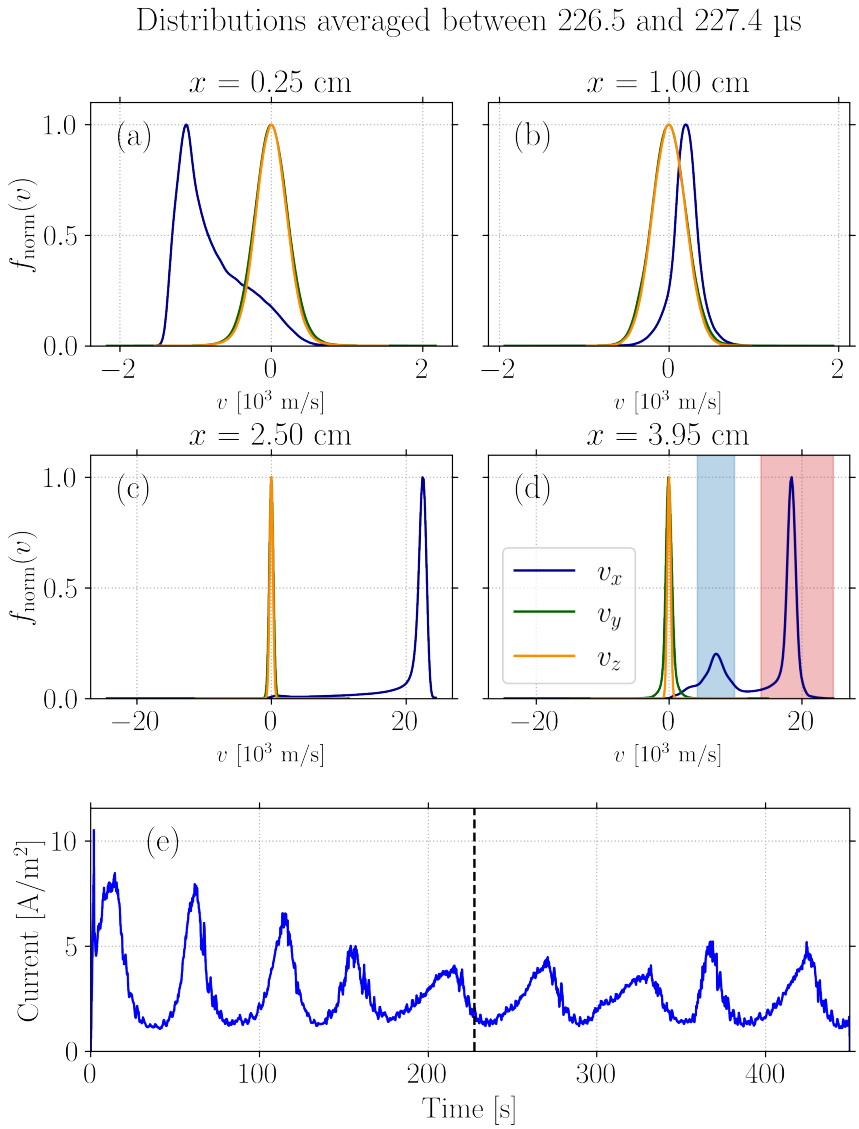


Figure 5.19: (a-d) Ion velocity distribution functions at four different axial positions at the end of a decreasing BM cycle, corresponding to the time indicated by the dashed line in (e). In (d) the shaded blue band represents the slow ions, while the shaded red band represents the fast ions.

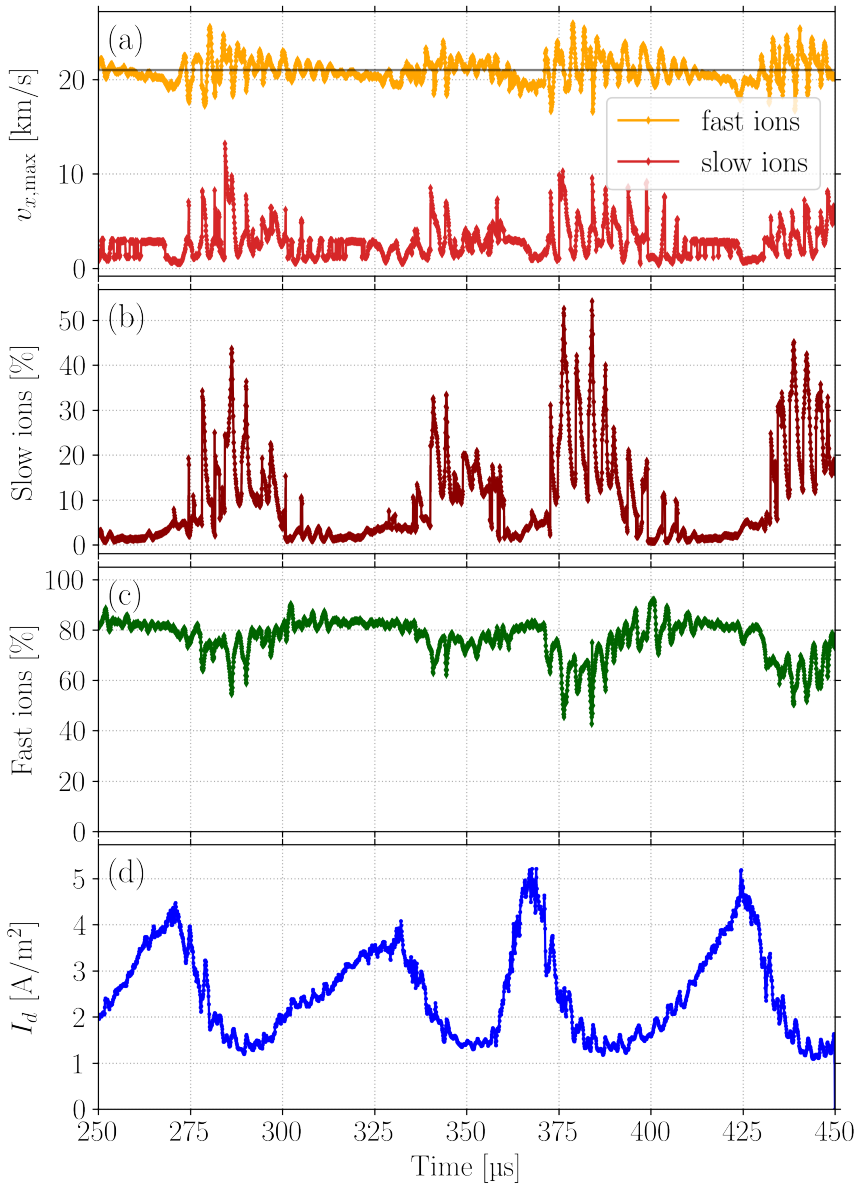


Figure 5.20: (a) Velocity of the slow (red) and fast (orange) ions packets. Percentage of slow (b) and fast (c) ions. (d) Discharge current density.

5.4 CHAPTER SUMMARY

The theoretical DRs of IAW and ITTI derived in Chapter 2, have been compared in this chapter with some results of PIC simulations. In particular, we demonstrated the need to consider the multidimensional nature of these instabilities to fully understand their origin and characteristics.

First of all, although the IAW is usually considered as a purely azimuthal instability, here, we have shown that it is important to consider the bi-dimensional nature of this instability to understand its growth and evolution. The PSD2P technique allowed us to demonstrate the good agreement between the spectral maps calculated in axial and azimuthal directions with the analytical DR. Moreover, the analysis of a sequence of time intervals has shown that this instability develops at the external part of the thruster channel (i. e., near the channel exit between 2 and 2.5 cm in this work case) and subsequently propagates inwards (towards the anode) and outwards (towards the cathode). Calculating the spectrum at different axial positions with the PSD2P technique has allowed us to study the shape of this instability along the thruster axis. With a simple analogy with the propagation of acoustic waves in media with different refractive indexes, we have explained how the temperature gradient in the inner part of the thruster channel generates the change of direction of the propagation fronts.

Secondly, we have shown that the ITTI, which is usually considered as a purely axial instability, is also influenced by the azimuthal direction. We have calculated the ITTI dispersion relation with a non-zero azimuthal component. The $k_y \neq 0$ has a weak impact on the real part of the DR, which is well described by a purely axial DR. However, it has a strong effect on the imaginary part of the DR and it explains why the *plus* wave is observed, and not the *minus* wave. When we considered an anomalous collisionality (related to the anomalous mobility in the axial direction), the ITTI growth rate is consistent with the growth time that we observe in the PIC simulations. It is possible to identify the packets of ions traveling from the density peak outwards (the ITTI is an instability related to the ion transit in the acceleration region) and to recognize their effect on the discharge current and the population of slow ions in the plume. This observation suggests a possible way to detect experimentally this instability on real devices.

6 VIRTUAL RADIAL (THIRD) DIMENSION

The radial direction plays a crucial role in the performance of HTs, however, it is not included in 2D axial-azimuthal simulations. In this chapter, the feasibility of incorporating radial effects into 2D models, without the need for 3D simulations, is explored. To account for radial boundaries, a Bohm flux of particles is removed from the simulation. Additionally, using a simplified model, the impact of Secondary Electron Emission (SEE) on the discharge is examined and it appears to have little effect. Finally, a comprehensive analysis of a self-consistent simulation that includes the radial direction is reported.

Chapter contents

6.1 Third radial dimension modeling . . . 138
6.1.1 Choice of the model for the virtual-*r* . . . 139
6.1.2 The Bohm flux at the walls . . . 139
6.1.3 Numerical implementation of the virtual-*r* . . . 140
6.2 Study of the effect of the virtual-r in 2D axial-azimuthal PIC simulations . . . 144
6.2.1 Macroscopic effects of the virtual-*r* . . . 146
6.2.2 Influence of the virtual-*r* on the instabilities . . . 153
6.2.3 Effect of the virtual-*r* on the thruster performance . . . 160
6.2.4 Summary of important results . . . 163
6.3 Secondary Electron Emission effects . . . 163
6.3.1 SEE Model . . . 163
6.3.2 SEE in virtual-*r* PIC simulations . . . 165
6.4 Analysis of consistent virtual-*r* width . . . 166
6.4.1 PIC results . . . 166
6.4.2 Mass utilization efficiency . . . 169
6.5 Chapter summary . . . 170

These results were partially presented at the 2022 IEPC meeting in Boston, Massachusetts (USA), please refer to Ref. [192] for the conference proceedings.

6.1 THIRD RADIAL DIMENSION MODELING

So far, we have used 2D PIC simulations, either in the radial-azimuthal plane (cf. Chapter 4), or in the axial-azimuthal plane (cf. Chapter 5) but it is quite clear that 3D modeling of the plasma is necessary to have a complete and consistent description of the discharge. However, 3D modeling requires large computational resources. In this chapter, we investigate the possibility of including radial effects in the 2D modeling, without the need for a 3D simulation. Antoine Tavant in the final chapter of his thesis [152] has shown that the radial absorption of charged particles in axial-azimuthal simulations plays an important role in determining the discharge main parameters. In the current chapter, we discuss the limitation of his model and we introduce an improved model of the radial dynamics in an axial-azimuthal simulation. In the following, we refer to the model of radial direction as the *virtual third direction*, or virtual-*r*.

The use of a virtual third direction has largely been used in radial-azimuthal simulations [106, 113, 180], where the out-of-plane electric field provides an energy that is not otherwise dissipated by the system (because the particles are constantly accelerated along this direction). In the axial-azimuthal simulations considered here, the energy injected in the system by the axial electric field is dissipated by the particles leaving the simulation domain at the axial boundaries (i. e., anode and cathode). For this reason, we do not observe a dramatic growth of the system's total energy. Nevertheless, the use of a third virtual dimension (a virtual radial direction model) in axial-azimuthal simulations introduces radial losses (that exist in reality) and can therefore increase significantly the accuracy of these simulations.

The first model of virtual radial dimension was introduced in Refs. [55, 99], where the authors used an artificial collision frequency (function of the particle energy) to consider the isotropic reflection of electrons by the wall. In more recent years, Tavant [152] considered a kinetic model, similar to the one used in radial-azimuthal simulations for the virtual axial direction [105]. In his work, Tavant used a thermal flux of particles leaving the simulation domain at the radial walls: an equal number of electrons and ions was absorbed radially at each time step. However, the particle flux at the radial boundaries is far from being thermal: the radial flux is a Bohm flux, as described in Chapter 1. The first attempt to consider the radial losses as a Bohm flux of exiting particles in a 2D PIC-MCC code was made by Fubiani and coworkers [100, 114]. They modeled the ion losses in the third direction by introducing an artificial loss frequency proportional to the Bohm velocity, while considering a thermal flux of electrons at the wall (i. e., only high-energy electrons are absorbed at the walls). However, this model does not maintain the overall charge neutrality in the simulation, which must be maintained at all times, when walls are made of ceramics. For this reason, in our work we consider a Bohm flux of ions leaving the domain and we remove from the simulation an equal number of electrons, the most energetic ones, so that the charge absorbed by the walls is globally zero. Moreover, we show that the choice of the third direction thickness plays a fundamental role and requires careful consideration.

The virtual radial model is reported from Section 6.1.1 to 6.1.3, while in Section 6.2 we discuss the results from PIC simulations. In particular, we show how the introduction of the virtual third dimension affects the discharge dynamics. Section 6.2.2

is devoted to the analysis of the effect of the virtual-r on the plasma instabilities. The macroscopic effects on the thruster performance are addressed in Section 6.2.3. Then, in Section 6.3 we introduce the SEE in our virtual-r model, studying its effect on the discharge dynamics. Along with SEE, we introduce the mechanism of neutral repopulation from the ions hitting the walls. Finally, in Section 6.4 we analyze a self-consistent simulation in which the virtual-r thickness is chosen equal to the real device dimensions.

6.1.1 Choice of the model for the virtual-r

Tavant in his thesis [152] proposed a *kinetic* model for the virtual radial dimension with two major drawbacks: (i) the ion flux leaving the plasma at the walls was a thermal flux, rather than a Bohm flux, and (ii) electrons were absorbed radially in the entire simulation domain and not only in the channel part. Here, we propose a different model that considers a more realistic Bohm flux of particles leaving radially the simulation domain, only in the thruster channel and not in the plume.

6.1.2 The Bohm flux at the walls

To model the virtual radial direction, we consider the plasma as a fluid. As demonstrated in Section 1.2.2, a charged sheath forms at the plasma boundaries. The sheath is a non-neutral charge region, thus, an electric field directed towards the wall forms. This field accelerates the ions towards the wall and repels the electrons, reducing the electron thermal flux that is absorbed by the walls. The ion flux towards each wall can be obtained from Bohm theory [1] and reads

$$\Gamma_{\mathrm{i}} = hn\sqrt{\frac{k_B T_e}{m_i}}, \tag{6.1}$$

where n is the plasma density in the center of the bulk and h is the ratio between the plasma density at the sheath edge and the center [83]. The electron flux is essentially a thermal flux, that can be expressed as

$$\Gamma_{\mathrm{e}} = \frac{n\bar{v}}{4}\exp\left(\frac{eV_f}{k_B T_e}\right),$$

with $\bar{v}$ the electron mean velocity in a Maxwellian distribution and V_f, that is negative, the potential difference between the wall and the bulk, named *floating potential*. The floating potential is not calculated self-consistently by the simulation, thus, it is not possible to directly use the formula above to extract the right number of electrons. Some previous works [99, 114] proposed to set a constant voltage drop $\Delta\Phi$ and absorb all the electrons with an energy larger than the given value. However, this approach is not realistic, since the potential difference between the wall and the bulk depends on the plasma characteristics, which vary considerably along the thruster channel. Moreover, it is difficult to conserve the overall charge neutrality, which is mandatory in the case of dielectric walls, if the absorption at the walls of electrons and ions follows two different mechanisms without any feedback between them. For this reason, it is necessary to first use the Bohm flux of ions and then assume that the number of ions and electrons absorbed at the wall is the same.

6.1.3 Numerical implementation of the virtual-*r*

Once we have calculated the flux, we calculate the number of outgoing particles per cell at each time step, as

$$N_{\mathrm{i,exit}} = 2\frac{\Gamma_{\mathrm{i}}\Delta t dx dy}{q_f L_z}, \tag{6.2}$$

where q_f is the weighting factor and L_z a typical thickness of the z (radial) direction. The factor 2 considers the two walls (e. g., internal and external radial boundaries of the thruster channel). The choice of the thickness L_z is crucial since in standard 2D simulations we do not need to define the thickness of the out-of-plane dimension. As highlighted in Chapter 1, the weight factor q_f in 2D simulation represents the weight of a superparticle on the bi-dimensional plane. Thus, its unit is one over a meter. The particles that move in this bi-dimensional grid are *degenerated* in the third dimension. When working with motion along the third direction, it is necessary to define a length L_z, otherwise, the particles along this direction are not well defined. So, we can define the non-dimensional weight factor $\tilde{q}_f$ as

$$\tilde{q}_f = q_f L_z. \tag{6.3}$$

By defining $\tilde{q}_f$, we are imposing that the particles are vertical segments of length L_z moving in the xy-plane. Defining this length is necessary to have a dimensionless number of exiting particles, but the choice of its value could be somehow arbitrary. Varying this number changes the charge of each superparticle; therefore, the larger is L_z, the greater the charge of each superparticle and the smaller is the number of particles we must remove from the simulation to absorb a Bohm flux at the walls. From the number of exiting particles at each wall, we can calculate the current density absorbed for each species as

$$J_{\mathrm{abs,i,e}} = e\frac{N_{\mathrm{i,exit}}\tilde{q}_z}{\Delta t dx dy}.$$

The previous equations, with no surprise, simplifies to

$$J_{\mathrm{abs,i,e}} = 2e\Gamma_{\mathrm{i}}.$$

So, the exiting current density does not depend on the choice of L_z, while the absolute number of absorbed superparticles does. The physical interpretation of the quantity in Eq. (6.3) is not trivial. In the following, we try to give two possible interpretations of it, depending on what we think a 2D simulation represents.

i. If we interpret the 2D simulation as the simulation of an infinitely thin slab of plasma in the bulk, it is arduous to give a physical interpretation of this out-of-plane dimension. This length should not be considered as a physical length or the real device thickness. A scheme of the thin slab in the plasma bulk is reported in Figure 6.1 (a).

   To better understand this interpretation, let us consider two different configurations of plasma between two walls: one such as the walls are separated by a length $\tilde{L}_1$ and the other by $\tilde{L}_2$, with $\tilde{L}_1 \ll \tilde{L}_2$. Assuming the plasma bulk

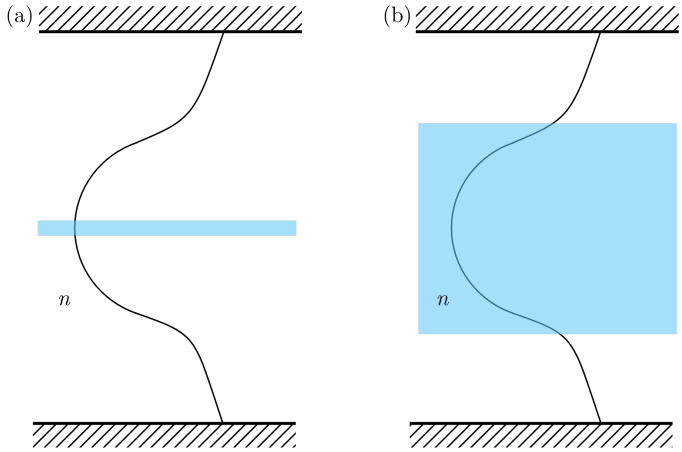


Figure 6.1: Black lines: plasma density profile between two walls. (a) interpretation of the 2D simulation as a thin slab of plasma at the bulk center. (b) interpretation of the 2D simulation as a thick slab of plasma accounting for the entire bulk.

at equilibrium, with the same plasma characteristics in the two cases (i. e., same n, T_e, and h), we have that the exiting current density at the walls is the same. However, the number of absorbed particles is different: the larger is $\tilde{L}$, the smaller is the number of absorbed particles. So, when we use $\tilde{L}_2$, we are absorbing a way lower number of particles in comparison to the case when we use $\tilde{L}_1$. Thus, in two situations in which the bulk is the same, the number of removed particles from the 2D simulation is different. This number does have an impact on the characteristics of the infinitely thin plasma slab at the center of the bulk.

Therefore, in this first interpretation, the number of absorbed particles is not related to the real device thickness, but to the arbitrary choice of L_z. The most reasonable value of L_z can only be estimated by simulation tests.

ii. In the second interpretation, the 2D simulation does not represent anymore a thin slab of plasma at the center of the bulk, but rather a thick slab of bulk plasma. In this case, the thickness of the slab is given by L_z and the plasma can be considered homogeneous in the out-of-plane direction. The number of absorbed particles is related to the real device thickness: the larger is L_z, the fewer particles are absorbed at the walls and the less the bulk plasma is affected by the radial losses. This is physical: a very thick bulk plasma is less affected by the radial losses than a thin one. See Figure 6.1 (b) for a schematic interpretation of this idea.

Whatever interpretation we choose, it is essential to characterize the parameter L_z by simulation tests. In the following, we examine different L_z to understand which one better helps in the description of the thruster physics and which are the

important parameters. At the end of this chapter, we analyze a simulation in which the value of L_z is chosen to be the same as the real device thickness.

In the PIC code the virtual radial direction is implemented in this way: first, we calculate the number of exiting particles for each grid domain as in Eq. (6.2) and from that the total number of particles exiting in a MPI domain (normally these domains do not exceed the size 1.6 mm $\times$ 1.6 mm). Then, we remove an equal number of electrons and ions in each MPI domain: the absorbed electrons are the most energetic ones, while no energy ordering is done for the ions.

The h-factor

In Eq. (6.1), the h-factor represents the edge-to-center density ratio. This value needs to be inserted as an input in our simulations. From the literature [63, 83], we have that in low pressure plasmas, like the one of HTs, h is close to 0.5. We decided to use this value in our simulations. To demonstrate the validity of this assumption we can use the simulations in the radial-azimuthal domain, which allow calculating this value. Figure 6.2 shows the species density profiles (a) and the net charge density (b) at the steady-state of the radial-azimuthal benchmark simulation [180]. We observe that a positively charged sheath exists near the walls, indeed in that region, we have $n_i > n_e$, while the internal (i. e., bulk) plasma remains quasi-neutral. To define the sheath edge, we use the following definition: the sheath edge is the point at which the Bohm velocity is equal to the ion fluid velocity [98]. By that definition, using as input the values from the radial-azimuthal simulation, we have that the h-factor is equal to 0.46, i. e., close to the value of 0.5 used in our simulations.

The current profiles

In Figure 6.3 we show the case of a channel depth of 2.5 cm. The input parameters of this simulation are those used for the axial-azimuthal simulations in Chapter 5, with the value of L_z equal to 2 cm and L_y = 1 cm. In red we show the profile of the ion absorbed current density by the walls, $J_{\text{abs,i}}$. The blue dashed, dotted and solid lines represent the electron, ion, and total axial current densities, respectively. One can notice that the total current density is rather constant and that the current in the plume is dominated by the ions, which is what we expect from a thruster. The radial current density calculated from the radially absorbed particles (red markers) corresponds to the Bohm current density profile (i. e., black line), as calculated using the local (i. e., at the corresponding axial position) plasma density and temperature. The large temperature and density make the Bohm current profile reach a maximum near the exit of the thruster channel: it is here that most of the particles are absorbed at the walls. We notice also that a small number of particles is absorbed near the anode. As one observes in Figure 6.3, the particles are not absorbed in the plume, i. e., for $x > 2.5$cm. This choice does have an impact: if we had not considered the channel/plume difference a large number of particles would have been absorbed in the near plume. The effect of the plume divergence has not been investigated here.

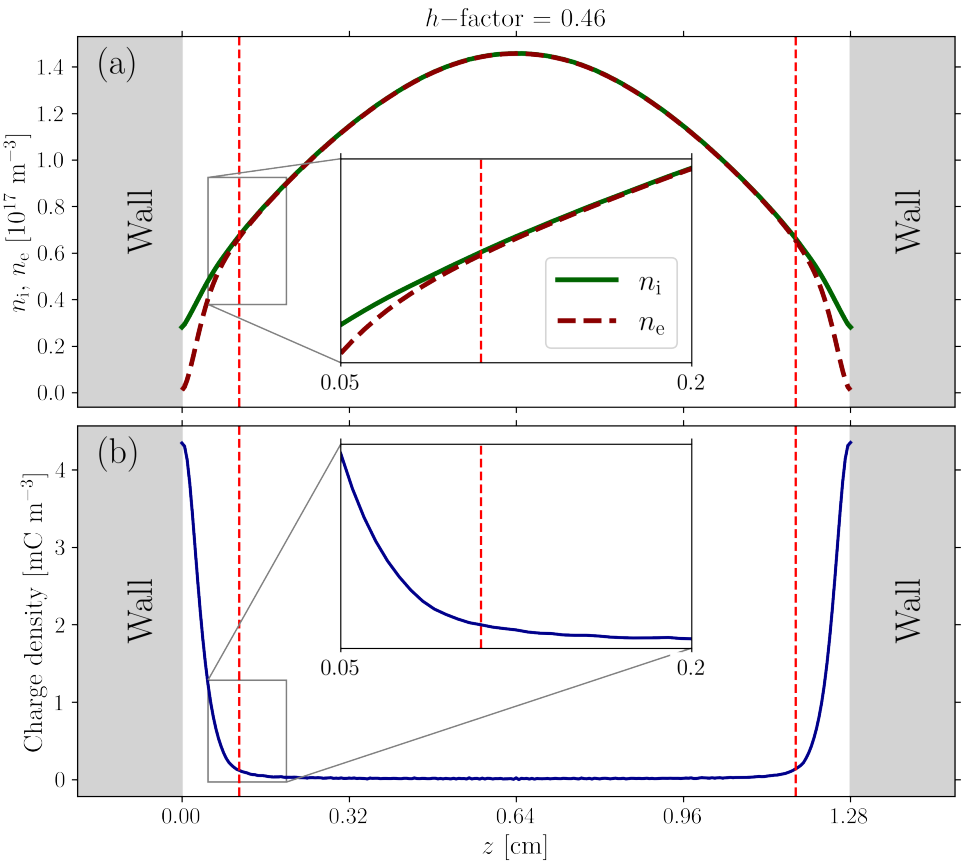


Figure 6.2: Radial (along z) profiles of (a) the electrons (brown) and ions (green) density and (b) charge density. The insets show the sheath-bulk transition. The red dashed lines delimit the sheath region. The test case corresponds to the radial-azimuthal benchmark [180] and the profiles are calculated at steady-state.

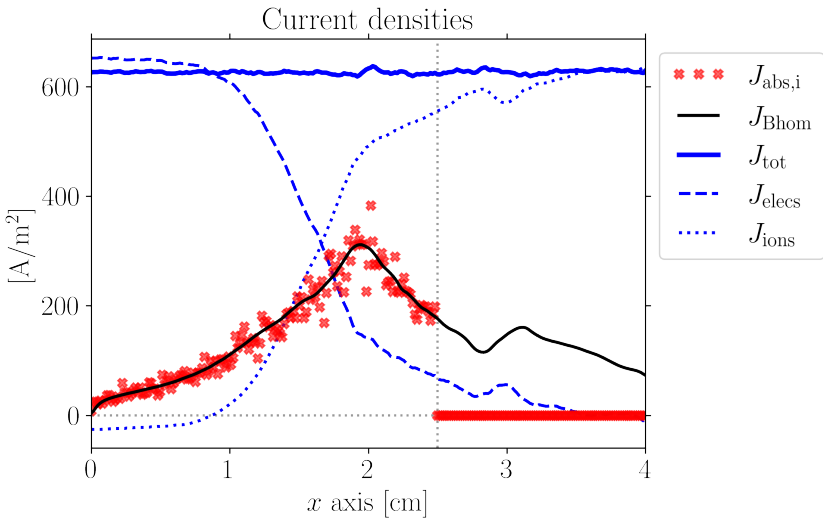


Figure 6.3: Blue dashed, dotted and solid lines represent the electron, ion, and total axial current densities at quasi-steady-state, respectively. The red markers represent the radial current density calculated from the radially absorbed particles and the black line represents the Bohm current density profile, calculated using plasma density and temperature. As one may notice, any particle is removed in the plume (i. e., for $x > 2.5\,\text{cm}$).

6.2 STUDY OF THE EFFECT OF THE VIRTUAL-R IN 2D AXIAL-AZIMUTHAL PIC SIMULATIONS

We present in this section the simulation that has been run to study the effect of the radial virtual dimension. The simulation domain is the one largely described in Chapters 3 and 5. As before, two different azimuthal domain lengths are investigated: first a reduced $L_y = 1\,\text{cm}$ domain and subsequently a domain with $L_y = 4\,\text{cm}$. The parameters of the simulations are reported in Table 6.1. The L_z tested are: 1 cm, 2 cm, and 4 cm, and correspond to 64, 128, and 256 grid points, respectively. The length L_z is varied in a range such that in some cases we are underestimating the real device dimension, while in some others we are overestimating it. This is done to test the effect of the virtual dimension on the simulation results, exaggerating or reducing the effect of the virtual dimension. The self-consistent case in which the L_z takes the real device dimension is analyzed later in this chapter.

The current and potential evolution for the simulation with $L_y = 1\,\text{cm}$ are reported in Figure 6.4 (a) and (b), respectively. As in Section 3.4, the current and potential evolutions are well controlled by the *RLC* filter. The average current decreases for decreasing value of L_z. Moreover, the BM oscillations appear to be more damped when the virtual-*r* is used.

In Figure 6.5 (a) and (b) we report the current and potential evolution in a case where the azimuthal domain length is increased to $L_y = 4\,\text{cm}$. The current and potential evolution are still well controlled by the *RLC* and the mean discharge current is still reduced by the presence of the virtual radial dimension. However, it

Table 6.1: Operating and numerical parameters used in PIC simulations.

Physical parameters	Symbol	Value	Unit
Gas		Xenon	(-)
Radial magnetic field (max)	B	170	G
Anode voltage	V_a	300	V
Cathode voltage	V_c	0	V
Axial length	L_x	4	cm
Azimuthal length	L_y	1 or 4	cm
Initial plasma density	n_0	1×10^{18}	m^{-3}
Initial electron temperature	T_e	1	eV
Initial ion temperature	T_i	0.05	eV
Neutral mass flow rate	$\dot{m}$	3.5	$\mathrm{mg\,s}^{-1}$
Thruster section	$Area$	3.768×10^{-3}	m^2
Internal radius	R_{int}	2.05	cm
External radius	R_{ext}	3.55	cm
Cathode injection temperature	T_e^{cath}	5	eV
Circuit parameters			
Resistance	R	120	Ω
Inductance	L	4.4	mH
Capacitance	C	15	nF
Simulation parameters			
Time step	Δt	1.6×10^{-11}	s
Cell size	$\Delta x = \Delta y$	1.6×10^{-4}	m
Number of cells	$x_{\max} \times y_{\max}$	250×63 or 255	(-)
Particles per cell init.	N/NG	400	particles/cell
Superparticles weight	q_f	6.5×10^7	m^{-1}
Iterations between outputs	N_a	5000	(-)
Permittivity scaling	α^0	64	(-)

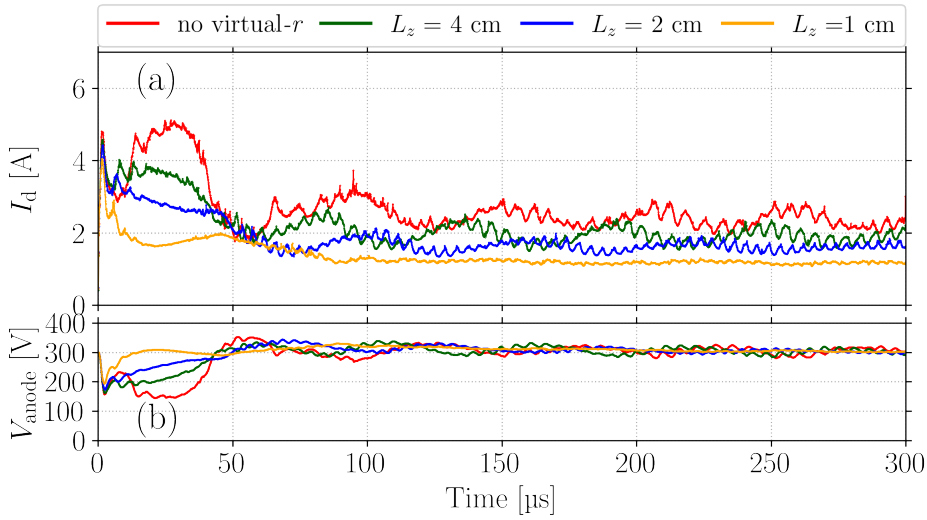


Figure 6.4: Plasma potential (a) and current (b) density profiles for the simulation with L_y = 1 cm for different values of the virtual-r length.

is clear that the circuit has more difficulties in controlling the current and potential oscillations: the anode potential continues to fluctuate and never really stabilizes at the nominal value, as it does in the case of a reduced azimuthal length. The amplitude of the BM oscillations appear to be reduced, but current and potential do not reach the quasi-steady-state that were observed in the case of L_y = 1 cm.

6.2.1 Macroscopic effects of the virtual-*r*

The time evolutions of the current and potential in Figures 6.4 and 6.5 show that these parameters do depend on the choice of the virtual dimension thickness. To quantify the dependence of these parameters on the L_z dimension, we report in Figure 6.6 the mean and standard deviation values for the current and the potential for each case.

The mean (time-averaged) current in Figure 6.6 (a) decreases with the decrease of L_z. This is expected: the plasma density is smaller when radial losses are larger, resulting in a decreasing current. Remarkably, there is a rather good agreement between the current evolution with small and large azimuthal lengths. We highlight that the simulated currents are comparable to those measured in the PPSX00 [154, 195] (i. e., I_d between 0.7 A and 3.3 A, since the simulations used the typical parameters of this particular thruster). However, some differences remain since the simulations still lack important features (3D, SEE, *et cetera*).

The amplitude of the BM relative to its mean value does not seem to depend on the value of the virtual-r length L_z: we observe in (b) that the relative standard deviation of the current divided by its mean value is almost constant. The mean value of the potential at the anode, reported in (c), does not depend on L_z.

The average voltage depends on the value of the azimuthal length L_y. With a small L_y, the anode voltage is on average larger than the nominal voltage (i. e., set to 300 V), while for large L_y the anode voltage is on average smaller than the nominal voltage.

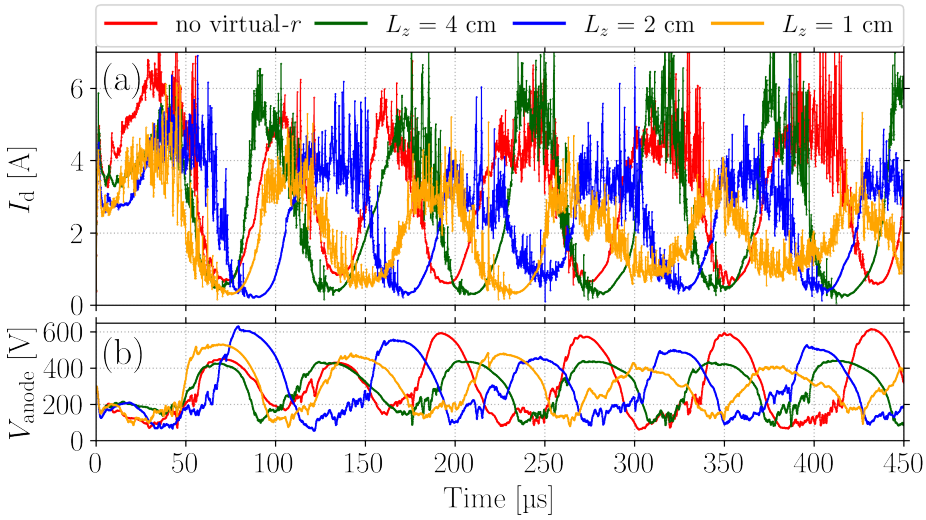


Figure 6.5: Plasma potential (a) and current (b) density profiles for the simulation with L_y = 4 cm for different values of the virtual-r length.

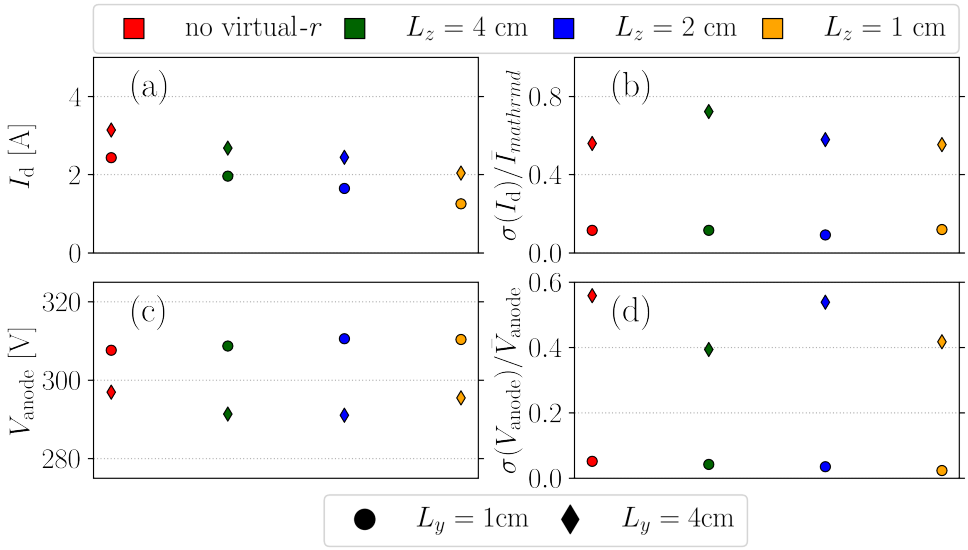


Figure 6.6: Mean (a) and relative standard deviation (b) of the current. Mean (c) and relative standard deviation (d) of the anode voltage. The circles represent the results obtained with L_y = 1 cm, while the diamonds represent the results obtained with L_y = 4 cm. The colors are indicated on top.

The relative standard deviation of the anode voltage, reported in (d), is larger for large L_y than for small L_y. This is because the BM oscillations are damped more effectively in the case of small L_y. As for the current, the relative standard deviation of the anode voltage in (c) does not depend on the value of L_z. Its value is rather close to zero when $L_y = 1\,\text{cm}$ (i. e., almost no BM), while it is larger when $L_y = 4\,\text{cm}$. A high-frequency modulation of the discharge current is visible in all cases, even though it is more difficult to identify in the case of large L_y. The frequency of these oscillations depends on the value of L_z: it is larger for thin L_z and smaller for large L_z.

6.2.1.1 Current absorbed at the walls

The electron/ion current absorbed at the walls is an important parameter to evaluate the accuracy of the virtual third dimension and to estimate the number of particles absorbed at the walls. By construction, the overall absorbed current is strictly zero, since we impose an equal contribution of electrons and ions. Nevertheless, the comparison of the one-species current exiting with the overall current in the device provides some information about the wall losses. This current, named hereafter $I_{\text{abs,i}}$, is calculated by rescaling the current absorbed in the simulation in an area $2L_yL_{\text{ch}}$, by the walls area of real device $2\pi\left(R_{\text{int}} + R_{\text{ext}}\right)L_{\text{ch}}$. The ratio between the current exiting at the walls and the discharge current indicates the number of ions that are absorbed at the walls for every ion accelerated to produce thrust, assuming that the current at the thruster exit is composed only of ions. The results for the different L_z values are shown in Figure 6.7.

Figure 6.7 (a) and (b) show the time evolutions of the total absorbed current for different L_z thicknesses: $L_y = 1\,\text{cm}$ (a) and $L_y = 4\,\text{cm}$ (b), respectively. We observe in both cases the BM modulation of the current (also observed in Figure 6.4 and 6.5). In Figure 6.7 (c) and (d) we show the ratio between the absorbed current and the total axial current, for $L_y = 1\,\text{cm}$ (a) and $L_y = 4\,\text{cm}$ (b), respectively. In (c) we observe that the BM modulation has almost disappeared: the ratio $I_{\text{abs,i}}/I_{\text{d}}$ is almost constant over time. We notice that when L_z is smaller the exiting current intensity is smaller. The results with an increased azimuthal length are more difficult to interpret, as can be seen in (d). In Figure 6.8 we can observe the corresponding mean values. In Figure 6.8 (b) we notice that the smaller the radial thickness, the smaller the ratio between the current absorbed at the walls and the axial discharge current. For $L_y = 1\,\text{cm}$ and $L_y = 4\,\text{cm}$ this ratio decreases in the same way. An interesting observation is that when L_z is larger, we absorb more current (that corresponds to a lower number of particles), since the plasma density and electron temperature are larger.

In Section 6.2.1 we have shown that the mean current does not depend much on the azimuthal length. Here, we observe that the radial current does. The large simulation domains, where the BM remains strong, show a larger radial current, which is about 30% to 50% larger. This fact suggests that the different dynamics developing when we consider larger azimuthal simulation domains favor the wall losses. The first suspect is, clearly, the BM. How can the presence of this instability in the case of $L_y = 4\,\text{cm}$ affect the wall losses? Considering that the BM depends on the ionization rate [175], while Eq. (6.1) depends on the electron temperature, we can hypothesize

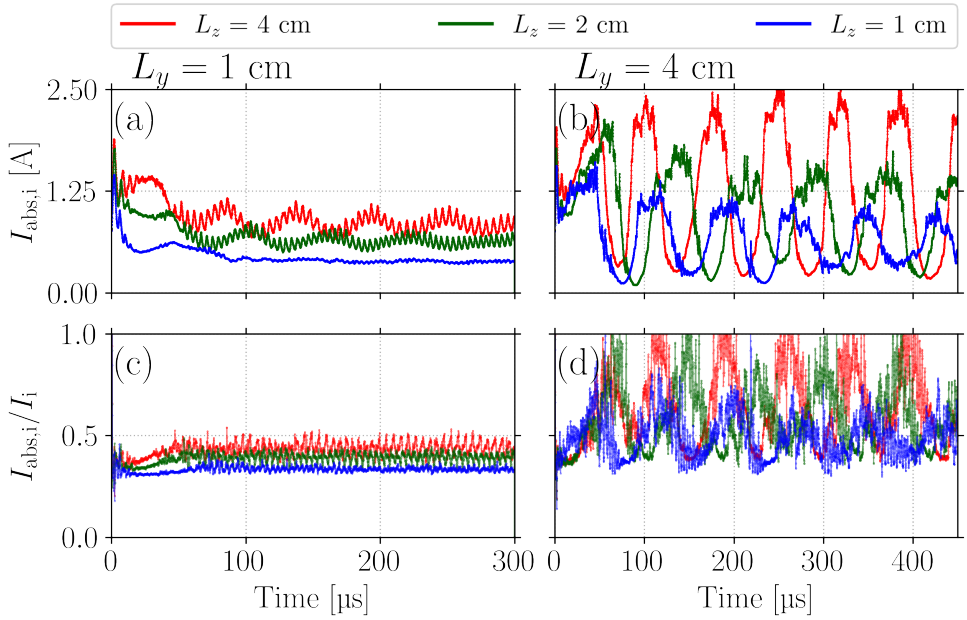


Figure 6.7: Absorbed current for $L_y = 1$ cm (a) and $L_y = 4$ cm (b), respectively. The absorbed current is divided by the total axial current for $L_y = 1$ cm (c) and $L_y = 4$ cm (d), respectively.

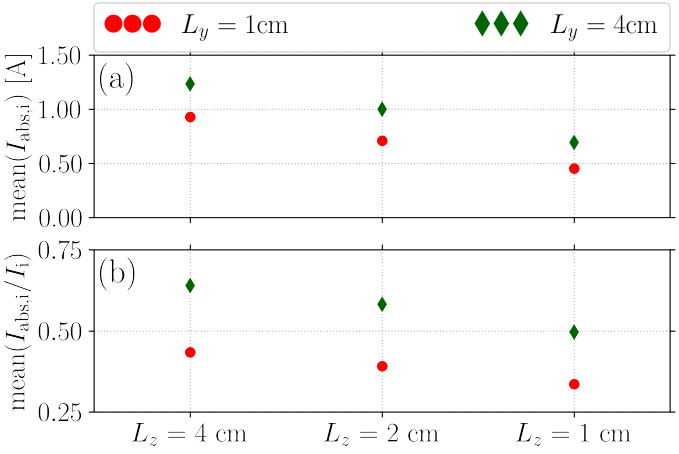


Figure 6.8: (a) mean absorbed current for $L_y = 1$ cm (circles) and $L_y = 4$ cm (diamonds). (b) Ratio of the absorbed current over the total axial current for $L_y = 1$ cm (circles) and $L_y = 4$ cm (diamonds).

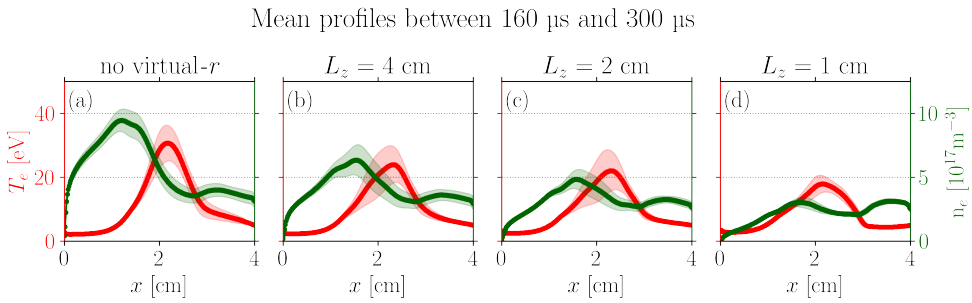


Figure 6.9: Electron temperature (red) and density (green) for $L_y = 1$ cm with different L_z. The shaded area shows the standard deviation around the mean value.

that the fluctuations of these quantities along a BM cycle are responsible for the larger wall losses. In the next section, a more detailed analysis of these plasma parameters is presented.

6.2.1.2 Effect of the virtual-r on the plasma parameters

To understand how the absorbed radial current depends on the choice of the azimuthal length we need to investigate how the plasma parameters vary in the simulations described above.

Small simulation domain in the azimuthal direction ($L_y = 1$ cm)

As seen in Eq. (6.1) the electron temperature and density define the Bohm flux of particles leaving the simulation domain. In this section, we analyze the evolution of these quantities in the simulations with an azimuthal length of $L_y = 1$ cm. The evolution of the electron temperature and density profiles are difficult to represent. So, we show in Figures 6.9 and 6.10 the mean profiles and the time evolution of these quantities in some selected points, respectively.

The density profiles in Figure 6.9 (green line) is strongly affected by the presence of the virtual third dimension. We see that the maximal average density decreases from $\approx 10 \times 10^{17}\,\mathrm{m}^{-3}$ to $\approx 3 \times 10^{17}\,\mathrm{m}^{-3}$. The oscillations around the mean value are much stronger when L_z is larger, while the decrease of L_z reduces significantly the fluctuations amplitude, cf. (d). Conversely, the density profile in the plume (i. e., for $x > 2.5$ cm) remains almost unchanged in all four cases. In Figures 6.10 (e-h) we draw the evolution of the density at four different axial positions: near the anode (red line), in the center of the channel (green line), at the channel exit (blue line) and in the plume (yellow line). We observe that the density near the anode and in the channel is strongly reduced by the virtual radial direction, while the one at the channel exit and in the plume is less affected. These figures also evidence how the plasma density (in particular in the channel and near the channel exit) oscillates as the total current does (cf. Figure 6.4).

The red line in Figure 6.9 displays the axial profile of the averaged electron temperature. Similarly to what we have observed for the density, the temperature peak decreases when we introduce the virtual radial dimension: it passes from

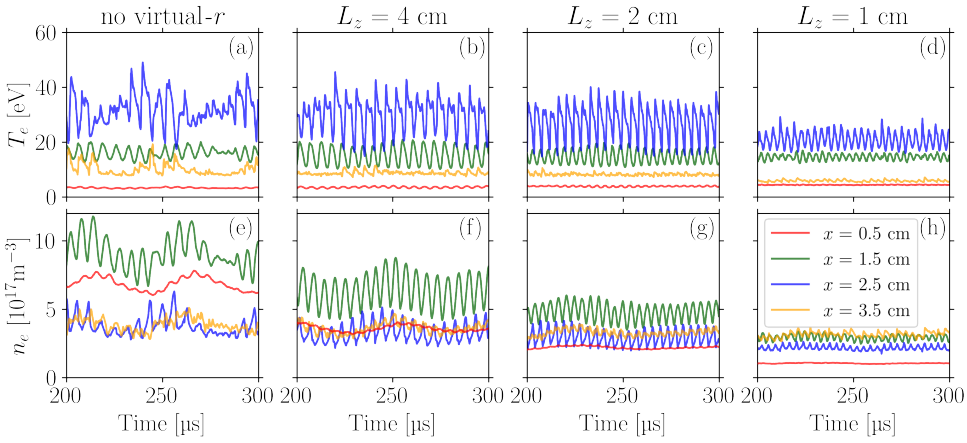


Figure 6.10: Temporal evolution at quasi-steady-state of the electron temperature (a-d) and density (e-h) for $L_y = 1$ cm. The red, green, blue, and yellow lines show the evolution at $x = 0.5$ cm, 1.5 cm, 2.5 cm and 3.5 cm, respectively. Each column corresponds to L_z value reported in the title.

≈ 30 eV with no virtual-r to ≈ 18 eV for $L_z = 1$ cm. The electron temperature value near the anode and in the plume (red and yellow lines, respectively) does not seem to depend much on the choice of the virtual-r thickness. Even if the temperature peak decreases, the temperature oscillations in Figure 6.10 do not seem to reduce much when we introduce the virtual-r, at least in (a-c).

The position of the temperature peak remains in any case close to the thruster channel exit, while the density peak is close to the anode. Moreover, we observe that the dependency of the temperature value on the virtual-r in Figure 6.10 is less obvious than the one of the density. In (a-c) the most significant effect of the virtual-r on the temperature is near the channel exit (blue lines), while elsewhere the effect is less pronounced. For all the values of the virtual-r, the electron temperature ordering of the axial points remains the same: the temperature is the lowest near the anode (red line) and the highest at the thruster exit (blue line). This is not the case for the density: its ordering depends on the virtual-r thickness. The density in the plume becomes similar to the density at its peak for $L_z = 1$ cm, while with no virtual-r the density at the peak is more than twice the density in the plume.

Large simulation domain in the azimuthal direction ($L_y = 4$ cm)

When we consider a larger simulation domain in the azimuthal direction ($L_y = 4$ cm), as already shown in Section 6.2.1, the BM is more intense and the plasma parameters are more affected by the presence of the virtual radial dimension. In Figure 6.11 we show the electron temperature and density profiles in the case of $L_y = 4$ cm. The larger shaded area shows that the BM oscillations in this case cause all plasma parameters to vary significantly. Moreover, in Figure 6.12 we show the temporal evolution of the electron temperature and density at four different axial positions for the four values of the virtual-r length L_z. Observing the oscillations of plasma density in these figures, we immediately notice the effect of the virtual radius on the

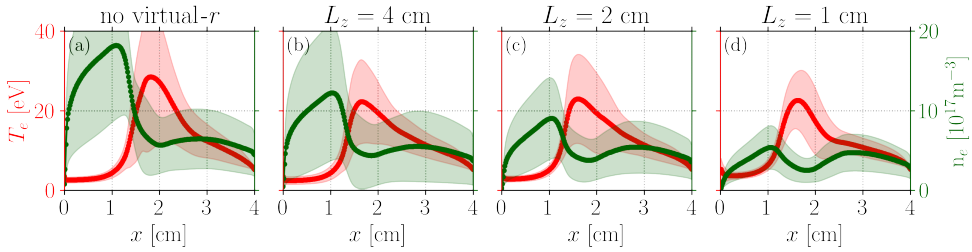


Figure 6.11: Electron temperature (red) and density (green) for $L_y = 4$ cm with different L_z. The shaded area shows the standard deviation around the mean value.

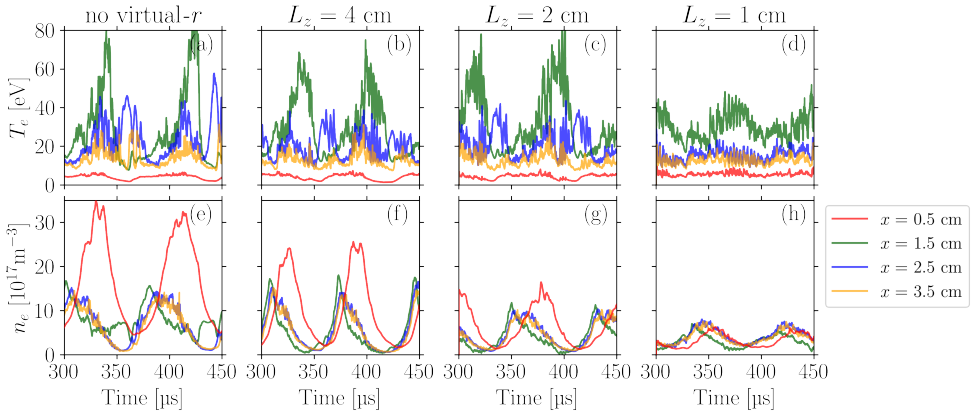


Figure 6.12: Temporal evolution during the BM cycle of the electron temperature (a-d) and density (e-h) for $L_y = 4$ cm. The red, green, blue and yellow lines show the evolution at $x = 0.5$ cm, 1.5 cm, 2.5 cm and 3.5 cm, respectively. Each column corresponds to L_z value reported in the title.

density near the anode: if no virtual-r is used, the density is higher than everywhere else. The presence of the virtual-r reduces the density at $x = 0.5$ cm to values similar to those at the other axial positions. Even if the trend is similar in Figure 6.10 (e. g., the density near the anode reduced by the virtual-r), the density is much larger near the anode when $L_y = 4$ cm. The average density is reduced by the virtual-r all along the axis, but the effect is weaker far from the anode.

We notice also that the large BM oscillations present in Figure 6.12 mask almost completely the high-frequency modulation that we observed in Figure 6.10 and that only a residual high-frequency modulation persists in the decreasing phase of the BM. This is consistent with what was observed in Section 5.2: during the growing phase of the BM the ITTI is almost invisible.

The electron temperature, in this case, is rather different from the one observed in Figure 6.10 for $L_y = 1$ cm. The temperature is higher at $x = 1.5$ cm than at the thruster exit. For all values of L_z, but the smallest, the temperature inside the channel remains quite large. We observe that the high-frequency modulation of the electron temperature for $L_y = 4$ cm is rather different from the one observed for $L_y = 1$ cm: the modulation is much stronger and the frequency is much higher.

6.2.1.3 Effect of the virtual-r on the electron energy distribution

In this section, we study the effect of the virtual-r on the EVDF. As explained at the beginning of this chapter, the virtual-r absorbs the most energetic electrons, thus it is interesting to observe how this impacts the EVDF.

In Figure 6.13 we study the EVDF for different cases (columns) at different axial positions (rows) for the simulations with an azimuthal length of $L_y = 1\,\text{cm}$. Near the anode (i. e., first row) the effect of the virtual-r is seen since the high-energy tails are depleted for small values of the virtual-r lengths L_z. In the middle of the channel (i. e., center line in the Figure) we observe that the temperature has strongly increased in all directions and that again the virtual-r reduces the temperature. Both near the anode and in the mid-channel, we observe that the presence of the $\mathbf{E} \times \mathbf{B}$ drift breaks the symmetry of the distribution: the azimuthal velocity distribution is shifted in the y direction (i. e., green lines).

The electrons emitted at the cathode are in all cases at the same temperature, $T_e^{\text{cath}} = 5\,\text{eV}$. However, in the last row of Figure 6.13, where we show the distribution in the plume, we notice that the EVDF high-energy tails depend on the chosen virtual-r value. The temperature (i. e., that is proportional to the width of the distribution) is higher when the virtual-r is not present: this is consistent with what we observe in Figure 6.10. Therefore, the electron distribution in the plume (i. e., so near the cathode where the electrons are emitted) depends on the value of the virtual-r thickness, even if there are no radial losses in the plume.

6.2.2 Influence of the virtual-r on the instabilities

As largely discussed in this thesis, the instabilities play a fundamental role in defining the characteristics of the $\mathbf{E} \times \mathbf{B}$ HT discharge. For this reason, in this section, we discuss the effect of the virtual-r on the instabilities. In particular, we focus on the BM and the ITTI.

Effect of the virtual-r on the BM oscillations

We have shown that the BM is responsible for the increased losses observed when the azimuthal length is $L_y = 4\,\text{cm}$. So, in this section, we focus on the BM oscillations in the discharge with $L_y = 4\,\text{cm}$.

In Figure 6.14 (a) we report the evolution of the discharge current for different values of the virtual-r thickness L_z, while in (b) and (c) we display the corresponding BM frequency and amplitude, respectively. We observe that the BM frequency and amplitude are both larger when the virtual-r is larger. By comparing the BM amplitude with the mean discharge current value, cf. subfigure (c), we observe that the amplitude of the oscillations is linked with its mean value. Without the virtual-r, the amplitude is large roughly half of the mean value, while for a large value of L_z (green markers) the BM amplitude becomes of the order of the current mean value. When the thickness of the virtual-r decreases (yellow markers), the amplitude of the BM shrinks to a value close to half of the mean current.

At the beginning of this chapter, we observed that when we reduce the value of L_z we are increasing the number of absorbed particles at the wall, cf. Eq. (6.2). A way

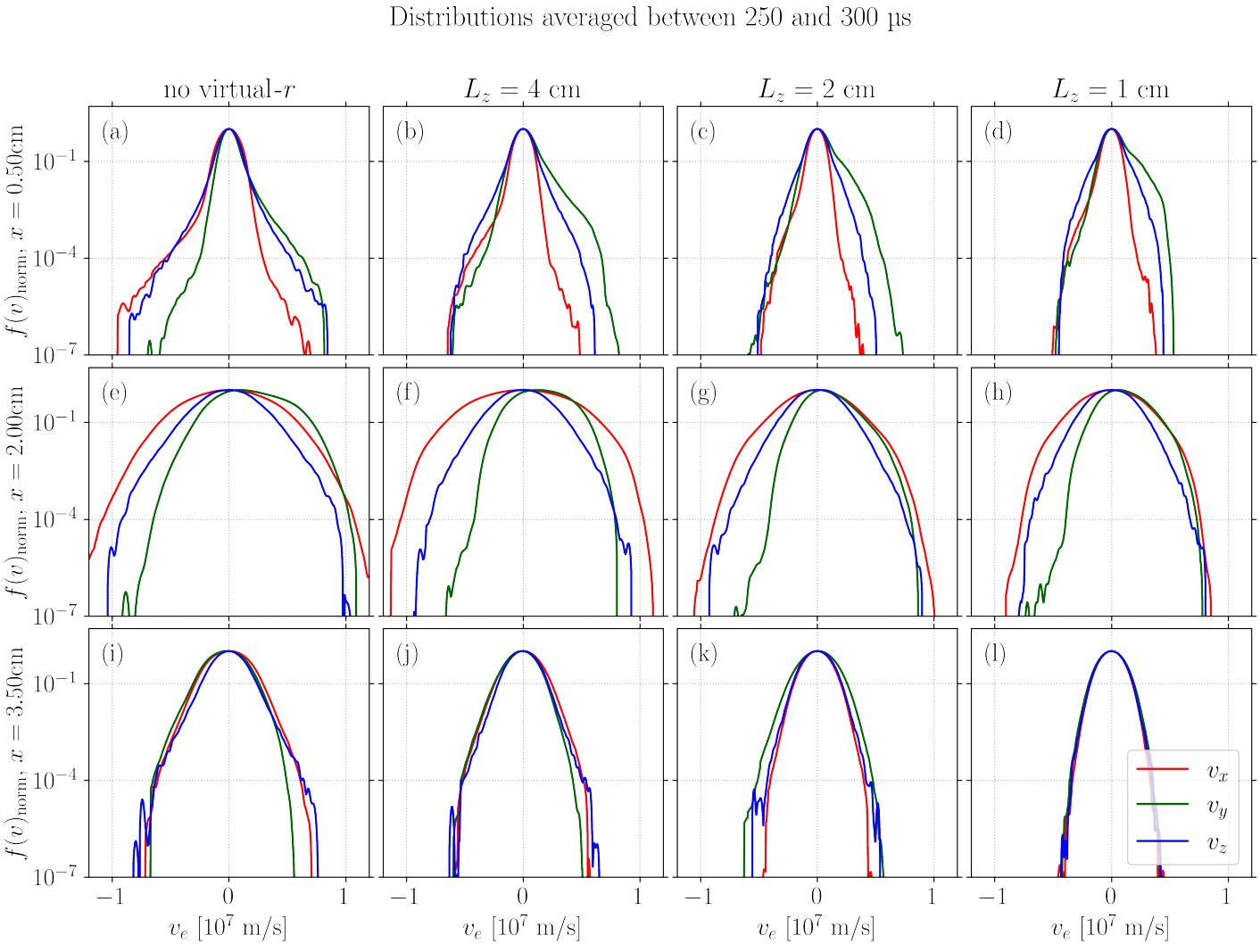


Figure 6.13: Each column shows the EVDF for different virtual-r thicknesses: no virtual-r (a,e and i), L_z =4 cm (b,f and j), L_z = 2 cm (c,g, and k), L_z = 1 cm (d,h, and l) and each row a different axial position: x = 0.5 cm (a,b,c and d), x = 2 cm (e,f,g, and h) and x = 3.5 cm (i,j,k and l).

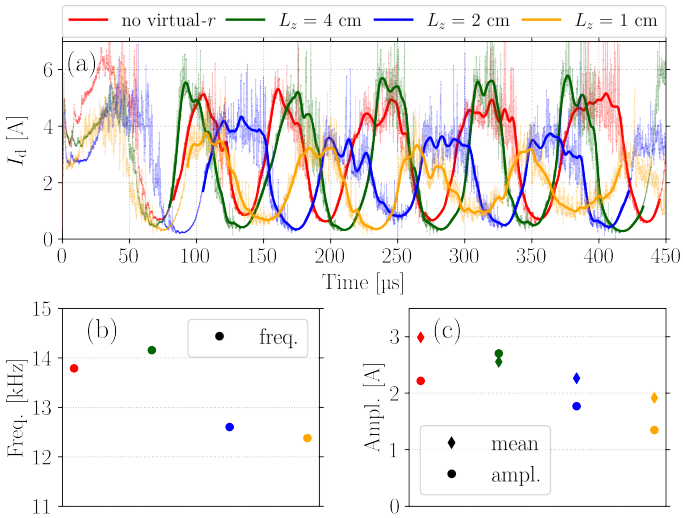


Figure 6.14: (a) Temporal evolution of the discharge current. The thick lines show the analyzed BM cycles. From these intervals are extracted the frequency (b) and amplitude (c) of the BM oscillations. The colors are reported on the legend on top.

to model the radial losses [114, 175] is to introduce an artificial collision frequency in the ion dynamics. So, decreasing the value of the thickness L_z would correspond to increasing the particle-wall collision frequency. A 1D fluid code that simulates the discharge (i. e., similar to the one described by Ref. [175]) is available at LPP: this allowed us to compare the PIC results with the effect of an increased collision frequency in a fluid code. Note that the BM frequency observed by this code (≈ 5 kHz) is lower than the one that we observe in our PIC simulations. This is not surprising: it is extremely difficult to reproduce with a 1D fluid code the complex physics of HTs.

By tuning in the fluid code, the wall losses (i. e., increasing and decreasing the wall losses by a factor α), we observed a variation of the BM frequency. In Figure 6.15 we show the evolution of the BM frequency for different values of the wall losses with this 1D fluid code, with $\alpha = 1$ corresponding to the case of standard wall losses. We observe here that for low wall losses (e. g., low α) the frequency is lower than in the nominal case. Then, it increases up to the standard value $\alpha = 1$ and subsequently drops for high wall losses. The behavior observed in the fluid code is consistent with the results obtained in the PIC simulations. In particular, we observe that the BM frequency slightly increases from the no-virtual-r case to the case with virtual-r length $L_z = 4$ cm. Then, when the losses at the walls increase, the BM frequency drops.

To conclude, it was shown that: (i) the wall losses affect both the BM frequency and amplitude, (ii) the BM frequency does not depend monotonically on the wall losses: there is a first phase in which the frequency increases with the wall losses, then it reaches a maximum value and finally it drops when the wall losses are above a certain threshold.

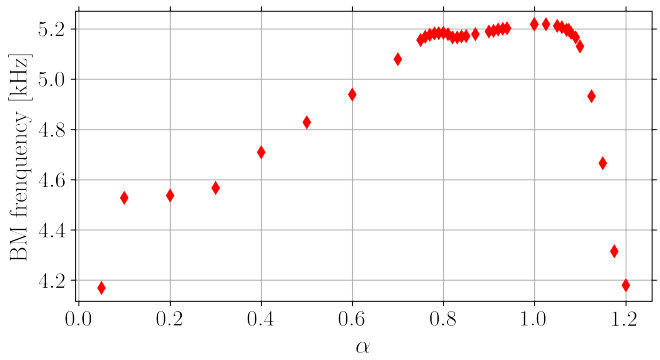


Figure 6.15: Evolution of the BM frequency for different values of the wall losses in a 1D fluid code developed at LPP (similar to the one described in Ref. [175]). The coefficient α is used to decrease or increase the wall losses. The standard wall losses correspond to $\alpha = 1$.

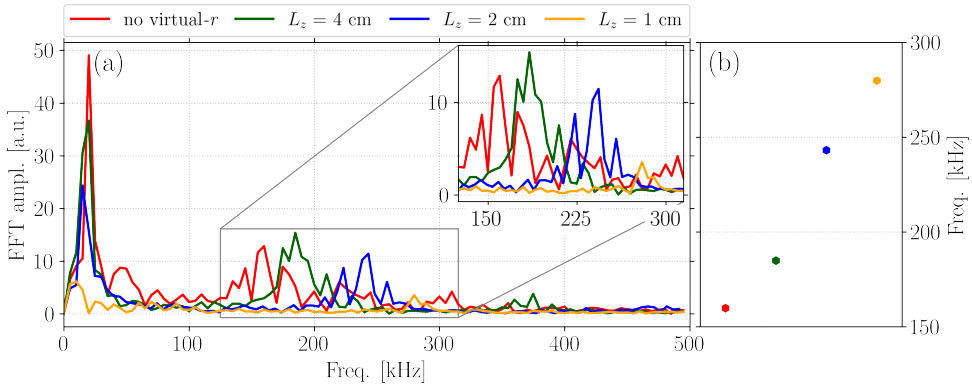


Figure 6.16: (a) FFT of the current for different values of virtual-r with $L_y = 1$ cm. (b) The dominant frequency. The colors are reported on the legend on top.

Effect of the virtual-r length on the ITTI

The large temperature gradients make it difficult to evaluate the effect of the virtual-r on the ITTI. However, some major effects can be observed. In particular, we first study the effect on the discharge current in the case of an azimuthal length of $L_y = 1$ cm, where the ITTI is well distinguishable in the discharge current, and then we discuss the effect on the ITTI frequency in the case of an azimuthal length of $L_y = 4$ cm, where the spectrum is easily computed with the PSD2P.

In Figure 6.16 we observe that performing a FFT transform of the discharge current in the case of a small azimuthal length of 1 cm allows for a clear evaluation of the current modulation frequency. Recent works [170, 202] and the discussion in Chapter 5 have shown that it is possible to link the current modulation with the ITTI frequency. In (b) we display the maximal frequency for each L_z: this frequency

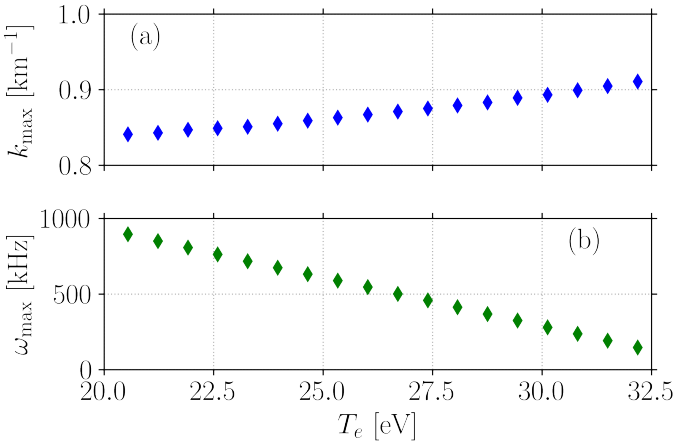


Figure 6.17: Wavenumeber (a) and frequency (b) corresponding to the most unstable mode calculated by Eq. (6.4) for different values of the electron temperature.

increases from $\approx 160\,\text{kHz}$ up to $\approx 280\,\text{kHz}$ when the virtual-r thickness is decreased. Thus, these results suggest that larger losses correspond to a higher ITTI frequency.

In Figure 6.16 (a) we also observe that high-order harmonics are present in the FFT spectrum. The origin of these harmonics in the current evolution remains still unknown. These might be related to different resistive modes growing at different axial positions. We have previously discussed the presence of strong axial temperature and density gradients: this corresponds to diverse plasma characteristics that excite different ITTI modes.

A theoretical explanation of the ITTI frequency shift requires the use of dispersion relations. At first, we analyze the 1D axial dispersion of the resistive wave as it was calculated by Koshkarov *et al.* [132] and derived in Chapter 2. The dispersion relation is given by

$$\frac{1}{\omega - k_x v_{i,0,x}} = \frac{\omega - k_x v_{e,0,x} + \imath\nu_e}{\omega_{LH}\left(\omega - k_x v_{e,0,x} + k_x^2 \rho_e^2 (\omega - k_x v_{e,0,x} + \imath\nu_e)\right)}. \tag{6.4}$$

This equation is a third-order equation that can be easily solved numerically to find $\omega(k_x)$. This equation depends on five parameters (i. e., $v_{i,0,x}, v_{e,0,x}, \nu_e, \rho_e$ and ω_{LH}). In the following, we consider these parameters as calculated in the simulation with $L_y = 1\,\text{cm}$ and $L_z = 2\,\text{cm}$. Following the discussion of the current chapter, we know that the virtual-r affects the electron temperature and density, while the velocities (which depend on the absolute intensities of electric and magnetic field) are weakly dependent on the virtual-r. Since the electron density does not play a role in the DR, we suppose that the variation of ITTI frequency should be related to the electron temperature variation caused by the virtual-r. In the dispersion reported in Eq. (6.4) the only parameter that depends on the temperature is the Larmor radius ρ_e: in the following, we study how the variation of this parameter around its nominal value affects the instability modes.

Considering the parameters extracted by the PIC simulation, we measured the values of $v_{i,0,x}, v_{e,0,x}, T_e$ and B at the thruster exit and we estimated the anomalous

collisionality ν_t by using the formula already used in Chapter 5, Eq. (5.1). By solving numerically Eq. (6.4) it is possible to calculate the wavenumber and frequency of the most unstable mode (i. e., the one corresponding to the maximal growth rate). In Figure 6.17 we show the results of this calculation for different values of the electron temperature (i. e., corresponding to a variation of ρ_e) around the one calculated by PIC. We observe that the frequency of the most unstable mode decreases with the electron temperature. This is consistent with the results reported in the previous section. The electron temperature drop originated by the virtual-*r* makes the ITTI frequency increase. However, the temperature fluctuation and the large temperature gradient along the thruster axis make it difficult to estimate precisely the exact value of the temperature during the ITTI growth. Moreover, the exact growing position of the ITTI is not known. Thus, the result of this calculation gives only a good indication of the effect of the virtual-*r* on the ITTI frequency and explains the decreasing trend of the frequency that is observed in the PIC simulations. One should note that the dispersion discussed here is the one of the *minus* wave (cf. Section 2.2.4), which is the only unstable branch when we work with a 1D DR. The limited azimuthal direction considered for these simulations makes it different to compare these results with those of the 2D DR, as done in Chapter 5.

6.2.2.1 ITTI captured with PSD2P

The PSD2P technique can be used also to study the effect of the virtual-*r* in the larger azimuthal domains. Considering the same axial position for the four cases, e. g., $x = 3.5\,\text{cm}$, we calculated the PSD2P during the decreasing phase of the BM, where we know that the ITTI is more intense. In Figure 6.18 we show the PSD2P for the four cases. We observe that the ITTI typical shape is captured by the PSD2P technique.

A first look at the maps suggests that the virtual-*r* does have an impact on the mode frequency. This frequency can be extracted by the PSD2P maps just by calculating the max value in the colormaps. The results are reported in Table 6.2. Unfortunately, the limited amount of time (i. e., $\approx 20\,\mu\text{s}$) that we can use for the PSD2P technique does not allow to have a good resolution of the low-frequency modes. We observe that the spectrum is much more localized in the cases with the virtual-*r*, while without virtual-*r* it is more spread. When we reduce the virtual-*r* thickness, we detect a transition to larger frequencies (e. g., the frequency corresponding to the max of the PSD2P is reported in Table 6.2). The trend is similar to the one observed before with $L_y = 1\,\text{cm}$: the ITTI frequency increases when we reduce the virtual-*r* thickness. In the case with the smallest virtual-*r* thickness, the ITTI frequency is, surprisingly, lower than the one measured in the case $L_z = 2\,\text{cm}$. But, again, this is probably related to the limited time of the PSD2P technique and its low resolution at low frequencies.

Even if the trend is similar, we notice that the frequency of the ITTI main mode is 2 to 3 times larger when $L_y = 4\,\text{cm}$, when compared to the case with $L_y = 1\,\text{cm}$. This can be explained considering the discussion about the azimuthal propagation held in the previous section. By changing the simulation domain azimuthal length, we are imposing different boundary conditions for the propagation of the ITTI mode. This is critical for the ITTI growth rate, which is very sensitive to a change in k_y. Moreover, the different temperatures measured in the case with larger L_y have an impact on the ITTI frequency.

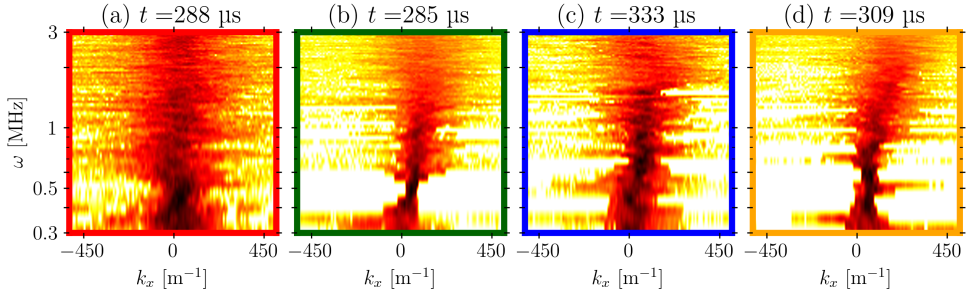


Figure 6.18: PSD2P time-axial spectra at $x = 3.5\,\text{cm}$ for no virtual-r (a), $L_z = 4\,\text{cm}$ (b), $L_z = 2\,\text{cm}$ (c) and $L_z = 1\,\text{cm}$ (d). The time at which is map is calculated is indicated in the subfigure title.

Case	ITTI frequency [kHz]
no virtual-r	420
$L_z = 4\,\text{cm}$	460
$L_z = 2\,\text{cm}$	670
$L_z = 1\,\text{cm}$	580

Table 6.2: Frequency of the ITTI mode calculated from the PSD2P maps.

6.2.2.2 IAW frequency

The PSD2P allows studying the axial-azimuthal propagation of the IAW. In Chapter 5 we showed that this instability is dominant during the growing phase of the BM. By applying the PSD2P technique to the four cases analyzed in this section, we study how the presence of the virtual-r affects the IAW frequency spectrum. The analysis is carried out in the last part of the growing BM phase when the IAW is stronger.

The results reported in Figure 6.19 are not so easy to interpret. First, we observe that the IAW modulation is clear in the snapshot of the case without virtual-r and becomes more and more concealed when we reduce the virtual-r thickness. This corresponds to an increase in the frequency of the ITTI discussed earlier, which is approximately at the same frequency. As one can observe in Figure 6.19 (a), with no virtual-r, the IAW dispersion is visible at frequencies of $\approx 1\,\text{MHz}$. In (b), (c), and (d) the IAW dispersion remains visible at approximately the same frequency, but it is more difficult to distinguish it from the one of ITTI. In these cases, the two dispersions merge, making it more difficult to study individually the two instabilities.

So, here, the clear IAW oscillations observed and discussed in Chapter 5 are not present anymore. The instability dynamics is much more coupled and the ITTI is present almost all along the simulations. The virtual-r makes the plasma parameters more homogeneous and less time-dependent, so the growth of the ITTI is always allowed and not only during the decreasing BM phase. Moreover, the IAW growth rate [105] depends on the temperature: the reduced temperature (i. e., caused by a smaller value of L_z) makes the IAW growth rate smaller. These are the reasons why it is harder to capture the IAW in the cases with the virtual-r.

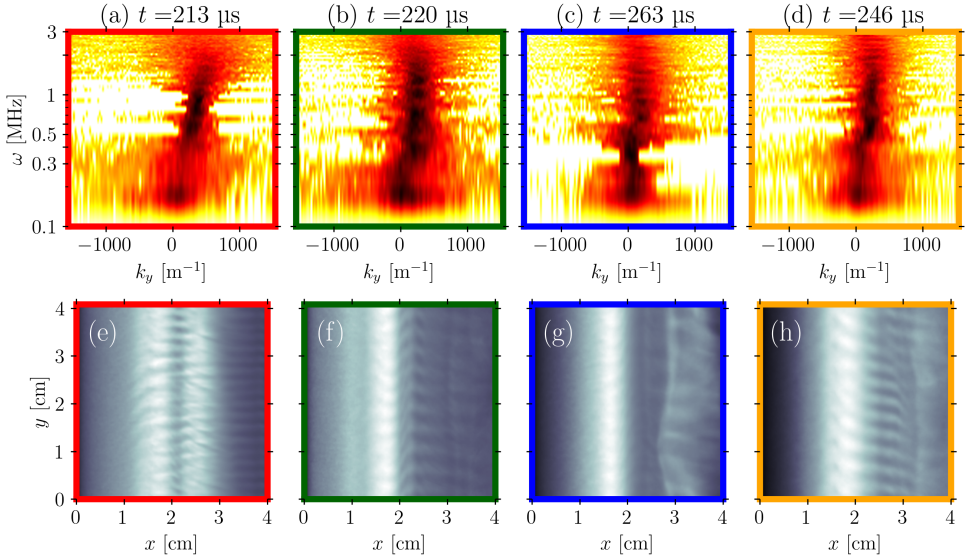


Figure 6.19: PSD2P at x = 2.0 cm for no virtual-r (a), 4 cm (b), 2 cm (c) and 1 cm (d). The time at which is map is calculated is indicated in the subfigure title and a snapshot of the density at that time is shown in the bottom figures (e-h).

6.2.3 Effect of the virtual-r on the thruster performance

The presence of the virtual-r has a major effect also on the thruster performance and power consumption. In this subsection, we analyze the effects of the virtual-r on important propulsion parameters such as the thrust, the specific impulse, and the power consumption. Moreover, we study the evolution of the power losses at the walls and how they impact the overall power provided to the system. The parameter definitions are given in Section 1.1.4.

6.2.3.1 Macroscopic effects on performance

We have shown all through this chapter that the presence of the virtual-r has an impact on plasma dynamics. As a result, it is not surprising to observe that it also influences the thruster performance. In Figure 6.20 we show the dependence of the average specific impulse, the thrust, the mass efficiency, and the thrust-to-power ratio on different virtual-r thicknesses. In this figure, we observe that the introduction and subsequent decrease of the virtual-r thickness causes a drop in all the parameters. The trend observed for different azimuthal lengths L_y = 1 cm and L_y = 4 cm is similar. With no virtual-r, the thruster parameters are significantly larger with the large azimuthal length. The difference reduces with virtual-r. When the virtual-r thickness is 1 cm the performance does not depend anymore on the azimuthal length.

The results in Figure 6.20 can be compared to the real thruster performance to understand which virtual-r thickness would better match with the real device, which is $\approx$ 1.5 cm thick. The thrust and specific impulse are of a good order of magnitude, compared to those of the PPSX00, to which our simulation corresponds the most.

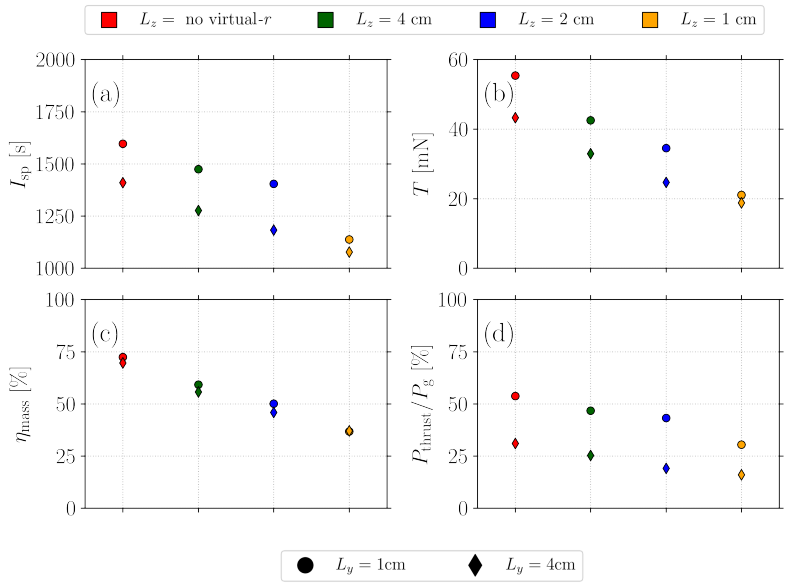


Figure 6.20: Specific impulse (a), thrust power (b) and mass efficiency (c), and thrust power-to-power ratio (d), as a function of the virtual-r thickness. The results are reported for both cases with $L_y = 1$ cm and 4 cm, as indicated in the legend at the bottom.

The I_{sp} nominal value reported by SAFRAN [195] is between 1300 s and 1650 s. The thrust appears as well to be of a good order of magnitude, with a substantial drop related to the presence of the virtual-r. However, we recall that the estimation of the thrust is done with the thruster section, which is critical in 2D simulations and it is not self-consistently treated in these simulations. The mass efficiency decreases as we increase the losses at the walls. However, we recall that the mechanism of neutral repopulation was not yet included in the process: the absorbed ions are lost.

6.2.3.2 Power Losses at the walls

The power losses at the wall are calculated as the sum of two losses: the thermal energy lost by both electrons and ions, and the acceleration of ions out of the plasma by the sheath. The thermal energy can be calculated directly from the energy of absorbed particles, while for the acceleration power, we need to use the floating potential, which gives the potential drop $\Delta\Phi$ from the plasma bulk to the grounded walls. The overall power loss is then given by

$$P = \sum_{j=1}^{N_{\text{tot}}} \frac{E_{i,j} + E_{e,j} + V_{f,j}}{\Delta t} \cdot q_f L_z, \tag{6.5}$$

where N_{tot} is the number of superparticles exiting pairs in a Δt. $E_{i,j}$ and $E_{e,j}$ are the energies of the ion and the electron of the j^{th} absorbed pair, respectively. The floating

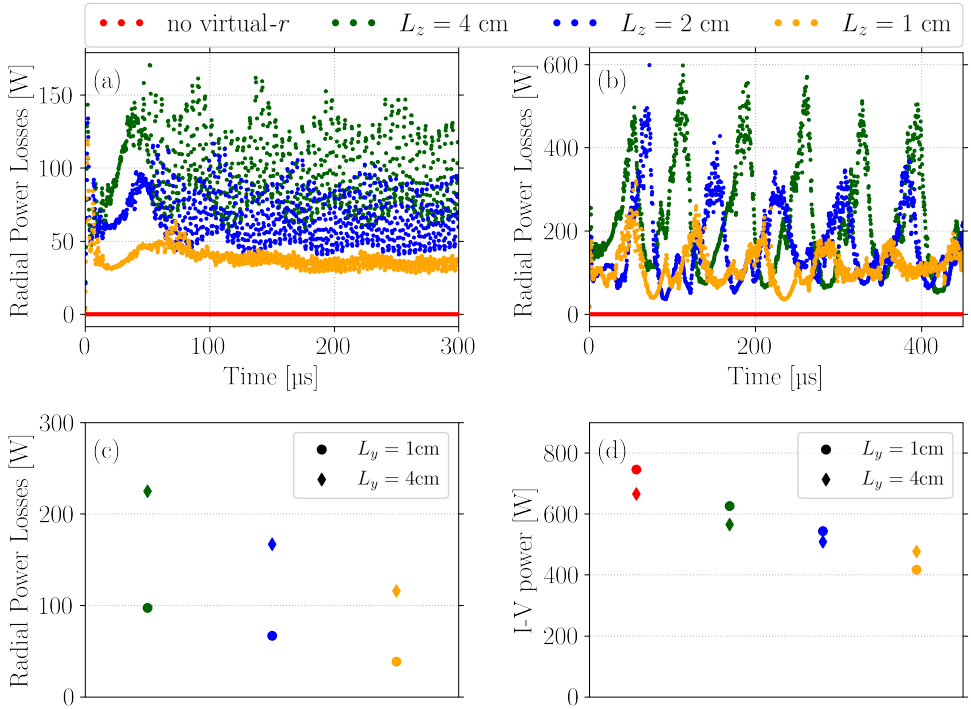


Figure 6.21: Power losses at the walls as a function of the virtual-r thickness. The time evolution is shown for cases with $L_y = 1$ cm (a) and 4 cm (b). In (c) we show the average power losses and (d) the total I-V power provided by the generator.

potential $V_{f,j}$ is calculated at the position in which the j^{th} pair is absorbed. By the bounded plasma theory [83], the floating potential can be written as

$$V_{f,j} = -\frac{k_B T_e}{2e} \ln\left(\frac{2\pi m_e}{m_i}\right). \tag{6.6}$$

The time evolution of the power absorbed at the walls is reported in Figure 6.21, in (a) for $L_y = 1$ cm and in (b) for $L_y = 4$ cm. In (c) we show the average total wall power absorption and in (d) the I-V power provided by the generator. We observe that the generator power is comparable to the nominal power of the PPSX00 device [195] (i. e., from 200 W to 1000 W). This power is calculated by multiplying the current by the voltage at the anode. This result is consistent with what we observed in Section 6.2.1, where we highlighted that the discharge current is of the same order of magnitude as one of the real devices. In (a) and (b) we see that the radial power loss has rather small fluctuations when the azimuthal simulation length is small. These fluctuations become much more prominent when the azimuthal dimension is increased.

In Figure 6.21 (c) we find that the radial power loss decreases as we decrease the thickness of the virtual-r. This is counterintuitive. However, it can be easily explained. We have shown in this chapter that for the same plasma characteristics and different L_z the number of absorbed superparticles varies, but the number of *real* absorbed particles does not, since the factor $q_f \cdot L_z$ compensates the lower number of absorbed

superparticles. So, the exiting power is strongly correlated with the bulk plasma characteristics. In Section 6.2.1.2 we have shown that one of the main effects of the virtual-r is to reduce the temperature in the plasma: a reduced plasma temperature means a reduced number of absorbed particles. This is the reason why the power absorbed at the walls decreases as we decrease the virtual-r thickness.

6.2.4 Summary of important results

The most important take-home messages of these sections are the following: (i) the azimuthal length of axial-azimuthal simulations does play an important role. The larger the azimuthal length is, the larger the BM is and the larger are the plasma parameters oscillations; (ii) the virtual-r can reduce the discharge current, the electron temperature, and density, more efficiently when the BM is small; (iii) the virtual-r affects the plasma instabilities in the discharge; (iv) the large BM oscillations increase the radial losses.

6.3 SECONDARY ELECTRON EMISSION EFFECTS

The Secondary Electron Emission (SEE) is a mechanism related to the emission of low-energy electrons from the walls after the absorption of an electron. The model of virtual-r studied until now does not consider any radial re-injection of particles. Many studies [39, 71, 77], however, have shown that the presence of SEE has a strong impact on the discharge characteristics and the thruster performance. In this section, we study the effect of the virtual-r considering a simple SEE model.

6.3.1 SEE Model

The effect of secondary electron emission on HT discharges has been studied in detail during Antoine Tavant's Ph.D. [152] with radial-azimuthal PIC simulations. In his work, Tavant used the kinetic SEE model proposed by Barral [59],

$$\sigma(\mathcal{E}) = \begin{cases} \sigma_0 + (1-\sigma_0)\mathcal{E}/\mathcal{E}_0 & \text{if } \mathcal{E} < \mathcal{E}_{\max}, \\ \sigma_{\max} & \text{if } \mathcal{E} \geq \mathcal{E}_{\max}, \end{cases} \tag{6.7}$$

where σ is the emission rate, $\mathcal{E}$ is the electron energy. σ_0, $\sigma_{\max}$ and $\mathcal{E}_0$ are parameters such that $\mathcal{E}_{\max} = \frac{\sigma_{\max}-\sigma_0}{1-\sigma_0}\mathcal{E}_0$. For each electron absorbed at the walls, he calculated the value of $\sigma(\mathcal{E})$, which corresponds to the number of electrons to inject from the walls. These electrons were injected at a fixed temperature, colder than the one of the outgoing flux.

A purely kinetic model cannot be used in axial-azimuthal simulations studied in the present thesis. In theory, we could calculate the number of SEE events for each exiting electron from Eq. (6.7), as was done by Barral and Tavant. Nonetheless, this would harm the flux neutrality at the walls. In radial-azimuthal simulations (or real devices) the potential at the walls adapts, compensating for the fluxes difference caused by SEE. Unfortunately, this is not possible in 2.5D simulations, where the

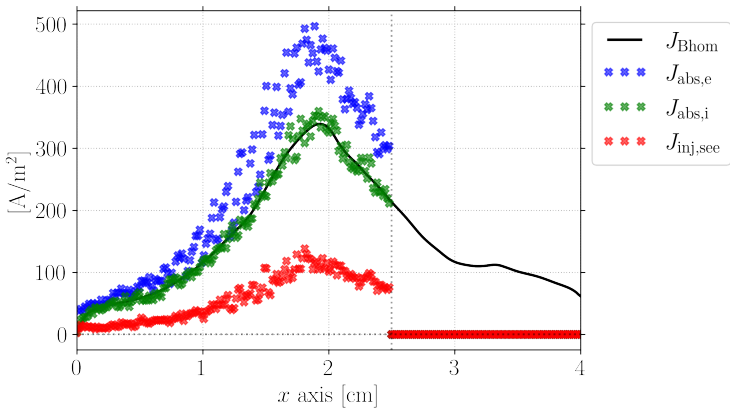


Figure 6.22: Axial currents profiles in a case with $\bar{\sigma} = 0.25$. The blue, green, and red markers correspond to the electron, ion, and SEE current density profiles, respectively. The black line shows the Bohm current density as calculated from Eq. (6.1).

Poisson equation is only solved in the xy-plane and not in the direction perpendicular to the wall. For this reason, in the current work, a simplified version of the previous expression is needed: considering a Maxwellian flux with temperature T_e, the average emission rate is

$$\bar{\sigma} \approx \sigma_0 + (1 - \sigma_0) 2T_e/\mathcal{E}_0. \tag{6.8}$$

We observe that the average number of SEE events depend on the electron temperature and thus varies along the thruster axis. Considering a fixed ion Bohm flux towards the walls (called Γ_i) and $\bar{\sigma} < 1$, we can write a simple current balance that maintains the plasma quasi-neutrality, obtaining that the electron and SEE fluxes read

$$\Gamma_e = \frac{1}{1-\bar{\sigma}}\Gamma_i \text{ and } \Gamma_{\text{SEE}} = \frac{\bar{\sigma}}{1-\bar{\sigma}}\Gamma_i, \tag{6.9}$$

respectively. These flux expressions require additional simplification. By considering the expression in Eq. (6.8), when $T_e \sim \mathcal{E}_0/2$, the value $\bar{\sigma} \to 1$, that implies a divergence in the number of absorbed and emitted electrons, as one notices from Eq. (6.9). For this reason, whenever the temperature is free to vary, we experience critical numerical problems in the determination of the number of absorbed/re-emitted electrons. Thus, we set the temperature to a constant value, so to keep the value of $\bar{\sigma}$ fixed. Other models that consider an emission rate depending on the temperature, but compatible with our model, are left for future work. In Figure 6.22 we show the axial profiles of the exiting electron and ion current densities, along with the axial profile of the Bohm current density. The SEE emission by the walls is calculated with $\bar{\sigma} = 0.25$, resulting in the red profile in Figure 6.22. Consistently with Eq. (6.9), we observe that the ion current density is the one fixed by the Bohm condition, while the electron current density is increased by the SEE. The SEE and electron current densities have an opposite sign: the first is entering the simulation domain by the walls, while the latter is leaving the domain. When we sum them, we correctly retrieve the overall neutrality of the plasma.

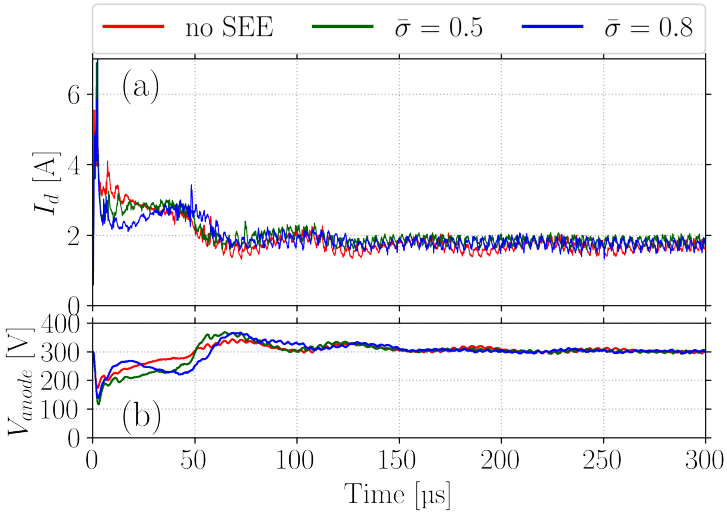


Figure 6.23: Current (a) and anode potential evolution for a simulation with $L_y = 1\,\text{cm}$ and $\tilde{L}z = 2\,\text{cm}$. Two different values of the SEE emission rate are considered: $\bar{\sigma} = 0.5$ (green) and $\bar{\sigma} = 0.8$ (blue), while the red line represents the base case.

Since we are considering the electron re-injection at the walls, we decided to include in the model the ion neutralization at the walls. The neutral gas flow model proposed by Charoy [170] has been improved by considering that the ions exiting at the walls capture an electron, thus forming a new neutral particle, that is re-injected in the plasma (as a new term source in the neutral gas fluid model). Note that this was not present in the model without SEE.

6.3.2 SEE in virtual-*r* PIC simulations

The effect of the secondary emission in PIC simulation has been tested first on simulations with a small azimuthal length of $L_y = 1\,\text{cm}$. The chosen value of the virtual-r is here 2 cm. In Figure 6.23 we show the time evolution of the current and potential for different values of the $\bar{\sigma}$ parameter. These results suggest the idea that the SEE has a weak importance on the discharge current and potential evolution. The average current increases from the case with no-SEE ($I = 1.68\,\text{A}$) to the case with $\bar{\sigma} = 0.5$ ($I = 1.84\,\text{A}$). Then, for a larger value of the SEE emission rate $\bar{\sigma} = 0.8$ we observe a slight drop in the discharge current ($I = 1.76\,\text{A}$). It is difficult to find a clear trend in the mean current evolution, but we observe that in this calculation the SEE has a rather weak effect on the discharge current and causes a small enhancement in its average value.

The electron temperature and density profiles are shown in Figure 6.24. The electron temperature and density are slightly decreased by the SEE emission, but the effect is not very significant. Unfortunately, it is rather difficult to draw a clear conclusion from these results, since the effect of the SEE emission is rather weak and does not have a clear trend.

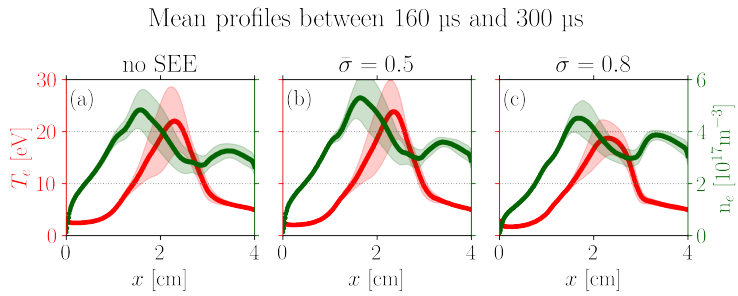


Figure 6.24: Electron temperature (red) and density (green) for $L_y = 1\,\text{cm}$ with different values of $\bar{\sigma}$ with $L_z = 2\,\text{cm}$. The shaded area shows the standard deviation around the mean value.

The SEE has also been tested in simulations with a larger azimuthal length, $L_y = 4\,\text{cm}$, as shown in Figure 6.25. The results prove that the evolution of the current and the anode potential are weakly affected by the presence of secondary emission. The differences in the BM period that are visible in Figure 6.25 are more likely related to the random nature of the simulations, more than to the SEE effect. In particular, we observe that the amplitude of the BM oscillations remains almost constant and is not affected by the SEE emission.

Thus, the preliminary results from the current model implemented in our PIC simulations suggest that the presence of the SEE (in the way it is modeled) may not strongly affect the discharge characteristics. The interpretation of this result is not trivial. A possible explanation is that the importance of the SEE lies in the competition of the potential shape in the sheath with the particle flux (i. e., the amplitude of the floating potential drop depends on the SEE rate), that cannot be reproduced in a 2D simulation like the one we are considering. Clearly, in future work, it would be interesting to implement a more refined model of SEE in the PIC simulations to study more accurately the influence of SEE on the discharge characteristics.

6.4 ANALYSIS OF CONSISTENT VIRTUAL–*R* WIDTH

In the previous section, we investigated the effect of the virtual third dimension when changing the radial thickness of the channel. We now study a simulation in which the radial thickness of the channel is fixed. In this case, we consider $\tilde{L}_z = R_{\text{ext}} - R_{\text{int}} = 1.55\,\text{cm}$. The thickness is used in the PIC simulation both to define the current (that is used to solve the circuit equations) and to define the neutral density from the total mass flow rate imposed to the neutral fluid equations. The other simulation parameters are chosen as previously and are given in Table 6.1.

6.4.1 PIC results

As before, we ran two different cases, the first with an azimuthal length $L_y = 1\,\text{cm}$ and the second with $L_y = 4\,\text{cm}$. The current and potential evolutions are shown

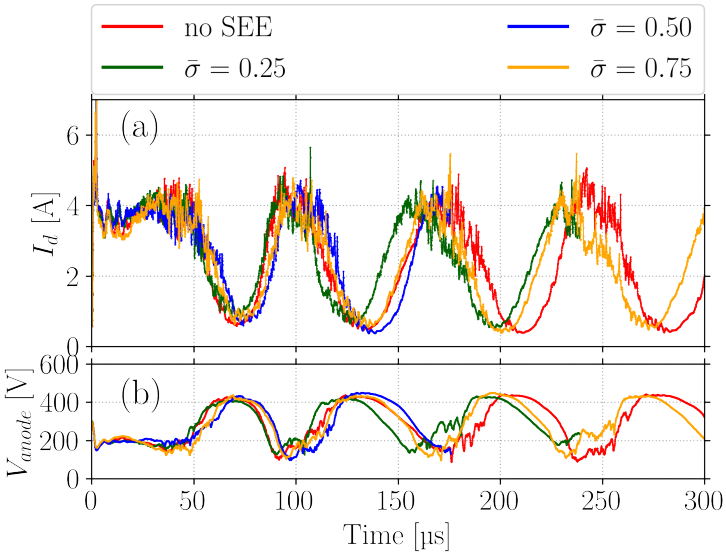


Figure 6.25: Current (a) and anode potential evolution for a simulation with $L_y = 4\,\text{cm}$ and $\tilde{L}_z = 4\,\text{cm}$. Three different values of the SEE emission rate are considered: $\bar{\sigma} = 0.25$ (green), $\bar{\sigma} = 0.50$ (blue), and $\bar{\sigma} = 0.75$ (yellow), while the red line represents the base case.

in Figure 6.26 (a) and (b) respectively. We observe that the comments made in the previous section are still valid: the case with a large azimuthal length has a strong BM, which is almost totally damped in the case with $L_y = 1\,\text{cm}$.

Even if the neutral flux (i. e., $5\,\text{mg/s}$) is somewhat higher than the one used experimentally, we can compare the current simulations to the PPSX00 [195]. In this case, the average current is around 2.5 A, which is consistent with what one can expect from a PPSX00 thruster. The current observed here also agrees with the values in Figure 6.6.

These two simulations can also be used to calculate some engineering parameters, such as the specific impulse, the thrust, and the thrust power, defined above. The averaged values obtained in the simulation and shown in Table 6.3 are in the right range. However, some important discrepancies between the case with $L_y = 1\,\text{cm}$ and the case with $L_y = 4\,\text{cm}$ still hold. All three parameters are lower in the case with $L_y = 4\,\text{cm}$: again, the presence of the BM affects the discharge characteristics and reduces the thruster performance. The reason for this behavior can be explained by analyzing the power losses as in Section 6.2.3.2. As one can see in Figure 6.27 (a) the radial power losses increase significantly when the breathing mode is present. In (b) we observe, conversely, that the power provided by the generator does not vary much between the two cases. In the first one, the average I-V power is about 750 W, while in the second one, it is around 650 W. The I-V power oscillations are more complex than what could be expected by looking at the current and voltage oscillations in Figure 6.26.

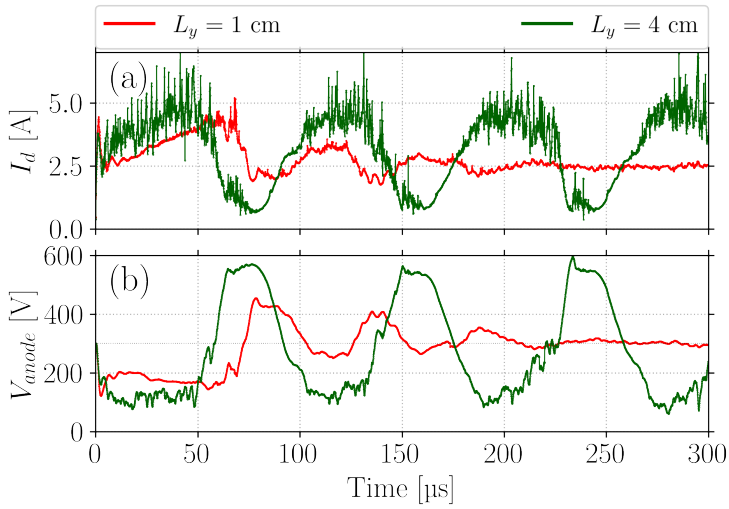


Figure 6.26: Current (a) and anode potential evolution for a simulation with a virtual-r with $\tilde{L}_z = 1.55$ cm and two different azimuthal lengths ($L_y = 1$ cm and 4 cm).

Table 6.3: Engineering parameters for the simulations with consistent virtual radius.

	$L_y = 1$ cm	$L_y = 4$ cm
I_{sp}	1539 s	1210 s
T	51.6 mN	35.6 mN
P_{thrust}	390.1 W	210.6 W

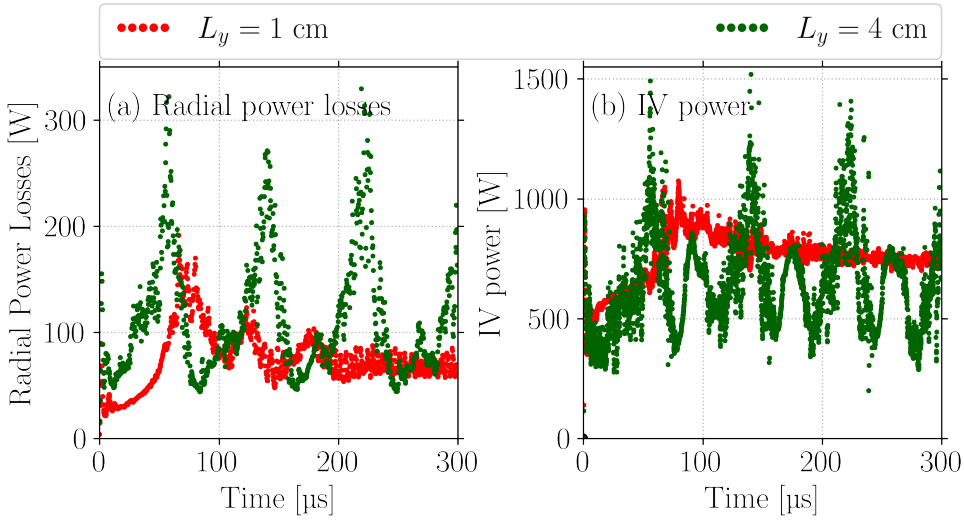


Figure 6.27: Radial power losses (a) and I-V power (b) for the simulations with $L_y = 1$ cm and $L_y = 4$ cm.

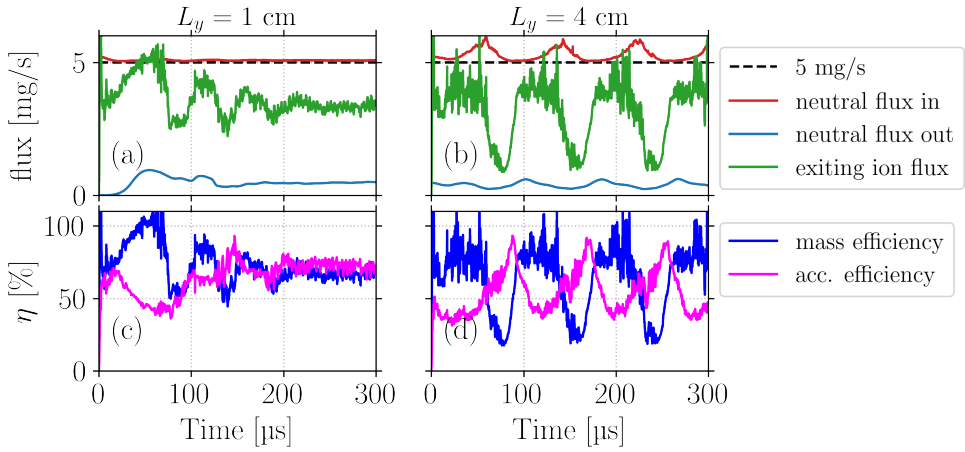


Figure 6.28: Fluxes for $L_y = 1$ cm (a) and $L_y = 4$ cm (b). Mass and acceleration efficiencies for $L_y = 1$ (c) and $L_y = 4$ cm (d).

6.4.2 Mass utilization efficiency

The mass utilization efficiency is one of the key parameters for any type of thruster. As discussed in Section 1.1.4, it can be calculated rather easily. However, even if this parameter gives an idea of the global efficiency of the thruster, it is not the only one that should be considered and one should also consider the efficiency of the thrust production. To evaluate this efficiency, we can define an *acceleration efficiency*. Ions are accelerated by the axial electric field to produce thrust. In an ideal case, each ion acquires an energy of $\sqrt{2V_{\text{anode}}/m_i}$. However, as shown in Chapter 5, there might be a significant number of ions that have smaller velocities. In this case, the acceleration efficiency is defined as

$$\eta_{\text{acc}} = \frac{v_i^{\text{out}}}{\sqrt{2\frac{V_{\text{anode}}}{m_i}}},$$

where v_i^{out} is the average ion velocity after the acceleration region.

In Figure 6.28 (a) and (b) we show the evolution of the neutral fluxes at the anode and the outgoing flux of unionized particles. We also show the flux of accelerated ions at the exit. One can see that the flux of outgoing neutrals is almost low and its value is rather constant in time. Interestingly, when the BM is present in the case with $L_y = 4$ cm, we have a significant backflow of ions towards the anode, which results in an increased neutral flux at the channel bottom. This phenomenon is almost invisible in the other case. This is consistent with what was observed by Chapurin *et al.* [169], in their study of the BM.

The ion current oscillations are similar to the current oscillations in Figure 6.26. One may notice that the fluxes do not sum up to zero at steady-state: this is related to the fact that some ions are absorbed at the walls.

In Figure 6.28 (c) and (d) we plot the mass and acceleration efficiencies. The mass efficiency is almost constant in both cases and higher than 90%. This is consistent

with what was observed above about the outgoing current. The acceleration efficiency behaves differently: in the case with $L_y = 1\,\text{cm}$, the acceleration efficiency has a rather long transient before reaching a steady-state at around 74%. In the case with $L_y = 4\,\text{cm}$, the acceleration efficiency fluctuations are locked to those of the BM. This can be understood by thinking about the anode voltage fluctuations in Figure 6.26 (b): when the current is low, the voltage is larger than the nominal one, while when the current is high, the voltage is lower than the nominal one. This means that the ions get a larger acceleration when the current is low.

6.5 CHAPTER SUMMARY

In this chapter, we introduced a virtual-*r* model that considers the radial losses in a 2D axial-azimuthal simulation. The model was built considering a Bohm flux of particles exiting the thruster to reach the radial walls, while the divergence effect is not taken into account in the thruster plume. The radial magnetic field in the simulation is constant, however, the magnetic field gradients near the wall may affect the Bohm flux. This is a topic that should be investigated in the future.

In the first part of the chapter, we discussed the effect of introducing the virtual-*r* by comparing four thicknesses. These tests, even if they are not consistent with the thruster section defined within the simulation, allowed us to characterize both the microscopic and macroscopic effect of the radial losses in the PIC simulations.

In the second part of the chapter, we proposed a simulation with a virtual-*r* and consistent channel thickness and we showed that it can successfully reproduce the major parameters of a HT better than a simulation without virtual-*r*. This allows us to conclude that including the virtual-*r* is a fundamental step in making more realistic simulations. Even if the results in this chapter are very promising, some work is still required to include the SEE in the simulations in a more convincing way. The simple model presented here does not reproduce the strong effect of SEE demonstrated experimentally.

7 LPPIC: AN ENGINEERING TOOL

In this chapter, it is presented a thorough analysis of the evolution of both microscopic and macroscopic plasma parameters during a BM cycle, which enables us to gain insight into the ionization mechanism in HTs. Additionally, several simulations obtained using LPPic are presented to demonstrate how the code can be used to explore the parametric space of key quantities for the design of HTs. This is achieved by varying various factors, such as anode potential, mass flow rate, magnetic field configuration, propellant, and cathode temperature, allowing for a better understanding of the plasma behavior under different conditions.

Chapter contents

7.1 Introduction . . . 172
7.2 Analysis of the BM dynamics using a PIC run . . . 172
7.2.1 Analysis of breathing mode . . . 172
7.2.2 Impact of electron temperature and densities on the ionization mechanism in the BM . . . 176
7.2.3 Study of the drift balance in the BM . . . 177
7.2.4 Electron transport in the axial direction of the thruster . . . 179
7.2.5 Discussion of the main results on the BM . . . 181
7.3 Variation of the HT configuration . . . 181
7.3.1 Anode voltage variation . . . 181
7.3.2 Neutral gas mass flow rate . . . 188
7.3.3 Magnetic field variation . . . 193
7.3.4 Alternative propellants . . . 197
7.3.5 Study of the cathode temperature . . . 201
7.4 Chapter summary . . . 205

7.1 INTRODUCTION

The PIC simulations provide a large amount of information on the studied plasma discharges. However, with the work presented in previous chapters, we are far from exploiting the volume of data produced by a 2.5D PIC code as *LPPic*. For this reason, in this chapter, we first analyze again some PIC results to show some additional interesting points. In particular, we analyze the evolution of plasma parameters (e. g., electron temperature, density, *et cetera*) during a BM cycle.

Later, we report several simulations obtained with the PIC code: we show how *LPPic* can be used to explore the parametric space of key quantities for the design of HTs, by varying anode potential, mass flow rate, magnetic field configuration, propellant and cathode temperature. For each of them, we analyze the effect on some plasma parameters (e. g., density, electron temperature, *et cetera*) and on engineering performance (e. g., thrust, specific impulse, *et cetera*).

7.2 ANALYSIS OF THE BM DYNAMICS USING A PIC RUN

The code used in this thesis, *LPPic*, is one of the first codes in which the charged species dynamics in 2.5D, treated with a PIC method, is coupled to a 1D neutral gas dynamics, modeled with fluid equations [170]. As shown in Chapters 3, 5, and 6, this allows us to reproduce the BM oscillations. However, even if the BM has been analyzed in the final part of Chapter 6, we have not discussed yet the microscopic mechanism of these oscillations. Barral and Ahedo [78] and more recently Lafleur *et al.* [175] have studied the BM plasma parameters using a 1D fluid code, which successfully reproduces the mechanism and allows us to inquire the origin of it. However, a 2.5D PIC simulation can provide a much more detailed analysis of the BM dynamics. In this section, we analyze the BM dynamics using the axial-azimuthal PIC simulation with self-consistent virtual-r described in Section 6.4 with an azimuthal length of $L_y = 4\,\mathrm{cm}$.

7.2.1 Analysis of breathing mode

In Figure 7.1 we show the spatiotemporal evolution (more precisely, the temporal evolution of the axial profiles) of some important plasma parameters averaged azimuthally: the normalized gas density n_g (a), gas speed v_g (b), electron density production rate by ionization S_{iz} (c), electron density n_e (d), electron azimuthal speed $v_{e,y}$ (e), electron temperature T_e (f), ionization rate coefficient $K_{iz} = S_{iz}/n_g n_e$ and the axial electric field E_x (g). We recall that the electron density production rate by ionization in Figure 7.1 (c), given by

$$S_{iz} = n_g n_e K_{iz}(T_e),$$

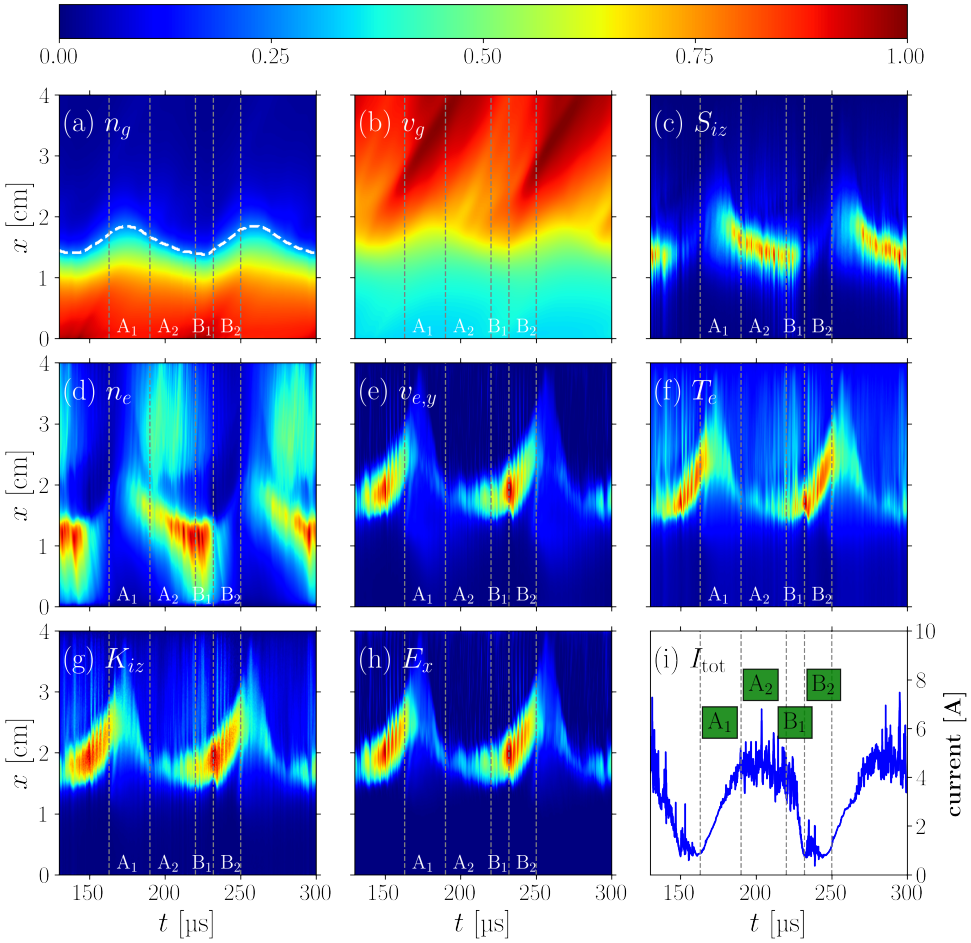


Figure 7.1: Spatiotemporal evolution of normalized gas density n_g (a), gas speed v_g (b), electron density production rate by ionization S_{iz} (c), electron density n_e (d), electron azimuthal speed $v_{e,y}$ (e), electron temperature T_e (f), ionization rate coefficient $K_{iz} = S_{iz}/n_g n_e$ (g) and axial electric field E_x(h). The maps are obtained by averaging azimuthally at every time. The color scale is the same for all the plots. In (i) we show the total current evolution. The vertical dashed lines allow to separate four phases of the BM cycle.

depends on the effective electron temperature and the electron and neutral densities and on the ionization rate coefficient K_{iz}, that is plotted in Figure 7.1 (g). We also recall that the ionization rate coefficient can be written as

$$K_{iz} = \frac{4\pi}{n_e} \int_{v_{iz}}^{\infty} \sigma_{iz}(v) f_e(v) v^3 dv,$$

with v_{iz} the ionization threshold velocity (i. e., $v_{iz} = \sqrt{2e\mathcal{E}_{iz}/m_e}$, with $\mathcal{E}_{iz}$ the energy threshold for ionization) and σ_{iz} the ionization cross-section. The effective electron temperature is directly calculated from the electron energy distribution function. The fluctuations of these quantities are crucial in the evolution of the BM, which is an ionization instability. Therefore, understanding their variations is essential for explaining the development of the BM.

Usually, the BM is divided into two phases: the phase in which the current grows and the phase in which it decreases. The complexity of the case under study here, however, suggests using more than two phases: we decided to subdivide the growing and decreasing phases in two parts. With reference to Figure 7.1 (i), the first phase (A_1) corresponds to the first part of the growing BM phase, where the current grows significantly and has no high-frequency fluctuations. This phase is followed by A_2, which corresponds to the interval in which the current reaches a plateau and only high-frequency fluctuations are present. Then, the decreasing BM phase is divided into two parts: B_1 and B_2. In B_1 the current suddenly drops, while in B_2 the current is low, and high-frequency fluctuations are present. The final part of phase B_2 corresponds to the initial part of A_1, thus we can consider that the BM cycle is concluded. The BM cycle observed in this simulation has a rather slow dynamic: in several other cases, the phases A_2 and B_2 are very short, or not even present. Even if it might not be the most typical BM shape, its slow-varying parameters are particularly convenient to analyze.

The reader could wonder why we include phase A_2 in the BM growing phase since the current in this segment does not increase. This choice has been made considering the neutral dynamics, reported in Figure 7.1 (a) and Figure 7.2 (a). In these figures, we observe that the neutral density remains unperturbed during the BM cycle near the anode or in the plume, while it is strongly perturbed in the mid-channel region. In A_1, where the current is increasing, we observe that the neutral density starts to decrease, while most of the neutral ionization occurs in A_2. This is the reason why we included A_2 in the BM growing phase: it is a phase of high neutral gas ionization, where S_{iz} is maximal. Then, when the BM decreasing phase starts in B_1, the phenomenon of neutral depletion is reversed: the neutral gas starts to repopulate. Most of the neutral repopulation occurs in B_2.

The plasma density in Figure 7.1 (d) experiences a complementary behavior: the plasma starts from a low level at the beginning of A_1, then increases during A_1 and A_2, has a maximum in B_1 and drops in B_2.

A low number of electron-ion pairs are created during A_1, as one can notice by looking at S_{iz} in Figure 7.1 (c). Most of the ionization events happen in A_2, when the neutral density is already decreasing. As a consequence, the plasma density peak is reached during B_1. In B_2 there is almost no ionization, and the plasma density remains low. The electron temperature decreases in A_1 and is low in the first part of A_2. Subsequently, in the second part of A_2 and in B_1, the electron temperature

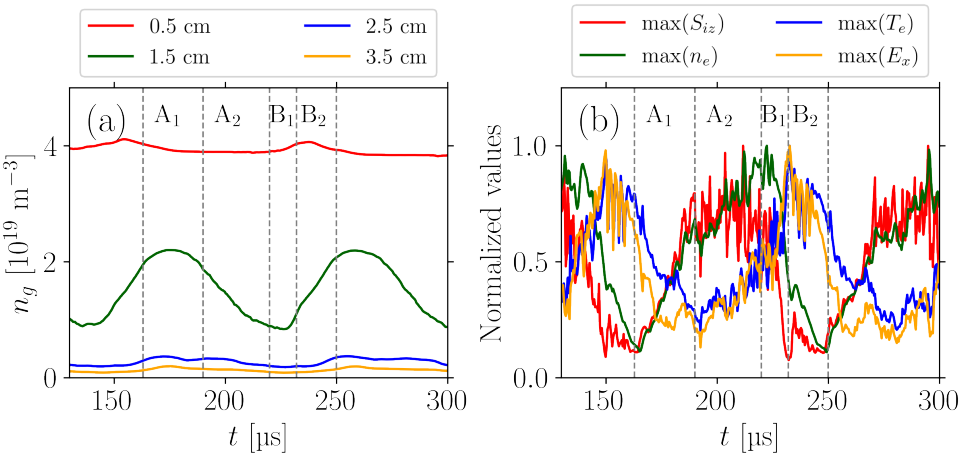


Figure 7.2: (a) Neutral density temporal evolution at three different positions. (b) Maximal normalized amplitude evolution of S_{iz}, n_e, T_e and E_x. The dashed vertical lines as in Figure 7.1 separate the different BM phases. These data are extracted directly from PIC outputs.

starts to increase. In B_2 the electron temperature is high, while the electron density is low. Before the ionization ignites again, the electron temperature has already dropped. So, the electron temperature corresponds to low ionization and vice versa (cf. Figure 7.1 (c) and (f)). However, T_e is related to other plasma parameters: the axial electric field E_x in Figure 7.1 (h) consequently and the electron azimuthal speed $v_{e,y}$ in Figure 7.1 (e). Indeed, when the electric field increases, the electron azimuthal drift (i. e., $v_{E\times B} = E/B$) and in turns the averaged electron energy also increases. The ionization rate coefficient K_{iz} in Figure 7.1 (g) is of course related to the electron temperature.

In Figure 7.2 (b) we plot the temporal evolution of the max of S_{iz}, n_e, T_e and E_x. As one can observe, the evolution of the electron density production rate is in phase with the evolution of the electron density amplitude. The electric field oscillation, in phase with the electron temperature, appears delayed with respect to the electron density oscillation. This is different from what was observed by Lafleur *et al.* [175] in a fluid simulation, in which the electric field increase was related to the electron density increase. During A_1, the increase in the electron density is sustained by the increase of the electron density production rate, so on n_e itself. The growth of S_{iz} cannot be explained by the increase of K_{iz}, which diminishes, as T_e, in this phase. At the end of A_2, the neutral density is extremely low, which cancels out the electron density production rate S_{iz}. Nevertheless, for a short period, the charged species density growth is sustained by the increased temperature, which increases the ionization rate coefficient. However, this does not last long: even if T_e remains high, in B_2 the electron density production rate and the density experience a sharp drop.

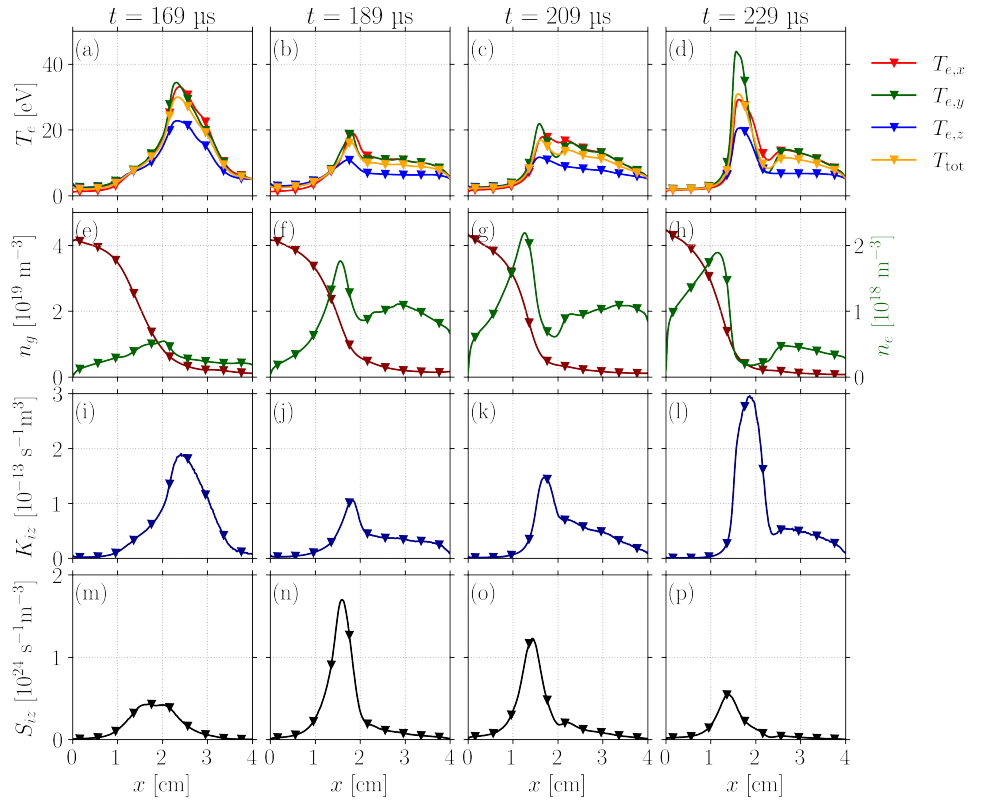


Figure 7.3: Each column represents a time instant (indicated in the first row). The first row shows the electron temperature profiles, the second the gas and electron density, the third the ionization rate coefficient K_{iz}, and the fourth the electron density production rate S_{iz}. These data are extracted directly from PIC outputs.

7.2.2 Impact of electron temperature and densities on the ionization mechanism in the BM

In this section, we further analyze how the electron temperature and densities impact K_{iz} and S_{iz}, by studying the evolution of their axial profiles, using data directly extracted from PIC. In the first row of Figure 7.3, we report the axial profiles of the electron temperature along the three simulation directions and the total temperature. We observe that the temperature profiles experience the same trend and that they are both low near the anode and the cathode, while they have a peak at the channel exit (i. e., between 1.5 cm and 2.5 cm). The temperature profile is almost identical in the three directions.

As we can see in the second row of Figure 7.3, the gas density profile varies very slowly during a BM cycle. Its evolution is more easily understandable in Figure 7.2 (a): the density is high and almost constant near the anode, while it is almost constant and close to zero in the plume. In between, in the ionization region, the gas density oscillates significantly. To better understand the physical mechanism governing this kind of oscillation, one should imagine the neutral gas mass oscillating back and

forth around a fixed position, see for example the iso-density white dashed line in Figure 7.1 (a). The electron density fluctuates in a much more strong way. The density is low near the anode, while it grows and reaches a maximum inside the thruster channel. The maximal density is followed by a steep drop, which is then followed by a slow increase in the plume. In the plume, it does not vary significantly.

In the third row of Figure 7.3, we show the ionization rate coefficient profile evolution. As already mentioned, K_{iz} follows the temperature at all times. The total ionization frequency, i. e., S_{iz}, is reported in the last row. As one can observe, the profile of S_{iz} is different from both the electron temperature and the density profiles.

It is therefore difficult to identify a positive feedback between the electron density production rate and the electron temperature: when the temperature increases, the ionization rate coefficient K_{iz} does, but the electron density production rate S_{iz} does not. The latter depends on the complex dynamics of both the gas and the plasma densities along with the ionization rate coefficient variations.

7.2.3 Study of the drift balance in the BM

As observed in the previous sections, the electron drift in the azimuthal direction is linked to the electron temperature and the ionization rate coefficient K_{iz}. In Figure 7.4 we show the electron azimuthal velocity profile at four different instants of the BM period. In this figure, we report the $\mathbf{E} \times \mathbf{B}$ drift (cf. Section 1.2.1),

$$v_{\mathrm{E}\times\mathrm{B}} = \frac{\mathbf{E} \times \mathbf{B}}{B^2}$$

in red and the diamagnetic drift

$$v_{\mathrm{D}} = \frac{-\nabla(k_B T_e n_e) \times \mathbf{B}}{q n_e B^2}$$

in green. The sum of these two terms is shown in blue, while in black we report the velocity measured directly in the PIC code. In the same figure, we show the evolution of the axial electric field (orange). The red markers in the current discharge evolution plotted in (e) show the instants analyzed in the above figures.

The profiles in Figure 7.4 clarify several points about the electron dynamics in the HTs. First, we observe that the electrons injected isotropically at the cathode ($x = 4\,\mathrm{cm}$) are not accelerated azimuthally right away. In the region near the cathode, both the $\mathbf{E} \times \mathbf{B}$ and diamagnetic drifts are very small. Only once an electron enters the zone where the axial electric field E_x is large, it starts to accelerate in the azimuthal direction. The diamagnetic drift, which depends on the pressure gradient, is opposite to the $\mathbf{E} \times \mathbf{B}$ drift. However, at all instants of the BM cycle, the diamagnetic drift is smaller than the $\mathbf{E} \times \mathbf{B}$ one. In the ionization zone (i. e., between around 1.5 cm and 2.5 cm), the diamagnetic drift is negligible with respect to the $\mathbf{E} \times \mathbf{B}$ drift: the effective ion drift (black line) is composed almost exclusively by the $\mathbf{E} \times \mathbf{B}$ one (red line). Only in the anode region, where both drifts change sign, the diamagnetic drift becomes comparable to the $\mathbf{E} \times \mathbf{B}$ drift. In this region, the two drifts balance, so the electron azimuthal speed results to be low. Boeuf and Garrigues in Ref. [124] observed a similar trend in a simplified axial-azimuthal configuration with a fixed ionization source term (with no gas flow), and then no BM. They reported that the

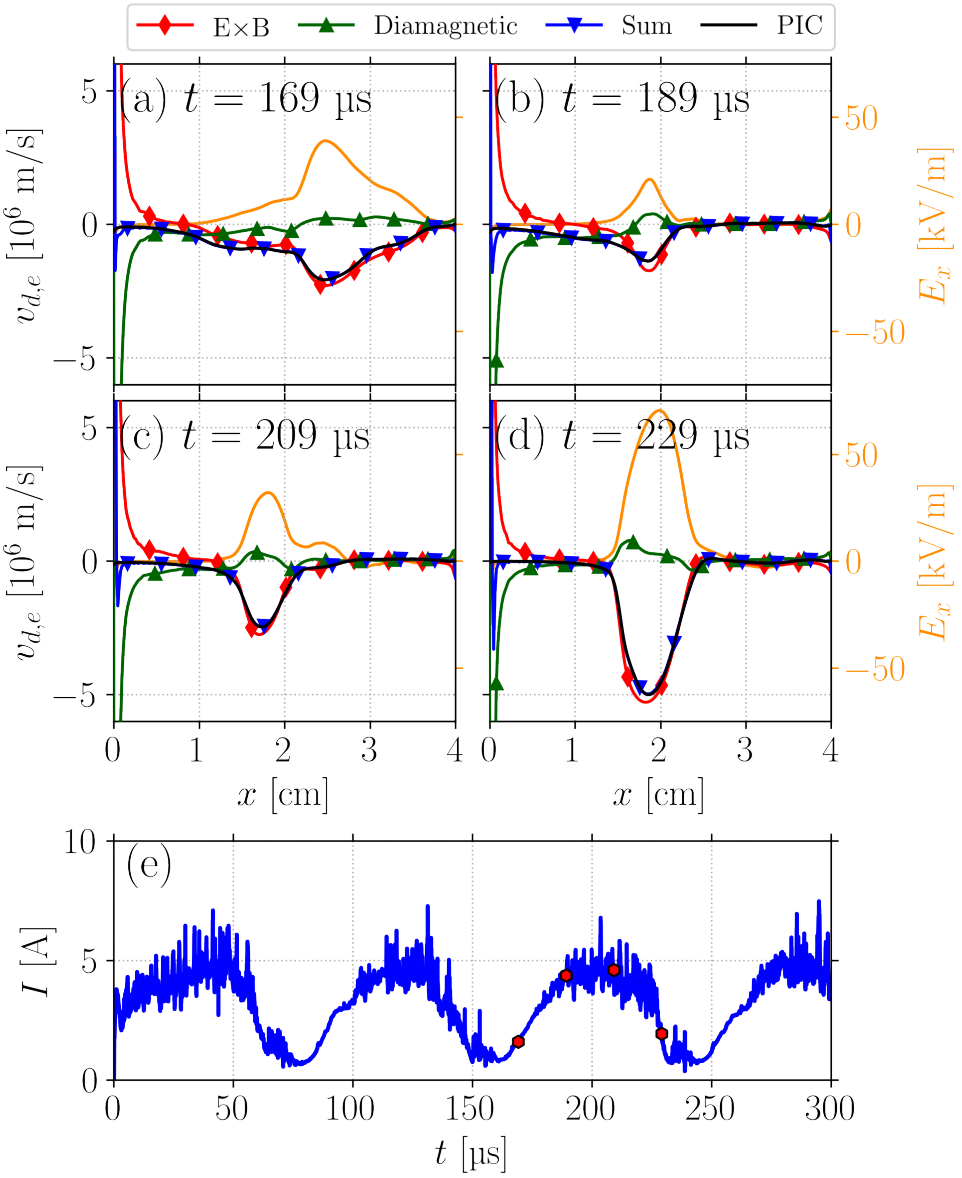


Figure 7.4: (a)-(d) Profiles of the electron velocity along the thruster axis. The red line represents the $\mathbf{E} \times \mathbf{B}$ drift, the green is the diamagnetic drift, the blue is the sum of the two, and the black is the drift as it is extracted by the electron speed in the PIC simulation. In (e) we show the discharge current, where the red markers indicate the instants analyzed in the above figures.

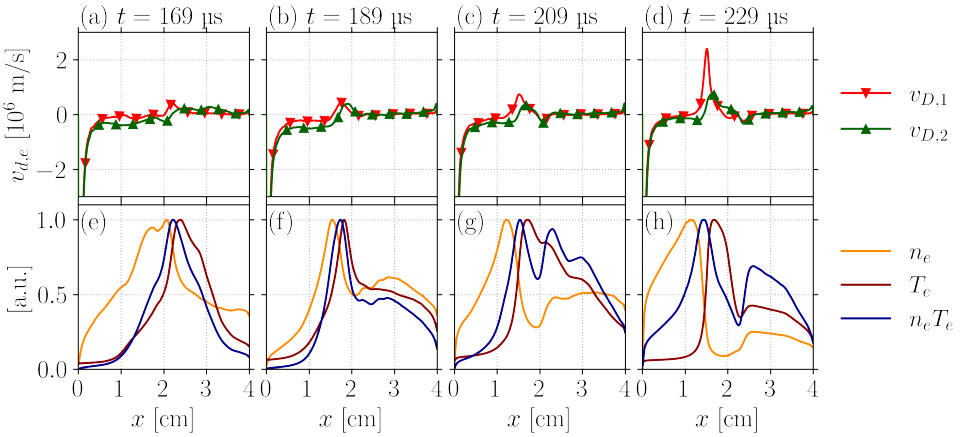


Figure 7.5: Diamagnetic drift profile along the thruster axis at different times (Top row). The velocity $v_{D,1}$ is calculated in the isothermal approximation, while $v_{D,2}$ considers the gradient of the entire pressure term. The density, temperature, and pressure profiles are shown in the bottom row.

diamagnetic drift and the $\mathbf{E} \times \mathbf{B}$ drift have a similar value. This is not what we observe here: the intense electric field issued by the high anode voltage at the end of the BM cycle, makes the $\mathbf{E} \times \mathbf{B}$ drift much larger than the diamagnetic one. The difference is probably related to the different conditions of their simulation.

The computation of the diamagnetic drift requires some further discussion: in some cases [76] the diamagnetic drift is written using the isothermal approximation, i. e., the pressure gradient is computed using the electron density only, while the temperature exits the gradient term. In Figure 7.5 (a)-(d) we show the axial profiles of the diamagnetic drift calculated with the isothermal approximation (red line) and the full pressure gradient (green line). We observe that the two profiles experience more or less the same trend, but there are some substantial differences in the central part of the domain. These differences can be explained with reference to the density, temperature, and pressure profiles in Figure 7.5 (e)-(h). We note that the isothermal approximation never holds.

7.2.4 Electron transport in the axial direction of the thruster

The anomalous electron transport in the axial direction is one of the most studied characteristics of HTs. In this thesis, we characterized in detail the instabilities driving this transport, nevertheless, we have not discussed yet in depth the transport itself. As already mentioned in Section 1.2.3, numerous studies [133, 170] have shown that a convenient way to model this transport is to use the correlation term, or friction force,

$$R_{ei} = q\langle \delta n \delta E_y \rangle,$$

where δn and δE_y are the density and the electric field fluctuations, respectively. We calculated the azimuthal average of this term and plotted its spatiotemporal evolution (i. e., the temporal evolution of its axial profile) in Figure 7.6.

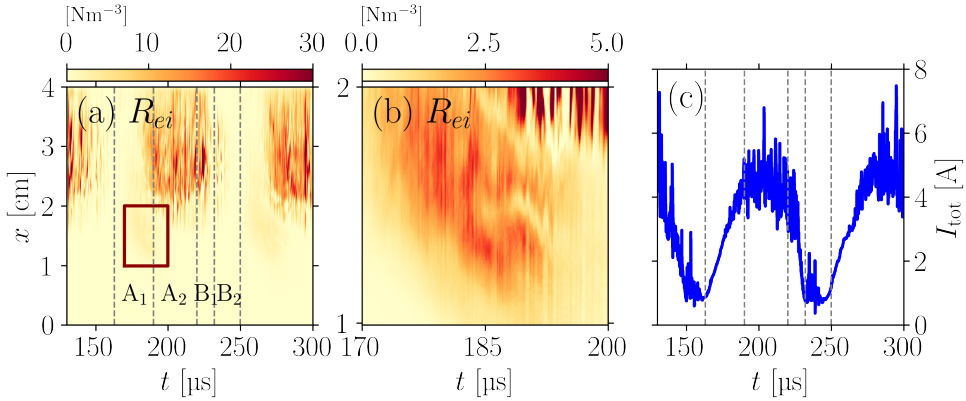


Figure 7.6: (a) Spatiotemporal evolution (i. e., the temporal evolution of the axial profile) of R_{ei} over the span discussed before. In (b) we report the same data, but we zoom on the region indicated by the ruby rectangular box in (a), i. e., $1\,\text{cm} < x < 2\,\text{cm}$ and $170\,\mu\text{s} < t < 200\,\mu\text{s}$. In (c) we show the discharge current evolution. The dashed vertical lines help to define the different times of the discharge.

As one can see in Figure 7.6 (a), the friction force term is particularly large at the channel exit and in the plume when the current is large: from the end of A_1 to the beginning of B_2. The friction force term is negligible elsewhere: in the inner channel region, i. e., $x < 2\,\text{cm}$, the value of R_{ei} is always very low, as it is during the BM phases when the current is low. This observation allows us to conclude that the anomalous transport, or at least its component depending on the correlation, is present only during the high-current phase of the breathing mode, while it disappears when the current drops. This agrees with the results of Ref. [201], reported in Chapter 5, where we discussed the growth of the instabilities during the BM cycle.

Even if the most significant part of the anomalous transport occurs mainly at the channel exit and in the plume, some clarifications can be added, thanks to the analysis of Figure 7.6. The friction force is so large in the plume that it is difficult to see if any increased transport is present in other regions. However, zooming on some precise intervals allows us to retrieve further results: in Figure 7.6 (b) we report the same data, but we zoom in the region indicated by the ruby rectangular box in Figure 7.6 (a), i. e., $1\,\text{cm} < x < 2\,\text{cm}$ and $170\,\mu\text{s} < t < 200\,\mu\text{s}$. In this region, the friction force is not negligible, but it is not as large as in the plume. This observation suggests that the anomalous transport is not only present in the plume, but also in the channel region. This agrees with the results of Ref. [202], reported in Chapter 5, about the wave propagation in the plasma from the mid-channel region towards the anode. In this figure, we observe that at the beginning of the BM growing phase, a non-zero R_{ei} starts to propagate from $x \sim 2\,\text{cm}$ to the anode. This propagation lasts for around $10\,\mu\text{s}$. However, the absolute value of R_{ei} in the channel remains significantly smaller than in the plume.

7.2.5 Discussion of the main results on the BM

The study of the plasma parameters evolution during the BM, captured with a PIC simulation allows us to draw some conclusions about the development of this mode. The main elements of our analysis are listed below.

- The BM can be divided into four phases: two during the current growing phase (i. e., A_1 and A_2), and two during the current decreasing phase (i. e., B_1 and B_2).
- Most of the particles creation happens during A_2, while the production rate is almost zero during B_1 and B_2.
- The electron density production rate, i. e. S_{iz}, evolution depends on the competition between neutral gas, plasma density, and ionization rate coefficient K_{iz}. In particular, S_{iz} and K_{iz} peaks occur during different BM phases.
- The $\mathbf{E} \times \mathbf{B}$ drift is dominating the electron motion in the azimuthal direction, being always larger than the diamagnetic drift. The latter cannot be calculated with the isothermal approximation.
- The electron anomalous transport is present in the plume during the high-current phase of the BM, while it vanishes when the current is low.

7.3 VARIATION OF THE HT CONFIGURATION

The simulations not only can explain the physics of a device and help understand the origin of a particular phenomenon but they can also be used to simulate different device configurations. In this section, we discuss the results of a study we performed to explore the characteristics of a HT under different working conditions. When not specified in the text, the simulation parameters are those reported in Table 3.2. In this section, simulations with both azimuthal lengths of $L_y = 1\,\text{cm}$ and $L_y = 4\,\text{cm}$ are presented. Despite having shown in Chapter 3 that using $L_y = 1\,\text{cm}$ does not permit the complete development of the BM, it is still valuable to investigate the plasma behavior in such cases to have a preliminary understanding of the trend. Nevertheless, one should keep in mind that the results with this reduced length are not fully reliable. In some of these simulations, we used the virtual-*r* model discussed in Chapter 6: if it is the case, it is explicitly mentioned.

7.3.1 Anode voltage variation

In this section, we study how the anode voltage impacts the plasma behavior and the engineering parameters. Since we wanted to observe the complete plasma dynamics reproducing the BM, we used a simulation domain with $L_y = 4\,\text{cm}$. The cathode temperature was fixed at 5 eV and the neutral gas mass flow rate at 5 mg/s, while the imposed DC supply voltage, i. e., V_0, was varied from 200 V to 800 V. To introduce the wall losses, we used the virtual-*r* model described in Chapter 6 with $L_z = 4\,\text{cm}$.

In Figure 7.7 we show the evolution of the discharge current and the voltage at the anode for different values of the imposed DC supply voltage. These results clearly

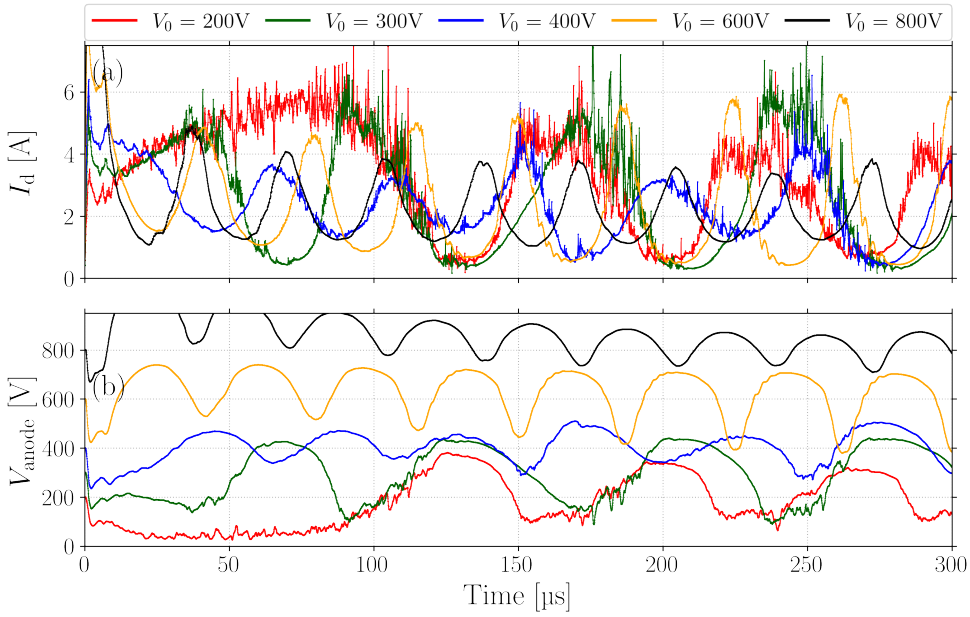


Figure 7.7: Discharge current (a) and anode potential (b) as a function of time, for different anode voltages.

show that the plasma dynamics is strongly influenced by the imposed anode voltage. For example, the BM frequency increases with the voltage, as observed experimentally.

Effect on current and potential

By averaging the results in Figure 7.7, we obtain in Figure 7.8 the mean discharge current (a) and the mean anode potential (c). To have a more quantitative evaluation of the results, we also show in Figure 7.8 the standard deviation of the discharge current (b) and the anode potential (d), divided by the corresponding mean value. The mean current appears to decrease with the voltage. This decrease, which is significant for voltages between 200 V and 400 V, is less obvious for larger values of the anode potential. In Figure 7.8 (c) we observe that the mean anode potential stabilized at the imposed voltage value. Some deviation is still observed at high anode voltage; however, it is rather small if compared to the mean value. In Figure 7.9 we show the evolution of the absorbed power for different generator voltages.

In Figure 7.7 (b) we plot the standard deviation of the discharge current divided by the current mean value: even if the amplitude of the fluctuations varies significantly (i. e., in the range $40\% - 80\%$), it is difficult to find a clear trend. Conversely, the fluctuations of the anode voltage, reported in (d), have a more linear behavior: when we increase the anode voltage, the fluctuation amplitude drops.

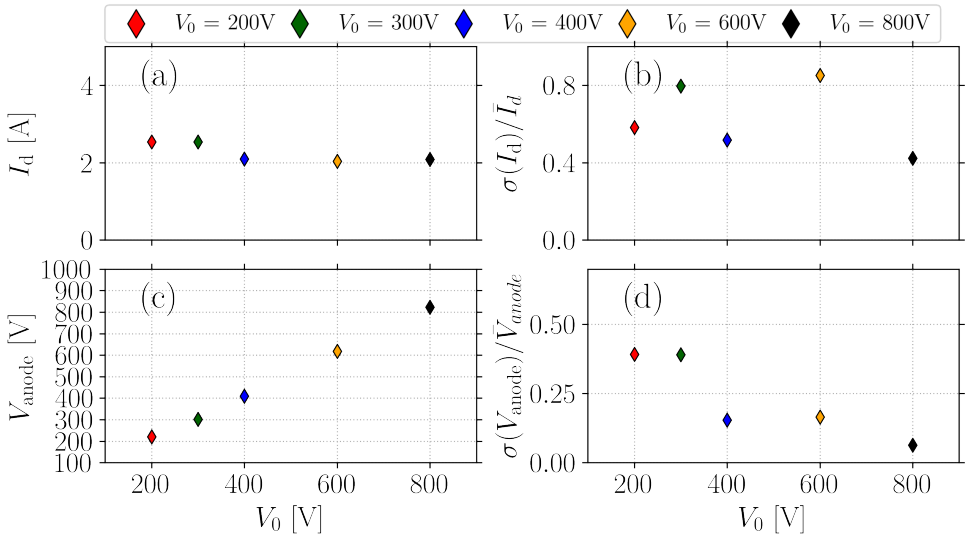


Figure 7.8: Average discharge current (a) and anode potential (c). (b) and (d) show the standard deviation of the discharge current and of the anode potential, respectively, divided by the corresponding mean value.

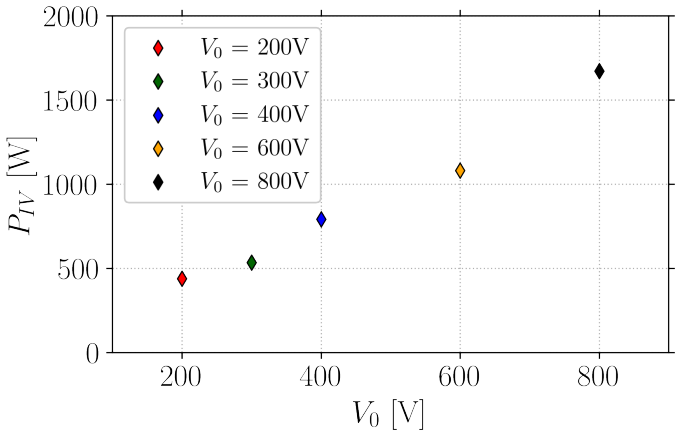


Figure 7.9: Average I-V power absorbed by the thruster for different generator voltages.

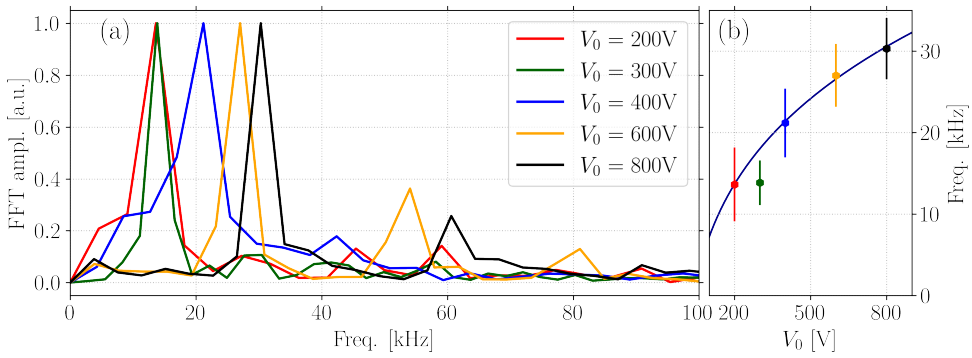


Figure 7.10: (a) Normalized FFT of the current for different anode voltages. (b) Evolution of the BM frequency as a function of the anode voltage. The blue line shows a polynomial fit of type $\omega = aV_0^{1/4} + b$, with a and b two coefficients calculated with linear regression.

Effect on the BM frequency

In the work of Fife [35], a simple formula for the BM frequency ω_{BM} was proposed:

$$\omega_{\text{BM}} \propto \left(v_g v_{i,x}\right)^{1/2},$$

where v_g is the gas injection velocity and $v_{i,x}$ is the ion ejection velocity in the x direction. Increasing the anode voltage causes an increase of the ion ejection velocity, e. g., $v_{i,x} \propto \sqrt{V_0}$, which in turn increases the BM frequency. By imposing a constant neutral flux, the neutral injection velocity is fixed and we should therefore observe the frequency scaling as

$$\omega_{\text{BM}} \propto V_0^{1/4}.$$

Figure 7.10 (b) shows the evolution of the modulation frequency as a function of the imposed anode voltage. The result shows that the trend follows the formula proposed by Fife [35]. One should notice that when the anode voltage is low, the simulation experiences a strong transient, and the shape of the BM peaks changes significantly. So, in these conditions, several other mechanisms might influence the BM frequency.

Figure 7.10 (a) shows that when we increase the anode voltage, we can detect higher order harmonics of the BM in the current, as it was observed by several experimental works [157, 171].

Plasma parameters

The change in the anode voltage affects all the plasma parameters. We study the axial profile of the average temperature and electron density profiles for different values of anode voltage. The values are reported in Figure 7.11, where the shaded area covers a standard deviation from the average value. The electron temperature, plotted in red, increases significantly with the increase of the anode voltage. The origin of this

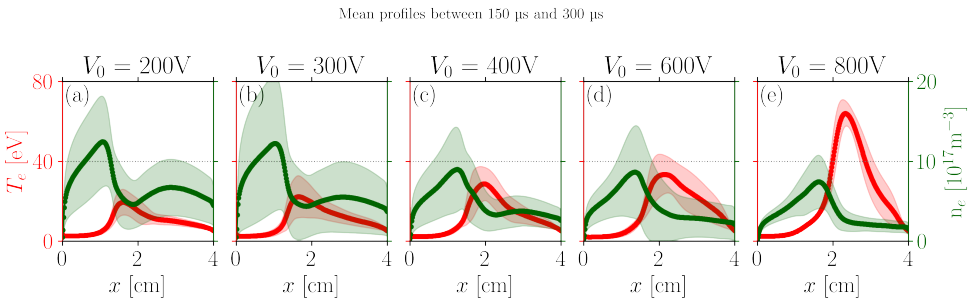


Figure 7.11: Mean electron temperature and density for different imposed anode voltages.

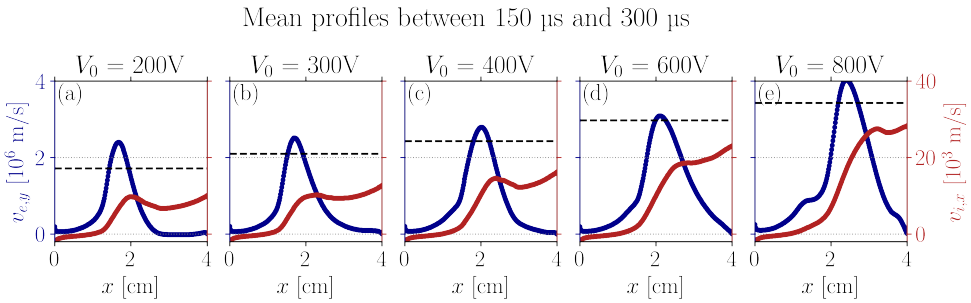


Figure 7.12: Mean electron azimuthal velocity ($v_{e,y}$, blue) and ion axial temperature ($v_{i,x}$, brick red) for different imposed anode voltages. The horizontal dashed line represents the ideal exhaust ion velocity.

phenomenon is strictly related to the plasma ignition mechanism of HTs. In these devices, electric energy from the generator is transferred to the plasma through the azimuthal drift. The larger the anode potential is, the larger the axial electric field is and, therefore, the larger the azimuthal velocity amplitude of the electrons.

These observations can be discussed concerning Figure 7.12, where we show the mean profiles of azimuthal electron velocity (in blue) and the axial ion velocity (in brick red). The azimuthal electron velocity, as explained, increases with the anode voltage. The profile shape remains almost unchanged in the channel region near the anode, while it varies substantially at the channel exit, where the axial electric field reaches its maximum.

The axial ion velocity is an important parameter for the thrusters since it is directly related to the specific impulse. The horizontal dashed lines in Figure 7.12 represent the ideal exhaust velocity

$$v_{i,\mathrm{exh}} = \sqrt{\frac{2eV_{\mathrm{anode}}}{m_i}},$$

for each anode voltage value. Consistently, the measured ion speed depends on the imposed potential. However, we notice that the speed at $x = 4$ cm is lower than the one predicted by the theory. The cause of the reduced exhaust velocity can be found in various phenomena: (i) part of the ions are not accelerated by the full voltage;

(ii) the presence of axial instabilities, discussed in Section 5.3.2.3 and (iii) the anode voltage oscillations.

The origin of (i) is easy to understand: the acceleration region and the ionization region are partially superimposed, so, some of the ions do not experience the full acceleration imposed by the potential drop. The physical origin of (ii) is discussed in Chapter 5, where we have shown how the axial instabilities induce a population of low-energy ions in the plasma plume. The origin of (iii) can be explained by the means inequality. An oscillating potential implies that the mean exhaust velocity is

$$\langle v_{i,\mathrm{exh}} \rangle = \sqrt{\frac{2}{m_i}} \langle \sqrt{eV_{\mathrm{anode}}} \rangle < \sqrt{\frac{2}{m_i}} \sqrt{e \langle V_{\mathrm{anode}} \rangle}.$$

So, the more the anode voltage oscillates, the lower is the average exhaust velocity. At high voltage, the effect is negligible, while at lower voltage the effect is more pronounced: a reduction of the ion velocity of the order of $5 - 10\%$ can be related to this phenomenon. Globally, we observe that the acceleration efficiency, defined as the ratio between the effective mean exhaust velocity and the theoretical one, increases with the anode voltage.

Effect on engineering parameters

The variation of the plasma parameters has a direct impact on the operating parameters of the thruster. In Figure 7.13 we show the variation of the specific impulse, thrust, mass efficiency, and thrust power-to-power ratio (P_{thrust}/P_G) as a function of the anode voltage. In all four subfigures, we observe that the thruster performance increases with the increase of the anode voltage.

As explained in Section 1.2, we have usually considered that thrusters do not scale well: the results presented here contradict this statement. However, the root of this phenomenon can be explained rather simply. First, the biggest scaling problems are found when we scale down the thruster, reducing the power and not increasing it, as we have done here. In addition, we observe that when we lower the anode voltage to 200 V, the discharge begins to be less stable: under these conditions, there is a real risk of turning off the discharge. Furthermore, these simulations do not take into account the third direction: when we increase the temperature in the plasma, we increase the particle flow and energy to the walls. Thus, we increase wall erosion and decrease the lifetime of the thruster.

The graphs in Figure 7.13 show that the voltage imposed at the anode and the thrust, specific impulse, and power ratio increase almost linearly with the imposed anode voltage. By increasing the DC supply voltage by a factor of 4, the thrust and specific impulse gain a factor of ≈ 3. In all cases, the mass efficiency is rather good (i. e., $> 75\%$). These results suggest that the development of a higher-power thruster should not require any special modification of the axial-azimuth configuration. However, the increased power will require a more careful design in the radial direction to control the wall erosion related to the high electron temperatures, that we observed for high anode voltages.

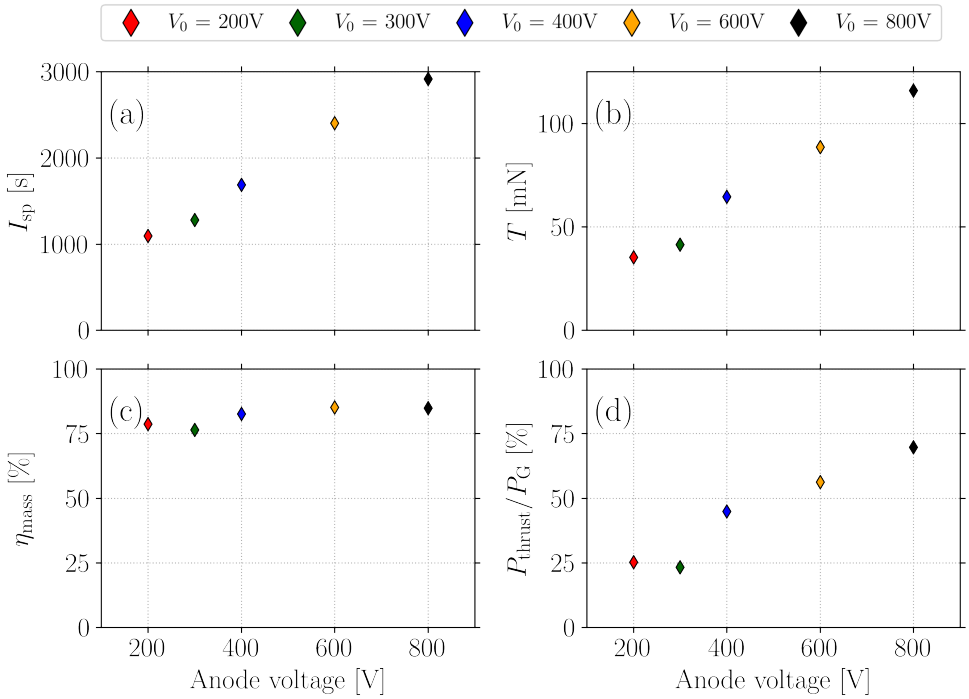


Figure 7.13: (a) Specific impulse, (b) thrust, (c) mass efficiency, and (d) thrust power-to-power ratio as a function of the anode voltage.

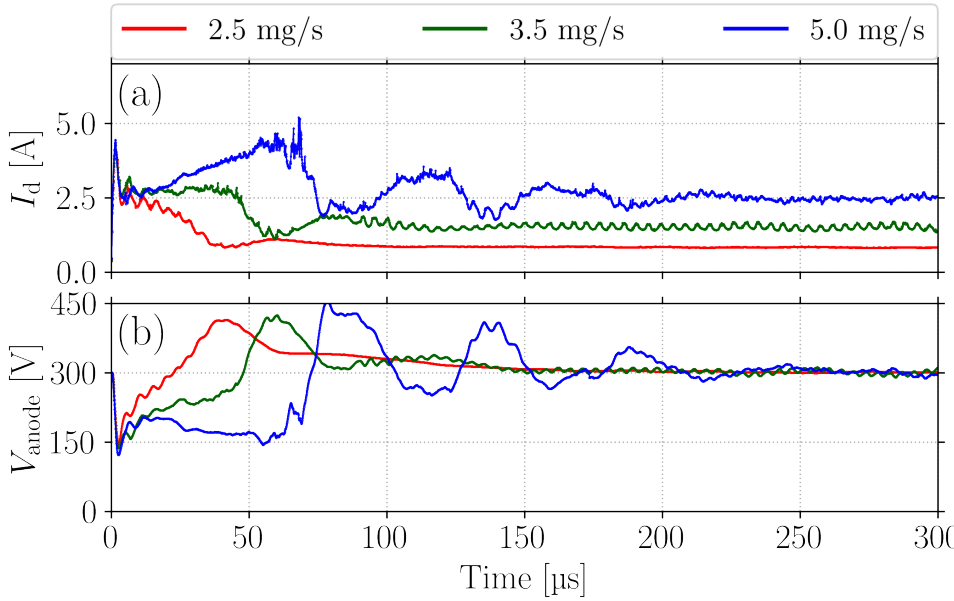


Figure 7.14: Current (a) and anode potential (b) temporal evolution for different values of the neutral gas flow rate.

7.3.2 Neutral gas mass flow rate

One of the parameters that are usually modified to change the thruster working point is the neutral gas mass flow rate. In real devices, neutral gas is injected through some nozzles at the bottom of the thruster channel, in correspondence with the anode. The shape and distribution of these openings can have a non-negligible effect on discharge characteristics and thruster efficiency. However, in our bi-dimensional code, the nozzles are not modeled and the gas is uniformly injected into the system. The present analysis is performed by varying the neutral gas flow rate at the anode boundary.

Effect on current and potential

The first tests on the variation of the neutral mass flow rate have been performed on some cases with $L_y = 1\,\text{cm}$ and consistent virtual-r (cf. Section 6.4). In Figure 7.14 we show the evolution of the current (a) and anode potential (b) for different values of the neutral gas flow rate. In this figure, the mass flow rate is varied from 2.5 mg/s to 5 mg/s. In all cases, a steady-state has been reached and the anode voltage after the transient is close to the nominal value of 300 V. The current, as expected, increases with the increasing mass flow rate. The BM is more pronounced in the initial phase when the mass flow rate is higher. However, it is damped over time. The transient appears to be longer for a larger mass flow rate. The high-frequency modulation (i. e., usually linked to ITTI) is present in the case of high mass flow rate, while it almost disappears in the case of low mass flow rate.

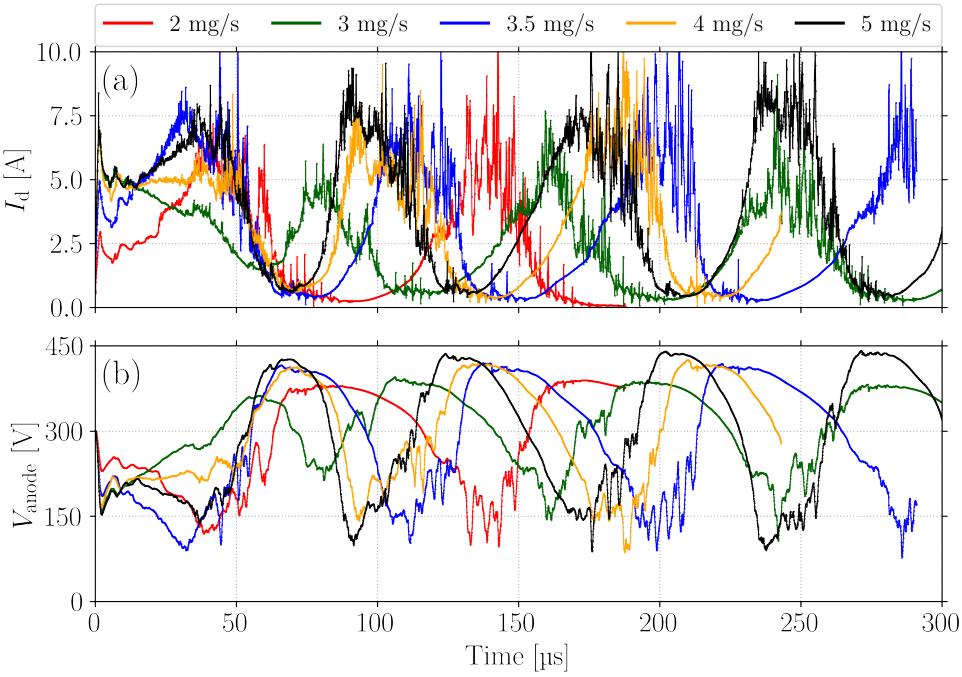


Figure 7.15: Current (a) and anode potential (b) temporal evolution for different values of the neutral gas flow rate.

The discharge current evolution in Figure 7.14 suggests that the mass efficiency depends on the mass flow rate. We note that the current corresponding to $\dot{m} = 5\,\mathrm{mg/s}$ is more than twice larger than the one corresponding to $\dot{m} = 2.5\,\mathrm{mg/s}$: the mass efficiency is higher in the case of higher mass flow rate. The efficiency increases from 45% in the case of $\dot{m} = 2.5\,\mathrm{mg/s}$ to 59% in the case of $\dot{m} = 3.5\,\mathrm{mg/s}$ and to 62% for $\dot{m} = 5\,\mathrm{mg/s}$. Therefore, the higher the mass flow rate is, the higher the mass efficiency is. This is probably related to the larger power absorbed by the plasma in the case of a large mass flow rate.

As we reported several times, the simulations with $L_y = 1\,\mathrm{cm}$ do not reproduce the BM. For this reason, we run some other cases, in similar conditions, but with $L_y = 4\,\mathrm{cm}$. A virtual-r of $L_z = 4\,\mathrm{cm}$ is used in these simulations in order to include some radial losses. This makes the simulations not fully consistent, but it eases the convergence of the simulation with a small neutral flux. Otherwise, the increase of the radial losses above a certain threshold risks switching off the discharge.

In Figure 7.15 we show the current (a) and anode voltage (b) evolutions for five different values of the neutral gas mass flow rate, varied between $2\,\mathrm{mg/s}$ and $5\,\mathrm{mg/s}$. For the case with a mass flow rate of $2\,\mathrm{mg/s}$, only one period BM was simulated: at the end of the descending phase, the lack of particles caused the plasma to shut down. The plasma behavior appears to be radically different from the one of $L_y = 1\,\mathrm{cm}$ reported in Figure 7.14: the large current fluctuations related to BM are present for all values of the neutral gas mass flow rate. Moreover, the BM does not seem to be damped over time. The high cost of each simulation forced us to limit the physical

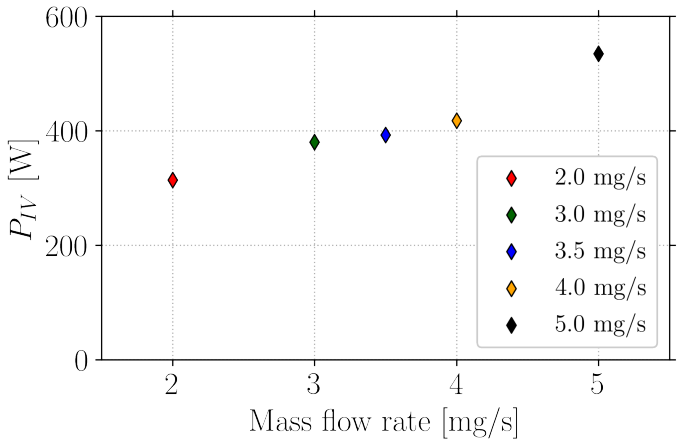


Figure 7.16: Average I-V power absorbed by the thruster for different mass flow rates.

time of each simulation: only a couple of BM periods are simulated for each test case. In Figure 7.16 we observe that the power absorbed by the discharge is lower at low mass flow rate. This, unfortunately, makes the comparison between the different cases less straightforward.

The first feature that stands out in Figure 7.15 is the BM: how do its frequency and amplitude depend on the imposed mass flow rate? In Figure 7.17 we show the BM frequency (b) and amplitude (c) for different values of the neutral gas mass flow rate. The BM frequency is calculated as the inverse of the time between consecutive peaks of the current. In the case of $\dot{m} = 2\,\mathrm{mg/s}$ the frequency is calculated using a single peak, so we expect that the error in this measurement is large and that the result, in this case, might be anomalous. For $\dot{m} = 3\,\mathrm{mg/s}, 3.5\,\mathrm{mg/s}, 4\,\mathrm{mg/s}$ the frequency is calculated using two peaks, while for $\dot{m} = 5\,\mathrm{mg/s}$ the frequency is calculated using several peaks. The error in the frequency measurement is therefore expected to be smaller for a higher mass flow rate. As an example, studying the blue line in (a), we observe that the current increase during the BM growing phase is much steeper at $t \approx 100\,\mu\mathrm{s}$ than at $t \approx 250\,\mu\mathrm{s}$. So, the choice of peaks might affect the frequency measurement, in a case like the present one, where a limited number of peaks can be used.

The results show that the BM frequency increases with the mass flow rate, as observed experimentally. This phenomenon is included in the theory by Fife [35], introduced in Section 7.2.1. At equilibrium, we have that the neutral (i. e., v_g) and ion (i. e., $v_{i,x}$) velocities can be written as

$$v_g = lK_{iz}n_i^0,$$
$$v_{i,x} = lK_{iz}n_g^0,$$

with n_g^0 and n_i^0 the equilibrium neutral and ion densities, respectively, and l the ionization length. The BM frequency is then given by

$$\omega = \left(n_i^0 n_g^0 K_{iz}^2\right)^{1/2}.$$

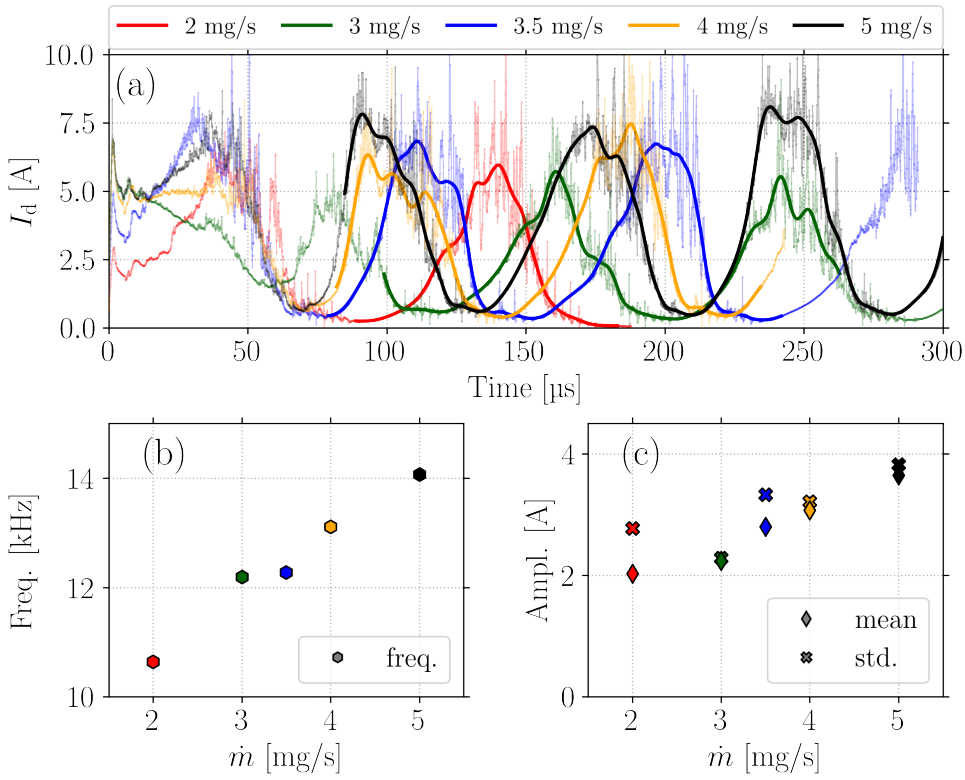


Figure 7.17: From the current (a), we calculated the BM frequency (b), mean current, and the BM amplitude (c), for different values of the neutral gas flow rate. In (a) we show explicitly the filtered BM peaks.

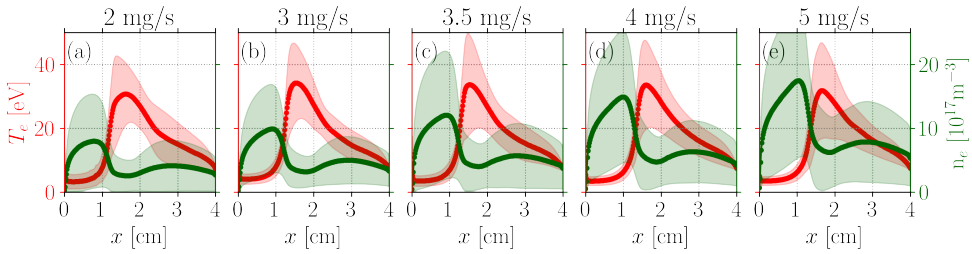


Figure 7.18: Electron temperature (red) and density (blue) profiles for different values of the neutral gas flow rate.

Hence, we see that an increased mass flow rate, which implies an increased density, leads to an increased BM frequency.

The BM amplitude is calculated as the current standard variation over a BM period and it is reported with the crosses in Figure 7.17 (c). The amplitude of the BM fluctuations appears to be strictly linked to the mean current: the amplitude of the fluctuations is as large as the current mean value.

Effect on plasma parameters

By averaging the electron temperature and density over time, we obtain the axial profiles in Figure 7.18. The electron temperature profile seems to be weakly affected by the variation of the injected gas mass flow rate. Not only is the average profile almost constant, but also the fluctuations around the average value (shaded area) are very similar in all cases.

Conversely, the electron density profile is strongly affected by the variation of the neutral gas mass flow rate: a larger neutral injection corresponds to a larger plasma density. However, the profile shape remains unchanged: it increases from the anode and reaches a maximum near $x = 1\,\text{cm}$. Then, it has a sharp drop, followed by a dome-like shape, which has a maximum at around $x = 3\,\text{cm}$.

The electron temperature and density show clearly that the principal effect of the variation of the neutral gas mass flow rate is to vary the mean plasma density in the thruster, without impacting T_e. Interestingly, the effect on the density on average is distributed over the whole thruster: we do not observe a particular increase of the density in a specific region.

Effect on engineering parameters

The analysis of the engineering parameters, as defined in Section 1.1.4, allows for quantifying the effect of the change of neutral flux on the thruster performance. In Figure 7.19 we show the variation of the specific impulse, thrust, mass efficiency, and thrust power-to-power ratio for different values of the neutral gas mass flow rate. The I_{sp} reported in Figure 7.19 (a) experiences a small increase with the increase of the neutral gas mass flow rate. Since its value does not depend on the mass flow, this result suggests that when we increase the neutral gas mass flow rate, we are improving the ion acceleration towards the plume. The thrust Figure 7.19 (b)

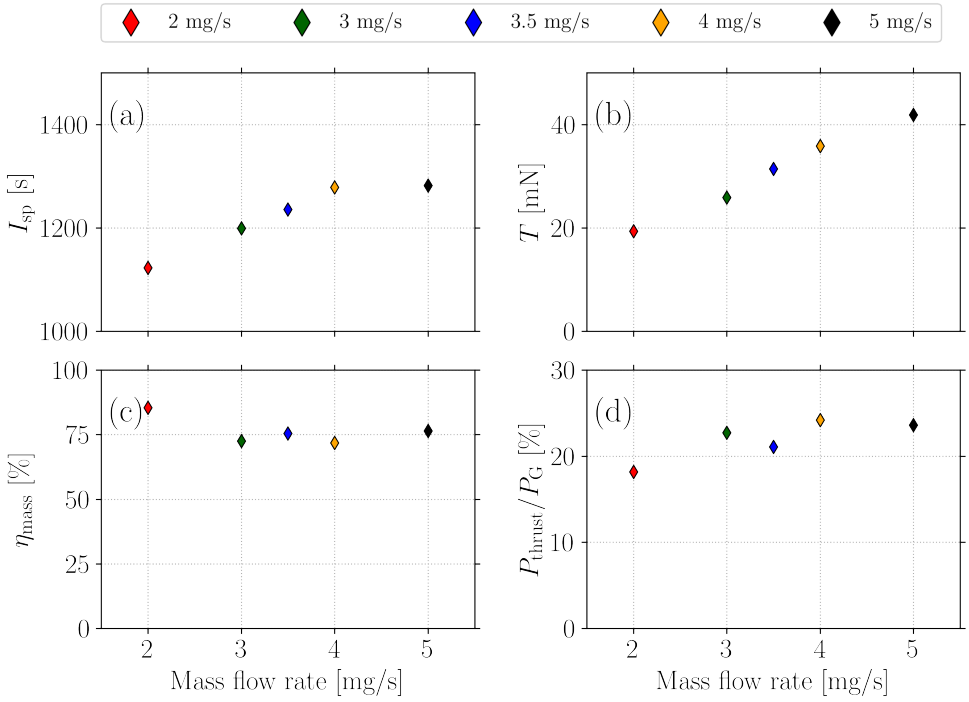


Figure 7.19: Specific impulse (a), thrust (b), mass efficiency (c), and thrust power-to-power ratio (d) for different mass flow rates.

increases linearly with the neutral gas mass flow rate: it means that the thruster works properly for the different values of injection mass flow rate.

In Figure 7.17 (c) we remark that the mean current over a BM period increases with the increase of neutral mass flow rate, as expected. Consistently, the mass consumption efficiency is almost constant (i. e., around $70 - 75\%$) for all cases but the first, where it takes the value of 85%. At low mass flow the efficiency seems better. However, as we discussed above the analysis in the case of $\dot{m} = 2\,\mathrm{mg/s}$ is not fully reliable.

The thrust power-to-power ratio (d) increases linearly with the neutral gas mass flow rate. However, the thrust power-to-power ratio reported here (i. e., at best 32%) is significantly lower than the one observed in literature for real devices [76]. We remember that the I-V power is not constant for the various cases, as one can observe in Figure 7.16.

7.3.3 Magnetic field variation

The magnetic configuration is one of the key elements for the proper operation of a HT and the architecture of the magnetic circuit represents one of the most important challenges in the design of the thrusters. The magnetic field is generated by the current flowing in the coils, and it is therefore possible to vary the magnetic field by changing this current. In our simulations, the coils are not modeled and only a

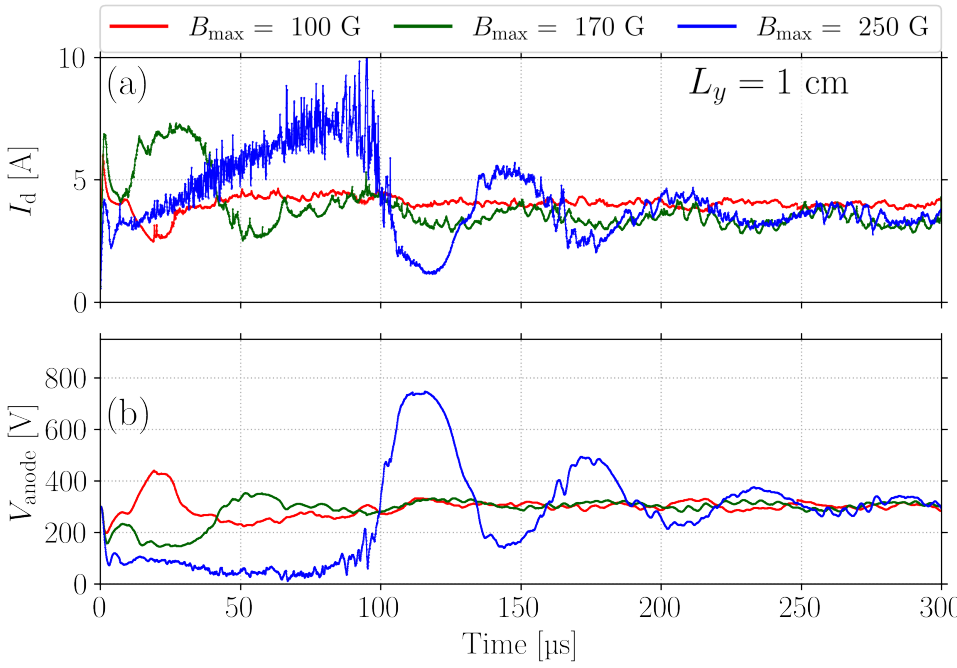


Figure 7.20: Current (a) and potential (b) for different values of B_{max}, the peak value of the magnetic field, for azimuthal length $L_y = 1\,\text{cm}$.

static magnetic field is considered. In this section, we present a preliminary study of the effect of varying the magnetic field on plasma parameters and thruster performance. The magnetic field, azimuthally homogeneous, varies axially as depicted in Figure 3.18. We recall that the standard magnetic field maximal value is $B_{max} = 170\,\text{G}$. In this chapter, we will change the amplitude of the magnetic field by keeping its axial profile constant. So, the different configurations will be labeled by the value of B_{max}.

Effect on current and potential

The first study has been performed on simulations with $L_y = 1\,\text{cm}$, by varying the magnetic field amplitude. The temporal evolutions of the current and anode voltage are reported in Figure 7.20. The fluctuations in these parameters appear to be strongly related to the value of the magnetic field: the larger B is, the larger the fluctuations in current and potential. When the magnetic field is reduced, the current is extremely steady and its mean value is higher than the one calculated for the case with $B_{max} = 170\,\text{G}$. In contrast, when the value of the magnetic field is increased to $B_{max} = 250\,\text{G}$, the oscillations of current and potential become larger: the circuit does not efficiently damp the BM. Although these results, obtained with a small azimuthal domain, are very interesting, they do not fully reproduce the BM. For this reason, we decided to analyze in detail some simulations performed with $L_y = 4\,\text{cm}$, which allows the full development of the BM.

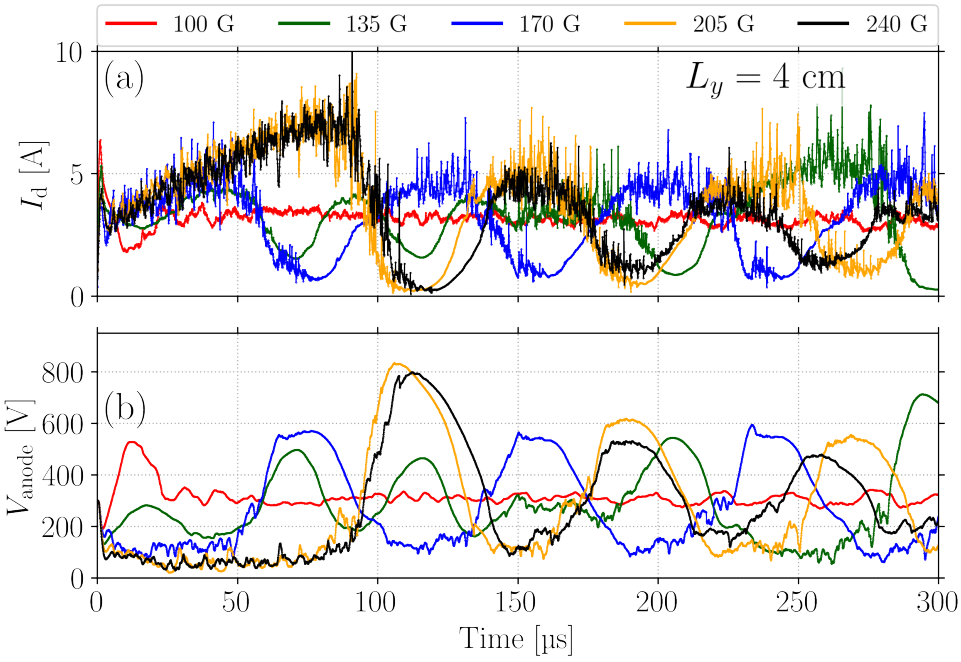


Figure 7.21: Current (a) and potential (b) for different values of B_{max}, the peak value of the magnetic field, for azimuthal length $L_y = 4\,cm$.

Following the same approach used before, in the case of $L_y = 4\,cm$, the peak value of the magnetic field is varied from $B_{max} = 100\,G$ to $B_{max} = 240\,G$, without changing the shape of its axial profile. The current and potential temporal evolution are reported in Figure 7.21 (a) and (b), respectively. These temporal evolutions appear to be strongly dependent on the chosen value of the magnetic field: when the peak value of the magnetic field is increased, the current and potential oscillations are more significant.

Similarly to what happened in the case with $L_y = 1\,cm$, the reduction of the magnetic field amplitude causes a reduction in current and potential oscillations: the BM almost disappears. A residual modulation of the BM is detectable in the modulation of the anode voltage, i. e., red line in Figure 7.21 (b). The frequency in the case of a small magnetic field appears to be increased if compared to that of the cases with a larger magnetic field. The power absorbed by the discharge, in Figure 7.22, is large (almost 1 kW) for $B_{max} = 100\,G$, while it reduces to $\approx 700\,W$ when the amplitude of the magnetic field is increased.

Effect on plasma parameters

To understand which plasma parameters are changed in these simulations we compare the mean profile of the electron density and temperature for different values of B_{max} in Figure 7.23. In Figure 7.23 (a) we observe that the mean profiles are very well defined for $B_{max} = 100\,G$, while in the others, for $B_{max} > 100\,G$, a rather large

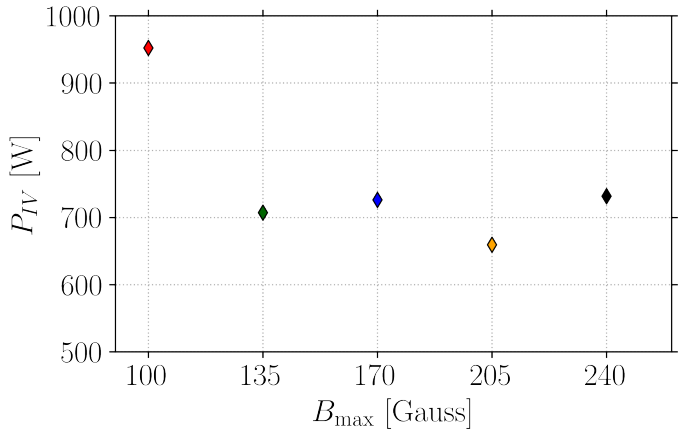


Figure 7.22: Average I-V power absorbed by the thruster for different values of $B_{\max}$.

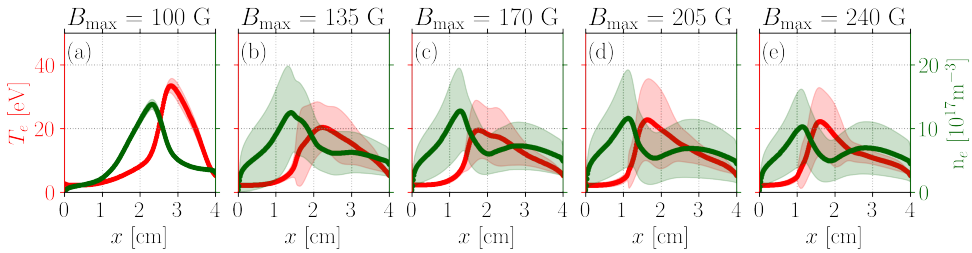


Figure 7.23: Electron temperature (red) and density (green) profiles for different values of the magnetic field.

interval (calculated as the value standard deviation) is present, in particular in the plume region.

The electron density profile in green varies significantly: the one in Figure 7.23 (a) has a maximum near the channel exit at around $x \approx 2.5$ cm, while in Figure 7.23 (b)-(e) the maximum is localized near the anode, around $x \approx 1$ cm. The electron temperature profile in red experiences the same trend: in (a) the max is at $x \approx 2.75$ cm, while in (b)-(e) it is between $x = 1.8$ cm and $x = 2.1$ cm. So, the variation of magnetic field intensity changes the localization of the plasma, which is less confined when the magnetic field is reduced. Most of the plasma density, then, is located near the channel exit and not near the anode when $B_{\max}$ is low. Moreover, the temperature peak is shifted towards the plume.

Effect on engineering parameters

The engineering parameters are reported in Figure 7.24. All parameters are maximal in the case with $B_{\max} = 100$ G. In the other four cases the performance is significantly poorer, which is liked to a lower power absorption, as one observes in Figure 7.22. This effect is particularly interesting for specific impulse and thrust: both these parameters are extremely large when the magnetic field is reduced. By comparing

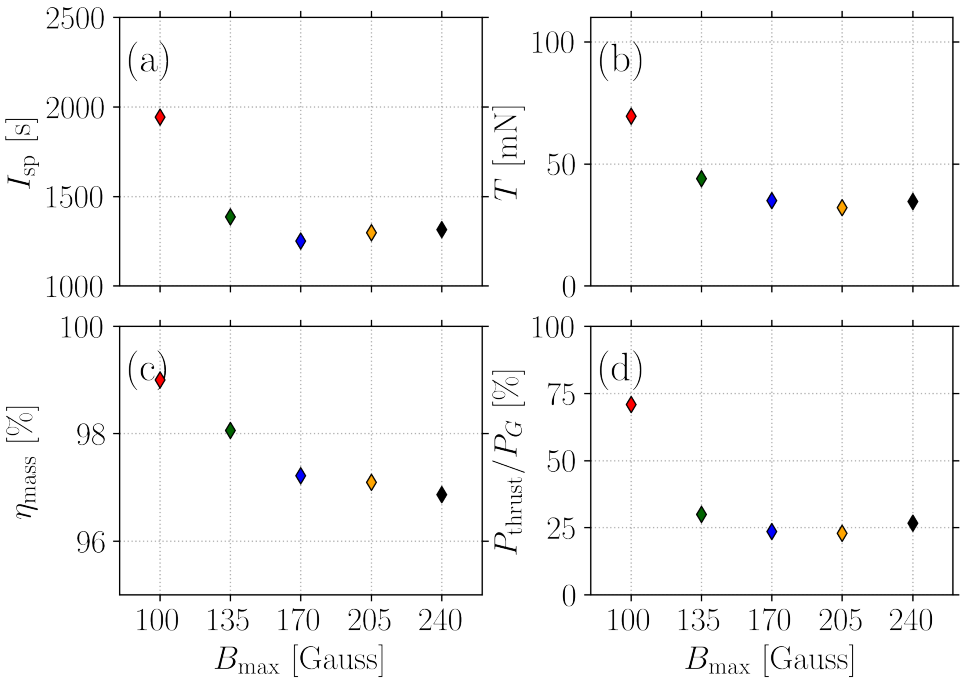


Figure 7.24: Specific impulse (a), thrust (b), mass efficiency (c), and thrust power-to-power ratio (d) for different values of the magnetic field maximum value.

the values calculated for the case with the nominal case $B_{max} = 170\,G$, we can observe that the specific impulse increases by $\approx 55\%$ and thrust almost doubles when the value of B_{max} is decreased to 100 G (here the power consumption increases by $\approx 50\%$). The efficiency, which is high in all cases, approaches the value of 1 when the magnetic field is reduced to $B_{max} = 100\,G$.

7.3.4 Alternative propellants

All the simulations presented in this thesis until now have been performed using xenon as propellant. However, in recent years, due to constraints on the xenon supply, several other propellants have been proposed and tested [125, 178, 200]. For this reason, we tested in our simulations the use of different propellants: krypton and iodine. See Table 7.1 for some details about these gases. Krypton, as xenon, is a noble gas, so it does not require any particular modification of the code. For krypton, we only need to take into account the right mass and collisional cross-sections [125]. Iodine, instead, requires more care, since it is not a noble gas (i. e., it is a halogen). Its chemistry is more complicated: the neutral gas is present in both atomic I and molecular I_2 forms and the presence of positive, double positive, and negative ions is reported [162]. Nevertheless, Esteves *et al.* [187] has shown that in the typical range of pressures of HTs (i. e., 1 mTorr) iodine can be considered as fully dissociated and that the presence of negative ions is negligible (in particular at these electron temperatures). For this reason, we considered a fully dissociated iodine plasma, with

Propellant	Mass	Ionization energy
Xenon	131.29 uma	12.13 eV
Krypton	83.80 uma	13.99 eV
Iodine (atomic)	126.90 uma	10.45 eV

Table 7.1: Characteristics of the used gases.

only positive atomic ions [146]. The mass and collisional cross-sections of iodine are taken from several sources. More details about the collisional processes and the cross-section data used are reported in Ref. [146].

Effect on current and potential

The temporal evolutions of the current and potential for krypton and iodine are reported in Figure 7.25 for two different values of the input mass flow rate. In the same figure, we added as a reference a xenon simulation. All the three simulations presented here use the consistent virtual-r thickness ($L_z = 1.55\,\text{cm}$) and $L_y = 1\,\text{cm}$. When we consider a neutral gas mass flow rate of $5\,\text{mg/s}$, the current obtained in the simulation is different: the heavier propellant (Xe) produces a smaller exiting current, while the lighter (Kr) one generates a larger one. We observe the same behavior for a neutral mass flow rate of $3.5\,\text{mg/s}$, but in this case, the difference is not so clear: the final current does not seem to depend much on the propellant. This is quite unexpected since the number of Kr ions injected in the simulation is much larger than the number of Xe ions when the imposed neutral mass flow rate is the same. In all cases, the circuit damps the BM oscillations and the anode voltage converges to the one imposed by the generator. Some high-frequency modulation seems to depend on the chosen propellant.

The difference among the currents becomes visible by calculating the current axial profiles in Figure 7.26. It can be seen that for all gases the outgoing current is composed almost exclusively of ions, which is positive for the operation of the thruster. Only minor differences are present in the profile shapes, meaning that both krypton and iodine are good candidates as HT propellant.

Effect on plasma parameters

The different mass and collisional cross-sections affect the plasma parameters. In Figure 7.27 we report the electron density (in green) and temperature (in red) profiles for the three different propellants and the two mass flow rates. First, we notice that both parameters are similar for all three propellants, only minor differences are present. This is a good sign since it means that the plasma parameters are not strongly dependent on the propellant and that the same thruster can be operated with different gases.

We observe also that in the case of krypton, the temperature obtained with $\dot{m} = 3.5\,\text{mg/s}$ is significantly lower than with other propellants with the same mass flow rate. This does not happen when we increase the neutral flux: the temperatures in this case are similar for the three gases. The origin of this difference is not clear. It

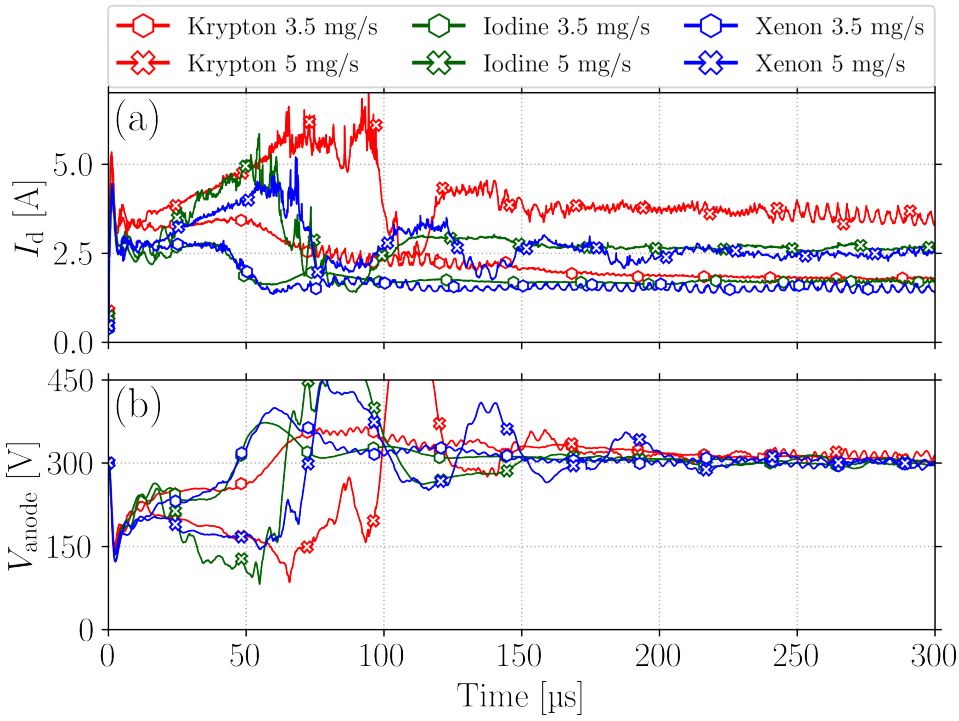


Figure 7.25: Current (a) and potential (b) for different propellants.

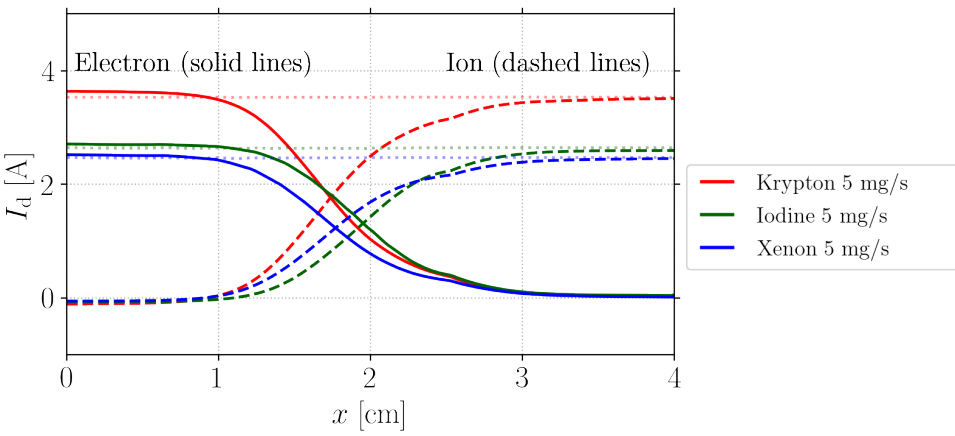


Figure 7.26: Electron (solid lines) and ion (dashed lines) current profiles for different propellants at 5 mg/s, averaged over the last 25 µs of simulation.

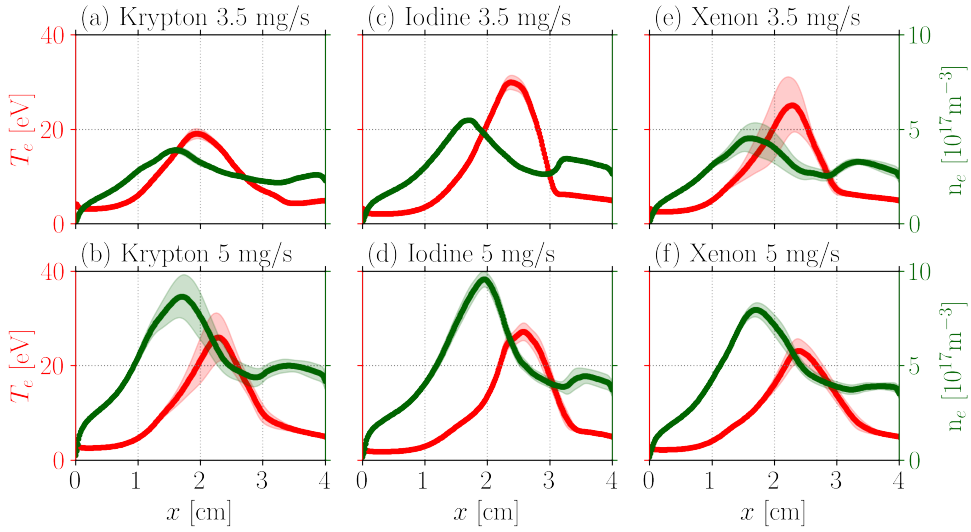


Figure 7.27: Electron density and temperature profiles for different propellants averaged between 250 and 300 µs.

might be related to the competition between the different ionization processes and the radial losses, which depend on the ion mass (cf. Section 6.1).

Engineering parameters

To evaluate the performance of the thruster with other gases, we have calculated some engineering parameters (cf. Section 1.1.4). In Figure 7.28 we show the specific impulse, thrust, mass efficiency, and thrust power-to-power ratio for the three different propellants and mass flow rates.

The mass has a direct effect on the exhaust velocity for a fixed anode potential. For this reason, we are not surprised to observe that the specific impulse is larger for krypton than for iodine and xenon. For all three gases, we notice that the I_{sp} is smaller for a mass flow rate of 3.5 mg/s, which means that for the reduced mass injection the acceleration of the particles is less efficient. The thrust appears to be slightly decreasing with the propellant atomic mass for $\dot{m}$ = 3.5 mg/s, while it is almost constant for $\dot{m}$ = 5 mg/s. By writing as

$$T = m_i v_{i,\mathrm{exh}}^2 n_i,$$

and the exhaust velocity as in Section 7.3.1 we notice that T does not depend on the mass of the ion. Conversely, T does depend on the density, which is expected to be larger for a lighter atom, with a fixed mass flow rate. This probably origins the slight decrease in thrust with the increase of the propellant atomic mass.

For all gases, the thrust measured with $\dot{m}$ = 5 mg/s is more than twice larger than the one measured with $\dot{m}$ = 3.5 mg/s. This can be related to the mass efficiency reported in Figure 7.28 (c), where we see that the mass efficiency decreases when the mass flow rate is reduced. The thrust power-to-power ratio, reported in (d), is not

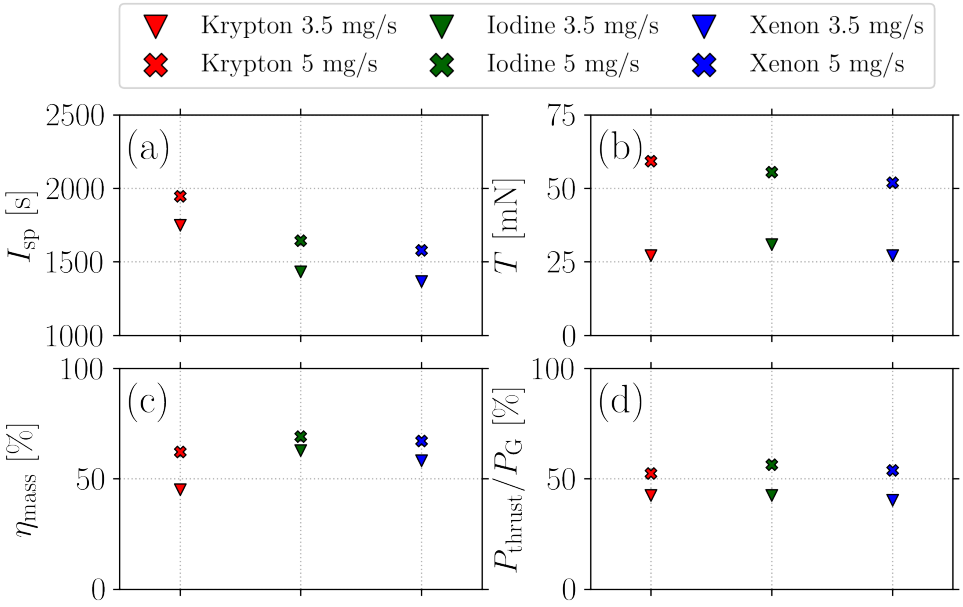


Figure 7.28: Specific impulse (a), thrust (b), mass efficiency (c), and thrust power-to-power ratio (d) for different propellants.

significantly affected by the propellant. The ratio seems to weakly increase with the increase in mass flow rate.

The results of this section show that Krypton and Iodine do not have macroscopic drawbacks and can be used in HT with performance comparable to xenon. Nonetheless, it should be noted that these 2D simulations provide only a preliminary assessment of the thruster operation with different propellants. Thus, to obtain a more accurate evaluation, an extensive experimental campaign is required, specifically to scrutinize the intricate effects of iodine on the thruster components.

7.3.5 Study of the cathode temperature

In Thomas Charoy's Ph.D. [170], a preliminary study about the effect of the cathode model was performed. The focus of this section lies between a numerical study examining the impact of different boundary conditions set in the *LPPic* code and a study investigating the actual effect of the cathode temperature on the plasma parameters. Thus, it aims to address two questions: firstly, which cathode boundary condition is most suitable to use in the *LPPic* code? Secondly, given the constraint that a real hollow cathode may not always allow the ejection temperature to be freely varied, what are the effects of electron temperature on plasma characteristics?

According to Refs. [120, 121, 172, 176], the ejection temperature of a hollow cathode should be in the order of some electron volts. For this reason, in this study the cathode temperature (i. e., T_e^{cath}) is varied from 0.1 eV to 15 eV. In Figure 7.29 we show the evolution of the discharge current for different values of the cathode temperature. In

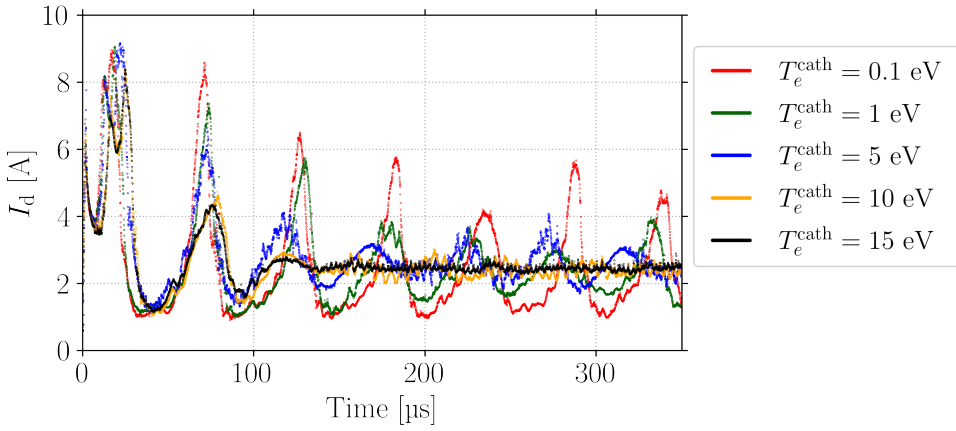


Figure 7.29: Current temporal evolution for different cathode temperatures.

this case, no circuit is used, and $L_y = 1$ cm. The anode voltage is set to 300 V and the mass flow rate to 3.5 mg/s.

Current oscillations

As one can see in Figure 7.29, the temperature of the cathode plays an important role in determining the dynamics of the discharge in a HT simulation. The effect of the current is macroscopic: when the injection temperature is low, we retrieve in the current the well-known BM oscillation, which gradually disappears when we increase the injection temperature. The average value of the current, reported in Table 7.2, does not appear to change significantly when the cathode temperature is changed. Variations in the mean value between cases appear to be mainly related to random fluctuations in the current and the mediation process itself: if we ran a longer simulation, we would expect all cases to converge to roughly the same value. However, some differences might still be present, since the BM impacts all plasma parameters.

To evaluate the amplitude of the BM oscillations, we used the standard deviation of the current density between 100 µs and 350 µs. The results are reported in Table 7.2. Between the case with the lowest cathode temperature and the one with the highest one, the standard deviation is reduced by a factor of more than 10. When T_e^{cath} is 0.1 eV, the amplitude of the current oscillations is on the order of the average value of the current. By increasing the temperature at the cathode, it is observed that the standard deviation becomes progressively smaller. In Figure 7.30 we note that the amplitude of the oscillation appears to be proportional to the inverse of the cathode temperature.

In addition, we note that the high-frequency modulation (i. e., of the order of some hundreds of kHz) related to ITTI is also present. This modulation, present in all cases, is distinguishable in the two cases with higher cathode temperature since the BM is almost absent. Even if the frequency of the modulation seems to be affected by the cathode temperature, we decided not to perform a detailed analysis of this

T_e^{cath}	I_{mean}	Ampl.
0.1 eV	2.39 eV	1.87 eV
1 eV	2.37 eV	1.22 eV
5 eV	2.61 eV	0.66 eV
10 eV	2.41 eV	0.30 eV
15 eV	2.47 eV	0.16 eV

Table 7.2: Current density and its standard variation calculated between 100 µs and 350 µs.

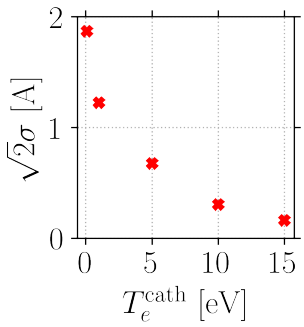


Figure 7.30: Amplitude of the oscillation as a function of the cathode temperature.

frequency, because the large BM oscillations for low cathode temperature do not allow an accurate estimation of the frequency.

Temperature and density

One of the main effects of increasing the injection temperature at the cathode is an increase in the overall electron temperature, as one can observe in Figure 7.31. In this figure, the red lines show the time-averaged value of the axial electron temperature profile. As one can see, the profile near the anode appears to be unaffected by the temperature change at the cathode. Some differences appear in the central part of the simulation at $x \approx 2\,\text{cm}$. In the case of low injection temperature, the electron temperature is significantly lower concerning the case of high injection temperature (i. e., from 27 eV to 37 eV). Moreover, consistently with the current evolution, we observe that some large oscillations around the mean value are present in the case of low T_e^{cath}, while the oscillations are much less intense in the case of high T_e^{cath}.

The greatest differences are observed in the plasma plume: if the cathode temperature is less than $\sim 5\,\text{eV}$, the electrons in the plume are cooler than those at the thruster exit. Conversely, at high T_e^{cath}, the electron profile is such that the temperature of the cathode (i. e., at the right boundary) is higher than that at the exit of the thruster: the temperature of the electron profile increases in the plume. This is also confirmed by the temperature gradient (i. e., $\nabla_x T_e$) in the plume, which is shown in Figure 7.32. The temperature gradient is positive in the case of high cathode temperature, while it is negative in the case of low cathode temperature. In this figure, one can see that in the case of $T_e^{\text{cath}} = 5\,\text{eV}$, the derivative appears rather continuous and regular, whereas, in all other cases, there is a discontinuity near the position of the cathode. This discontinuity suggests that the corresponding chosen cathode temperature is not the *natural* temperature to which the system would converge.

We observe that large density fluctuations are present when the BM is present, i. e., for low T_e^{cath}, while no fluctuations are visible for high temperatures. The average profile in the channel does not seem to depend on the cathode temperature, whereas the density in the plume does. For low temperatures, the density decreases towards

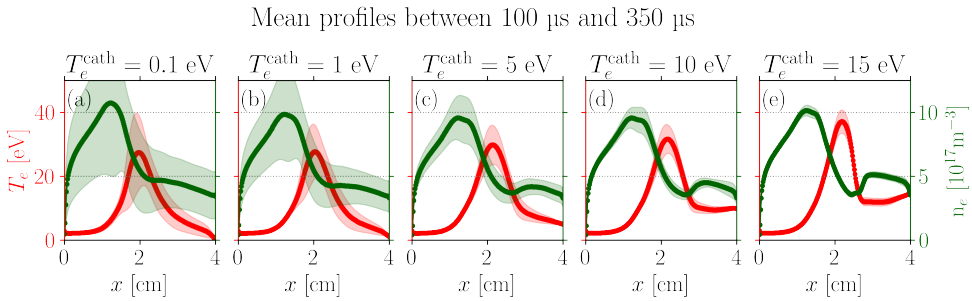


Figure 7.31: Average electron temperature (red) and density (green) profiles for different values of the cathode temperature. The shaded areas cover ± one standard deviation of the profiles.

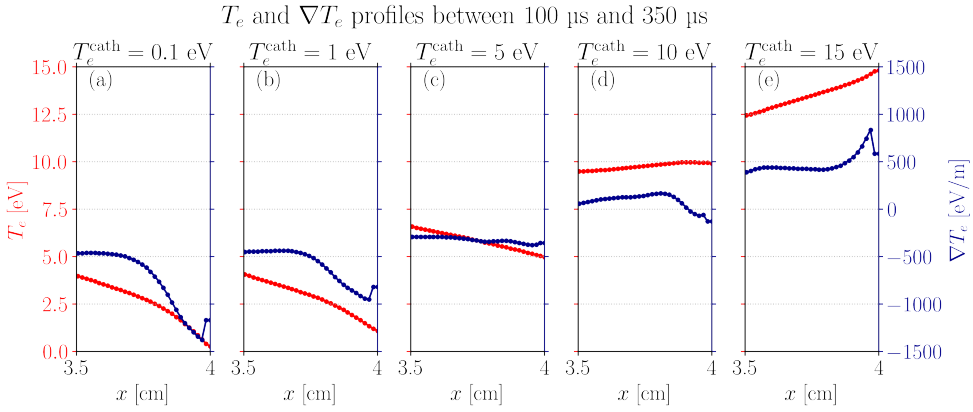


Figure 7.32: Profiles of the temperature (red) and temperature gradient (blue) in the plasma plume for different values of the cathode temperature.

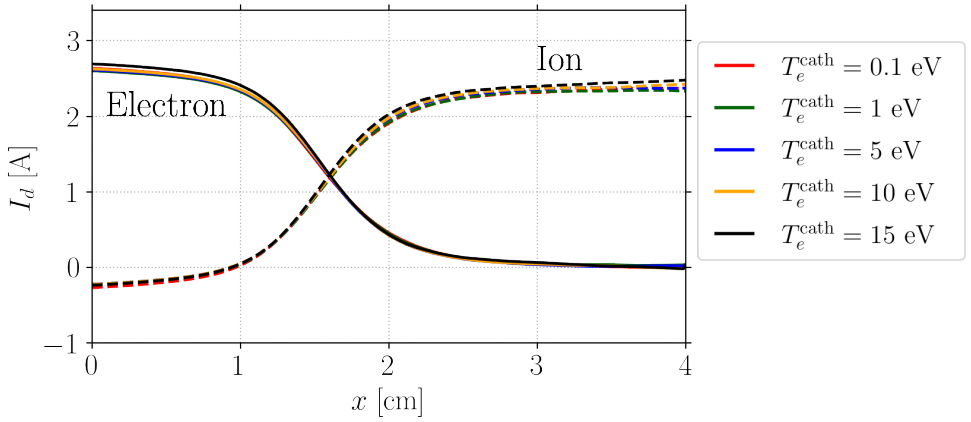


Figure 7.33: Profiles of the electron (solid lines) and ion (dashed line) average currents for different values of the cathode temperature.

the plume, whereas, for high temperatures, the density in the plume seems to be much more important. This difference is related to ionization: the high temperature at the cathode leads to a higher electron density production rate and, consequently, to a higher density in the plume. However, the different density in the plume does not imply a different current density of ions or electrons. As can be seen in Figure 7.33, the current profiles of ions and electrons appear to be almost independent of the temperature imposed at the cathode.

7.4 CHAPTER SUMMARY

The results reported at the beginning of this chapter unveil some important features of the BM: this instability engenders an oscillation of all plasma parameters, e. g., gas and plasma densities, temperature, ionization rate coefficient, electron density production rate, electric field, electron temperature, and velocity, *et cetera*. These parameters oscillate at the same frequency as the BM, but with a phase shift among them.

By analyzing the extensive data obtained from the PIC simulation, we discovered that the ionization rate coefficient, K_{iz}, is significantly correlated with the electron temperature. However, the electron density production rate, S_{iz}, is found to be independent of the electron temperature. These observations led us to conclude that the ionization process in Hall thrusters is influenced by the interplay between temperature and species density, and an increase in temperature alone is not sufficient to sustain an increase in density.

In the second part of the chapter, we used *LPPic* to simulate different thruster configurations. The simulations are extremely sensitive to changes in input parameters, so we decided to change one parameter at a time. Initially, by variating the fixed anode voltage, we have shown that the BM amplitude and frequency depend on this parameter. Moreover, these simulations have shown that at high voltage we

can recover some BM higher-order harmonics. Afterwards, by variating the input neutral gas mass flow rate, we pointed out that the BM amplitude and frequency only slightly increase, when this parameter varies. The magnetic field has also a significant effect on the BM: the oscillations almost disappear when the value of the magnetic field reduces. This is accompanied by minor confinement of the plasma, which concentrates at the thruster exit. Subsequently, we have shown that *LPPic* can be used to test other propellants, e. g., krypton and iodine. The preliminary findings indicate that these alternative gases are viable options for use in HTs. However, we note that further investigations are required to confirm these results since these results have been obtained with an azimuthal length of 1 cm only and simplified chemistry for iodine. Finally, we analyze the effect of different cathode injection temperatures. The results show that setting the injection temperature of 5 eV is the most suitable in this kind of simulation and that the BM amplitude is larger for lower injection temperature, while the BM is almost totally damped when the injection temperature is higher than 5 eV.

8 CONCLUSION

Chapter contents

8.1 Summary 207
8.1.1 Results from the linear theory 207
8.1.2 Results in the radial-azimuthal simulation plane 208
8.1.3 Results in the axial-azimuthal simulation plane 209
8.2 Perspectives 210
8.2.1 *LPPic* code improvements 210
8.2.2 Comparison with experiments 210
8.2.3 Use the 2.5D *LPPic* code as a design tool for future HTs . . 211

8.1 SUMMARY

Hall thrusters are a prominent technology for space propulsion. However, the physics of these devices remains not fully understood. In this framework, the current thesis used kinetic simulations to deepen our understanding of the governing principles of these devices. Moreover, the recent developments of the *LPPic* code allow us to challenge the possibility of using PIC simulation to guide the design of new thrusters.

The roots of this thesis are in the previous Ph.D. works of Croes [112], Tavant [152] and Charoy [156] at LPP. Their developments are the necessary basis used for all the results presented in this work. Croes and Tavant studied the interaction of plasma and walls in radial-azimuthal simulations: this was the basis for the work described in Chapter 4. The rest of the thesis (i. e., Chapters 5, 6 and 7), where we studied the plasma discharges in the axial-azimuthal configuration, owes much to the previous works of Tavant and Charoy, who developed the *LPPic* code and the methodology to study the discharges in this configuration.

8.1.1 Results from the linear theory

The HTs are characterized by a large number of instabilities. Even if these devices are strongly non-linear, the linear theory perturbation method is a good candidate to study the growth and development of these instabilities. In Chapter 2 we have

calculated a 3D dispersion relation and we have shown that one can derive from it the most known electrostatic DRs.

The importance of the results in Chapter 2 is that they allow us to demonstrate that IAW, MTSI, and ITTI can be included in the same expression. Moreover, the approach followed in this chapter has provided insight into the limits of validity of the simplifications to derive simple versions of the electrostatic DRs and to study the relation between the different instabilities, among which the ECDI. After having calculated the DRs, we discussed the conditions that allow and favor the growth of the different instabilities and the physical mechanisms that are important for the growth.

In the second part of Chapter 2, we discussed the strengths and limitations of the spectral techniques that are used in the rest of the thesis. The DFT, which is commonly used, is a rather simple technique and it has been successfully used for years, but it is not localized and requires periodic signals. The PSD2P allows for reconstructing the spectrum of much more complex signals, but the implementation of the algorithm is not trivial. The DMD is extremely powerful to have a qualitative idea of the amount of energy carried by each mode. However, it is less adapted to a precise and quantitative analysis of the modes.

8.1.2 Results in the radial-azimuthal simulation plane

The radial-azimuthal simulations have been used in Chapter 4 to study the evolution of the plasma instabilities in this simulation plane. We considered a plasma slab at the exit of the thruster channel, with a homogeneous radial magnetic field and an axial electric field imposed externally. We observed the evolution of the plasma parameters and we performed several simulations to understand the nature of these instabilities.

We developed a solver to obtain the numerical DR of the MTSI and we compared the results with analytical predictions. This allowed for demonstrating that the size of the simulation domain does play a role in determining whether the MTSI instability grows, or not. Moreover, we could define an instability criterion based on the plasma and simulation characteristics. Then, using several PIC simulations, we have shown that reducing the azimuthal dimension of the simulation domain kills the growth of the MTSI, while the ECDI remains active. This analysis has been also successfully applied to some already published works.

Afterwards, we calculated the effect of the MTSI on the plasma parameters, in particular, we have shown that the MTSI can lead to a significant increase in the plasma temperature in the radial direction. Using some advanced spectral techniques (e. g., the DMD) we calculated the effect of the MTSI on the electron transport in the axial direction, showing that the MTSI increases this transport. Finally, the study of the non-linear regime allowed us to observe the appearance of an ion acoustic wave in the azimuthal direction.

The work in the radial-azimuthal plane has been completed through participation in an international benchmark. In this benchmark, by injecting in the simulation a fixed and constant number of electron/ion pairs, we have shown that 7 international groups could reach the same density and temperature profiles, and could observe two instabilities, i. e., MTSI and ECDI.

8.1.3 Results in the axial-azimuthal simulation plane

The axial-azimuthal simulations have been studied in Chapters 3, 5, 6 and 7. The simulation domain is a rectangular cartesian mesh, going axially from the anode at one boundary to the cathode at the other. The ionization is treated self-consistently within the MCC module, while the axial neutral dynamics is solved with 1D isothermal Euler equations. These conditions allow the development of the BM, which is one of the main plasma instabilities in HTs.

In Chapter 3 we showed that the use of the external circuit allowed the current oscillations to be controlled and the discharge to be stabilized. This fact made it possible to run longer simulations and avoid the large current oscillations that were observed [170] whenever the azimuthal domain was larger than 1 cm.

Subsequently, in Chapter 5 we studied the evolution of the plasma instabilities in the axial-azimuthal simulation plane. Using the PSD2P we investigate the instabilities development during the growing and decreasing phases of the BM and we have shown that the IAW dominates the growing phase, while the ITTI dominates the decreasing phase. Subsequently, we used the results from Chapter 2 to compare the numerical spectral maps to the analytical DRs. This allows showing some significant characteristics of the plasma instabilities: the IAW and ITTI should be considered as 2D instabilities. If we describe them as 1D, it is not possible to explain the observed behavior. Moreover, the spectral analysis allowed us to explain the origin of the wavefronts bending observed for the IAW: it is related to a variation of the refractive index of the plasma. The analysis of the ITTI allowed us to show that the instability is related to the presence of low-energy ions in the plume, the presence of which is particularly detrimental for the spacecraft.

In Chapter 6, a model to include in axial-azimuthal simulations the radial losses occurring within the thruster channel. The simulations have shown that the choice of the length of the virtual radial dimension affects all aspects of the discharge. At the end of the chapter, we analyzed and fully characterized a self-consistent case of an axial-azimuthal simulation with a virtual-r.

In Chapter 7 we have shown how *LPPic* can be used to explore the parametric space of HT operation. Using the PIC results, we have shown that it is possible to derive some important considerations about the development of the BM in HTs. In particular, we have shown that the ionization mechanism is a consequence of the competition between neutral gas consumption, the fluctuations in plasma density, and in the electron temperature. However, our results made it clear that electron temperature growth alone cannot sustain ionization growth. Later, we changed some simulation input parameters, i. e., anode voltage, neutral mass flow rate, magnetic field value, propellant, and cathode temperature. By varying these parameters, we could evaluate their impact on some discharge characteristics, such as the electron temperature and density axial profiles, and on some engineering parameters, such as the thrust, the specific impulse, and the mass consumption efficiency. The results in this chapter allow us to demonstrate the flexibility of our code and to show that it can be used to guide the design of a new thruster.

8.2 PERSPECTIVES

The future perspectives of this work are numerous. We identified three main research directions: the *LPPic* code developments, the comparison with experiments, and the use of simulations as a design tool for future HT developments.

8.2.1 *LPPic* code improvements

The *LPPic* code represents the core of this thesis: without an efficient and reliable code, it would have been impossible to perform the simulations and obtain the results presented in this manuscript. However, the current 2.5D *LPPic* code could be further improved in several ways, to include more physical effects.

- The current model of virtual-r does not successfully reproduce the SEE. The current simplified model of secondary emission has a weak impact on the discharge, while we were expecting to observe the opposite. This is probably related to the approximation we made, which dampens the effects of SEE. Thus, it is necessary to improve the model and to find a way to include the SEE more realistically.
- The virtual-r is implemented in using the Bohm flux; however, some recent works [199] use some reduced-order schemes to decouple the solution of the Poisson equation along the different direction. By using this approach, it could be possible to have a more consistent third direction, with a real plasma sheath and a more realistic particle flux. Some attempts have already been made (cf. Appendix A.3), but they have not been successful.
- The percentage of doubly charged ions is estimated in the range $0 - 25\%$ [41, 42, 49]. Even if their presence in low-power thrusters might be negligible (the percentage is higher at higher power), it would be great to consistently (i. e., via MCC) evaluate the number of multiply charged particles and study their effect on the discharge.
- The iodine studied in Chapter 7 was considered in this work as a perfect atomic gas. This, unfortunately, is not the case in real life. Currently, during his Ph.D. at LPP, Nicolas Lequette is developing a MCC module to include the detailed chemistry of iodine plasmas. It will be of great interest to carry out the first axial-azimuthal PIC simulations of HTs with the detailed chemistry for iodine.

8.2.2 Comparison with experiments

In parallel to this Ph.D. work on HT simulations, experiments on HTs have been carried out at LPP. In collaboration with Tarek Ben Slimane some steps have been made to compare experiment and simulation results. The detailed analyses of the simulations presented in this work, together with those carried out by Ben Slimane and collaborators [184], make it possible to identify some key points that can form the basis for a reliable comparison between simulations and experiments. We identified three possible ways to compare the simulation and experimental results:

- use of a Collisional Radiative Model (CRM) to compare synthetic spectra produced by PIC results to the experimental spectra calculated from emission spectroscopy;
- study the variation of the discharge current in different operating regimes, i. e., changing the anode voltage and the mass flow rate;
- compare the effects of the different propellants on the discharge parameters and thruster performance.

Although the work is promising, we highlight some critical points that we are currently studying. First, when the CRM is used to compare the simulation results with the experimental measurements we need to consider data at the same axial position (i. e., distance from the anode). So, when we try to make the comparison, we are limited by the reduced portion of the axial direction that at the same time is included in the simulation and that can be probed experimentally. Namely, the length of the plume in the simulation is rather small ($< 2\,\text{cm}$) and difficult to enlarge. Conversely, from the experimental point of view, it has not been possible to probe the plasma inside the channel. Secondly, the laboratory thruster conditions are rather different (i. e., lower anode voltage and mass flow rate, higher discharge current, *et cetera*) from those used in the simulation presented in the thesis, thus the results of *LPPic* are not always stable and the discharge tends to switch off. An improvement of the comparison techniques is fundamental to advance the understanding of the discharge and to validate the *LPPic* code.

8.2.3 Use the 2.5D *LPPic* code as a design tool for future HTs

The simulations of Chapter 7 have shown that it is possible to use *LPPic* as an engineering tool: it is robust when we change the input parameters. Nevertheless, the parameter exploration that we performed in that chapter was not exhaustive. It would be great to perform a more complete study, to find the optimal conditions for the discharge. In particular, with the use of the virtual-*r*, one should address the problem of geometrical design and test new thruster configurations, working with lower anode voltages and mass flow rates. The study of the effect of the magnetic field also deserves to be carried out: in Chapter 7 we have shown that the plasma profile is strongly by the absolute value of the magnetic field. It would be interesting to quantify this more precisely and to assess the consequences of a plasma localized more mid-channel or towards the channel output.

The optimal design is not only the one that provides the larger thrust of specific impulse: along this thesis, we have shown that plasma instabilities are fundamental to define the plasma parameters. Therefore, when designing a new thruster, it should be kept in mind that high-frequency oscillations must be damped to reduce anomalous transport in the axial direction, and the BM must be blunted to reduce wall losses and erosion. The code can provide some important insights about the thruster design that reduces plasma instabilities.

A APPENDIX

A.1 OTHER CIRCUIT IMPLEMENTATION

The circuit solution described above is the one that has been used in the simulation presented in this thesis. However, other circuit implementations are possible. In this section, we present a possible different circuit implementation. The main difference with the circuit described in Eq. (3.11) is that the current is now solved with a 2nd order scheme. This scheme consists in using the same discretization for the voltage, and a second-order scheme for the current, as

$$\frac{dI}{dt} = \frac{I_{n-1} - 2I_{n-2} + I_{n-3}}{2\Delta t_{RLC}} + O\left(\Delta t_{RLC}^2\right).$$

As one can see, to calculate the current first derivative at the second order, we are obliged to use the current at the previous three times steps, centered in $n-2$.

In Figure A.1 we show the current (a) and anode voltage temporal evolution for two simulations run with the 2nd order scheme. The results are shown for two simulations with $L_y = 1\,\text{cm}$ and $L_y = 4\,\text{cm}$. In the small L_y case, the current does not reach a constant value and the BM is persistent in the simulation, moreover, the amplitude of the current oscillations is larger than in the non-circuit case discussed above. With $L_y = 4\,\text{cm}$ we observe the same current oscillations present in the $L_y = 1\,\text{cm}$ simulation. So, the discharge current seems to be independent of the azimuthal length, which is different from what we have observed above. Conversely, the anode voltage is stable: its oscillations are much smaller than with the 1st order current and the mean value remains closer to the generator value.

The reason why the 1st order version of the circuit is preferred to the 2nd order one is listed below.

- In the 2nd order version, when we try to reconstruct the current in the different circuit components the equality $I_{tot} + I_c = I_r + I_l$ is not satisfied. This can be seen noticing that $I_r = (U_g - U)/R$, $I_l = I_{l,0} + \int_0^t (U_g - U)/L$ and $I_c = C dU/dt$ are almost constant, since U is almost constant and U_g is constant. Conversely, the total current I_{tot} is oscillating significantly.
- The circuit, which is designed to dampen the BM, fails in its task at all: in the small L_y case the BM is persistent and the current oscillations are larger than in the non-circuit case.

The numerical origin of these problems cannot be found easily. One hypothesis is that those problems are related to a bad coupling of the voltage and current discretization in the 2nd order scheme.

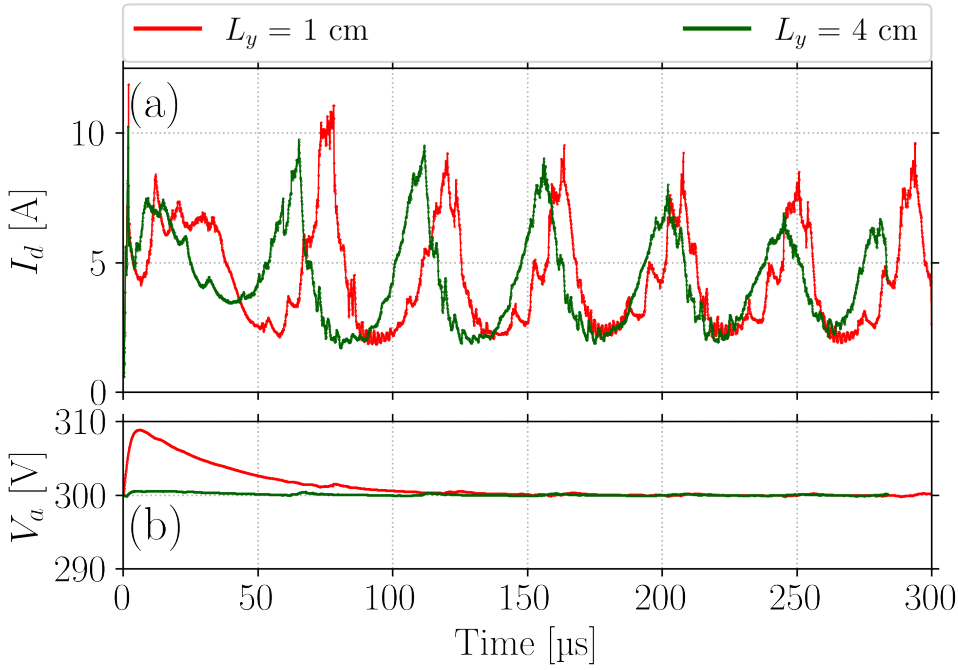


Figure A.1: Discharge current (a) and voltage (b) with a 2nd order scheme. The results are shown for two simulations with $L_y = 1cm$ and $L_y = 4$ cm.

A.2 AXIAL–AZIMUTHAL SIMULATION LIST

The simulations listed in Table A.1 are ordered as they appear in the manuscript, the chapter is indicated in the first column. In the second column, we highlight the main topic of the simulation, while in the third we report the used azimuthal length L_y. In the fourth column, we show the number of simulations that are compared. In the last, we describe in more detail the simulation characteristics. We remember that the simulation parameters are given in Table 3.2 if not specified differently.

Table A.1: List of all axial-azimuthal simulations in this thesis.

Chapter	Subject	L_y	How many simul.	Description of the major variations
Ch. 3	α	1 to 2 cm	4	Study the effect of varying the permittivity scaling α. No circuit is used.
	Circ. *RLC*	1 cm	3	Compare the effect of the circuit by varying the impedances. The values of R, L and C are detailed in Table 3.2
		4 cm	3	Compare the effect of the circuit by varying the impedances. The value of R, L and C are detailed in Table 3.2. The effect of the cathode temperature is also studied.
Ch. 5	Instabilities	4 cm	2	Analysis of two cases, introduced in Ch. 3, to study the plasma instabilities.
Ch. 6	Virtual-r value	1 cm	4	Different values of the virtual thickness are compared (i.e. $L_z = \infty$, $L_z = 4$ cm, $L_z = 2$ cm and $L_z = 1$ cm). All the other simulation parameters, including the section, are kept constant. The values are of the virtual thickness are used to vary the flux of particles towards the walls.
		4 cm	4	
	SEE	1 cm	3	Different emission rates are compared by varying σ, with $L_z = 2$ cm. All the other values, including the section, are kept constant.
		4 cm	4	
	Consistent case	1 and 4 cm	2	The thickness ($L_z = 1.55$ cm) is consistent with the section used to define the mass flow rate and the current.
Ch. 7	Virtual-r value	4 cm	1	The same simulation analyzed at the end of Ch. 6 is used to study the BM.
	Change V_0	4 cm	5	The anode potential is varied between 200 V and 800 V, with a virtual-r of $L_z = 4$ cm.
	Change $\dot{m}$	1 cm	3	The mass flow rate is varied with a consistent virtual-r of thickness $L_z = 1.55$ cm.
		4 cm	4	The mass flow rate is varied with $L_z = 4$ cm.
	Change B	1 cm	3	The amplitude of the magnetic field is varied, while no virtual-r is used.
		4 cm	3	The amplitude of the magnetic field is varied, with a consistent virtual-r of thickness $L_z = 1.55$ cm.
	Change gas	1 cm	6	Krypton, iodine and xenon are tested with $L_z = 1.55$ cm and two values of the mass flow rate: 3.5 and 5 mg/s
	Change T_e^{cath}	1 cm	5	Variation of the cathode temperature, with no circuit, nor virtual-r.

A.3 PSEUDO-VIRTUAL RADIAL DIMENSION

A.3.1 Introduction

The term *pseudo* was introduced by Faraji *et al.* [188, 199], who presented the concept of a pseudo-scheme. The main idea is to consider the potential Φ spatially separable and to work with coupled 1D problems. This approach not only allows us to reduce significantly the cost of Poisson's equation solution but also lowers the number of superparticles needed in the simulation domain. *LPPic* is a 2D code, so we can try to enhance it to pseudo-3D by considering a potential such that

$$\Phi(x, y, z) = C_{xy}\Phi(x, y) + C_z\Phi(z), \tag{A.1}$$

with x, y and z in the simulation domain and C_{xy}, C_z two coefficients. From this expression of the potential, we can easily write two separate Poisson equations for the potential and charge density in the xy-plane and along the z-axis. In the current work, we consider $C_{xy} = C_z = 1/2$.

In our simulation domain, we implemented a rather simple scheme: the solution of the Poisson equation remains the same in the axial-azimuthal plane, but the potential is multiplied by the coefficient C_{xy}. To simulate the radial direction, we make a 1D discretization of the radius and we solved a 1D problem along these directions. The walls are considered grounded, so Dirichlet boundary conditions are applied along this direction. The superparticles, already followed along z, are interpolated on the radial grid points and a 1D Poisson equation is solved using Thomas' algorithm to find $\Phi(z)$.

A.3.2 Mono-domain

The first attempt has been performed by considering the potential in the radial direction free to fluctuate, while kept at zero at the boundaries. The simulation domain is divided into two parts: the channel and the plume. The radial-Poisson's equation is not solved in the plume and reflective walls are used to keep the particles inside the z-domain. Conversely, the Poisson equation is solved inside the channel and the particles exiting the domain are absorbed by the walls. In this way, we are creating the sheaths on the internal walls, while the plasma along the radial direction in the plume only moves in thermal motion. In Figure 3.19 we show the evolution of the current and the potential in a 1 cm $\times$ 4 cm simulation with $L_z = 4$ cm This value is particularly high, otherwise the high losses turn off the discharge. The evolution of the current is rather different when compared to the standard similar cases discussed in Ref. [201] and discussed in Section 3.4 in the presence of a circuit: the oscillation is sharper and the steady-state voltage of 300 V is not reached. Moreover, some higher frequency oscillations are observed at the anode voltage.

In Fig. A.3 (a) and (b) we observe the axial and radial profiles of the potential, taken when the current is low. The axial profile in this case, i. e., in (a), is rather standard for this kind of simulation. Also, the potential profile in the radial direction between the center of the simulation and the walls, i. e., in (b), has an expected configuration: our code successfully manages to recreate the sheaths and the classical shape of a

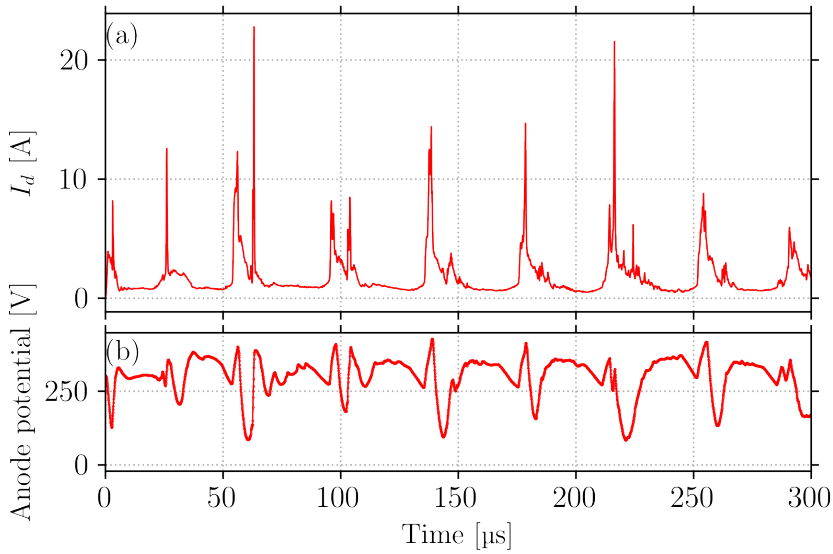


Figure A.2: Current (a) and potential (b) evolution in a 1 cm × 4 cm simulation.

plasma between two walls. However, the absolute value of the potential is one order of magnitude lower than the one that is expected in the thrusters [152].

In Figure A.4 we show the potential profiles at the current peak. In this case, the behavior appears to be curious: we observe a large increase of the potential components, both the one calculated in the *xy*-plane and the one along the radial axis. The potential in the plasma bulk has increased significantly: we have a substantial potential increase from the anode to the channel center. This is very uncommon and physically only possible for a short amount of time. This is the reason why the large current peaks, generated by the extremely large electric field derived by this potential, last for a few time steps. However, these potential developments make us think that plasma dynamics has some non-physical parts.

A.3.3 Other approaches

Similarly, with what we have done with the virtual radial dimension in Chapter 6, we solved a different radial-direction problem for every CPU domain. The goal of that was to consider the different plasma characteristics at a different axial position and, consequently, the fact that the sheath has different shapes at different positions (e. g., near the anode, the temperature and density are quite different compared to the channel outlet). So, we interpolated the z position of each particle and we solved different Poisson's equations for each CPU. Unfortunately, this method turned out to be unsatisfactory. In the simulation corners, where a double (radial and anodic) sheath forms, there are no particles left. Thus, we obtain nonphysically large electric fields that make the simulation crash.

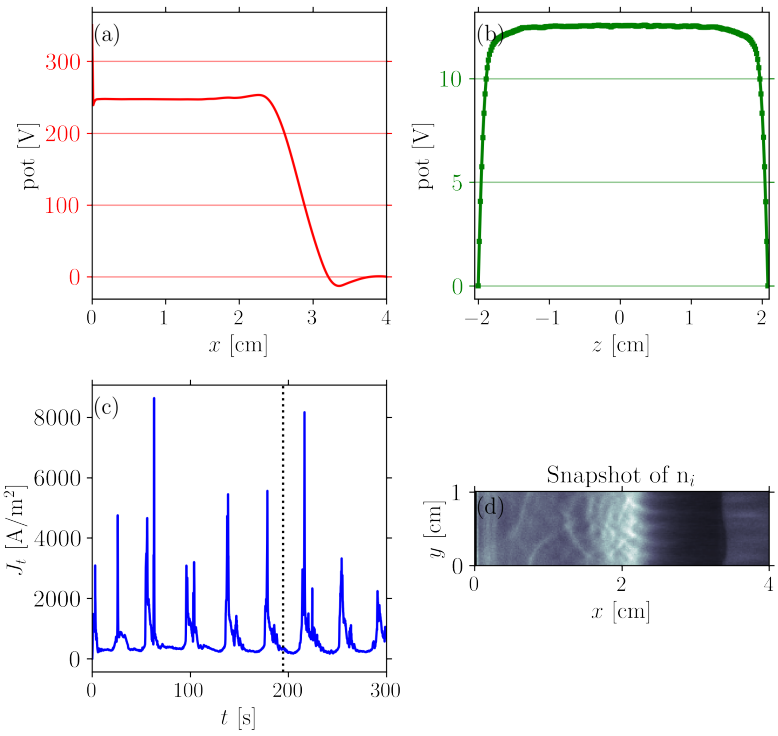


Figure A.3: Axial profile (a) and radial (b) profile of the plasma potential in a 1 cm × 4 cm simulation. In (c) we show the current density evolution and in (d) a snapshot of the ion density.

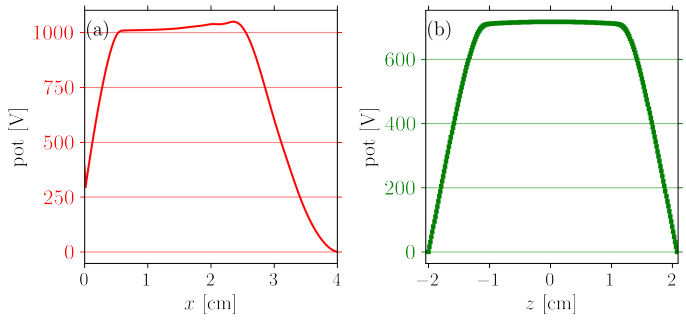


Figure A.4: Axial profile (a) and radial (b) profile of the plasma potential in a 1 cm × 4 cm simulation at the current peak at t = 178.4 µs.

Another option was to set the center potential at the value of the anode and then solve two Poisson equations (bottom half and top half of the $z-$axis) keeping the walls grounded. In this way, we expected to have a more reasonable voltage drop in the radial direction. However, the fact of fixing the potential at the center with a Dirichlet condition favors the creation of a thin sheath in the middle of the plasma at $z = 0$, which is not physical at all.

A.3.4 Conclusions on pseudo-3D

The pseudo-3D appears to be an interesting option to take into account the radial direction when the code is 2D axial-azimuthal. However, the test presented here shows two main problems:

- the potential drop between the plasma bulk and the walls is too small. This is probably because we are separating the potential contribution in different directions;
- working with more refined subdomains makes the simulation crash since at the corners the presence of a double sheath makes the walls absorb most of the electrons.

Even if the results in this section are not conclusive, we consider that this path might be fruitful and that it requires some further investigation.

BIBLIOGRAPHY

[1] D. Bohm. "The use of probes for plasma exploration in strong magnetic fields." In: *Characteristics of Electrical Discharges in Magnetic Fields* 13 (1949) (cit. on pp. 10, 139).

[2] N.A. Krall and M.N. Rosenbluth. "Trapping Instabilities in a Slightly Inhomogeneous Plasma." In: *Physics of Fluids* 5.11 (1962), p. 1435. ISSN: 00319171. DOI: 10.1063/1.1706542 (cit. on pp. 14, 29).

[3] N.A. Krall and M.N. Rosenbluth. "Low-Frequency Stability of Nonuniform Plasmas." In: *Physics of Fluids* 6.2 (1963), p. 254. ISSN: 00319171. DOI: 10.1063/1.1706723 (cit. on pp. 14, 29).

[4] G.S. Janes and R.S. Lowder. "Anomalous electron diffusion and ion acceleration in a low-density plasma." In: *The Physics of Fluids* 9.6 (1966), pp. 1115–1123. DOI: 10.1063/1.1761810 (cit. on pp. 11, 12).

[5] L. Tonks. "The Birth of "Plasma"." In: *American Journal of Physics* 35 (1967). DOI: 10.1119/1.1974266 (cit. on p. 2).

[6] A.I. Morozov. "Wall conduction in a highly magnetized plasma." In: *Journal of Applied Mechanics and Technical Physics* 9.3 (1968), pp. 249–251. DOI: 10.1007/BF00916781 (cit. on p. 11).

[7] V. N. Sokolsky. *Konstantin E. Tsiolkovsky Selected Works*. MIR publishers, 1968 (cit. on p. 5).

[8] James W Cooley, Peter AW Lewis, and Peter D Welch. "The fast Fourier transform and its applications." In: *IEEE Transactions on Education* 12.1 (1969), pp. 27–34. DOI: 10.1109/TE.1969.4320436 (cit. on p. 37).

[9] N.A. Krall and D.L. Book. "Ion Sound Instability in a Collisionless Shock Wave." In: *Physics of Fluids* 12.2 (1969), p. 347. ISSN: 00319171. DOI: 10.1063/1.1692487 (cit. on pp. 14, 29).

[10] J.P. Boris et al. "Relativistic plasma simulation-optimization of a hybrid code." In: *Proc. Fourth Conf. Num. Sim. Plasmas*. 1970, pp. 3–67 (cit. on p. 47).

[11] S.P. Gary. "Longitudinal waves in a perpendicular collisionless plasma shock: II. Vlasov ions." In: *Journal of Plasma Physics* 4.4 (Dec. 1970), pp. 753–760. ISSN: 0022-3778, 1469-7807. DOI: 10.1017/S0022377800005407 (cit. on pp. 12, 14, 24, 28, 29, 102).

[12] S.P. Gary and J.J. Sanderson. "Longitudinal waves in a perpendicular collisionless plasma shock: I. Cold ions." In: *Journal of Plasma Physics* 4.4 (Dec. 1970), pp. 739–751. ISSN: 0022-3778, 1469-7807. DOI: 10.1017/S0022377800005390 (cit. on pp. 12, 14, 24, 28, 105).

[13] H. Okuda. "Collisions in a Plasma of Finite-Size Particles." In: *Physics of Fluids* 13.8 (1970), p. 2123. ISSN: 00319171. DOI: 10.1063/1.1693210 (cit. on p. 103).

[14] D.W. Forslund, R.L. Morse, and C.W. Nielson. "Nonlinear electron-cyclotron drift instability and turbulence." In: *Physical Review Letters* 27.21 (1971), p. 1424. DOI: https://doi.org/10.1103/PhysRevLett.27.1424 (cit. on p. 14).

[15] M. Lampe. "Theory and Simulation of the Beam Cyclotron Instability." In: *Physics of Fluids* 15.4 (1972), p. 662. ISSN: 00319171. DOI: 10.1063/1.1693961 (cit. on pp. 14, 98).

[16] J.B. McBride. "Theory and Simulation of Turbulent Heating by the Modified Two-Stream Instability." In: *Physics of Fluids* 15.12 (1972), p. 2367. ISSN: 00319171. DOI: 10.1063/1.1693881 (cit. on pp. 12, 15, 24, 25, 28, 30, 82, 83, 85, 95).

[17] C.N. Lashmore-Davies and T.J. Martin. "Electrostatic instabilities driven by an electric current perpendicular to a magnetic field." In: *Nuclear Fusion* 13.2 (Mar. 1973), pp. 193–203. ISSN: 0029-5515, 1741-4326. DOI: 10.1088/0029-5515/13/2/007 (cit. on pp. 12, 24, 102).

[18] Y.B. Esipchuk, A.I. Morozov, G.N. Tilinin, and A.V. Trofimov. "Plasma oscillations in closed-drift accelerators with an extended acceleration zone." In: *Soviet Physics Technical Physics* 18 (1974), p. 928 (cit. on p. 14).

[19] N.T. Gladd. "The lower hybrid drift instability and the modified two stream instability in high density theta pinch environments." In: *Plasma Physics* 18.1 (1976), p. 27. DOI: 10.1088/0032-1028/18/1/002 (cit. on p. 82).

[20] G.N. Tilinin. "High-frequency plasma waves in a Hall accelerator with an extended acceleration zone." In: *Soviet Physics Technical Physics* 22 (1977), pp. 974–978 (cit. on pp. 12, 13).

[21] J.M. Beall, Y.C. Kim, and E.J. Powers. "Estimation of wavenumber and frequency spectra using fixed probe pairs." In: *Journal of Applied Physics* 53.6 (June 1982), pp. 3933–3940. ISSN: 0021-8979, 1089-7550. DOI: 10.1063/1.331279 (cit. on pp. 38, 108).

[22] F.F. Chen. *Introduction to plasma physics and controlled fusion*. 2nd ed. New York: Plenum Press, 1984. ISBN: 978-0-306-41332-2 (cit. on pp. 11, 30, 36, 37).

[23] C.K. Birdsall and A.B. Langdon. *Plasma physics via computer simulation*. New York: McGraw-Hill, 1985. ISBN: 978-0-07-005371-7 (cit. on pp. 45, 47, 55, 73, 84).

[24] S.P. Gary and N. Omidi. "The ion-ion acoustic instability." In: *Journal of plasma physics* 37.1 (1987), pp. 45–61. DOI: 10.1017/S0022377800011983 (cit. on p. 12).

[25] E.O. Brigham. *The fast Fourier transform and its applications*. Prentice-Hall, Inc., 1988 (cit. on p. 37).

[26] C.K. Birdsall. "Particle-in-cell charged-particle simulations, plus Monte Carlo collisions with neutral atoms, PIC-MCC." In: *IEEE Transactions on Plasma Science* 19.2 (Apr. 1991), pp. 65–85. ISSN: 00933813. DOI: 10.1109/27.106800 (cit. on pp. 21, 101).

[27] A.S. Boever, V. Kiim, A.S. Koroteev, L.A. Latyshev, A.I. Morozov, G.A. Popov, Y.P. Rylov, and V.V. Zhurin. "State of the Works of Electrical Thrusters in the USSR." In: *22nd International Electric Propulsion Conference, Viareggio, Italy*. Ed. by IEPC. 1991 (cit. on p. 3).

[28] Y. Sakawa, C. Joshi, P.K. Kaw, F.F. Chen, and V.K. Jain. "Excitation of the modified Simon–Hoh instability in an electron beam produced plasma." In: *Physics of Fluids B: Plasma Physics* 5.6 (June 1993), pp. 1681–1694. ISSN: 0899-8221. DOI: 10.1063/1.860803 (cit. on p. 37).

[29] A.V. Phelps. "The application of scattering cross sections to ion flux models in discharge sheaths." In: *Journal of applied physics* 76.2 (1994), pp. 747–753. DOI: 10.1063/1.357820 (cit. on p. 48).

[30] V. Vahedi and M. Surendra. "A Monte Carlo collision model for the particle-in-cell method: applications to argon and oxygen discharges." In: *Computer Physics Communications* 87.1-2 (May 1995), pp. 179–198. ISSN: 00104655. DOI: 10.1016/0010-4655(94)00171-W (cit. on p. 48).

[31] T. Dudok de Wit, V.V. Krasnosel'skikh, S.D. Bale, M.W. Dunlop, H. Lühr, S.J. Schwartz, and L.J.C. Woolliscroft. "Determination of dispersion relations in quasi-stationary plasma turbulence using dual satellite data." In: *Geophysical Research Letters* 22.19 (Oct. 1995), pp. 2653–2656. ISSN: 00948276. DOI: 10.1029/95GL02543 (cit. on pp. 38, 40).

[32] M. Hirakawa and Y. Arakawa. "Numerical simulation of plasma particle behavior in a Hall thruster." In: *32nd Joint Propulsion Conference and Exhibit*. 1996, p. 3195 (cit. on p. 107).

[33] J.P. Boeuf and L. Garrigues. "Low frequency oscillations in a stationary plasma thruster." In: *Journal of Applied Physics* 84.7 (1998), pp. 3541–3554. DOI: 10.1063/1.368529 (cit. on pp. 12, 13, 20).

[34] J. Ashkenazy, A. Fruchtman, Y. Raitses, and N.J. Fisch. "Modelling the behaviour of a Hall current plasma accelerator." In: *Plasma physics and controlled fusion* 41.3A (1999), A357. DOI: 10.1088/0741-3335/41/3A/029E (cit. on p. 20).

[35] J.M. Fife. "Hybrid-PIC Modeling and Electrostatic Probe Survey of Hall Thrusters." PhD thesis. Massachusetts Institute of Technology, Feb. 1999 (cit. on pp. 13, 20, 184, 190).

[36] E.F. Toro. *Riemann solvers and numerical methods for fluid dynamics: a practical introduction*. 2nd ed. Berlin ; New York: Springer-Verlag, 1999. ISBN: 978-3-540-65966-2 (cit. on p. 52).

[37] I. Kaganovich, M. Mišina, S.V. Berezhnoi, and R. Gijbels. "Electron Boltzmann kinetic equation averaged over fast electron bouncing and pitch-angle scattering for fast modeling of electron cyclotron resonance discharge." In: *Physical Review E* 61.2 (Feb. 2000), pp. 1875–1889. ISSN: 1063-651X, 1095-3787. DOI: 10.1103/PhysRevE.61.1875 (cit. on p. 10).

[38] A.I. Morozov and V.V. Savelev. "One-dimensional hybrid model of a stationary plasma thruster." In: *Plasma Physics Reports* 26.10 (2000), pp. 875–880. DOI: 10.1134/1.1316827 (cit. on p. 20).

[39] A.I. Morozov and V.V. Savelyev. *Fundamentals of stationary plasma thrusters theory*. Springer, 2000 (cit. on pp. 3, 11, 12, 21, 24, 163).

[40] E.Y. Choueiri. "Plasma oscillations in Hall thrusters." In: *Physics of Plasmas* 8.4 (2001), p. 1411. ISSN: 1070664X. DOI: 10.1063/1.1354644 (cit. on p. 12).

[41] L. Garrigues, I.D. Boyd, and J.P. Boeuf. "Computation of Hall thruster performance." In: *Journal of Propulsion and Power* 17.4 (2001), pp. 772–779. DOI: 10.2514/2.5832 (cit. on p. 210).

[42] F.S. Gulczinski III and A.D. Gallimore. "Near-field ion energy and species measurements of a 5-kW Hall thruster." In: *Journal of Propulsion and Power* 17.2 (2001), pp. 418–427. DOI: 10.2514/2.5758 (cit. on p. 210).

[43] M. Keidar, I.D. Boyd, and I.I. Beilis. "Plasma flow and plasma-wall transition in Hall thruster channel." In: *Physics of Plasmas* 8.12 (2001), pp. 5315–5322. DOI: 10.1063/1.1421370 (cit. on p. 20).

[44] A.A. Litvak and N.J. Fisch. "Resistive instabilities in Hall current plasma discharge." In: *Phys. Plasmas* 8.2 (2001), p. 5. DOI: 10.1063/1.1336531 (cit. on pp. 14, 24, 33).

[45] N.B. Meezan, W.A. Hargus Jr, and M.A. Cappelli. "Anomalous electron mobility in a coaxial Hall discharge plasma." In: *Physical Review E* 63.2 (2001), p. 026410. DOI: 10.1103/PhysRevE.63.026410 (cit. on p. 11).

[46] J.J. Szabo. "Fully Kinetic Numerical Modeling of a Plasma Thruster." PhD thesis. 2001 (cit. on pp. 21, 46).

[47] R.D. Falgout and U.M. Yang. "hypre: A library of high performance preconditioners." In: *International Conference on computational science*. Springer. 2002, pp. 632–641 (cit. on p. 47).

[48] S. Roy and B.P. Pandey. "Numerical investigation of a Hall thruster plasma." In: *Physics of Plasmas* 9.9 (2002), pp. 4052–4060. DOI: 10.1063/1.1498261 (cit. on p. 20).

[49] G.J. Williams Jr, M.T. Domonkos, and J.M. Chavez. "Measurement of doubly charged ions in ion thruster plumes." In: *27nd International Electric Propulsion Conference*. IEPC. 2002 (cit. on p. 210).

[50] E. Ahedo, J.M. Gallardo, and M. Martínez-Sánchez. "Effects of the radial plasma-wall interaction on the Hall thruster discharge." In: *Physics of Plasmas* 10.8 (Aug. 2003), pp. 3397–3409. ISSN: 1070-664X, 1089-7674. DOI: 10.1063/1.1584432 (cit. on pp. 11, 20).

[51] S. Barral, K. Makowski, Z. Peradzyński, N. Gascon, and M. Dudeck. "Wall material effects in stationary plasma thrusters. II. Near-wall and in-wall conductivity." In: *Physics of Plasmas* 10.10 (Oct. 2003), pp. 4137–4152. ISSN: 1070-664X, 1089-7674. DOI: 10.1063/1.1611881 (cit. on pp. 10, 20).

[52] L. Garrigues, G.J.M. Hagelaar, J. Bareilles, C. Boniface, and J.P. Boeuf. "Model study of the influence of the magnetic field configuration on the performance and lifetime of a Hall thruster." In: *Physics of Plasmas* 10.12 (2003), pp. 4886–4892. DOI: 10.1063/1.1622670 (cit. on p. 20).

[53] N. Gascon, M. Dudeck, and S. Barral. "Wall material effects in stationary plasma thrusters. I. Parametric studies of an SPT-100." In: *Physics of Plasmas* 10.10 (2003), pp. 4123–4136. DOI: 10.1063/1.1611880 (cit. on p. 10).

[54] G.J.M. Hagelaar, J. Bareilles, L. Garrigues, and J.P. Boeuf. "Role of anomalous electron transport in a stationary plasma thruster simulation." In: *Journal of Applied Physics* 93.1 (Jan. 2003), pp. 67–75. ISSN: 0021-8979, 1089-7550. DOI: 10.1063/1.1527218 (cit. on pp. 14, 20, 24, 33).

[55] J.C. Adam, A. Héron, and G. Laval. "Study of stationary plasma thrusters using two-dimensional fully kinetic simulations." In: *Phys. Plasmas* 11.1 (2004), p. 12. DOI: 10.1063/1.1632904 (cit. on pp. 11, 21, 24, 82, 138).

[56] E.Y. Choueiri. "A critical history of electric propulsion: The first 50 years (1906-1956)." In: *Journal of propulsion and power* 20.2 (2004), pp. 193–203. DOI: 10.2514/1.9245 (cit. on p. 3).

[57] M. Keidar, I.D. Boyd, and I.I. Beilis. "Modeling of a high-power thruster with anode layer." In: *Physics of plasmas* 11.4 (2004), pp. 1715–1722. DOI: 10.1063/1.1421370 (cit. on p. 20).

[58] F. Taccogna, S. Longo, M. Capitelli, and R. Schneider. "Stationary plasma thruster simulation." In: *Computer Physics Communications* 164 (2004). DOI: 10.1016/j.cpc.2004.06.025 (cit. on p. 46).

[59] S. Barral, K. Makowski, Z. Peradzyński, and M. Dudeck. "Transit-time instability in Hall thrusters." In: *Physics of Plasmas* 12.7 (July 2005), p. 073504. ISSN: 1070-664X, 1089-7674. DOI: 10.1063/1.1947796 (cit. on pp. 12, 14, 24, 28, 33, 163).

[60] P. Chabert. *Propulseur à Plasma électronégatif*. Tech. rep. French patent number, 2005 (cit. on p. 44).

[61] S. Chable and F. Rogier. "Numerical investigation and modeling of stationary plasma thruster low frequency oscillations." In: *Physics of Plasmas* 12.3 (Mar. 2005), p. 033504. ISSN: 1070-664X, 1089-7674. DOI: 10.1063/1.1857913 (cit. on p. 34).

[62] G.J.M. Hagelaar and L.C. Pitchford. "Solving the Boltzmann equation to obtain electron transport coefficients and rate coefficients for fluid models." In: *Plasma sources science and technology* 14.4 (2005), p. 722. DOI: 10.1088/0963-0252/14/4/011 (cit. on p. 19).

[63] M.A. Lieberman and A.J. Lichtenberg. *Principles of plasma discharges and materials processing*. John Wiley & Sons, 2005 (cit. on pp. 16, 142).

[64] F. Taccogna, S. Longo, M. Capitelli, and R. Schneider. "Self-similarity in Hall plasma discharges: Applications to particle models." In: *Physics of Plasmas* 12.5 (2005), p. 053502. DOI: 10.1063/1.1877517 (cit. on pp. 21, 46).

[65] A. Ducrocq. "Rôle des instabilités électroniques de dérive dans le transport électronique du propulseur à effet Hall." PhD thesis. Ecole Polytechnique, 2006 (cit. on pp. 11, 12).

[66] A. Ducrocq, J.C. Adam, A. Héron, and G. Laval. "High-frequency electron drift instability in the cross-field configuration of Hall thrusters." In: *Physics of Plasmas* 13.10 (Oct. 2006), p. 102111. ISSN: 1070-664X, 1089-7674. DOI: 10.1063/1.2359718 (cit. on pp. 14, 21, 24, 27, 29, 108).

[67] L. Garrigues, G.J.M. Hagelaar, C. Boniface, and J.P. Boeuf. "Anomalous conductivity and secondary electron emission in Hall effect thrusters." In: *Journal of applied physics* 100.12 (2006), p. 123301. DOI: 10.1063/1.2401773 (cit. on p. 11).

[68] J.W. Koo and I.D. Boyd. "Modeling of anomalous electron mobility in Hall thrusters." In: *Physics of Plasmas* 13.3 (Mar. 2006), p. 033501. ISSN: 1070-664X, 1089-7674. DOI: 10.1063/1.2172191 (cit. on p. 11).

[69] M.K. Scharfe, N. Gascon, M.A. Cappelli, and E. Fernandez. "Comparison of hybrid Hall thruster model to experimental measurements." In: *Physics of Plasmas* 13.8 (Aug. 2006), p. 083505. ISSN: 1070-664X, 1089-7674. DOI: 10.1063/1.2336186 (cit. on p. 20).

[70] D. Sydorenko, A.I. Smolyakov, I. Kaganovich, and Y. Raitses. "Kinetic simulation of secondary electron emission effects in Hall thrusters." In: *Physics of Plasmas* 13.1 (Jan. 2006), p. 014501. ISSN: 1070-664X, 1089-7674. DOI: 10.1063/1.2158698 (cit. on pp. 10, 21).

[71] I.D. Kaganovich, Y. Raitses, D. Sydorenko, and A.I. Smolyakov. "Kinetic effects in a Hall thruster discharge." In: *Physics of Plasmas* 14.5 (May 2007), p. 057104. ISSN: 1070-664X, 1089-7674. DOI: 10.1063/1.2709865 (cit. on pp. 10, 163).

[72] D. Sydorenko, A.I. Smolyakov, I. Kaganovich, and Y. Raitses. "Effects of non-Maxwellian electron velocity distribution function on two-stream instability in low-pressure discharges." In: *Physics of Plasmas* 14.1 (2007), p. 013508. DOI: 10.1063/1.2435315 (cit. on p. 21).

[73] F. Taccogna, S. Longo, M. Capitelli, and R. Schneider. "Particle-in-Cell Simulation of Stationary Plasma Thruster." In: *Contributions to Plasma Physics* 47.8-9 (2007), pp. 635–656 (cit. on p. 21).

[74] J.C. Adam, J.P. Boeuf, N. Dubuit, M. Dudeck, L. Garrigues, D. Gresillon, A. Heron, G.J.M. Hagelaar, V. Kulaev, N. Lemoine, S. Mazouffre, J. Perez Luna, V. Pisarev, and S. Tsikata. "Physics, simulation and diagnostics of Hall effect thrusters." In: *Plasma Physics and Controlled Fusion* 50.12 (Dec. 2008), p. 124041. ISSN: 0741-3335, 1361-6587. DOI: 10.1088/0741-3335/50/12/124041 (cit. on pp. 11, 24).

[75] E. Fernandez, M.K. Scharfe, C.A. Thomas, N. Gascon, and M.A. Cappelli. "Growth of resistive instabilities in E×B plasma discharge simulations." In: *Physics of Plasmas* 15.1 (Jan. 2008), p. 012102. ISSN: 1070-664X, 1089-7674. DOI: 10.1063/1.2823033 (cit. on pp. 14, 20, 24, 28, 33–35, 67, 108, 115, 128).

[76] D.M. Goebel and I. Katz. *Fundamentals of Electric Propulsion: Ion and Hall Thrusters*. JPL space science and technology series. Wiley, 2008 (cit. on pp. 5, 6, 11, 179, 193).

[77] D. Sydorenko, A.I. Smolyakov, I. Kaganovich, and Y. Raitses. "Plasma-sheath instability in Hall thrusters due to periodic modulation of the energy of secondary electrons in cyclotron motion." In: *Physics of Plasmas* 15.5 (2008), p. 053506. DOI: 10.1063/1.2918333 (cit. on pp. 10, 21, 163).

[78] S. Barral and E. Ahedo. "Low-frequency model of breathing oscillations in Hall discharges." In: *Physical Review E* 79.4 (Apr. 2009), p. 046401. ISSN: 1539-3755, 1550-2376. DOI: 10.1103/PhysRevE.79.046401 (cit. on pp. 12, 13, 172).

[79] S. Tsikata, N. Lemoine, V. Pisarev, and D.M. Gresillon. "Dispersion relations of electron density fluctuations in a Hall thruster plasma, observed by collective light scattering." In: *Physics of Plasmas* 16.3 (2009), p. 033506. DOI: 10.1063/1.3093261 (cit. on pp. 11, 14).

[80] P.J. Schmid. "Dynamic mode decomposition of numerical and experimental data." In: *Journal of Fluid Mechanics* 656 (Aug. 2010), pp. 5–28. ISSN: 0022-1120, 1469-7645. DOI: 10.1017/S0022112010001217 (cit. on pp. 41, 97).

[81] S. Tsikata, C. Honoré, N. Lemoine, and D.M. Grésillon. "Three-dimensional structure of electron density fluctuations in the Hall thruster plasma: E× B mode." In: *Physics of Plasmas* 17.11 (2010), p. 112110. DOI: 10.1063/1.3499350 (cit. on pp. 11, 14).

[82] S. Barral and J. Miedzik. "Numerical investigation of closed-loop control for Hall accelerators." In: *Journal of Applied Physics* 109.1 (Jan. 2011), p. 013302. ISSN: 0021-8979, 1089-7550. DOI: 10.1063/1.3514151 (cit. on pp. 69, 71, 108).

[83] P. Chabert and N. Braithwaite. *Physics of Radio-Frequency Plasmas*. Cambridge University Press, 2011. ISBN: 978-0-521-76300-4 (cit. on pp. 10, 139, 142, 162).

[84] K. Dannenmayer and S. Mazouffre. "Elementary scaling relations for Hall effect thrusters." In: *Journal of Propulsion and Power* 27.1 (2011), pp. 236–245. DOI: 10.2514/1.48382 (cit. on p. 15).

[85] Y. Raitses, I.D. Kaganovich, A. Khrabrov, D. Sydorenko, N.J. Fisch, and A.I. Smolyakov. "Effect of Secondary Electron Emission on Electron Cross-Field Current in E×B Discharges." In: *IEEE Transactions on Plasma Science* 39.4 (2011), pp. 995–1006. DOI: 10.1109/TPS.2011.2109403 (cit. on p. 10).

[86] Antares Development Team. *Antares Documentation Release 1.15.0*. https://cerfacs.fr/antares/. 2012–2020 (cit. on p. 41).

[87] C.L. Ellison, Y. Raitses, and N.J. Fisch. "Cross-field electron transport induced by a rotating spoke in a cylindrical Hall thruster." In: *Physics of Plasmas* 19.1 (2012), p. 013503. DOI: 10.1063/1.3671920 (cit. on p. 12).

[88] W. Frias, A.I. Smolyakov, I.D. Kaganovich, and Y. Raitses. "Long wavelength gradient drift instability in Hall plasma devices. I. Fluid theory." In: *Physics of Plasmas* 19.7 (July 2012), p. 072112. ISSN: 1070-664X, 1089-7674. DOI: 10.1063/1.4736997 (cit. on p. 37).

[89] I.G. Mikellides and I. Katz. "Numerical simulations of Hall-effect plasma accelerators on a magnetic-field-aligned mesh." In: *Physical Review E* 86.4 (Oct. 2012), p. 046703. ISSN: 1539-3755, 1550-2376. DOI: 10.1103/PhysRevE.86.046703 (cit. on p. 20).

[90] M. Moisan and J. Pelletier. *Physics of collisional plasmas: introduction to high-frequency discharges*. Dordrecht New York: Springer, 2012. ISBN: 978-94-007-4558-2 (cit. on p. 17).

[91] T. Umeda, Y. Kidani, S. Matsukiyo, and R. Yamazaki. "Modified two-stream instability at perpendicular collisionless shocks: Full particle simulations: microinstability at perpendicular shocks." In: *Journal of Geophysical Research: Space Physics* 117.A3 (Mar. 2012), n/a–n/a. ISSN: 01480227. DOI: 10.1029/2011JA017182 (cit. on p. 83).

[92] J. Cavalier, N. Lemoine, G. Bonhomme, S. Tsikata, C. Honoré, and D. Grésillon. "Hall thruster plasma fluctuations identified as the E×B electron drift instability: Modeling and fitting on experimental data." In: *Physics of Plasmas* 20.8 (Aug. 2013), p. 082107. ISSN: 1070-664X, 1089-7674. DOI: 10.1063/1.4817743 (cit. on pp. 14, 24, 29, 67, 91, 108).

[93] S. Cho, K. Komurasaki, and Y. Arakawa. "Kinetic particle simulation of discharge and wall erosion of a Hall thruster." In: *Physics of Plasmas* 20.6 (2013), p. 063501. DOI: 10.1063/1.4810798 (cit. on p. 46).

[94] A. Héron and J.C. Adam. "Anomalous conductivity in Hall thrusters: Effects of the non-linear coupling of the electron-cyclotron drift instability with secondary electron emission of the walls." In: *Physics of Plasmas* 20.8 (Aug. 2013), p. 082313. ISSN: 1070-664X, 1089-7674. DOI: 10.1063/1.4818796 (cit. on pp. 15, 21, 24, 49, 50, 82, 83).

[95] H. Qin, S. Zhang, J. Xiao, J. Liu, Y. Sun, and W.M. Tang. "Why is Boris algorithm so good?" In: *Physics of Plasmas* 20.8 (Aug. 2013), p. 084503. ISSN: 1070-664X, 1089-7674. DOI: 10.1063/1.4818428 (cit. on p. 47).

[96] M.M. Turner, A. Derzsi, Z. Donkó, D. Eremin, S.J. Kelly, T. Lafleur, and T. Mussenbrock. "Simulation benchmarks for low-pressure plasmas: Capacitive discharges." In: *Physics of Plasmas* 20.1 (Jan. 2013), p. 013507. ISSN: 1070-664X, 1089-7674. DOI: 10.1063/1.4775084 (cit. on pp. 54, 100).

[97] J.P. Boeuf. "Rotating structures in low temperature magnetized plasmas—insight from particle simulations." In: *Frontiers in Physics* 2 (2014), p. 74. DOI: 10.3389/fphy.2014.00074 (cit. on p. 21).

[98] P. Chabert. "What is the size of a floating sheath?" In: *Plasma Sources Science and Technology* 23.6 (Oct. 2014), p. 065042. ISSN: 0963-0252, 1361-6595. DOI: 10.1088/0963-0252/23/6/065042 (cit. on p. 142).

[99] P. Coche and L. Garrigues. "A two-dimensional (azimuthal-axial) particle-in-cell model of a Hall thruster." In: *Physics of Plasmas* 21.2 (Feb. 2014), p. 023503. ISSN: 1070-664X, 1089-7674. DOI: 10.1063/1.4864625 (cit. on pp. 11, 12, 15, 21, 24, 108, 124, 138, 139).

[100] G. Fubiani and J.P. Boeuf. "Plasma asymmetry due to the magnetic filter in fusion-type negative ion sources: Comparisons between two and three-dimensional particle-in-cell simulations." In: *Physics of Plasmas* 21.7 (July 2014), p. 073512. ISSN: 1070-664X, 1089-7674. DOI: 10.1063/1.4891658 (cit. on p. 138).

[101] S. Cho, H. Watanabe, K. Kubota, S. Iihara, K. Fuchigami, K. Uematsu, and I. Funaki. "Study of electron transport in a Hall thruster by axial–radial fully kinetic particle simulation." In: *Physics of Plasmas* 22.10 (2015), p. 103523. DOI: 10.1063/1.4935049 (cit. on p. 21).

[102] I. Katz, I.G. Mikellides, B.A. Jorns, and A. Lopez Ortega. "Hall2De simulations with an anomalous transport model based on the electron cyclotron drift instability." In: *34nd International Electric Propulsion Conference*. Vol. 402. 2015 (cit. on p. 11).

[103] S. Tsikata and T. Minea. "Modulated Electron Cyclotron Drift Instability in a High-Power Pulsed Magnetron Discharge." In: *Physical Review Letters* 114.18 (May 2015), p. 185001. ISSN: 0031-9007, 1079-7114. DOI: 10.1103/PhysRevLett.114.185001 (cit. on pp. 14, 24).

[104] J. Vaudolon and S. Mazouffre. "Observation of high-frequency ion instabilities in a cross-field plasma." In: *Plasma Sources Science and Technology* 24.3 (2015), p. 032003. DOI: 10.1088/0963-0252/24/3/032003 (cit. on p. 14).

[105] T. Lafleur, S.D. Baalrud, and P. Chabert. "Theory for the anomalous electron transport in Hall effect thrusters. I. Insights from particle-in-cell simulations." In: *Physics of Plasmas* 23.5 (May 2016), p. 053502. ISSN: 1070-664X, 1089-7674. DOI: 10.1063/1.4948495 (cit. on pp. 11, 14, 21, 24, 51, 64, 82, 83, 95, 122, 138, 159).

[106] T. Lafleur, S.D. Baalrud, and P. Chabert. "Theory for the anomalous electron transport in Hall effect thrusters. II. Kinetic model." In: *Physics of Plasmas* 23.5 (May 2016), p. 053503. ISSN: 1070-664X, 1089-7674. DOI: 10.1063/1.4948496 (cit. on pp. 11, 14, 15, 24, 28, 29, 63, 82, 95, 98, 101, 138).

[107] V.P. Lakhin, V.I. Ilgisonis, A.I. Smolyakov, and E.A. Sorokina. "Nonlinear excitation of long-wavelength modes in Hall plasmas." In: *Physics of Plasmas* 23.10 (Oct. 2016), p. 102304. ISSN: 1070-664X, 1089-7674. DOI: 10.1063/1.4964724 (cit. on p. 98).

[108] S. Mazouffre. "Electric propulsion for satellites and spacecraft: established technologies and novel approaches." In: *Plasma Sources Science and Technology* 25.3 (2016), p. 033002. DOI: 10.1088/0963-0252/25/3/033002 (cit. on p. 5).

[109] I.G. Mikellides, B. Jorns, I. Katz, and A. Lopez Ortega. "Hall2De simulations with a first-principles electron transport model based on the electron cyclotron drift instability." In: *52nd AIAA/SAE/ASEE Joint Propulsion Conference*. 2016, p. 4618 (cit. on p. 20).

[110] J.P. Boeuf. "Tutorial: Physics and modeling of Hall thrusters." In: *Journal of Applied Physics* 121.1 (Jan. 2017), p. 011101. ISSN: 0021-8979, 1089-7550. DOI: 10.1063/1.4972269 (cit. on pp. 7, 24, 28, 84).

[111] J.P. Boeuf and A.I. Smolyakov. *LANDMARK, Low temperAture magNetizeD plasMA benchmaRKs*. https://jpb911.wixsite.com/landmark/contact. 2017 (cit. on p. 100).

[112] V. Croes. "Modélisation bidimensionnelle de la décharge plasma dans un propulseur de Hall." PhD thesis. Université Paris-Saclay, 2017 (cit. on pp. 21, 22, 44, 46, 54, 82, 83, 207).

[113] V. Croes, T. Lafleur, Z. Bonaventura, A. Bourdon, and P. Chabert. "2D particle-in-cell simulations of the electron drift instability and associated anomalous electron transport in Hall-effect thrusters." In: *Plasma Sources Science and Technology* 26.3 (Feb. 2017), p. 034001. ISSN: 1361-6595. DOI: 10.1088/1361-6595/aa550f (cit. on pp. 12, 15, 21, 28, 51, 82, 83, 101, 138).

[114] G. Fubiani, L. Garrigues, G.J.M. Hagelaar, N. Kohen, and J.P. Boeuf. "Modeling of plasma transport and negative ion extraction in a magnetized radio-frequency plasma source." In: *New Journal of Physics* 19.1 (Jan. 2017), p. 015002. ISSN: 1367-2630. DOI: 10.1088/1367-2630/19/1/015002 (cit. on pp. 46, 138, 139, 155).

[115] L. Grimaud and S. Mazouffre. "Ion behavior in low-power magnetically shielded and unshielded Hall thrusters." In: *Plasma Sources Science and Technology* 26.5 (2017), p. 055020. DOI: 10.1088/1361-6595/aa660d (cit. on p. 14).

[116] K. Hara and S. Cho. "Radial-azimuthal particle-in-cell simulation of a Hall effect thruster." In: *35nd International Electric Propulsion Conference, Atlanta, GA, October 2017*. 2017, pp. 2017–495 (cit. on p. 82).

[117] T. Lafleur, S.D. Baalrud, and P. Chabert. "Characteristics and transport effects of the electron drift instability in Hall-effect thrusters." In: *Plasma Sources Science and Technology* 26.2 (Jan. 2017), p. 024008. ISSN: 1361-6595. DOI: 10.1088/1361-6595/aa56e2 (cit. on pp. 11, 12, 14, 28, 82).

[118] T. Lafleur and P. Chabert. "The role of instability-enhanced friction on 'anomalous' electron and ion transport in Hall-effect thrusters." In: *Plasma Sources Science and Technology* 27.1 (Dec. 2017), p. 015003. ISSN: 1361-6595. DOI: 10.1088/1361-6595/aa9efe (cit. on pp. 11, 14, 21, 22, 24, 28, 82, 95, 98, 112, 118, 122, 124, 128).

[119] L.C. Pitchford, L.L. Alves, K. Bartschat, S.F. Biagi, M.C. Bordage, I. Bray, C.E. Brion, M.J. Brunger, L. Campbell, A. Chachereau, et al. "Lxcat: An open-access, web-based platform for data needed for modeling low temperature plasmas." In: *Plasma Processes and Polymers* 14.1-2 (2017), p. 1600098. DOI: 10.1002/ppap.201600098 (cit. on p. 47).

[120] G. Sary, L. Garrigues, and J.P. Boeuf. "Hollow cathode modeling: I. A coupled plasma thermal two-dimensional model." In: *Plasma Sources Science and Technology* 26.5 (Mar. 2017), p. 055007. ISSN: 1361-6595. DOI: 10.1088/1361-6595/aa6217 (cit. on p. 201).

[121] G. Sary, L. Garrigues, and J.P. Boeuf. "Hollow cathode modeling: II. Physical analysis and parametric study." In: *Plasma Sources Science and Technology* 26.5 (Mar. 2017), p. 055008. ISSN: 1361-6595. DOI: 10.1088/1361-6595/aa6210 (cit. on p. 201).

[122] A.I. Smolyakov, O. Chapurin, W. Frias, O. Koshkarov, I. Romadanov, T. Tang, M. Umansky, Y. Raitses, I.D. Kaganovich, and V.P. Lakhin. "Fluid theory and simulations of instabilities, turbulent transport and coherent structures in partially-magnetized plasmas of E × B discharges." In: *Plasma Physics and Controlled Fusion* 59.1 (Jan. 2017), p. 014041. ISSN: 0741-3335, 1361-6587. DOI: 10.1088/0741-3335/59/1/014041 (cit. on pp. 25, 35, 37).

[123] T. Andreussi, V. Giannetti, A. Leporini, M.M. Saravia, and M. Andrenucci. "Influence of the magnetic field configuration on the plasma flow in Hall thrusters." In: *Plasma Physics and Controlled Fusion* 60.1 (Jan. 2018), p. 014015. ISSN: 0741-3335, 1361-6587. DOI: 10.1088/1361-6587/aa8c4d (cit. on p. 20).

[124] J.P. Boeuf and L. Garrigues. "E × B electron drift instability in Hall thrusters: Particle-in-cell simulations vs. theory." In: *Physics of Plasmas* 25.6 (June 2018), p. 061204. ISSN: 1070-664X, 1089-7674. DOI: 10.1063/1.5017033 (cit. on pp. 15, 21, 108, 177).

[125] V. Croes, A. Tavant, R. Lucken, R. Martorelli, T. Lafleur, A. Bourdon, and P. Chabert. "The effect of alternative propellants on the electron drift instability in Hall-effect thrusters: Insight from 2D particle-in-cell simulations." In: *Physics of Plasmas* 25.6 (June 2018), p. 063522. ISSN: 1070-664X, 1089-7674. DOI: 10.1063/1.5033492 (cit. on p. 197).

[126] A. Domínguez Vázquez, F. Taccogna, and E. Ahedo. "Particle modeling of radial electron dynamics in a controlled discharge of a Hall thruster." In: *Plasma Sources Science and Technology* 27.6 (June 2018), p. 064006. ISSN: 1361-6595. DOI: 10.1088/1361-6595/aac968 (cit. on p. 49).

[127] K. Hara and K. Hanquist. "Test cases for grid-based direct kinetic modeling of plasma flows." In: *Plasma Sources Science and Technology* 27.6 (2018), p. 065004. DOI: 10.1088/1361-6595/aac6b9 (cit. on p. 21).

[128] S. Janhunen, A.I. Smolyakov, O. Chapurin, D. Sydorenko, I. Kaganovich, and Y. Raitses. "Nonlinear structures and anomalous transport in partially magnetized E×B plasmas." In: *Physics of Plasmas* 25.1 (Jan. 2018), p. 011608. ISSN: 1070-664X, 1089-7674. DOI: 10.1063/1.5001206 (cit. on pp. 15, 21, 83, 98).

[129] S. Janhunen, A.I. Smolyakov, D. Sydorenko, M. Jimenez, I. Kaganovich, and Y. Raitses. "Evolution of the electron cyclotron drift instability in two-dimensions." In: *Physics of Plasmas* 25.8 (Aug. 2018), p. 082308. ISSN: 1070-664X, 1089-7674. DOI: 10.1063/1.5033896 (cit. on pp. 15, 21, 24, 28, 30, 33, 50, 82–85, 94, 98, 105, 106, 108).

[130] V. Joncquieres, F. Pechereau, A. Alvarez Laguna, A. Bourdon, O. Vermorel, and B. Cuenot. "A 10-moment fluid numerical solver of plasma with sheaths in a Hall Effect Thruster." In: *2018 Joint Propulsion Conference*. 2018, p. 4905 (cit. on p. 20).

[131] I. Katz, V.H. Chaplin, and A. Lopez Ortega. "Particle-in-cell simulations of Hall thruster acceleration and near plume regions." In: *Physics of Plasmas* 25.12 (2018), p. 123504. DOI: 10.1063/1.5054009 (cit. on p. 21).

[132] O. Koshkarov, A.I. Smolyakov, I.V. Romadanov, O. Chapurin, M.V. Umansky, Y. Raitses, and I.D. Kaganovich. "Current flow instability and nonlinear structures in dissipative two-fluid plasmas." In: *Physics of Plasmas* 25.1 (Jan. 2018), p. 011604. ISSN: 1070-664X, 1089-7674. DOI: 10.1063/1.5017521 (cit. on pp. 14, 20, 24, 34–36, 130, 157).

[133] T. Lafleur, R. Martorelli, P. Chabert, and A. Bourdon. "Anomalous electron transport in Hall-effect thrusters: Comparison between quasi-linear kinetic theory and particle-in-cell simulations." In: *Physics of Plasmas* 25.6 (June 2018), p. 061202. ISSN: 1070-664X, 1089-7674. DOI: 10.1063/1.5017626 (cit. on pp. 11, 12, 14, 20, 21, 24, 66, 82, 95, 108, 179).

[134] A.T. Powis, J.A. Carlsson, I. D. Kaganovich, Y. Raitses, and A.I. Smolyakov. "Scaling of spoke rotation frequency within a Penning discharge." In: *Physics of Plasmas* 25.7 (July 2018), p. 072110. ISSN: 1070-664X, 1089-7674. DOI: 10.1063/1.5038733 (cit. on p. 46).

[135] F. Taccogna and P. Minelli. "Three-dimensional particle-in-cell model of Hall thruster: The discharge channel." In: *Physics of Plasmas* 25.6 (2018), p. 061208. DOI: 10.1063/1.5023482 (cit. on p. 108).

[136] A. Tavant, V. Croes, R. Lucken, T. Lafleur, A. Bourdon, and P. Chabert. "The effects of secondary electron emission on plasma sheath characteristics and electron transport in an E × B discharge via kinetic simulations." In: *Plasma Sources Science and Technology* 27.12 (Dec. 2018), p. 124001. ISSN: 1361-6595. DOI: 10.1088/1361-6595/aaeccd (cit. on pp. 11, 21, 82–84, 94, 100, 101, 105, 106).

[137] M. Villemant. "Modélisation et caractérisation expérimentale de l'influence de l'émission électronique sur le fonctionnement des propulseurs à courant de Hall." PhD thesis. Institut supérieur de l'Aéronautique et de l'Espace (ISAE), 2018 (cit. on p. 10).

[138] Z. Asadi, F. Taccogna, and M. Sharifian. "Numerical Study of Electron Cyclotron Drift Instability: Application to Hall Thruster." In: *Frontiers in Physics* 7 (Sept. 2019), p. 140. ISSN: 2296-424X. DOI: 10.3389/fphy.2019.00140 (cit. on pp. 15, 95, 101, 112, 118).

[139] Z.A. Brown and B.A. Jorns. "Spatial evolution of small wavelength fluctuations in a Hall Thruster." In: *Physics of Plasmas* 26.11 (Nov. 2019), p. 113504. ISSN: 1070-664X, 1089-7674. DOI: 10.1063/1.5116708 (cit. on pp. 14, 24, 112, 118).

[140] T. Charoy, J.P. Boeuf, A. Bourdon, J.A. Carlsson, P. Chabert, B. Cuenot, D. Eremin, L. Garrigues, K. Hara, I.D. Kaganovich, A.T. Powis, A.I. Smolyakov, D. Sydorenko, A. Tavant, O. Vermorel, and W. Villafana. "2D axial-azimuthal particle-in-cell benchmark for low-temperature partially magnetized plasmas." In: *Plasma Sources Science and Technology* 28.10 (Oct. 2019), p. 105010. ISSN: 1361-6595. DOI: 10.1088/1361-6595/ab46c5 (cit. on pp. 21, 24, 52, 54, 67, 73, 83, 100, 108, 124).

[141] T. Chernyshev, E. Son, and O. Gorshkov. "2D3V kinetic simulation of Hall effect thruster, including azimuthal waves and diamagnetic effect." In: *Journal of Physics D: Applied Physics* 52.44 (2019), p. 444002. DOI: 10.1088/1361-6463/ab35cb (cit. on p. 21).

[142] E.T. Dale and B.A. Jorns. "Non-invasive time-resolved measurements of anomalous collision frequency in a Hall thruster." In: *Physics of Plasmas* 26.1 (Jan. 2019), p. 013516. ISSN: 1070-664X, 1089-7674. DOI: 10.1063/1.5077008 (cit. on p. 109).

[143] Y. Ding, H. Fan, D. Ma, L. Wang, B. Jia, H. Sun, W. Xu, H. Su, L. Wei, H. Li, and D. Yu. "Extending service life of hall thrusters: recent progress and future challenges." In: *Reviews of Modern Plasma Physics* 3.1 (Dec. 2019), p. 15. ISSN: 2367-3192. DOI: 10.1007/s41614-019-0036-y (cit. on p. 3).

[144] K. Hara. "An overview of discharge plasma modeling for Hall effect thrusters." In: *Plasma Sources Science and Technology* 28.4 (Apr. 2019), p. 044001. ISSN: 1361-6595. DOI: 10.1088/1361-6595/ab0f70 (cit. on pp. 24, 83, 101, 108).

[145] O. Koshkarov, A.I. Smolyakov, Y. Raitses, and I. Kaganovich. "Self-Organization, Structures, and Anomalous Transport in Turbulent Partially Magnetized Plasmas with Crossed Electric and Magnetic Fields." In: *Physical Review Letters* 122.18 (May 2019), p. 185001. ISSN: 0031-9007, 1079-7114. DOI: 10.1103/PhysRevLett.122.185001 (cit. on pp. 14, 34, 35).

[146] R. Lucken. "Theory and simulation of low-pressure plasma transport phenomena: Application to the PEGASES Thruster." PhD thesis. Ecole Polytechnique, 2019 (cit. on pp. 44, 47, 48, 54, 198).

[147] R. Martorelli, T. Lafleur, A. Bourdon, and P. Chabert. "Comparison between ad-hoc and instability-induced electron anomalous transport in a 1D fluid simulation of Hall-effect thruster." In: *Physics of Plasmas* 26.8 (2019), p. 083502. DOI: 10.1063/1.5089008 (cit. on p. 11).

[148] A.D. Pierce. *Acoustics: An Introduction to Its Physical Principles and Applications*. Cham: Springer International Publishing, 2019. ISBN: 978-3-030-11213-4 978-3-030-11214-1. DOI: 10.1007/978-3-030-11214-1 (cit. on p. 124).

[149] A.L. Raisanen, K. Hara, and I.D. Boyd. "Two-dimensional hybrid-direct kinetic simulation of a Hall thruster discharge plasma." In: *Physics of Plasmas* 26.12 (Dec. 2019), p. 123515. ISSN: 1070-664X, 1089-7674. DOI: 10.1063/1.5122290 (cit. on pp. 21, 83).

[150] F. Taccogna and L. Garrigues. "Latest progress in Hall thrusters plasma modelling." In: *Reviews of Modern Plasma Physics* 3.1 (Dec. 2019), p. 12. ISSN: 2367-3192. DOI: 10.1007/s41614-019-0033-1 (cit. on pp. 24, 82, 101).

[151] F. Taccogna, P. Minelli, Z. Asadi, and G. Bogopolsky. "Numerical studies of the E × B electron drift instability in Hall thrusters." In: *Plasma Sources Science and Technology* 28.6 (June 2019), p. 064002. ISSN: 1361-6595. DOI: 10.1088/1361-6595/ab08af (cit. on pp. 15, 21, 82, 83).

[152] A. Tavant. "Plasma-wall interaction and electron transport in Hall Effect Thrusters." PhD thesis. Université Paris-Saclay, 2019 (cit. on pp. 21, 22, 44, 49, 51, 53, 54, 82, 138, 139, 163, 207, 217).

[153] A. Tavant, R. Lucken, A. Bourdon, and P. Chabert. "Non-isothermal sheath model for low pressure plasmas." In: *Plasma Sources Science and Technology* 28.7 (July 2019), p. 075007. ISSN: 1361-6595. DOI: 10.1088/1361-6595/ab279b (cit. on pp. 21, 82).

[154] J. Vaudolon, V. Vial, N. Cornu, and I. Habbassi. "PPSRX00 Thruster Development Status at Safran." In: 36nd International Electric Propulsion Conference - Vienna, 2019 (cit. on p. 146).

[155] T. Charoy. "Numerical study of electron transport in Hall thrusters." PhD thesis. Ecole Polytechnique, 2020 (cit. on pp. 22, 44, 51, 52, 54, 108).

[156] T. Charoy, T. Lafleur, A. Tavant, P. Chabert, and A. Bourdon. "A comparison between kinetic theory and particle-in-cell simulations of anomalous electron transport in E × B plasma discharges." In: *Physics of Plasmas* 27.6 (June 2020), p. 063510. ISSN: 1070-664X, 1089-7674. DOI: 10.1063/5.0003978 (cit. on pp. 24, 28, 63, 64, 67, 77, 95, 207).

[157] V. Giannetti, M.M. Saravia, and T. Andreussi. "Measurement of the breathing mode oscillations in Hall thruster plasmas with a fast-diving triple Langmuir probe." In: *Physics of Plasmas* 27.12 (Dec. 2020), p. 123502. ISSN: 1070-664X, 1089-7674. DOI: 10.1063/5.0022928 (cit. on p. 184).

[158] K. Hara and S. Tsikata. "Cross-field electron diffusion due to the coupling of drift-driven microinstabilities." In: *Physical Review E* 102.2 (Aug. 2020), p. 023202. ISSN: 2470-0045, 2470-0053. DOI: 10.1103/PhysRevE.102.023202 (cit. on pp. 24, 124).

[159] K. Holste et al. "Ion thrusters for electric propulsion: Scientific issues developing a niche technology into a game changer." In: *Review of Scientific Instruments* 91.6 (June 2020), p. 061101. ISSN: 0034-6748, 1089-7623. DOI: 10.1063/5.0010134 (cit. on p. 3).

[160] I.D. Kaganovich et al. "Physics of E × B discharges relevant to plasma propulsion and similar technologies." In: *Physics of Plasmas* 27.12 (Dec. 2020), p. 120601. ISSN: 1070-664X, 1089-7674. DOI: 10.1063/5.0010135 (cit. on pp. 15, 82).

[161] I. Levchenko, S. Xu, S. Mazouffre, D. Lev, D. Pedrini, D. Goebel, L. Garrigues, F. Taccogna, and K. Bazaka. "Perspectives, frontiers, and new horizons for plasma-based space electric propulsion." In: *Physics of Plasmas* 27.2 (2020), p. 020601. DOI: 10.1063/1.5109141 (cit. on p. 5).

[162] F. Marmuse. "Iodine plasmas: experimental and numerical studies. Application to electric propulsion." PhD thesis. Sorbonne université, 2020 (cit. on p. 197).

[163] I.G. Mikellides and A. Lopez Ortega. "Growth of the modified two-stream instability in the plume of a magnetically shielded Hall thruster." In: *Physics of Plasmas* 27.10 (Oct. 2020), p. 100701. ISSN: 1070-664X, 1089-7674. DOI: 10.1063/5.0020075 (cit. on pp. 15, 24, 83).

[164] M. Sengupta and A.I. Smolyakov. "Mode transitions in nonlinear evolution of the electron drift instability in a 2D annular E × B system." In: *Physics of Plasmas* 27.2 (Feb. 2020), p. 022309. ISSN: 1070-664X, 1089-7674. DOI: 10.1063/1.5139035 (cit. on pp. 82, 83).

[165] A.I. Smolyakov, T. Zintel, L. Couedel, D. Sydorenko, A. Umnov, E. Sorokina, and N. Marusov. "Anomalous Electron Transport in One-Dimensional Electron Cyclotron Drift Turbulence." In: *Plasma Physics Reports* 46.5 (May 2020), pp. 496–505. ISSN: 1063-780X, 1562-6938. DOI: 10.1134/S1063780X20050086 (cit. on pp. 12, 15).

[166] P. Virtanen et al. "SciPy 1.0: Fundamental Algorithms for Scientific Computing in Python." In: *Nature Methods* 17 (2020), pp. 261–272. DOI: 10.1038/s41592-019-0686-2 (cit. on p. 31).

[167] T. Yuan, J. Ren, J. Zhou, Z. Zhang, Y. Wang, and H. Tang. "The effects of numerical acceleration techniques on PIC-MCC simulations of ion thrusters." In: *AIP Advances* 10.4 (Apr. 2020), p. 045115. ISSN: 2158-3226. DOI: 10.1063/1.5113561 (cit. on p. 46).

[168] Z. Zhang, Z. Zhang, H. Tang, W. Y. L. Ling, Z. Chen, J. Ren, and J. Cao. "Measurement of the distribution of charge exchange ions in a Hall-effect thruster plume." In: *Plasma Sources Science and Technology* 29.8 (2020), p. 085001. DOI: 10.1088/1361-6595/aba12c (cit. on pp. 53, 133).

[169] O. Chapurin, A.I. Smolyakov, G.J.M. Hagelaar, and Y. Raitses. "On the mechanism of ionization oscillations in Hall thrusters." In: *Journal of Applied Physics* 129.23 (June 2021), p. 233307. ISSN: 0021-8979, 1089-7550. DOI: 10.1063/5.0049105 (cit. on pp. 13, 25, 169).

[170] T. Charoy, T. Lafleur, A. Alvarez Laguna, A. Bourdon, and P. Chabert. "The interaction between ion transit-time and electron drift instabilities and their effect on anomalous electron transport in Hall thrusters." In: *Plasma Sources Science and Technology* 30.6 (June 2021), p. 065017. ISSN: 0963-0252, 1361-6595. DOI: 10.1088/1361-6595/ac02b3 (cit. on pp. 14, 24, 28, 35, 56, 57, 64, 67, 73, 76, 108, 109, 112, 118, 122, 130, 156, 165, 172, 179, 201, 209).

[171] E.T. Dale and B.A. Jorns. "Experimental characterization of Hall thruster breathing mode dynamics." In: *Journal of Applied Physics* 130.13 (Oct. 2021), p. 133302. ISSN: 0021-8979, 1089-7550. DOI: 10.1063/5.0046048 (cit. on pp. 130, 184).

[172] D.M. Goebel, G. Becatti, I.G. Mikellides, and A. Lopez Ortega. "Plasma hollow cathodes." In: *Journal of Applied Physics* 130.5 (Aug. 2021), p. 050902. ISSN: 0021-8979, 1089-7550. DOI: 10.1063/5.0051228 (cit. on p. 201).

[173] R. Kleiber, M. Borchardt, A. Könies, and C. Slaby. "Modern methods of signal processing applied to gyrokinetic simulations." In: *Plasma Physics and Controlled Fusion* 63.3 (Mar. 2021), p. 035017. ISSN: 0741-3335, 1361-6587. DOI: 10.1088/1361-6587/abd4c1 (cit. on p. 38).

[174] P. Kumar, S. Tsikata, and K. Hara. "Effects of multiply charged ions on microturbulence-driven electron transport in partially magnetized plasmas." In: *Journal of Applied Physics* 130.17 (Nov. 2021), p. 173307. ISSN: 0021-8979, 1089-7550. DOI: 10.1063/5.0067305 (cit. on p. 24).

[175] T. Lafleur, P. Chabert, and A. Bourdon. "The origin of the breathing mode in Hall thrusters and its stabilization." In: *Journal of Applied Physics* 130.5 (Aug. 2021), p. 053305. ISSN: 0021-8979, 1089-7550. DOI: 10.1063/5.0057095 (cit. on pp. 13, 20, 25, 148, 155, 156, 172, 175).

[176] S. Mazouffre, R. Joussot, B. Vincent, and S. Tsikata. "Discharge and plasma plume characterization of a 100 A-class LaB6 hollow cathode." In: *Journal of Applied Physics* 130.17 (2021), p. 173301. DOI: 10.1063/5.0064535 (cit. on p. 201).

[177] F. Petronio, A. Tavant, T. Charoy, A. Alvarez Laguna, A. Bourdon, and P. Chabert. "Conditions of appearance and dynamics of the modified two-stream instability in E × B discharges." In: *Physics of Plasmas* 28.4 (Apr. 2021), p. 043504. ISSN: 1070-664X, 1089-7674. DOI: 10.1063/5.0046843 (cit. on pp. 15, 21, 23, 24, 28, 30, 32, 81, 82, 84, 87–94, 96, 97, 99, 112, 118, 122).

[178] D. Rafalskyi, J. Martínez Martínez, L. Habl, E. Zorzoli Rossi, P. Proynov, A. Boré, T. Baret, A. Poyet, T. Lafleur, S. Dudin, and A. Aanesland. "In-orbit demonstration of an iodine electric propulsion system." In: *Nature* 599.7885 (Nov. 2021), pp. 411–415. ISSN: 0028-0836, 1476-4687. DOI: 10.1038/s41586-021-04015-y (cit. on p. 197).

[179] W. Villafana. "Numerical Particle-In-Cell studies of Hall thrusters using unstructured grids." PhD thesis. Université de Toulouse, 2021 (cit. on pp. 15, 108).

[180] W. Villafana, F. Petronio, A.C. Denig, M.J. Jimenez, D. Eremin, L. Garrigues, F. Taccogna, A. Alvarez Laguna, J.P. Boeuf, A. Bourdon, P. Chabert, T. Charoy, B. Cuenot, K. Hara, F. Pechereau, A.I. Smolyakov, D. Sydorenko, A. Tavant, and O. Vermorel. "2D radial-azimuthal particle-in-cell benchmark for E × B discharges." In: *Plasma Sources Science and Technology* 30.7 (July 2021), p. 075002. ISSN: 0963-0252, 1361-6595. DOI: 10.1088/1361-6595/ac0a4a (cit. on pp. 15, 21, 24, 28, 81, 82, 100–103, 108, 138, 142, 143).

[181] L. Xu, D. Eremin, and R.P. Brinkmann. "Direct evidence of gradient drift instability being the origin of a rotating spoke in a crossed field plasma." In: *Plasma Sources Science and Technology* 30.7 (July 2021), p. 075013. ISSN: 0963-0252, 1361-6595. DOI: 10.1088/1361-6595/ac0487 (cit. on p. 38).

[182] A. Alvarez Laguna, B. Esteves, A. Bourdon, and P. Chabert. "A regularized high-order moment model to capture non-Maxwellian electron energy distribution function effects in partially ionized plasmas." In: *Physics of Plasmas* 29.8 (Aug. 2022), p. 083507. ISSN: 1070-664X, 1089-7674. DOI: 10.1063/5.0095019 (cit. on pp. 18, 20).

[183] S. Balay et al. *PETSc Web page*. https://petsc.org/. 2022 (cit. on p. 47).

[184] T. Ben Slimane, T. Charoy, A. Leduc, L. Schiesko, A. Bourdon, and P. Chabert. "Comparison of PIC simulation results of Hall Effect Thrusters against OES measurement using a xenon Collisional Radiative Model." In: *37nd International Electric Propulsion Conference*. IEPC. June 2022 (cit. on p. 210).

[185] T. Ben Slimane, C. Honoré, T. Charoy, A. Bourdon, and P. Chabert. "Analysis of small scale fluctuations in Hall effect thrusters using virtual Thomson scattering on PIC simulations." In: *Physics of Plasmas* 29.2 (Feb. 2022), p. 023501. ISSN: 1070-664X, 1089-7674. DOI: 10.1063/5.0073215 (cit. on pp. 64, 108, 112, 124).

[186] O. Chapurin, A.I. Smolyakov, G.J.M. Hagelaar, J.P. Boeuf, and Y. Raitses. "Fluid and hybrid simulations of the ionization instabilities in Hall thruster." In: *Journal of Applied Physics* 132.5 (Aug. 2022), p. 053301. ISSN: 0021-8979, 1089-7550. DOI: 10.1063/5.0094269 (cit. on p. 13).

[187] B. Esteves, F. Marmuse, C. Drag, A. Bourdon, A. Alvarez Laguna, and P. Chabert. "Charged-particles measurements in low-pressure iodine plasmas used for electric propulsion." In: *Plasma Sources Science and Technology* 31.8 (Aug. 2022), p. 085007. ISSN: 0963-0252, 1361-6595. DOI: 10.1088/1361-6595/ac8288 (cit. on p. 197).

[188] F. Faraji, M. Reza, and A. Knoll. "Enhancing one-dimensional particle-in-cell simulations to self-consistently resolve instability-induced electron transport in Hall thrusters." In: *Journal of Applied Physics* 131.19 (May 2022), p. 193302. ISSN: 0021-8979, 1089-7550. DOI: 10.1063/5.0090853 (cit. on p. 216).

[189] V. Giannetti, A. Piragino, C.A. Paissoni, E. Ferrato, D. Estublier, and T. Andreussi. "Experimental scaling laws for the discharge oscillations and performance of Hall thrusters." In: *Journal of Applied Physics* 131.1 (2022), p. 013304. DOI: 10.1063/5.0070945 (cit. on p. 15).

[190] K. Hara, A.R. Mansour, and S. Tsikata. "Theory of gradient drift instabilities in low-temperature, partially magnetised plasmas." In: *Journal of Plasma Physics* 88.4 (Aug. 2022), p. 905880408. ISSN: 0022-3778, 1469-7807. DOI: 10.1017/S002237782200068X (cit. on p. 37).

[191] D.R. Jovel, Mitchell L.R. Walker, and D. Herman. "Review of High-Power Electrostatic and Electrothermal Electric Propulsion." In: *Journal of Propulsion and Power* 38.6 (Nov. 2022), pp. 1051–1081. ISSN: 1533-3876. DOI: 10.2514/1.B38594 (cit. on p. 3).

[192] F. Petronio, A. Alvarez Laguna, A. Bourdon, and P. Chabert. "The introduction of a virtual radial direction in axial-azimuthal PIC simulations of Hall Thrusters." In: Boston, Massachussets, June 2022 (cit. on p. 137).

[193] SAFRAN. *PPS1350 datasheet*. 2022 (cit. on p. 51).

[194] SAFRAN. *PPS5000 datasheet*. 2022 (cit. on p. 3).

[195] SAFRAN. *PPSX00 datasheet*. 2022 (cit. on pp. 146, 161, 162, 167).

[196] L. Schiesko, A. Revel, T. Minea, and E. Carbone. "On the use of ultra-high resolution PIC methods to unveil microscale effects of plasma kinetic instabilities: electron trapping and release by electrostatic tidal effect." In: *Plasma Sources Science and Technology* 31.4 (2022), 04LT01. DOI: 10.1088/1361-6595/ac5eca (cit. on p. 21).

[197] U.K. Seth, G. Hautreux, C. Jourdain, and V. Cameo. "Optimization of the LPPic2D code for scaling magnetized cold plasma simulations." In: (Oct. 2022). Publisher: Zenodo. DOI: 10.5281/ZENODO.7061340 (cit. on pp. 54, 55).

[198] L. Wang, A. Hakim, J. Juno, and B. Srinivasan. "Electron cyclotron drift instability and anomalous transport: two-fluid moment theory and modeling." In: *Plasma Sources Science and Technology* (Sept. 2022). ISSN: 0963-0252, 1361-6595. DOI: 10.1088/1361-6595/ac90e7 (cit. on pp. 12, 15, 20, 24).

[199] F. Faraji, M. Reza, and A. Knoll. "Verification of the generalized reduced-order particle-in-cell scheme in a radial–azimuthal E×B plasma configuration." In: *AIP Advances* 13.2 (2023), p. 025315. DOI: 10.1063/1.5082029 (cit. on pp. 210, 216).

[200] T.F. Munro-O'Brien and C.N. Ryan. "Performance of a low powered magnetically shielded Hall effect thruster with several gaseous propellants." In: *Acta Astronautica* (Jan. 2023), S0094576523000449. ISSN: 00945765. DOI: 10.1016/j.actaastro.2023.01.033 (cit. on p. 197).

[201] F. Petronio, T. Charoy, A. Alvarez Laguna, A. Bourdon, and P. Chabert. "Two-dimensional effects on electrostatic instabilities in Hall Thrusters. I. Insights from particle-in-cell simulations and two-point power spectral density reconstruction techniques." In: *Physics of Plasmas* (Jan. 2023). DOI: 10.1063/5.0119253 (cit. on pp. 21, 28, 44, 63, 64, 71, 73, 74, 107, 110, 111, 113, 114, 116, 117, 120, 180, 216).

[202] F. Petronio, T. Charoy, A. Alvarez Laguna, A. Bourdon, and P. Chabert. "Two-dimensional effects on electrostatic instabilities in Hall Thrusters. II. Comparison of particle-in-cell simulation results with linear theory dispersion relations." In: *Physics of Plasmas* (Jan. 2023). DOI: 10.1063/5.0119255 (cit. on pp. 14, 21, 23, 63, 64, 107, 119, 121, 123, 124, 126–129, 131, 132, 156, 180).

[203] W. Villafana, B. Cuenot, and O. Vermorel. "3D particle-in-cell study of the electron drift instability in a Hall Thruster using unstructured grids." In: *Physics of Plasmas* 30.3 (Mar. 2023), p. 033503. ISSN: 1070-664X, 1089-7674. DOI: 10.1063/5.0133963 (cit. on pp. 15, 108).

DECLARATION

F.P. acknowledges financial support from a Safran Spacecraft Propulsion doctoral research award and the Association Nationale de la Recherche et de la Technologie (ANRT) as part of a CIFRE convention. This work has been partially funded by ANR (No. ANR-16-CHIN-00301) and Safran Spacecraft Propulsion with the project POSEIDON. This work was granted access to the HPC resources of CINES under Allocation Nos. A0080510439, A0100510439 and A0120510439 made by GENCI.

Paris, 2019-2023

Federico Petronio

COLOPHON

This document was typeset using the typographical look-and-feel `classicthesis` developed by André Miede and Ivo Pletikosić. The style was inspired by Robert Bringhurst's seminal book on typography "*The Elements of Typographic Style*". `classicthesis` is available for both LaTeX and LyX:

https://bitbucket.org/amiede/classicthesis/

Happy users of `classicthesis` usually send a real postcard to the author, a collection of postcards received so far is featured here:

http://postcards.miede.de/

Thank you very much for your feedback and contribution.

Final Version as of June 28, 2023 (thesisFP v0.1).

ECOLE
DOCTORALE

Titre : Instabilités dans les plasmas des propulseurs à effet Hall : une étude théorique et numérique

Mots clés : Propulsion électrique, Propulseurs de Hall, Physique des plasmas, instabilités électrostatiques, simulations PIC

Résumé : Les propulseurs à effet Hall (HTs) sont des systèmes de propulsion électrique utilisés dans diverses applications spatiales. La configuration des HTs permet l'ionisation d'un gaz propulseur et l'accélération des ions pour créer une poussée. Actuellement, pour répondre rapidement aux enjeux de l'industrie spatiale, il devient crucial de développer une méthodologie expérimentale/numérique qui puisse proposer des designs innovants pour ces propulseurs. Dans ce cadre, cette thèse présente des résultats théoriques et numériques sur la physique des plasmas froids magnétisés à basse pression dans les plans radial-azimutal et axial-azimutal d'un HT. Une analyse détaillée des instabilités, qui affectent fortement la durée de vie des HTs, est effectuée. Ensuite, ce travail étudie l'origine de la croissance des instabilités et leur rôle dans le transport anormal des électrons, qui a un rapport direct avec la performance du propulseur. L'influence de différents paramètres d'entrée sur les caractéristiques de la décharge suggère qu'un code PIC 2D pourrait être utilisé pour sélectionner des conditions/configurations potentiellement intéressantes.

Title : Plasma instabilities in Hall Thrusters: a theoretical and numerical study

Keywords : Electric propulsion, Hall thrusters, plasma physics, electrostatic instabilities, PIC simulations

Abstract : Hall thrusters (HTs) are electric propulsion systems used in various space applications. The configuration of HTs allows for the ionization of propellant gas and the acceleration of ions to create thrust. There is currently a need to develop an experimental/numerical methodology to propose innovative designs for the space industry. Towards this objective, this thesis presents theoretical and simulation results on the physics of low-temperature low-pressure magnetized plasmas in the radial-azimuthal and axial-azimuthal planes of a HT. In this work, a detailed analysis of the instabilities in HTs, strongly affecting the device lifetime, is carried out to explain the origin of their growth and underline their role in the anomalous transport of electrons, which has a direct relevance in the thruster performance. The influence of different input parameters on the discharge characteristics has been studied and suggests that a 2D PIC code could be used to select potentially interesting conditions/configurations.

Institut Polytechnique de Paris
91120 Palaiseau, France